NANOMATERIAL MODIFICATION FOR BIOCONJUGATION AND ENHANCED STABILITY TOWARDS OPTICAL SENSOR DEVELOPMENT

A Dissertation

by

ASHVIN T. NAGARAJA

Submitted to the Office of Graduate and Professional Studies of
Texas A&M University
in partial fulfillment of the requirements for the degree of

DOCTOR OF PHILOSOPHY

Chair of Committee, Michael J. McShane
Committee Members, Kenith E. Meissner
Brian E. Applegate
James D. Batteas
Head of Department, Anthony Guiseppi-Elie

December 2015

Major Subject: Biomedical Engineering

ABSTRACT

The evolving field of nanomaterial synthesis needs adaptable techniques for the modification and construction of multifunctional components. In this work, a unique layer-by-layer (LbL) method is demonstrated as a generic pathway for nanomaterial stabilization and bioconjugation, facilitating manipulation and handling for new applications. In particular, nanomaterials have unique optical properties that can potentially improve the sensitivity and long-term performance in applications such as optical biosensors, particularly those based on energy transfer. However, the reproducible integration of nanomaterials into stable assays remains a significant challenge. Therefore, the generalized LbL technique was specifically applied towards the fabrication of a novel nanomaterial-enabled optical sensor.

The broader implications of this LbL technique on nanoparticles were explored by characterizing the capabilities and performance of multiple nanoscale core materials and prospective polymer coatings. The modified nanomaterials were characterized for their colloidal and optical stability under varying pH, buffer, and ionic strength conditions. A single bilayer coating of weak and weak-strong polymers using the developed procedure was capable of imparting colloidal stability with a minimal hydrodynamic size increase; an essential feature for energy transfer sensors.

The application of this LbL coating was demonstrated for the construction of a nanomaterial-enabled energy transfer sensor utilizing concanavalin A (ConA)-coated gold nanorods (energy acceptors) combined with fluorescent gold nanoclusters (NCs)

grown within ovalbumin (OVA) (energy donors). The successful construction of the sensor components was verified and the concept demonstrated *via* reversible quenching in the presence of increasing glucose concentrations.

Calcium carbonate was explored as a porous template for the encapsulation of affinity sensing chemistry. The entire process was studied; synthesis of the carbonate template, capsule formation *via* LbL, and dissolution of carbonate to form a hollow capsule, along with the incorporation of assay components using co-precipitation. The knowledge gained provides fundamental insight for improving the function of sensor schemes utilizing carbonate and to guide future considerations for encapsulation.

These results demonstrate significant advances for the reliable fabrication of nanomaterial-enabled optical sensors. The fundamental knowledge and experimental expertise developed shall guide the rational design of future sensor iterations for improved performance.

ACKNOWLEDGEMENTS

I would like to thank my committee chair, Dr. McShane, for all his guidance and support. I would like to thank my committee member, Dr. Meissner, for his extensive contributions to the content of this dissertation and towards my development as a researcher. I would also like to thank my other committee members, Dr. Batteas and Dr. Applegate, for their support throughout the course of this research.

I would like to thank all the current and past members of the BioSyM lab for their help and encouragement. In particular, I would like to thank Yil-Hwan You for his significant contributions in all aspects of this work and for teaching me about many principles of materials science. I would like to thank Aniket Biswas for his contributions for the fabrication of nanocapsules and nanomaterial sizing. I would like to thank Dr. Ravish Majithia and Dr. Aishwarya Sooresh for their contributions with the quantum dot portions of this dissertation. I would like to thank Andrea Locke for her contributions towards the work with Concanavalin A encapsulation and for many helpful discussions regarding competitive binding sensors.

I would also like to thank all of the biomedical engineering department faculty and staff for making my experience at Texas A&M University a wonderful experience.

NOMENCLATURE

AFM	Atomic force microscope
AgNP	Silver nanoparticle
AMP	Adenosine 5'-monophosphate
AuNC	Gold nanocluster
AuNP	Gold nanoparticle
AuNR	Gold nanorod
BSA	Bovine serum albumin
$CaCO_3$	Calcium carbonate
CCNP	Calcium carbonate nanoparticles
CGM	Continuous glucose monitoring
CGMS	Continuous glucose monitoring system
CHES	N-Cyclohexyl-2-aminoethanesulfonic acid
ConA	Concanavalin A
CTAB	Cetyltrimethylammonium bromide
DHLA	Dihydrolipoic acid
DI	Deionized
DLS	Dynamic light scattering
EA	Ethanolamine
EDC	N-(3-dimethylaminopropyl)-N’-ethylcarbodiimide hydrochloride
EDTA	Ethylenediaminetetraacetic acid

EE	Encapsulation efficiency
FAD	Flavin adenine dinucleotide
FBR	Foreign body response
FITC	Fluorescein isothiocyanate
FRET	Förster resonance energy transfer
GBP	Glucose binding protein
GDH	Glucose dehydrogenase
GDL	Glucono delta-lactone
GOx	Glucose oxidase
HEPES	4-(2-hydroxyethyl)-1-piperazineethanesulfonic acid
LbL	Layer-by-layer
MA	Maleic acid
MAA	Mercaptoacetic acid
MEF	Metal enhanced fluorescence
MES	2-(N-morpholino) ethanesulfonic acid
MPA	Mercaptoproprionic acid
MUA	Mercaptoundecanoic acid
NC	Nanocluster
NHS	N-Hydroxysulfosuccinimide
NP	Nanoparticle
NSET	Nanosurface energy transfer
NTA	Nanoparticle tracking analysis

OVA	Ovalbumin
PAA	Poly (acrylic acid)
PAH	Poly (allylamine hydrochloride)
PDADMAC	Poly (diallyldimethylammonium chloride)
PE	Polyelectrolyte
PEG	Poly (ethylene glycol)
PEI	Poly (ethylenimine)
PEM	Polyelectrolyte multilayer
PHOS	Phosphate buffer
PL	Photoluminescence
PSMA	Poly (styrene-co-maleic anhydride)
PSS	Poly (sodium-4-styrenesulfonate)
PSS-*co*-MA	Poly (4-styrenesulfonic acid-*co*-maleic acid)
PVSA	Poly (vinylsulfonic acid)
QD	Quantum dot
QY	Quantum yield
RCF	Relative centrifugal force
RET	Resonance energy transfer
SEM	Scanning electron microscope
SMBG	Self-monitoring of blood glucose
SNR	Signal-to-noise
SP	Solvent precipitation

SS	Styrene sulfonate
TEM	Transmission electron microscope
TMAH	Tetramethylammonium hydroxide pentahydrate
TOPO	Trioctylphosphine oxide
TRIS	Tris (hydroxymethyl) aminomethane
TRITC	Tetramethyl rhodamine isothiocyanate
UCNP	Upconverting nanoparticle
UV	Ultraviolet

TABLE OF CONTENTS

Page

LIST OF FIGURES

Page

LIST OF TABLES

Page

1. INTRODUCTION

Chronic diseases such as heart disease, diabetes, cancer, and arthritis are the leading cause of death and disability in the United States.[1, 2] Nearly 50% of all adults are affected by chronic disease and 25% of those affected have two or more chronic conditions.[1] Chronic diseases and the associated complications account for 86% of all health care spending;[2] diabetes alone totals $245 billion annually.[3] In many cases chronic disease can be prevented or controlled but usually is not curable. The etiology of chronic disease is not completely understood because it involves a complex combination of genetic, environmental, and lifestyle factors. The management, prevention, and understanding of chronic disease could be improved by utilizing implantable biosensors to continuously monitor disease related biomarkers. The information gathered could then be coupled with therapeutic options to deliver adaptive treatment.

The vision of a closed-loop system for real-time diagnosis and treatment is particularly suitable for the treatment of diabetes mellitus. Diabetic patients manage their disease by monitoring blood glucose levels throughout the day typically using the finger-prick method. However, while this method is accurate, the discreet testing does not provide a complete picture of the fluctuations and trends of blood glucose throughout the day. Improper treatment with insulin based on a single inaccurate measurement may lead to potentially life threatening consequences. More effective treatment requires continuous monitoring to provide more information on how blood glucose levels are

trending. There are currently several FDA approved devices that utilize an indwelling percutaneous electrochemical electrode for continuous glucose monitoring (CGM).[4, 5] These devices provide continuous monitoring but have insufficient accuracy and a limited *in vivo* lifespan of 3 – 7 days due to complications that stem from the foreign body response (FBR).[6] These devices become inaccurate without frequent calibration and performance diminishes as the FBR progresses. Research to solve this problem has focused on alleviating the FBR, but little progress has been made for improving the accuracy or lifespan of these electrochemical sensors.

Affinity sensors offer an alternative sensing method with the potential for long-term, real-time sensing capabilities without reagent consumption or byproduct formation. However, these systems are currently limited by component instability and their usage of organic dyes. For energy transfer systems, the spectral overlap greatly affects sensitivity. Due to the physiochemical properties of most available dyes, there is a trade-off between the overlap integral and background noise introduced due to direct excitation or spectral bleed-through. Organic dyes also photobleach when they are repeatedly optically interrogated, leading to decreased accuracy and sensitivity. Replacement of dyes with spectrally tunable and large Stoke-shift nanomaterials, should vastly improve the sensitivity, accuracy, and long-term photo-stability of optical sensors.

Quantum confined luminescent nanomaterials provide a superior alternative as fluorescence donors because of their size tunable properties, multiplexing capabilities, resistance to photobleaching, and large effective Stokes-shift.[7-9] As acceptors, noble metal NPs have large extinctions and strong resonant interactions with light due to

surface plasmons.[10] The size tunable optical properties and resistance to photobleaching make metallic NPs a superior alternative as acceptors in energy transfer schemes.[11] Additionally, energy transfer between some nanomaterials has been shown to follow the $1/R^4$ distance dependence of nanosurface energy transfer (NSET) rather than the $1/R^6$ dependence of Förster resonance energy transfer (FRET). This increased energy transfer efficiency should significantly improve the sensitivity of competitive binding energy transfer sensors.[12]

Integration of these and other nanomaterials into bioassays requires precise control over synthesis and modification in order to achieve the desired properties and effectively couple with biological components.[13] The capabilities for nanomaterial synthesis are rapidly advancing; producing higher quality materials that improve optical performance, simplify synthesis, and mitigate toxicity.[14] Nanomaterials such as quantum dots (QDs) are produced in organic solvents, requiring an additional procedure for surface modification and transfer to aqueous solvents. These different methods having varying tradeoffs between complexity, stability (colloidal and optical), quantum yield (QY), and hydrodynamic size.[13, 15-17] These different materials and surface coatings require individual optimization and specific chemical modification for further use; thus, a generic surface modification approach is highly desired.

The sensing chemistry must be encapsulated in a hollow capsule for *in vivo* deployment. The sensing components are packaged in hollow particles with a semi-permeable polymer shell that acts as a barrier between the sensor and host environment. The membrane mesh size must be small enough to prevent the larger macromolecule

sensing components from being released into the host environment and to keep the larger bimolecular components of the host environment from disrupting the sensor chemistry. The mesh size must be large enough to allow the small analyte molecules (*i.e.* glucose) to diffuse into the capsule interior to be analyzed by the sensor. The outside wall of the capsule can also be engineered for enhanced biocompatibility with the surrounding tissue when implanted.[18] A major challenge for the encapsulation of material is the retention of the protein activity during the capsule formation process; requiring gentle processing and mild conditions for entrapment, shell deposition, and dissolution. Calcium carbonate ($CaCO_3$) is a commonly used template for material encapsulation because of its high effective surface area, biocompatibility, high porosity, large pore size, ease of production under ambient conditions, and ability to be dissolved with mild treatment.[19-23] The development of a fully encapsulated and nanomaterial-enabled competitive binding sensor would be a substantial step towards long-term implantable biosensors.

The content of this dissertation has been organized to explain the development of the fundamental and applied knowledge required to construct a nanomaterial-enabled energy transfer biosensor. Section 2 provides an overall background of glucose sensing with a focus on affinity based approaches and theory; more specific background is included in each subsequent section. Section 3 describes the method development for pH dependent modification of high surface curvature nanomaterials with a focus on characterizing colloidal and optical properties after modification. Portions of this section were published in *ACS Nano.*[24] Section 4 describes the characterization of

polymer modified nanomaterials as low hydrodynamic size nanomaterials for bioconjugation, with a focus on colloidal stability and determining nanoparticle (NP) concentration in relation to changes in optical properties. Section 5 describes the construction and testing of a reversible energy transfer sensor utilizing gold nanorods (AuNRs) and protein stabilized gold nanoclusters (AuNCs). Section 6 describes the development of a new method to synthesize $CaCO_3$ NPs and subsequently nanocapsules. The development of a new method to dissolve $CaCO_3$ without chelation for the application of encapsulating ConA is also explored. Portions of this section were published in the *Journal of Colloid and Interface Science*[25] and *Applied Materials and Interfaces*.[26] Finally, section 7 describes the future direction of this work for the development of new nanomaterial sensors and encapsulation schemes.

2. BACKGROUND

2.1. Diabetes Mellitus

As of 2014, an estimated 29.1 million people in the US have diabetes mellitus, with 8.1 million of them currently undiagnosed.[27] Diabetes mellitus is characterized as the inability to maintain normal blood glucose levels due to either an inability to produce insulin (type 1) or correctly utilize insulin (type 2). Type 1 diabetes is an autoimmune disorder where pancreas beta cells are no longer able produce insulin at concentrations required to effectively modulate blood glucose. Type 2 diabetes is an acquired disorder that occurs due to a combination of genetic and lifestyle factors. Type 1 patients require regular insulin injections in order to maintain healthy blood glucose levels, while type 2 patients can typically manage their disease through proper diet and exercise. In both cases, monitoring blood glucose levels is critical for disease management because sustained hyperglycemia leads to severe long-term tissue damage to the retina, kidney, and nerves, while acute hypoglycemia can result in coma or death.[28, 29]

2.2. Continuous Glucose Monitoring

Disease management requires monitoring of blood glucose levels throughout the day. The growing prevalence of diabetes has led to significant research efforts towards more reliable and less invasive technologies; however, the self-monitoring of blood glucose (SMBG) by measuring whole blood using the finger-stick method still remains the current standard of care. Disease management requires measurement of blood glucose a minimum of 5 – 8 times a day. However, due to the inconvenience (*i.e.*

aversion to pain, cost of supplies) patients often forgo measurements, providing an incomplete history of the daily fluctuations in blood glucose levels.[30] These non-compliance issues can be averted by the use of implantable sensors that continuously monitor throughout the day and during activities which preclude manual measurement.

2.2.1. Commercial Glucose Sensing Technology

There are currently several FDA approved continuous glucose monitoring systems (CGMSs) currently available from Medtronic and DexCom.[4, 5, 31] These devices utilize an indwelling transcutaneous electrochemical electrode for amperometric detection of the hydrogen peroxide byproduct that is produced by the enzymatic consumption of glucose and oxygen. CGM improves diabetes management by providing the patient with more comprehensive information of glycemic excursions and alerts the user before they reach predefined levels of hyper- or hypo- glycemia. The CGMS trending information allows for better glycemic control compared to SMBG,[32, 33] which improves hemoglobin A1c levels[34] and reduces incidence of nocturnal hypoglycemic events[35] for both type 1 and type 2 patients.[36, 37]

2.2.2. Foreign Body Response of Implanted Sensors

The main problem faced by these devices is their decreased effectiveness over time due to the foreign body response (FBR).[6] The biological response to the initial tissue damage and the presence of the foreign element involves a complex cascade of protein infiltration, reactive oxygen release, and inflammatory cell recruitment. These factors contribute to decreasing sensor performance due to biofouling of the implant surface, degradation of sensor components, and depletion of the local oxygen and

glucose.[4, 38] The device requires frequent calibration to compensate for the transport changes and sensor lag that occurs as the FBR progresses;[39] even with appropriate calibration the sensor performance degrades and eventually the device fails within 3 – 7 days. However, some of these sensors have been found to still be functional after explantation, indicating that the sensor chemistry is not completely failing but rather becomes ineffective due to diffusional restrictions from the tissue reorganization.[40]

2.2.3. Research Towards Improving Glucose Sensing

A significant amount of research and development has been focused on improving the accuracy and long term function of these devices.[4] The main approach has been to improve tissue integration of the implanted sensor by mediating the inflammation response and increasing vascularization. This can be done by the release of drugs (*i.e.* dexamethasone, vascular endothelial growth factor, nitric oxide, etc…) or by improving the implant biocompatibility by engineering the chemical and mechanical properties.[41, 42] The sensing chemistry can also contribute to the inflammation response due to the enzymatic consumption of substrates (*i.e.* glucose, oxygen) and formation of the harmful byproducts (*i.e.* hydrogen peroxide, acid). Non-enzymatic affinity based sensing chemistries have been pursued as an alternative to mitigate this toxicity. Additionally, affinity systems to not require oxygen as a co-substrate so they are not affected by the oxygen depletion or the decreased oxygen transport. Recent emerging technologies have demonstrated long term *in vivo* sensing based on affinity systems utilizing either diboronic acid (Senseonics)[43] or a human based binding protein (Precisence).[44]

Regardless of the sensing chemistry used, the ultimate goal is to miniaturize the implanted system to be minimally invasive. This should reduce the initial tissue damage and removes the risk of infection and prolonged motion induced irritation associated with indwelling probes.[45] A highly active area of research has been focused on replacing the electrochemical approach with optical transduction techniques towards sensor miniaturization.

2.3. Optical Glucose Sensing

Optical detection methods have the potential for higher sensitivity, better accuracy and less interference compared to electrochemical sensors, with the capability of multiplexing for multianalyte detection in a single domain.[46] Non-invasive optical detection methods have been extensively explored for detecting glucose using polarimetry, luminescence, NIR spectroscopy, optical coherence tomography, Raman spectroscopy, and photo-acoustic tomography.[47] These methods have received significant attention but have failed to produce a commercially viable device for transdermal interrogation with the desired sensitivity and specificity.[46, 47] The main problems faced by these systems are the complex tissue optical properties and the inhomogeneous distribution of biological artifacts that reduce the SNR.[48] Overcoming these issues requires amplification of the glucose signal and/or utilizing more invasive measurement modalities (*i.e.* iontophoresis, microneedles, microdialyses, fiber optic probes, or implants). To achieve the ultimate goal of a worry free CGMS, a miniaturized, minimally invasive, and subcutaneous implant that uses transdermal optical interrogation was envisioned as a "smart tattoo" sensor.[49-51] The implanted

device acts to transduce and amplify glucose detection using biological or chemical recognition elements. The transduction techniques for optical glucose biosensors can be broadly subdivided as either biocatalytic (enzymatic) or bioaffinity.[52]

2.3.1. Enzymatic Sensors

Biocatalytic glucose sensors commonly utilize highly specific enzymes, such as glucose oxidase (GOx) or glucose dehydrogenase (GDH), which catalyze glucose using oxygen as a co-substrate. GOx is preferred over GDH because it has a higher specificity for glucose.[52] Glucose concentration can be measured directly by changes in the protein intrinsic fluorescence (usually tryptophan)[53] or with the addition of a fluorescently labeled ligand as a competitive assay.[54] Direct measurement techniques have not gained much interest because the intrinsic fluorescence is typically very weak. Glucose can also be measured indirectly by monitoring the oxygen consumption, hydrogen peroxide production, or local pH change.[46] The measurement of depleted oxygen has received the most attention because oxygen phosphors are highly sensitive and have long lifetimes that can be reliably determined without complex instrumentation.[55-59] However, enzymatic optical sensors suffer from many of the same drawbacks as electrochemical sensors. The consumption of oxygen and glucose while producing hydrogen peroxide and acid places stress on the surrounding *in vivo* environment. Additionally, without compensation of local oxygen, pH, and temperature the sensor becomes highly inaccurate.[60, 61] For these reasons, affinity based sensors have been pursued as more appealing alternatives because they allow real-time sensing capabilities without reagent

consumption or byproduct formation and are not dependent on local oxygen concentration.

2.4. Affinity Binding Sensors

Affinity based biosensors quantify the presence of specific analytes by incorporating receptor molecules capable of binding reversibly. Affinity assays have the potential for long-term sensing because they are generally considered "reagentless" even though some proteins require bound co-factors such as calcium. Affinity assays are not reaction rate dependent nor rate limited, therefore changes in analyte diffusion do not affect sensor range or sensitivity. Affinity systems do not consume oxygen so they are not affected by the depletion of local oxygen that occurs during the FBR. They also do not form byproducts that could further elicit an immune response.

The receptor element is commonly comprised of a protein[62, 63] (*i.e.* antibodies, binding proteins), DNA[64] (*i.e.* aptamers, oligonucleotides), or synthetic materials (*i.e.* boronic acid, polymers).[65] The binding event can be transduced by luminescence, electrochemical, calorimetric, mass sensitive, magnetic, or piezoelectric methods.[62, 66] For *in vivo* applications luminescence is the most commonly used modality and generally uses either a single dye that is environmentally sensitive or two dyes that are capable of energy transfer. The energy transfer approach is frequently employed using a competitive binding method.

2.4.1. Competitive Binding Affinity Sensors

The competitive binding scheme for glucose sensing involves three components: the (1) saccharide receptor (R) (*i.e.* ConA, apo-GOx), (2) saccharide analogue or ligand (L) (*i.e.* dextran, ovalbumin, or beta cyclodextrin), and the (3) analyte (A) (*i.e.* glucose, mannose, galactose, etc...). In the absence of the analyte glucose, the saccharide receptor and saccharide analogue are bound in an equilibrium state depending on their affinity. As the analyte enters the system it "competes" for the receptor binding site, displacing the saccharide analogue if the analyte has a higher affinity for the binding site or is present in a greater concentration. The association constants K_1 for the ligand-receptor (LR) system and K_2 for the analyte-receptor (AR) complex are given by equations 2.1 & 2.2 respectively.

(2.1) $$K_1 = \frac{[LR]}{[L][R]}$$

(2.2) $$K_2 = \frac{[AR]}{[A][R]}$$

If the binding assay is encapsulated then the total receptor (R_t) and ligand (L_t) concentrations are given by equations 2.3 and 2.4 respectively. The system can be described in dimensionless terms by equation 2.5.[67]

(2.3) $$[R_t] = [R] + [AR] + [LR]$$

(2.4) $$[L_t] = [L] + [LR]$$

(2.5) $$\left(\frac{[\mathrm{L}]}{[\mathrm{L_t}]}\right)^2 + \left(\frac{[L]}{[L_t]}\right)\left(\left[\frac{[R_t]}{[L_t]} - 1\right] + \frac{[A]K_2 + 1}{[L_t]K_1}\right) - \frac{[\mathrm{A}]\mathrm{K}_2 + 1}{[\mathrm{L_t}]\mathrm{K}_1} = 0$$

It is clear that several factors dramatically affect the sensor dynamics. Using these equations the sensor response can be modeled if the association constants are

known. Most importantly, the sensitivity and analytical range of competitive binding sensors can be optimized based on the on ligand and receptor relative and absolute concentrations.[67-69]

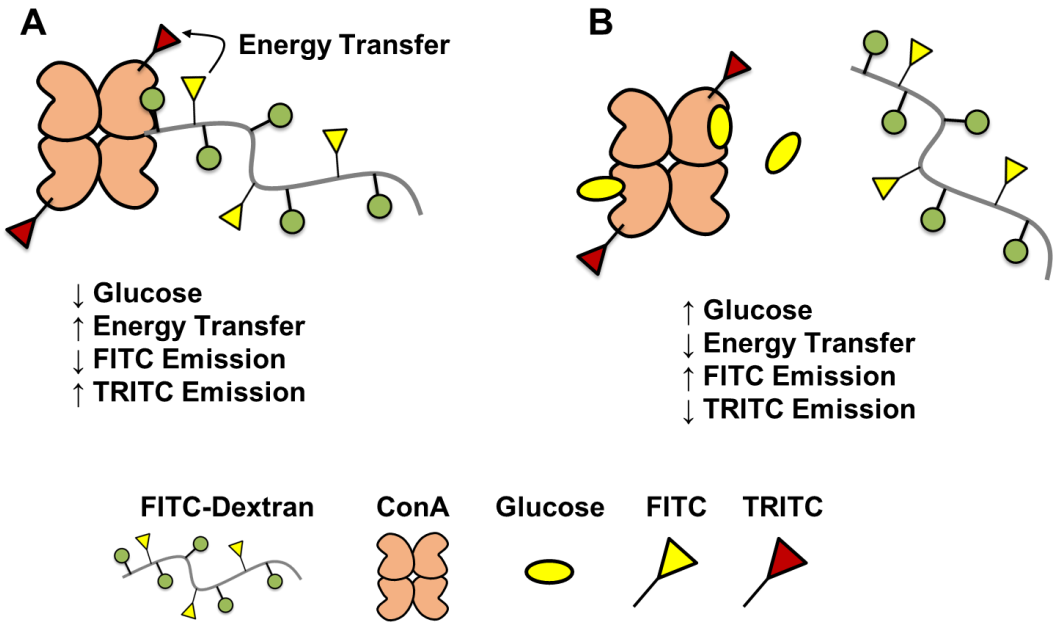

Figure 2.1: Competitive binding glucose sensor using TRITC labeled ConA and FITC labeled dextran.

The ConA/dextran competitive binding system is the most frequently studied and is considered a model competitive binding assay.[68] An example of this competitive binding FRET assay is shown in Figure 2.1 where ConA is labeled with the acceptor dye (*i.e.* TRITC) and dextran is labeled with the donor dye (*i.e.* FITC). In the absence of glucose, ConA binds to dextran and the fluorophores are brought in close proximity resulting in non-radiative energy transfer from the donor to acceptor dye (Figure 2.1A). When the analyte glucose is added to the system it displaces the dextran, reducing energy transfer (Figure 2.1B). The ratiometric FRET changes in FITC/TRITC are then

used to determine glucose concentration. Several donor/acceptor dye pairs have been studied using this approach.

2.4.2. Receptors for Glucose Affinity Sensors

Several natural and synthetic approaches have been developed for creating affinity binding luminescence glucose sensors. The advantages and limitations of sensors utilizing ConA, glucose binding protein (GBP), apo-GOx, and boronic acid are discussed.

2.4.2.1. Concanavalin A

ConA is a ≈104 kDa tetrameric plant lectin isolated from Jack beans. ConA is an agglutinating protein containing 4 binding sites capable of binding to glycosylated molecules such as glycoproteins, glycolipids, and various sugars.[70] The binding of ConA to sugars has been exploited to produce a variety of optical sensors using label free,[71] single labeled,[72] and dual labeled approaches with fluorophores,[51, 73-80] nanomaterials,[81-86] or a combination of both.[87-89] The most commonly used dual-labeled approach is the FRET based competitive binding assay using either dextran,[51, 73-76, 79, 80, 90-92] glycosylated dendrimers,[77, 78] or β-cyclodextrin[72, 86, 89] as the competing ligand. ConA based glucose assays have shown significant *in vitro* potential but are limited for *in vivo* applications due to their limited range, low sensitivity, and variable stability under physiological conditions.[46]

The multiple binding sites of ConA often leads to aggregation in the presence of ligands presenting multiple carbohydrate moieties. This behavior can be used to make highly sensitive aggregation based sensors using plasmonic NPs.[81, 93-95] For luminescent

sensors the precipitation of ConA due to aggregation at higher temperature and low glucose concentrations prevents long term use. Monovalent ligands are required to avoid aggregation due to intermolecular binding.[96, 97]

The instability of ConA is a significant hurdle for long-term *in vivo* sensing. This has been mitigated by using ConA immobilized in a Sepharose matrix on the end of a fiber optic probe.[73-76] The immobilization improves conformational stability and prevents self-agglutination[98], but alters the receptor-ligand binding kinetics. More recently, PEGylation of free-floating ConA has been shown to improve stability for up to 30 days at 37°C, without significantly compromising binding capability.[99]

2.4.2.2. Apo-Glucose Oxidase

Apo-GOx is produced by removal of the FAD co-factor from GOx to eliminate the catalytic activity of the enzyme, while still retaining the its binding capacity.[100] Apo-enzymes can be used as non-consuming affinity sensors for analyte detection using the intrinsic fluorescence of the tryptophan residue.[100, 101] However, this method is not practical because the intrinsic fluorescence is typically weak. Chinnayelka *et al*. addressed this problem by developing a competitive binding FRET approach analogous to the ConA-dextran assay.[102] Apo-GOx is considered a beneficial alternative to ConA because it has a higher specificity for glucose, it is generally regarded as safe, and it has only a single binding site.[103] The apo-GOx assay was still functional when entrapped in hollow microcapsules[49, 69, 104] or dissolved core alginate spheres.[105, 106] The encapsulated assays demonstrated glucose sensing across the physiologically relevant range but had

limited sensitivity. The limited sensitivity and generally poor stability of apo-enzymes are major problems that have hindered progress towards use for CGM.[46]

2.4.2.3. Glucose Binding Protein

Glucose binding protein (GBP) is a highly specific binding protein that belongs to the family of transport mediating proteins found in the periplasmic space of gram negative bacteria. GBP is a 33 kDa protein consisting of two globular domains connected by a flexible hinge that undergoes a large conformational change when binding to glucose. Using site directed mutagenesis a single cysteine group can be introduced at position 26 of the C terminus near the binding site of the hinged region. This cysteine allowed for the site-specific covalent conjugation of an environmentally sensitive dye.[107] When no glucose is present the environmentally sensitive fluorophore is confined within a hydrophobic pocket of GBP. When GBP binds to glucose the conformational change exposes the dye to the aqueous environment, resulting in an increase in fluorescence intensity. This mechanism has been exploited by several groups to produce intensity, intensity ratio, and lifetime based systems using a variety of dyes.[107-116]

Several FRET based sensing mechanisms have also been developed either by labeling the globular domains with dyes or by introducing fused fluorescent proteins by genetically modifying the recombinant host.[108, 117-119] The FRET based sensors are inherently ratiometric, which provides more reliable intensity measurements but have much lower sensitivity than the environmentally sensitive single dye systems.[108]

Wild type GBP is not suitable for use in glucose sensors due to its micromolar binding affinity that quickly saturates at the physiologically relevant millimolar concentrations. Site directed mutagenesis rationally guided by X-ray crystallography was used to engineer mutants with a binding affinity for glucose an order of magnitude lower than the native protein.[114, 120] Screening of these mutants produced several variants with binding constants in the millimolar range.[114, 121]

GBP has received considerable attention as an *in vitro* platform because of its high specificity and sensitivity, but only limited work has addressed the *in vivo* capabilities. When immobilized on an optical fiber GBP showed a response time of 10 min[110] but only retained its binding capability for 3-5 days under physiological conditions.[122] Improving the stability of GBP at physiological temperatures was recently explored by engineering a series semi-synthetic binding proteins with unnatural amino acids; however, the resulting mutants were not tested for their long-term stability.[123]

2.4.2.4. Boronic Acid

Boronic acid belongs to a broad class of synthetic compounds capable of reversibly binding a variety of diols.[124] The binding capability has been exploited as a separation tool, a building block for "smart materials", a chemosensor ligand, and for protein manipulation.[125] Saccharide binding leads to a conformational change in the boronic acid structure that can be optically transduced *via* photoelectron transfer, internal charge transfer, or FRET.[126] Boronic acid can be leverage for a multitude of optical sensing modalities,[127-130] but the most popular class of sensors utilize the fluorescence change in the amine modified boronic acid derivative.[131] For *in vivo*

glucose sensing applications, the boronic acid moiety must be engineered to improve its solubility, binding affinity, selectivity, sensitivity, and stability under physiological conditions. Early in this development, a modular ligand scheme was developed consisting of a fluorophore, a spacer, and the receptor to allow for development of each portion independently and to provide a common reference platform for future development.[132] The pKa of boronic acid was tuned to near neutral pH by combining the boronic acid moiety with electron donor or withdrawing groups to improve affinity and increase fluorescence intensity.[133, 134] The synthesis of a diboronic acid was considered a key development because it increased the affinity and selectivity for glucose by 300-fold and 1400-fold respectively.[135] It is now established that a two receptor unit is required to obtain this desired selectivity for saccharides.[136] The recently developed system by Senseonics has demonstrated long-term *in vivo* sensing capabilities of an anthracene based diboronic acid sensor coupled with an implantable micro-fluorometer encased in a biocompatible polymer.[43, 137] This system demonstrated CGM for 90 days in human subjects with no significant decrease in glucose prediction accuracy over this time period. A critical feature of this device was the inclusion of a platinum catalyst to prevent oxidation of the boronic acid molecule by the hydrogen peroxide or reactive oxygen produced during the initial inflammation response.[138] Thus far, this is the most promising example of a fully implantable CGMS using an affinity based approach.

2.5. FRET Theory Overview

The design rules and tradeoffs for choosing appropriate donor and acceptor fluorophores can be determined using the well described FRET phenomenon. FRET is the non-radiative resonant energy transfer (RET) between complementary donor and acceptor fluorophores. The FRET phenomenon involves RET through dipole-dipole interactions between a donor in its excited state to an acceptor in its ground state. The RET efficiency (E) is a distance dependent function described by equation 2.6. The Förster distance (R_0) given by equation 2.7 is the distance at which the RET is 50% and depends on the refractive index (n) of the surrounding media, QY of the donor (QY_D), dipole orientation factor, and the spectral overlap. The orientation factor (κ^2) is between 0 and 4 but typically the value of the average of two randomly oriented dipoles (2/3) is used. The overlap integral J(λ) is calculated by equation 2.8 where ε_A is the acceptor extinction coefficient and F_D is the normalized donor emission.

(2.6) $$E = 1 \Big/ \left[1 + \left(\frac{r}{R_0}\right)^6\right]$$

(2.7) $$R_0 = 0.211 \times [\, n^{-4} \times QY_D \times \kappa^2 \times J(\lambda)]^{1/6}$$

(2.8) $$J(\lambda) = \int_0^\infty \varepsilon_A\,(\lambda)\, F_D(\lambda)\lambda^4 \; d\lambda$$

Typically the R_0 value is between 20-80 Å, providing useful information on the proximity between the fluorophore labeled components. This provides a method to determine biomolecule interaction below the optical threshold by transducing near-field nanoscale interactions into a far-field signal that can be optically resolved. This nanoscale ruler has been exploited extensively in bioimaging for quantitative analysis of

molecular interactions for cellular dynamics and for investigating basic molecular biology principles such as the conformational changes of proteins and DNA.[139, 140] The same idea can be applied to develop functional assays for analyte detection by exploiting protein-protein, antibody-antigen, or ligand-receptor binding interactions.

The overlap between donor emission and acceptor absorption is a critical component that must be optimized for optimal RET efficiency by choosing appropriate fluorophores or FRET pairs. The FRET pairs must have sufficient overlap to allow optical coupling, while the emission peaks still being visually distinguishable. Additionally, the required overlap between donor emission and acceptor absorbance often leads to donor emission overlap with acceptor emission and/or direct excitation of the acceptor. This produces a tradeoff between sensitivity and noise when choosing an excitation wavelength. One method to alleviate these concerns is to employ a non-fluorescent quencher such as a black hole dye or metallic NP as the acceptor. This allows for tuning the overlap integral to improve RET efficiency without introducing the noise of the acceptor emission. However, this also removes the ratiometric aspect of the system, a desirable feature for accurate quantitation when using intensity based approaches. Thus, incorporation of a reference emitter that does not partake in the energy transfer process is necessary to reintroduce the ratiometric property. Another way to overcome the donor-acceptor overlap trade-off is to replace the donor with a large Stokes-shift component such as a UV excitable QD. The QD tunable properties allow synthesis for optimum overlap between donor emission and acceptor absorption,

but the donor QD can be excited well below the acceptor absorption to prevent direct excitation.

It is important to recognize that the limited distance over which dye-dye interactions occurs limits the energy transfer efficiency between larger components such as high molecular weight or multi-domain proteins. For single-domain proteins efficient RET requires site-specific labeling to provide a minimum distance between the binding site and the bound component. This requires having a unique target residue for labeling; this may be present naturally, or introduced through protein engineering.[107] For multi-domain proteins that contain multiple binding sites it is necessary to have each sub-unit labeled otherwise ligand-receptor distances become large and variable.

2.6. Nanomaterial-Enabled Energy Transfer

The large extinction cross-section and local electromagnetic field of plasmonic NPs such as gold or silver can be used to modulate the FRET response.[141] For brevity only AuNPs will be discussed as it is the most thoroughly studied template, however, identical phenomena is observed for other noble metal NPs (*i.e.* silver) or different morphologies (*i.e.* nanorods, nanostars, nanocubes, etc..) with associated changes depending on their extinction spectra.[142-144]

The energy transfer efficiency between a plasmon and fluorophore is guided by the FRET response but with a longer range energy transfer efficiency; capable of quenching over distances twice that of typical dye-dye FRET pairs (Figure 2.2). The quenching process dominates below the R_0 distance of ≈10 nm, while fluorescence enhancement is probable at R_0 distances greater than ≈10 nm. This enhancement, known

as metal enhanced fluorescence (MEF), can exist either as excitation or emission enhancement depending on the spectral overlap and donor-acceptor distance (R_{D-A}). Excitation enhancement occurs when the plasmon resonance overlaps with the excitation wavelength and the $R_{D-A} < R_0$. If the plasmon resonance overlaps with the emission spectra either an emission enhancement will occur when $R_{D-A} > R_0$ or emission quenching when $R_{D-A} < R_0$. For designing plasmon-enabled sensors these basic design rules must be followed when choosing optical components to obtain pure quenching or enhancement regimes. For quenching based assays it is important to control these distances by using low hydrodynamic size particles to maintain a $R_{D-A}<R_0$. This interplay between enhancement and quenching can lead to decreased energy transfer efficiency and variable results when R_{D-A} approaches R_0.

When AuNP size decreases below 2 – 3 nm to the nanocluster (NC) regime due to quantum size effects the SPR disappears and the energy transfer phenomena becomes electron hole dependent. When AuNCs are used as the acceptor the energy transfer phenomenon is described by the nanosurface energy transfer (NSET) formalism which follows a $1/R^4$ distance dependence shown in equation 2.9.[12] The distance at which 50% efficiency is achieved (d_0) is given by equation 2.10, where c is the speed of light, Φ_{dye} is the QY of the donor dye, ω_{dye} is the angular frequency of the dye, ω_F and K_F are the angular frequency and Fermi wavevector respectively of bulk gold.[12]

(2.9) $$E = 1/\left[1 + \left(\frac{d}{d_0}\right)^4\right]$$

(2.10) $$d_0 = \left(0.225 \frac{c^3 \Phi_{dye}}{\omega^2{}_{dye} \omega_F k_F}\right)^{\frac{1}{4}}$$

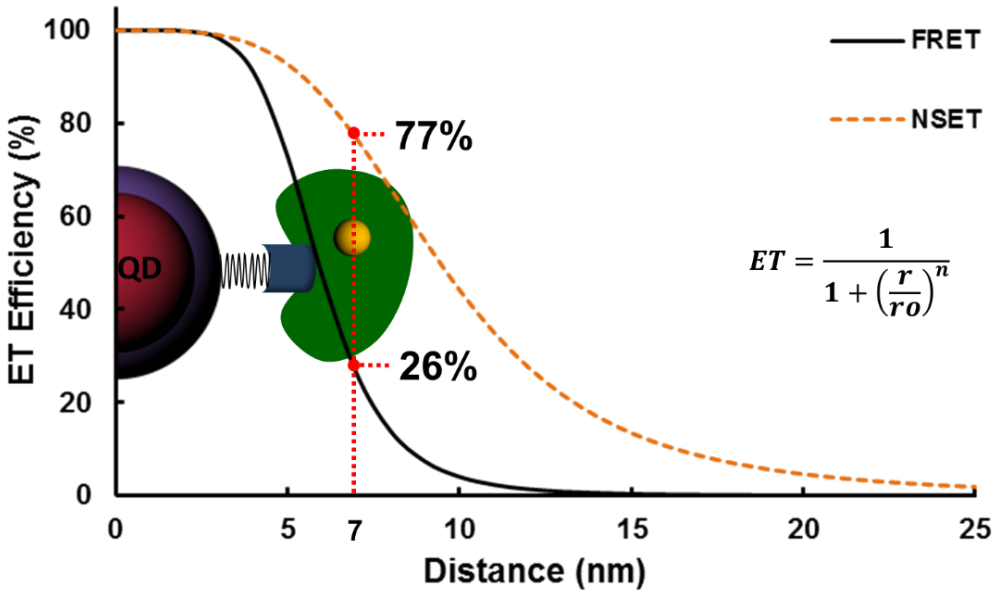

Figure 2.2: Energy transfer efficiency as a function of distance calculated using FRET and NSET formalism.

Figure 2.2 shows an example of the distance dependent energy transfer efficiency calculated for energy transfer between the dye FAM and AuNC (1.4 nm) using both the FRET and NSET formalisms.[12] This plot illustrates the importance of energy transfer efficiency when using larger bimolecular recognition elements (*i.e.* proteins) and larger optical components (*i.e.* QDs). At a given distance of 7 nm, approximated for the distance when the two components are closest, the energy transfer using the FRET mechanism has a 26% efficiency while the NSET mechanism provides 77% efficiency; an overall 50% improvement in energy transfer efficiency and much better sensor sensitivity. The majority of NSET research involves studying the interaction of plasmonic nanomaterials and organic dyes;[12, 142, 145-154] the main considerations being NP size, distance dependent efficiency, and wavelength dependence. Additional work found that the NSET phenomenon extends towards other nanomaterials such as QDs and

AuNPs. However, the underlying mechanism is still not completely understood and some results are contradictory.

Experimental validation of this theory has involved studying the interaction of donor and acceptor components at controlled distances using defined spacers.

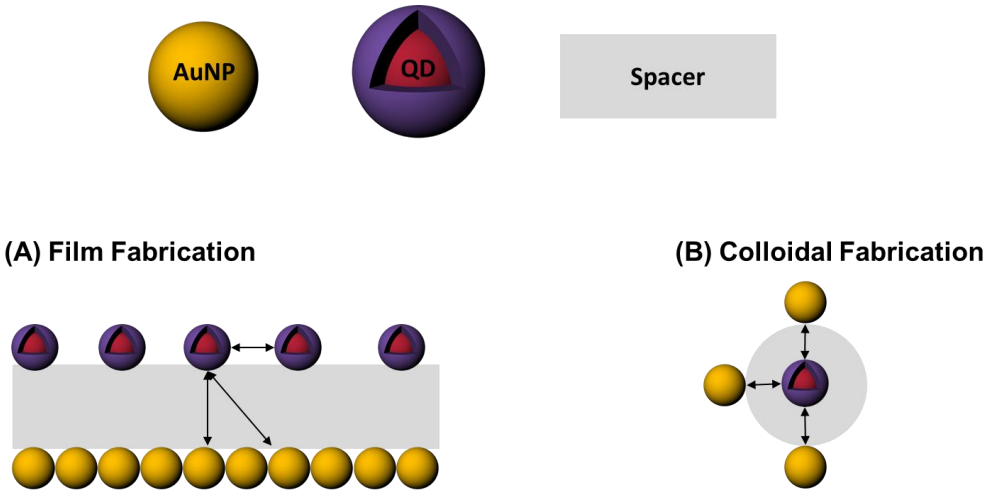

Figure 2.3: Schematic diagram of experimental setups for studying distance dependent energy transfer using (A) thin film fabrication techniques or (B) colloidal fabrication techniques.

The energy transfer phenomena has been studied on two-dimensional support structures using thin-film fabrication techniques.[155-158] However, this involves multiple interactions between the QD and the thin-film like metallic layer and some interaction between neighboring QDs, (Figure 2.3A) both of which may prevent full understanding of the energy transfer theory. More elegant solutions involve colloidal fabrication techniques (Figure 2.3B) typically using DNA oligonucleotides,[159, 160], DNA origami,[161] silica,[152] or protein[162] to control the spacing distance. The spacer provides defined lengths for controlled interactions between a single AuNP and a single QD. These

results have shown that AuNP-QD interactions extend well beyond the 10 nm FRET barrier to distances greater than 20 nm[161, 163] depending on AuNP size.[160] The long range interaction between nanomaterials has motivated the development of nanomaterial-enabled sensors. The sensitivity of existing glucose sensing assays could be significantly improved by replacing the organic dyes with nanomaterials. However, the construction and analyses of these nanomaterial-enabled assays remains a significant challenge.

2.7. Glucose Affinity Sensors Utilizing Nanomaterial Energy Transfer

Energy transfer glucose sensors utilizing dye-dye interactions are the most commonly studied and have thus far displayed the most promise towards *in vivo* applications. However, the limitations of organic dyes in terms of lower sensitivity and rapid photobleaching has sparked interest in replacing one or both organic dyes with nanomaterials. The development of glucose sensors utilizing two nanomaterials for energy transfer has been limited; existing sensors are summarized in Table 2.1.

Table 2.1: Overview of nanomaterial glucose sensors using nanomaterials for both donor and acceptor components.

Author	Donor	Acceptor
Tang et al. 2008	QD-ConA	β-CD-AuNP
Peng et al. 2011	UCNP-ConA	β-CD-AuNP
Zhang et al. 2011	UCNP-ConA	GO-Chitosan
Hu et al. 2012	QD557-ConA	QD609-Glucose
Lim et al. 2013	QD-PEG-NH2	AuNP-Mannose

Tang *et al*. reported a two nanomaterial FRET based system where QD-ConA conjugates were quenched by β-CD coated 13.8 nm AuNPs in the absence of glucose.[86] Wang *et al*. demonstrated a glucose sensing with only QD-ConA conjugates, where the glucose binding to the ConA resulted in a decrease in QD photoluminescence (PL);[85] no explanation was given for this unusual quenching mechanism. Lim *et al* developed an assay for ConA based on the attenuated quenching of amine poly (ethylene glycol) (PEG) terminated QDs by mannose stabilized 10 nm AuNPs.[81] In this assay, the QD-PEG-NH_2 is initially quench by localized AuNPs-mannose that are attached through the hydrogen bond between the mannose and amine. The PL is recovered when ConA binds to the AuNP-Mannose, disrupting the hydrogen bonds and releasing the QD-PEG-NH_2. Hu *et al*. developed a glucose assay based on the inhibited energy transfer between a green QD-ConA and a red QD-glucose.[82] Analogous assays have been developed by exchanging the donor QD with an upconverting NP (UCNP) or replacing the AuNP with graphene oxide (GO).[83, 84] These papers exist as proof of concept studies but the characterization of the sensors is limited. One obvious issue is the contradiction in mechanism of PL quenching for QD-ConA assays. While Tang *et al*. showed QD-ConA PL quenched in the presence of AuNP-β-CD, Wang *et al*. showed QD-ConA PL quenching directly due to glucose. Clearly there are multiple sources of quenching possible, but neither paper used negative controls to explore any of these possibilities. This incomplete experimental design renders the results inconclusive.

Another significant issue that is not considered in these papers is the aggregation that occurs when mixing multivalent ConA with multivalent glycosylated NPs. The

aggregation behavior of ConA with glycosylated NPs is commonly utilized method for the colorimetric detection of glucose based on the plasmonic coupling between the aggregated NPs.[95] For energy transfer sensors this type of aggregation can lead to data misinterpretation. For example, large aggregates of ConA and NPs can settle out of solution rapidly precluding them from measurement. When glucose is added, the aggregates are broken up and the NPs are released back into solution. This gives a change in PL intensity that appears as reversible energy transfer. Aggregation of the optically active nanomaterials results in changes in their optical properties such a shift in absorbance spectra for AuNPs and self-quenching for QDs. Large aggregates will also scatter light that can cause fluctuations in intensity depending on the measurement setup. None of these papers characterized the degree of aggregation during the synthesis of the sensor components or during the assay testing.

In general, these works fail to identify the major hurdles that currently exist that are preventing the implementation of nanomaterial sensors. This is a critical aspect of fundamental research that is required for the field to move forward. By not exploring the system in detail they are misrepresenting the status of the technology making it more difficult for future researchers to navigate.

2.8. Summary

This work encompasses the development of a competitive binding glucose sensor utilizing nanomaterial energy transfer. An essential design requirement was to produce colloidally and optical stable sensor components, while minimizing the hydrodynamic size in order to optimize energy transfer efficiency. An emphasis was placed on

developing robust methods and chemistry for sensor component construction that could be easily adapted to integrate different nanomaterials and eventually even for sensing different analytes. LbL was chosen as the primary surface modification technique as it has a demonstrated capability to modify a large cross section of macroscopic materials with nanometer precision. However, the application of LbL on nanomaterial templates is not a well understood process, therefore, much of this work focuses on the method development and characterization of this procedure. The following sections contain the nanomaterial fabrication, sensor construction, and the encapsulation process; exploring fundamental theory, while developing the required methodologies for practical implementation.

3. INVESTIGATION OF THE PH DEPENDENT LBL MODIFICATION OF HIGH SURFACE CURVATURE NANOPARTICLES*

3.1. Introduction

Nanomaterials exhibit unique size, shape, and surface dependent properties that can be tailored for the development of nanotherapeutic and diagnostic devices.[164-168] A subset of such nanomaterials are inorganic in nature; these NP colloids are typically synthesized in organic solvents as a variety of core and core/shell nanomaterials that require further surface modification for stabilization, functionalization, and transfer to aqueous conditions.[169] Facilitating nanomaterial interaction with biological media requires passivation of the inorganic core with an organic shell to prevent degradation and aggregation that would otherwise compromise the nanomaterial physiochemical properties leading to undesirable nanotoxicological effects.[170] Numerous surface modification techniques currently exist with varying tradeoffs between method complexity, resulting colloidal stability, chemical reactivity, and coating thickness.[15] Modification with charged polymers is of particular interest due to the combination of a steric barrier and electrostatic repulsion that provides a superior electrosteric stabilization.[171] LbL is recognized as a low cost and versatile nanofabrication technique

*Parts of this section are reprinted with permission from "Processing and Characterization of Stable, pH-Sensitive Layer-by-Layer Modified Colloidal Quantum Dots" by Nagaraja, A. T.; Sooresh, A.; Meissner, K. E.; McShane, M. J., *ACS Nano* 2013 *7* (7), 6194-6202. Copyright 2013 by American Chemical Society Inc.

to modify a broad range of templates with a diverse array of materials to produce tunable, responsive, and multifunctional devices.[172-175]

3.2. AuNPs a Model Template for LbL Method Development

The deposition of weak and weak-strong PEs onto model AuNPs was investigated to understand how solution pH affects PE adsorption; assessing the PE modified AuNPs for aggregation, surface charge, and colloidal stability. AuNPs are chosen as a model template because their modification and aggregation state can be rapidly monitored with UV-Vis.

3.2.1. Background

3.2.1.1. LbL on Nanoparticle Templates

The application of LbL has been thoroughly investigated on planar substrates for the hierarchal assembly of multifunctional films for an assortment of applications[176-178] and was easily adapted for microparticle templates by exchanging the rinsing steps with multiple centrifugation/dispersion cycles.[179] However, translating this process to NP templates is significantly more challenging due to the added restrictions to prevent aggregation and becomes especially difficult for NPs smaller than 30 nm.[180-192] For very small NPs, the high surface curvature resists wrapping by rigid polyelectrolytes (PEs). Both theoretical and empirical work demonstrated that PE chain length should be approximately equal to NP circumference to promote stable wrapping.[180, 181, 193, 194] Schneider and Decher contributed significantly to this area by finding the optimal conditions to prevent flocculation by mainly controlling stoichiometry between a dilute gold NP (AuNP) concentration and a large PE excess; demonstrating a correlation

between the aggregation state of AuNPs viewed by TEM and the plasmon peak location of the UV-Vis absorbance.[182, 183] We adapted this technique for coating 5 nm AuNPs, but found that controlling stoichiometry alone was not sufficient to prevent aggregation.

Solution pH is recognized as a critical parameter for controlling deposition thickness and morphology of the weak PEs poly (allylamine hydrochloride) (PAH) and poly (acrylic acid) (PAA) on planar,[195-201] microparticle,[202-206] and NP[207-209] templates. To our knowledge, only two publications have explored the pH dependent coating of high surface curvature NPs less than 10 nm.[181, 185, 192] Mayya *et al*. studied the coating of 7 nm AuNPs with strong PEs, poly (diallyldimethylammonium chloride) (PDADMAC) and poly (sodium-4-styrenesulfonate) (PSS), maintaining solution at pH 9 throughout the LbL process to ensure the AuNP surface ligands remained fully ionized.[185] Dorris and coworkers studied how pH affected the interaction of 5 nm cationic AuNPs with PDADMAC and PSS in terms of retention of the initial stabilizing ligand and subsequent PE layers.[181] These works established the importance of choosing the correct solution pH in relation to the NP charge density, but did not address the impact of PE charge density on the coating process.

Strong PEs maintain a high charge density over a broad pH range that enhances electrostatic stability and limits film reorganization. However, coating of high surface curvature NPs with strong PEs requires an increase in NaCl concentration to reduce chain rigidity, which simultaneously reduces NP charge density, leading to flocculation if the concentration is not kept fairly low. In contrast, the advantage of PEs containing weak acid/base moieties arises from the ability to manipulate their linear charge density

and conformation through solution pH. NPs coated with weak PEs exhibit pH dependent properties that can be exploited as stimuli responsive triggers but this also renders them susceptible to aggregation under pH extremes. Poly (4-styrenesulfonic acid-*co*-maleic acid) (PSS-*co*-MA) is an inexpensive, low molecular weight, commercially available, and high charge density weak-strong random copolymer of styrene sulfonate (SS) and maleic acid (MA). The deposition of this weak-strong copolymer can be tuned by controlling the MA ionization but shows more resistance to post exposure film reorganization because of the highly charged SS groups.[210-214] Using this copolymer for NP templates is expected to impart enhanced colloidal stability for these same reasons but to our knowledge this has not been reported on 5 nm AuNPs.

The small size of NPs (QDs and AuNPs) makes recovery and efficient separation of excess PE a significant challenge.[181, 188] High speed centrifugation for long periods of time improves sedimentation, but under improper conditions leads to the formation of tightly-packed pellets of irreversibly aggregated NPs. Separation by any size-exclusion method (filtration, size exclusion chromatography, or dialysis) is virtually impossible, as particle circumference and PE chain length must be specifically chosen to be of similar size;[185] resulting in either PE retention or NP loss. Furthermore, a tradeoff in volume and concentration exists: processing a large amount of dilute NPs is both tedious and expensive, whereas high concentration of sample slows down the process and the excess PE clogs small pore-size filters.

3.2.1.2. Theory of pH Dependent LbL

The LbL modification of small NPs with weak PEs requires careful control of solution pH throughout the process. We found that the process had to be split into two phases: (1) the adsorption phase and (2) the centrifugation (or separation) phase. Prevent aggregation throughout this process requires maintaining a high surface charge density on the NPs. Because of this stipulation the belief is that pH should be chosen so that the PE being used is fully ionized. However, for small NPs this prevents adequate adsorption because the fully ionized PE is too rigid to completely wrap the NP. Figure 3.1A shows a generic example of pH dependent adsorption with an anionic NP and a cationic PE. In the acidic (red) region the PE is fully ionized and rigid, prevents proper wrapping. Additionally, the NP charge density is much lower, leading to a decrease in interparticle distance, which increases the chance for bridging and flocculation. As pH is increased to a basic region (blue) the PE becomes more flexible and NP charge density increases. We believe this is the ideal region for deposition because the more flexible PE should be able to wrap the NP, and the high NP charge density prevents interparticle bridging. However, the PE coated NP in basic pH is now weakly charged and ultracentrifugation under basic conditions causes aggregation. To overcome this the solution is exchanged from basic to acid pH to increase the surface before ultracentrifugation (Figure 3.1B).

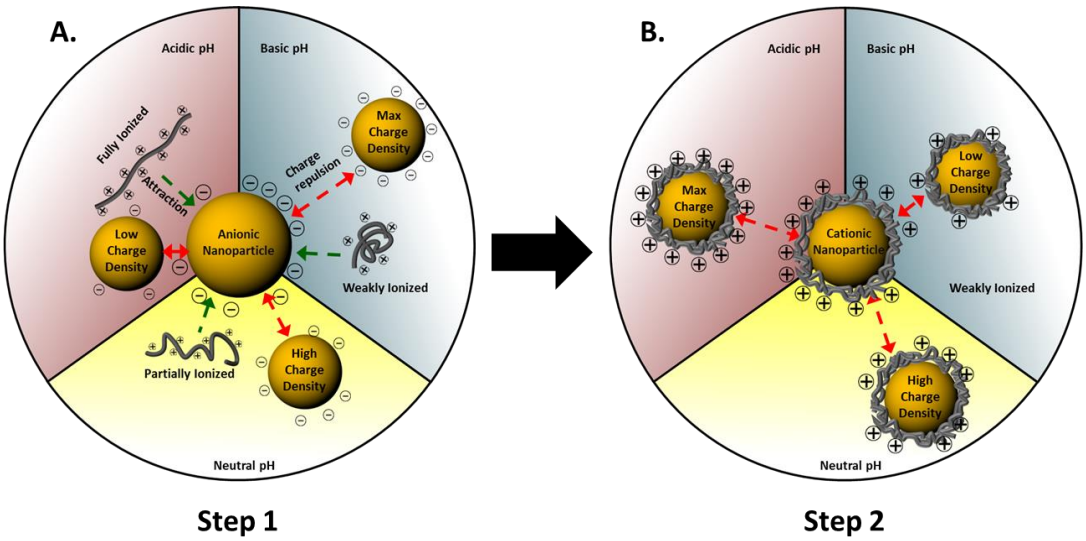

Figure 3.1: Diagram depicting the pH dependent charge density interplay for both the NP template and the PE during (A) PE adsorption and (B) condition for ultracentrifugation of the PE coated NP.

This process can be generalized to coat any anionic NP with a cationic PE by considering the pH dependent charge density of both components (Figure 3.2A). The adsorption should occur at least 1 pH unit above the pKa of the anionic NP in the region of saturated charge density, while adsorption should occur at least 1 pH unit below the pKa of the cationic PE used to coat the NP. For the addition of the second layer of anionic PE onto the now cationic NP, the process can be done in reverse (Figure 3.2B); this also applies to an initial coating of a cationic NP with an anionic PE.

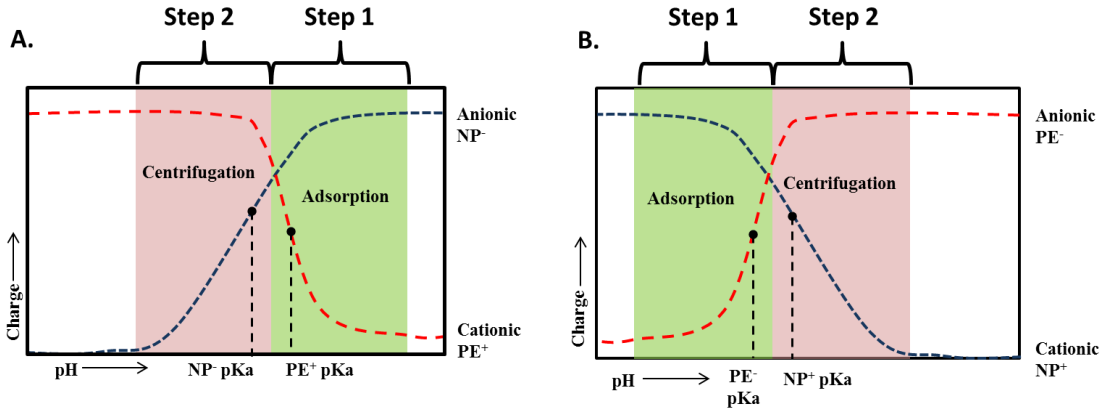

Figure 3.2: A generic example of the charge density interplay between PEs and the template NP for the two-step deposition cycle of the (A) first cationic layer and (B) the second anionic layer. The pH regions for optimum charge density interaction during adsorption is marked in green and for centrifugation marked in red.

This technique is particularly suited for coating small NPs but we believe that consideration of this charge density interplay provides a fundamental method to coat any template material with a variety of other species to form multifunctional NPs.

3.2.2. Materials and Methods

3.2.2.1. Chemicals

Poly (allylamine hydrochloride) (Mw = 15000 kDa), poly (acrylic acid) (PAA) (Mw = 15000 kDa), poly (4-styrenesulfonic acid-*co*-maleic acid) sodium salt (PSS-*co*-MA) (Mw = 20000 kDa), 11-mercaptoundecanoic acid (MUA) (98% or 95%), 3-mercaptopropionic acid (MPA) (99%) , gold (III) chloride trihydrate (99.9%), tetraoctylammonium bromide (98%) and sodium borohydride (99%) were all obtained from Sigma Aldrich.

3.2.2.2. AuNP Synthesis

The Brust-Schiffrin method was utilized to synthesize monodisperse gold NPs (AuNPs).[185, 215, 216] 3 mL of aqueous gold (III) chloride trihydrate ($HAuCl_4 \cdot 3H_2O$, 25.4 mM) was transferred into 8 mL of toluene by adding 25 mM of tetraoctylammonium bromide followed by cleaning three times of deionized (DI) H_2O. The cleaned gold salt in toluene phase was reduced by adding 1 mL of sodium borohydride aqueous solution (793 mM) under vigorous stirring. The reduced gold salt phase was washed with 0.1 M HCl, 0.1 M NaOH and DI-H_2O. 1 mL of MUA in toluene (2.29 M) was prepared at 60°C and then added slowly into the preheated AuNP solution (at 60°C) causing precipitation. The black precipitated MUA modified AuNPs were gathered and cleaned with toluene to eliminate excessive MUA. The final precipitates were suspended in 50 mM TRIS buffer. The same procedure was used for producing MPA modified AuNPs.

3.2.2.3. PAH/PAA LbL

PAH was dissolved in 50 mM TRIS buffer at pH 7.2 or pH 9 and PAA was dissolved in 50 mM sodium acetate buffer at pH 4.5 or 50 mM TRIS buffer at pH 7.2; some additional titration was required with NaOH/HCl. The PE solutions were then sonicated for 1 h. A 5 mL solution of 12 nM $AuNP_{MUA}$ in TRIS buffer was rapidly added to 5 mL of PAH in a 50 mL conical tube under sonication for 10 min and incubated with mild shaking for at least 1 h. The solution was precipitated by the addition of isopropanol (2:1 V/V) and centrifuged at 10 000 RCF at room temperature for 10 min. For PAH at pH 9, TRIS HCl was added at 60 mg/ml before the addition of isopropanol. The supernatant was decanted, leaving a gelatinous pellet that was

resuspended in 1 mL of pH 7.2 50 mM TRIS buffer. Excess PAH was removed by three rounds of ultracentrifugation at 180,000 RCF (2 h, 1 h, and 30 min respectively). A 5 mL, 12 nM solution of PAH coated AuNPs was added to the PAA solution under sonication for 10 min and incubated with mild shaking for 1 h. The solution was precipitated by the addition of isopropanol (2:1 V/V) and centrifuged at 10,000 RCF at room temperature for 10 min. Excess PAA is removed by three rounds of ultracentrifugation at 180,000 RCF (2 h, 1 h, and 30 min respectively).

3.2.2.4. PAH/PSS-*co*-MA LbL

PSS-*co*-MA was dissolved in DI-H_2O, sonicated for 1 h, and was titrated to pH 2 with HCl. A 5 mL solution of 12 nM PAH coated AuNPs (produced using the buffer method mentioned previously) in DI-H_2O was rapidly added to 5 mL of PSS-*co*-MA in a 50 mL conical tube under sonication for 10 min and incubated with mild shaking for 1 h. The solution was titrated with NaOH to pH 9 and precipitated by the addition of isopropanol (2:1 V/V) and centrifuged at 10,000 RCF at room temperature for 30 min. The supernatant was decanted leaving a gelatinous pellet that was resuspended in 1 mL of pH 9, 50 mM TRIS buffer. Excess PSS-*co*-MA is removed by three rounds of ultracentrifugation at 180,000 RCF (2 h, 1 h, and 30 min respectively).

3.2.2.5. Microelectrophoresis

The zeta potential of AuNPs were determined with a ZetaSizer Nano Series ZEN 3600 spectrometer (Malvern). AuNPs (6-10 nM) were dispersed in 1 mM TRIS in a DT1070 cuvette and measured 3 times. For pH dependent measurements the MPT-2 autotitrator accessory (Malvern) and pH probe (Malvern) were used. A 10 mL, 10 nM

AuNP solution in DI-H_2O was titrated with either 0.1 M NaOH or 0.1M HCl at 0.5 pH increments. The 10ml AuNP solution was sampled 4 times for measurement at each pH increment.

3.2.2.6. UV-Vis

Absorbance spectra were obtained on a Cary 300 UV-Vis spectrophotometer (Agilent) with a 6x6 multi-cell Peltier block (Agilent). Measurements were acquired at 300 nm/min, 0.5 nm resolution, 0.1s integration time. Samples were measured in a semi-micro PMMA cuvette and baseline corrected with a cuvette filled with buffer. Raw spectra were filtered with a 25 wide median filter to remove noise.

3.2.2.7. TEM Analysis

A 10 µL portion of the AuNP stock solution for analysis was dropped onto a commercially-available carbon film coated-300 square mesh copper grid (CF-300 Cu, Electron Microscopy Sciences, Hatfield, PA) followed by 24 h of atmosphere drying. The AuNPs were examined by TEM (HF3300, Hitachi Scientific Instruments, Tokyo, Japan) operated at 300 kV with a cold field emission gun (FEG).

3.2.3. Results and Discussion

3.2.3.1. LbL on AuNPs

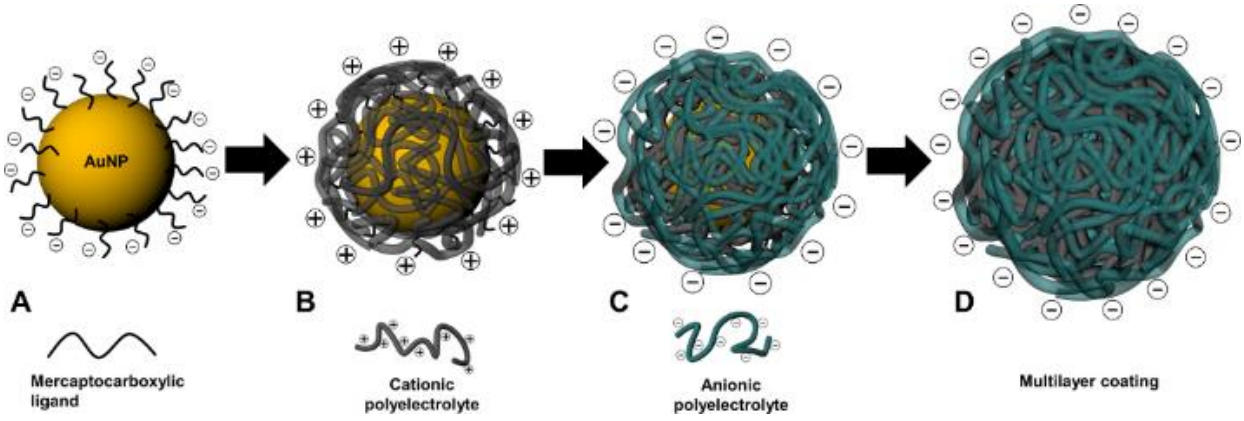

Figure 3.3: (A) Mercaptocarboxylic acid stabilized AuNPs after the addition of a (B) cationic PE followed by an (C) anionic PE. (D) Multilayer coated AuNP after repeating steps B and C several times.

The basic process for LbL modifying AuNPs is depicted in Figure 3.3. AuNPs are synthesized with a stabilizing ligand, which is commonly a mercaptocarboxylic acid (Figure 3.3A), followed by coating with a cationic PE (Figure 3.3B) and then an anionic PE (Figure 3.3C) with multiple centrifugation/redispersion cycles between each step. This process can theoretically be repeated indefinitely to yield a multilayer coated NP with a desired thickness and terminal coating (Figure 3.3D).

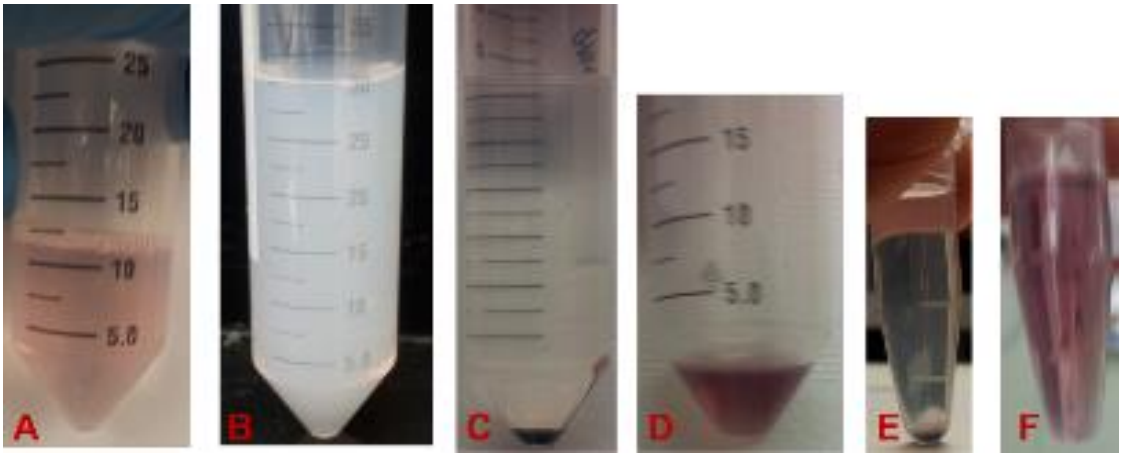

Figure 3.4: The LbL experimental process shown visually: (A) $AuNP_{MUA}$ are mixed with excess PE, (B) solvent precipitation by the addition of isopropanol, (C) sedimentation of PE and AuNPs by centrifugation, (D) resuspension in buffer, (E) ultracentrifugation, (F) decanting of supernatant and resuspension in buffer.

The procedure we developed for NP LbL splits each layer deposition cycle into a multistep process. Initially, the MUA stabilized AuNP template is mixed with the oppositely charged PE (Figure 3.4A) at the adsorption pH. The adsorption pH is selected to maximize the surface charge density of template AuNP but can be varied around the PE pKa to tune the PE charge density. The mixture is then precipitated by the addition of isopropanol (Figure 3.4B) and centrifuged to completely sediment both coated AuNPs and excess PE into a gelatinous pellet (Figure 3.4C). The solvent precipitation (SP) step serves to make sample processing more amenable by concentrating the sample volume (≈10:1) and changing suspension media from the adsorption pH to the centrifugation pH before ultracentrifugation. The sediment is resuspended in a small volume of buffer at the centrifugation pH (Figure 3.4D) and ultracentrifuged to sediment the coated AuNPs (Figure 3.4E). Since the high speed of ultracentrifugation can often lead to complete aggregation of NPs that have a low surface

charge, it is imperative that the centrifugation pH be selected to maximize the charge density of the terminal PE. The supernatant containing the excess PE is decanted and the AuNP sediment is resuspended in buffer (Figure 3.4F). The ultracentrifugation and supernatant decanting is repeated twice more to ensure removal of excess PE. NP stability can be visually assessed after centrifugation steps (Figure 3.4C and Figure 3.4E) as we found that stable NPs always form a sediment at the bottom of the tube that can be easily redispersed without sonication. The sample can then be analyzed or used for deposition of the next layer following the same process, while exchanging the adsorption pH and centrifugation pH to correspond to the next PE layer. For brevity, the adsorption pH and centrifugation pH for each PE layer is denoted by a superscript and subscript respectively ($PE^{\text{Adsorption pH}}_{\text{Centrifugation pH}}$).

3.2.3.2. Solvent Precipitation

The solvent precipitation (SP) step serves to make sample processing more amenable by concentrating the sample volume (≈10:1) and changing suspension media from the adsorption pH to the centrifugation pH before ultracentrifugation. SP was explored as an alternative to ultracentrifugation, but resulted in an inability to either remove excess PE or recover a substantial amount of NPs. We use the term "SP efficiency" to describe the duration of centrifugation for complete particle recovery and the percentage yield of that recovery. Through qualitative empirical observation we found that SP efficiency is a function of PE concentration, PE ionization, pH, and ionic strength. SP efficiency is higher for samples containing buffer (requires less time for recovery) than for sample in titrated DI-H_2O regardless of pH (Figure 3.5, Figure 3.6).

SP efficiency could be further improved by the addition of excess monovalent buffer salt (TRIS HCl for PAH or sodium acetate for PAA) immediately before the addition of isopropanol (Figure 3.5, Figure 3.6). This additional buffer salt improves precipitation, without inducing the aggregation that occurs with the addition of NaCl.

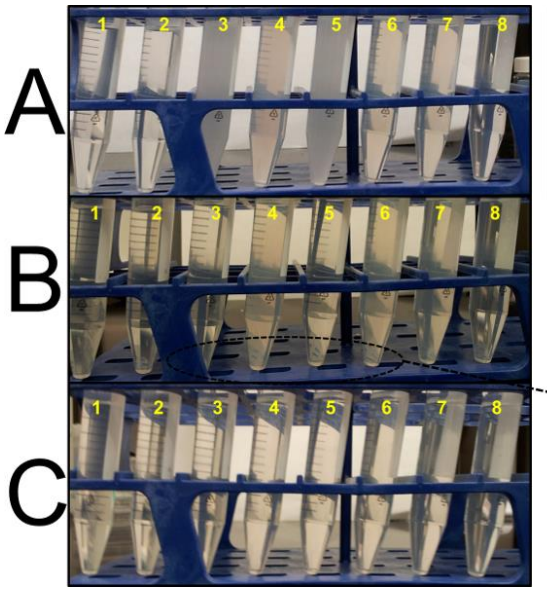

Sample	poly (allylamine hydrochloride)	Solvent
8	pH 7.2: Titrated DI-H_2O	Isopropanol
7	pH 9: Titrated DI-H_2O	
6	pH 9: Titrated to pH 7.2 before SP	
5	pH 7.2: 50mM TRIS	
4	pH 9: 50mM TRIS	
3	pH 9: 50mM TRIS + excess TRIS HCl (60mg/ml)	
2	pH 9: 50mM TRIS	Acetone
1	pH 9: 50mM TRIS	Ethanol

Figure 3.5: Solvent precipitation of PAH under different conditions after (A) solvent addition, (B) Centrifugation for 5 min at 10,000 RCF and (C) 60 min at 10,000 RCF.

Complete sedimentation of samples by SP in DI-H_2O requires about 60 min at 10,000 RCF, while the buffer system with added buffer salt takes about 5 mins at the same speed (Figure 3.5, Figure 3.6). Figure 3.5 shows several different conditions that lead to different levels of solvent precipitation for poly (allylamine hydrochloride) (PAH) depending on solvent, buffer concentration, and pH when (Figure 3.5A) solvent is added to water/buffer at a ratio of 2:1, after (Figure 3.5B) centrifugation for 5 min at 10,000 RCF and (Figure 3.5C) after centrifugation for 60 min at 10,000 RCF.

Comparison between isopropanol, acetone and ethanol (Figure 3.5A: 1, 2, 4) shows that under identical conditions isopropanol leads to precipitation and was consequently used for all experiments. For samples in 50 mM TRIS buffer at pH 7.2 (Figure 3.5A: 5) we get better precipitation than at pH 9 (Figure 3.5A: 4) and for samples without buffer precipitation is less (Figure 3.5A: 7, 8, 9). Due to the SP efficiency at pH 9 for buffered solutions excess TRIS HCl was added at 60 mg/ml, which reduces pH to around 7.2 and increases buffer strength to improve SP efficiency (sample 3). After centrifugation for 5 min the sample at pH 7.2 and at pH 9 with added buffer (Figure 3.5B: 3, 5) have formed a clear gelatinous sediment, while the other samples have minimal sediment and remain turbid (Figure 3.5B: 4, 6, 7). After centrifugation for 1 h those samples form sediment (Figure 3.5C: 4, 6, 7). Samples that did not become significantly turbid (Figure 3.5A: 1, 2, 8) did not form any sediment regardless of centrifugation time tested.

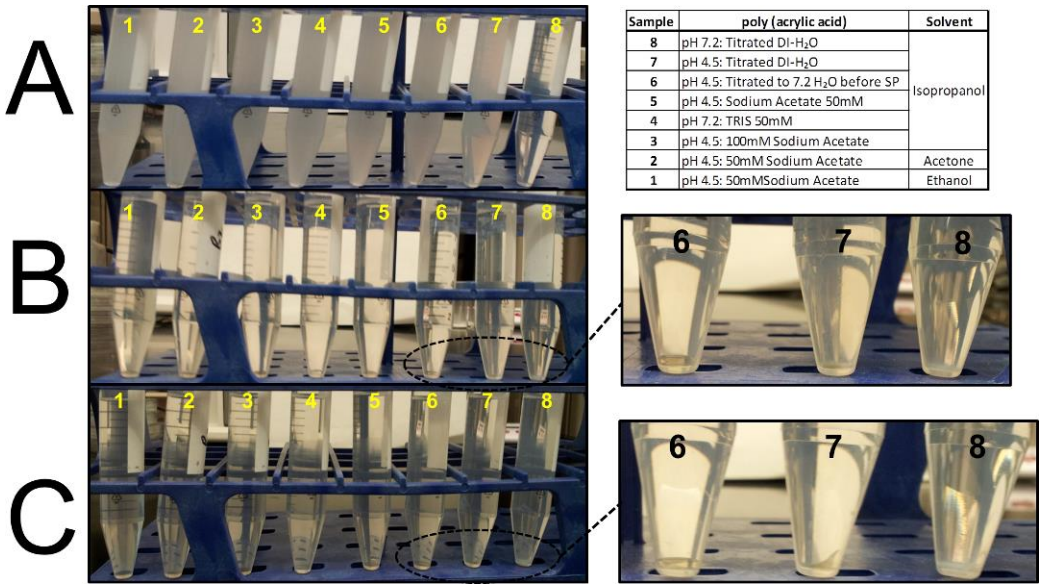

Sample	poly (acrylic acid)	Solvent
8	pH 7.2: Titrated DI-H_2O	Isopropanol
7	pH 4.5: Titrated DI-H_2O	
6	pH 4.5: Titrated to 7.2 H_2O before SP	
5	pH 4.5: Sodium Acetate 50mM	
4	pH 7.2: TRIS 50mM	
3	pH 4.5: 100mM Sodium Acetate	
2	pH 4.5: 50mM Sodium Acetate	Acetone
1	pH 4.5: 50mMSodium Acetate	Ethanol

Figure 3.6: SP of PAA under different conditions after (A) solvent addition, (B) centrifugation for 5 min at 10,000 RCF and (C) 60 min at 10,000 RCF.

Figure 3.6 shows several different conditions lead to different levels of PAA precipitation depending on solvent, buffer concentration, and pH when (Figure 3.6A) solvent is added to water ratio of 2:1, after (Figure 3.6B) centrifugation for 5 min at 10,000 RCF and (Figure 3.6C) after centrifugation for 60 min at 10,000 RCF. The SP efficiency of PAA is generally higher than for PAH as noted by the high turbidity in samples 1-6 and partial turbidity in sample 7 (Figure 3.6A). It is even possible to precipitate a solution of PAA at pH 4.5 in 50mM sodium acetate buffer using either isopropanol, acetone, or ethanol (Figure 3.6A: 1, 2, 4), however the efficacy of the ethanol and acetone SP was not fully tested. After centrifugation at 10,000 RCF for 5 min samples 1-6 were all clear with a visible pellet, while both samples 7 & 8 showed incomplete sedimentation (Figure 3.6B). After 60 min of centrifugation sample 7 formed a pellet but sample 8 only showed partial pellet formation. Overall, PAA could be more easily precipitated but still showed higher efficiency with added buffer compared to DI-H_2O. One way to overcome the low SP efficiency of pH 4.5 DI-H_2O samples is by titration back to pH 7.2 before SP, which leads to greater SP efficiency as shown by sample 6.

3.2.3.3. PAH/PAA LbL on 5 nm $AuNP_{MUA}$

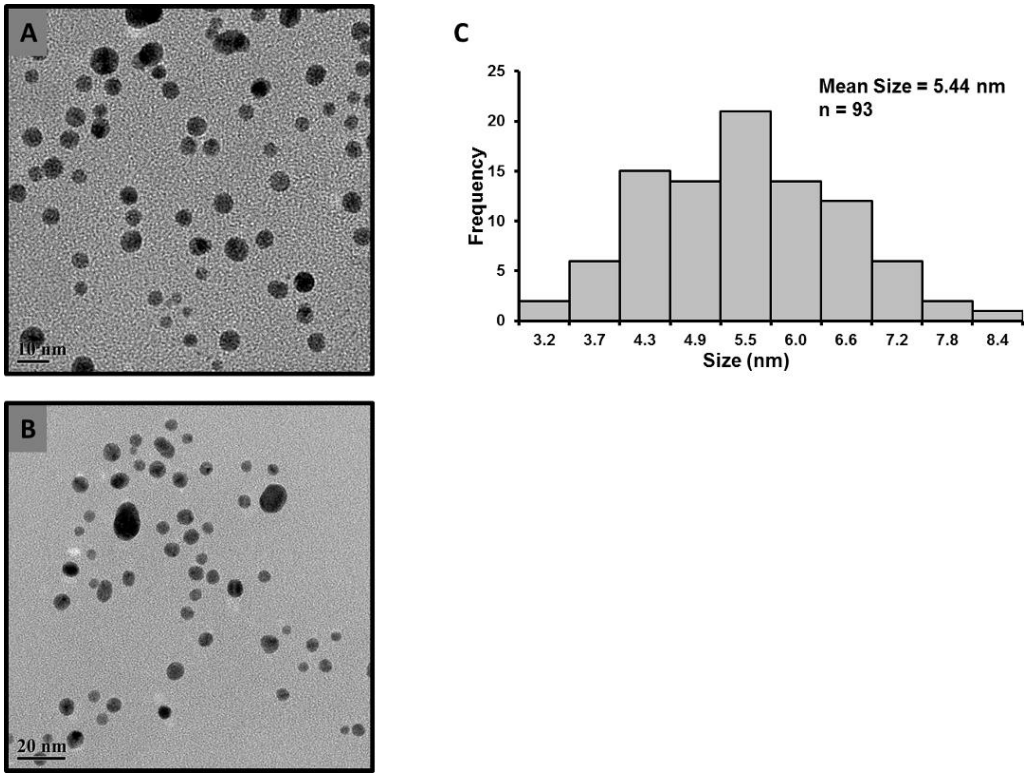

Figure 3.7: (A)(B) TEM images of $AuNP_{MUA}$ and (C) Histogram plot of AuNP diameter.

The $AuNP_{MUA}$ was synthesized using procedures described in the literature.[185, 215, 216] The resulting average diameter was determined spectrally[217] to be approximately 5 nm and was confirmed by TEM (Figure 3.7). Adsorption of the first cationic PE layer onto the anionic AuNP must occur above the surface group's pKa (≈4.5) and near or below the pKa of the cationic PE.

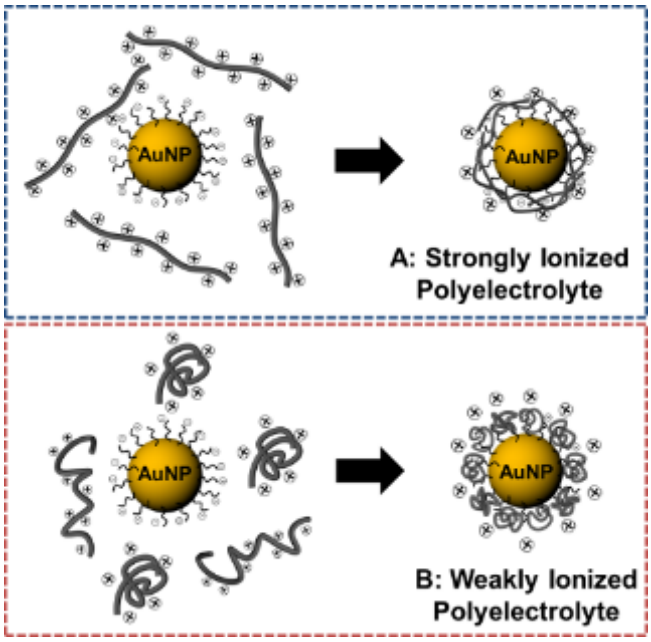

Figure 3.8: Two different scenarios for pH dependent LbL: (A) PE is fully ionized and rigid resulting in thin films of linear PE, (B) PE is partially/weakly ionized and randomly coiled leading to thicker films of coiled PE.

Two cases for PE ionization shown in Figure 3.8 were tested to understand how the choice of pH affects PE adsorption. Deposition at a pH where the PE is expected to be more strongly ionized and rigid, leading to thinner film growth (Figure 3.8A), and at a pH where the PE is weakly ionized and coiled, resulting in thicker film growth (Figure 3.8B).[200] Experimentally, the weakly ionized case involved deposition of PAH ($pK_a \approx 8$-9)[197] at pH 9 and PAA ($pK_a \approx 4.5$-6.5)[197, 199] at pH 4.5, while the strongly ionized case used pH 7.2 for both PAH and PAA; in both the weakly and strongly ionized cases the centrifugation was at pH 7.2.

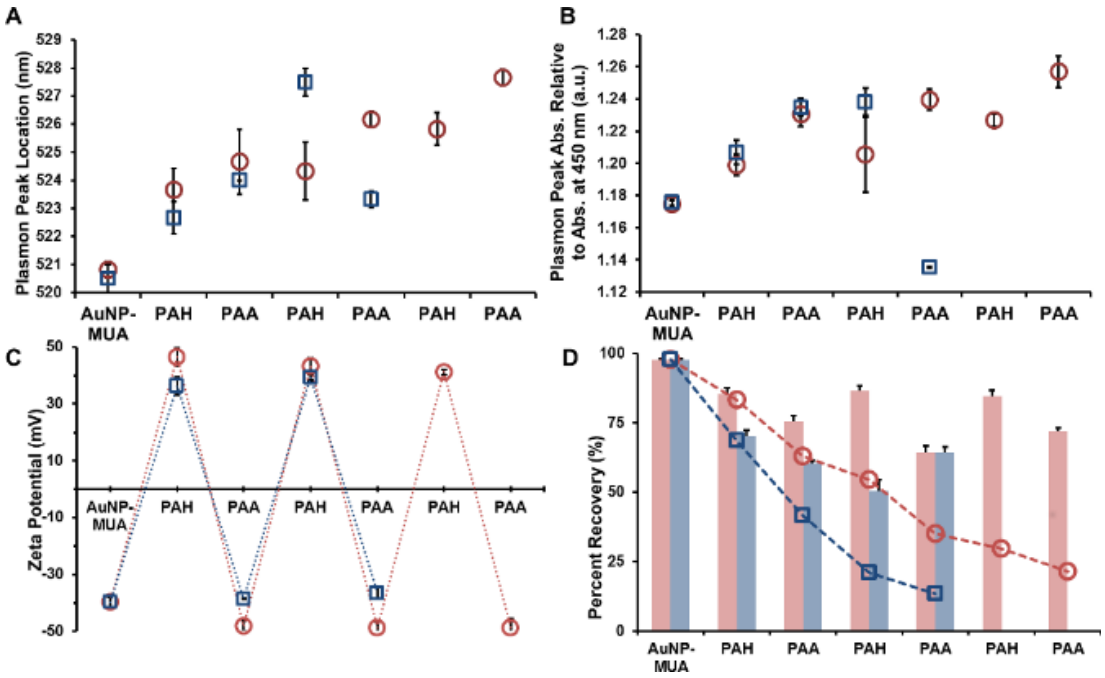

Figure 3.9: LbL on AuNP$_{MUA}$ with PAH and PAA in buffer. (A) Plasmon peak absorbance location, (B) plasmon peak absorbance increase relative to the absorbance at 450 nm and (C) microelectrophoresis measurements after each layer deposition cycle for AuNP$_{MUA}$-($PAH^{7.2}_{7.2}$/$PAA^{7.2}_{7.2}$) multilayers (blue □) and AuNP$_{MUA}$-($PAH^{9}_{7.2}$/$PAA^{4.5}_{7.2}$) multilayers (red ○). (D) Percent recovery of AuNPs per layer (blue bars) and cumulative (blue --□--) for AuNP$_{MUA}$-($PAH^{7.2}_{7.2}$/$PAA^{7.2}_{7.2}$) and per layer (red bars) and cumulative (red --○--) for AuNP$_{MUA}$-($PAH^{9}_{7.2}$/$PAA^{4.5}_{7.2}$). For AuNP$_{MUA}$ the percent recovery represents three rounds of ultracentrifugation only and no SP. Error bars represent standard deviations of three different samples (n = 3).

AuNPs are used as a model template because their aggregation state can be determined by monitoring changes in the plasmon peak location, which correlates to aggregation state observed by TEM.[182, 183] When AuNPs aggregate, interparticle coupling produces larger redshifts in the plasmon peak location, while polymer adsorption without aggregation produces dielectric changes manifested as smaller redshifts.[182, 183] The magnitude of these redshifts can vary depending on AuNP properties (size, concentration, stabilizing ligand, etc…) limiting direct comparison of

our results to those of others. However, by measuring the relative change in plasmon peak absorption location after each layer deposition cycle, the conditions for preventing aggregation during this pH dependent LbL can be explored. For the weakly ionized case an approximate 4 nm redshift occurs in the plasmon peak absorbance location after the deposition of the first PAH layer, followed by redshifts of less than 1 nm for subsequent layers (Figure 3.9A). For the strongly ionized PE case slightly smaller redshifts are observed for the first bilayer but deposition of the third layer causes a larger redshift in plasmon peak absorbance location followed by a sharp blueshift (Figure 3.9A). For the weakly ionized conditions plasmon peak absorbance intensity follows the same trend as plasmon peak absorbance location but for the strongly ionized case a sharp decrease in plasmon peak intensity after deposition of the 4^{th} layer (Figure 3.9B). It is not completely clear why this sharp decrease occurs, but this likely represents the onset of significant AuNP aggregation. For both the weakly and strongly ionized cases there are no secondary peaks observed in the absorbance spectra to indicate any substantial aggregation (Figure 3.10). The microelectrophoresis measurements for the weakly ionized case show a large magnitude of charge reversal greater than 40 mV after the addition of both PAH and PAA, but a decrease in magnitude of 5 mV between the first and last layer of PAH (Figure 3.9C). For the strongly ionized charge reversal is 4-12 mV less than the weakly ionized case for PAH and PAA layers (Figure 3.9C). The high charge reversal in all cases is indicative of high colloidally stability.

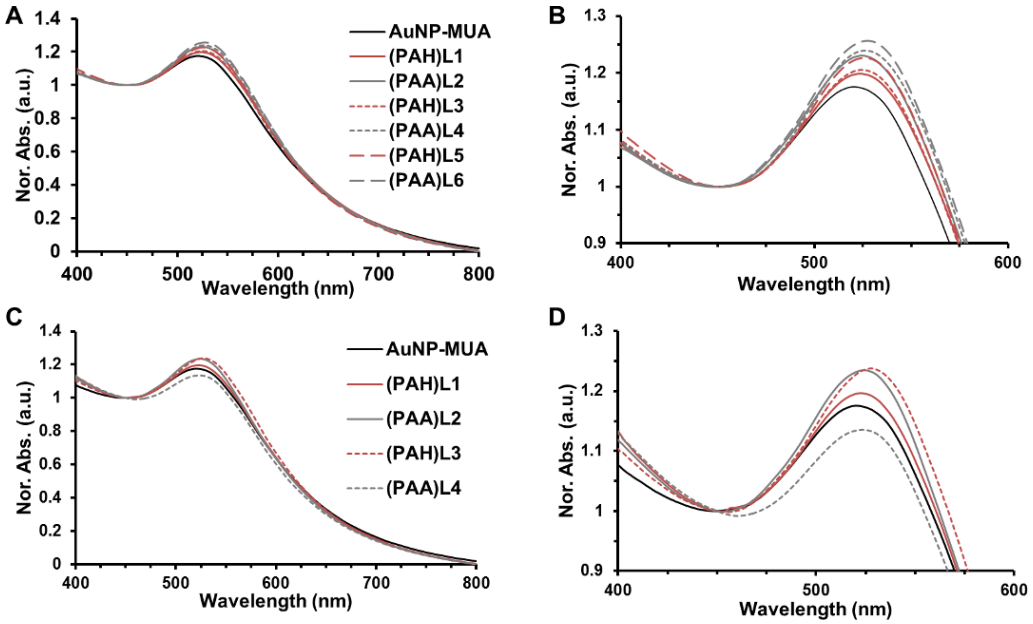

Figure 3.10: (A)(B) UV-Vis spectra for weakly ionized LbL AUNP$_{MUA}$-($PAH^{9}_{7.2}$/$PAA^{4.5}_{7.2}$) and (C),(D) strongly ionized LbL AuNP$_{MUA}$-($PAH^{7.2}_{7.2}$/$PAA^{7.2}_{7.2}$).

AuNP concentration and percent recovery was determined after each layer deposition cycle by the absorbance at 450 nm.[217] The cumulative percent recovery represents the accumulating loss of the multilayer process. Overall, the percent recovery for each layer and the cumulative percent recovery are lower for the strongly ionized case compared to the weakly ionized case (Figure 3.9D). After the deposition of 4 layers only 13.5% of AuNPs remained for the strongly ionized case compared to 35% recovery for the weakly ionized case (Figure 3.9D). We did not continue past layer 4 for the strongly ionized case due to this low recovery. For the weakly-ionized case, an average recovery of 78% per layer is achieved, which is lower than the reported 94%[182] recovery for 13.5 nm AuNPs; however, it is much higher than the 30%[181] reported for similarly-sized 5 nm AuNPs.

The loss of AuNPs can be attributed to the combination of several factors: (1) transfer loss between the adsorption, solvent precipitation and ultracentrifugation steps; (2) accidental discarding during supernatant removal after each ultracentrifugation cycle; (3) unstable particles that cannot be recovered after ultracentrifugation. The first two factors can be mitigated by careful handling and represent only a small percentage of the lost AuNPs (≈2.2% for $AuNP_{MUA}$) (Figure 3.9D). The third factor represents AuNPs that become unstable because of inadequate PE coating or are ultracentrifuged under improper pH conditions. These unstable AuNPs become strongly immobilized on the tube wall or form a tightly packed pellet that is not redispersible by vortexing or sonication. In contrast, when properly coated AuNPs are ultracentrifuged they form sediment on the bottom of the tube (Figure 3.4E) that is easily redispersed by pipette aspiration. For these reasons, ultracentrifugation can be used to qualitatively assess AuNP stability, while also serving to purify the sample of poorly coated AuNPs. The much higher loss in the strongly ionized case indicates that the pH conditions used are leading to a higher percentage of unstable AuNPs that are being excluded during ultracentrifugation. The weakly ionized case is able to provide very high stability even after only a single layer for two possible reasons: (1) charge overcompensation by a more weakly ionized PE on the AuNP template requires more PE chains to adsorb, leading to a more homogenous coating of the particle surface[208] and/or (2) the coiled conformation of the weak PE provides a more effective steric barrier.[190]

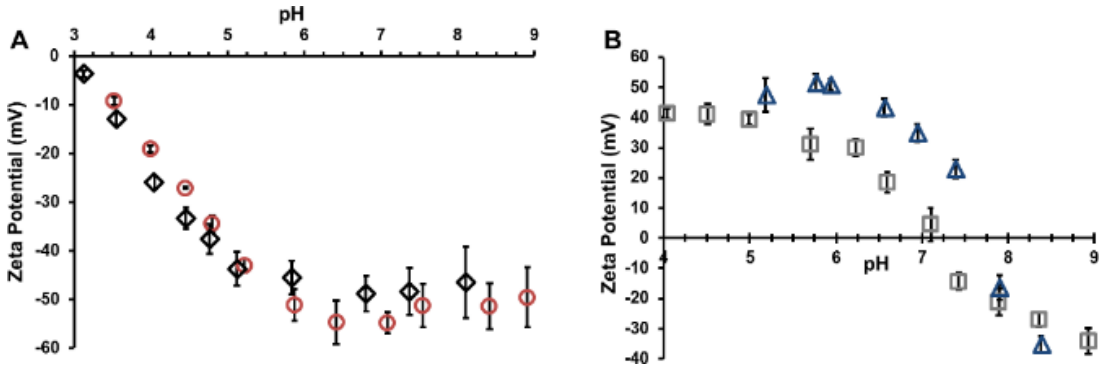

Figure 3.11: Zeta potential measured as a function of pH for (A) $AuNP_{MUA}$ (red ○), $AuNP_{MUA}$-$(PAH^{9}_{7.2}/PAA^{4.5}_{7.2})_1$ (black ◊) and (B) $AuNP_{MUA}$-$(PAH^{9}_{7.2})$ (grey □), $AuNP_{MUA}$-$(PAH^{9}_{7.2}/PAA^{4.5}_{7.2})_{1.5}$ (blue Δ). Error bars represent standard deviations (n = 4).

To understand the pH dependent charge density and electrostatic stability the zeta potential as a function of pH was measured starting from pH 9 (where surface charge and particle stability is expected to be highest) to pH 3 (Figure 3.11A). The $AuNP_{MUA}$ and $AuNP_{MUA}$-$(PAH^{9}_{7.2}/PAA^{4.5}_{7.2})_1$ show an expected profile of a carboxylic acid terminal coating with surface charge decreasing as pH decreases near the carboxylic acid pKa. From pH 7-9 both MUA and PAA terminated AuNPs maintain a strong negative charge between -45 mV and -55 mV, suggesting that the difference in pH adsorption from pH 7.2 to pH 9 was only affecting the PAH ionization and not the anionic AuNP charge density. The pH dependent microelectrophoresis for $AuNP_{MUA}$-$(PAH^{9}_{7.2})$ and $AuNP_{MUA}$-$(PAH^{9}_{7.2}/PAA^{4.5}_{7.2})_{1.5}$ reveals an interesting apparent dynamic instability when the sample is titrated from pH 4-5 to pH 9 (Figure 3.11B). The zeta potential for all PAH terminated particles at pH 7.2 was initially measured greater than 40 mV, however after pH was decreased to pH 4-5 before titration and then increased again, the particle charge became neutral when returning to pH 7.2, leading to aggregation. We suspect that exposure to a

lower pH is causing multilayer rearrangement or multilayer interpenetration similar to what is observed for planar films.[199] This dynamic instability is an interesting observation considering our previous work found that PAH coated QDs stored at pH 8 were stable for several months,[24] while under these dynamic conditions the AuNPs rapidly aggregate. The $AuNP_{MUA}$-$(PAH^{9}_{7.2}/PAA^{4.5}_{7.2})_{1.5}$ profile also shows an apparent shift in the surface pK_a towards basic pH, which is consistent with reports of PAH/PAA multilayers on larger NPs.[207] It is worth noting that LbL can also be done successfully in pH titrated PE solutions without buffer. Since PE adsorption is done close to the PE pKa, the PE itself can used as a buffer.

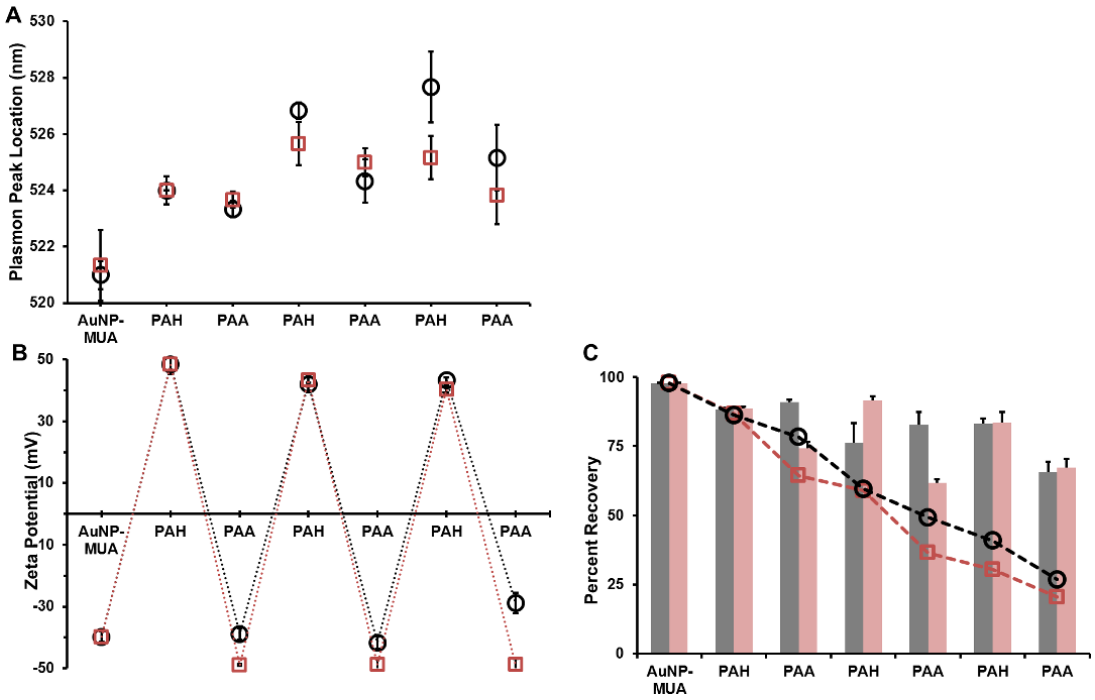

Figure 3.12: (A) Plasmon peak absorbance location and (B) microelectrophoresis measurements after each layer deposition cycle for $AuNP_{MUA}$-$(PAH^{7.2}_{7.2}/PAA^{7.2}_{7.2})$ multilayers in buffer (red □) and $AuNP_{MUA}$-$(PAH^{9}_{7.2}/PAA^{4.5}_{7.2})$ multilayers in water (black ○). (C) Percent recovery of AuNPs per layer (red bars) and cumulative (red --□--) for $AuNP_{MUA}$-$(PAH^{7.2}_{7.2}/PAA^{7.2}_{7.2})$ in buffer and per layer (black bars) and cumulative (black --○--) for $AuNP_{MUA}$-$(PAH^{9}_{7.2}/PAA^{4.5}_{7.2})$ in water. For $AuNP_{MUA}$ the percent recovery represents three rounds of ultracentrifugation only and no SP. Error bars represent standard deviations of three different samples (n = 3).

The results shown in Figure 3.12A and Figure 3.12 below show that very similar results can be achieved in non-buffer solutions for plasmon peak absorbance and percent recovery respectively. However, AuNPs coated in buffered solutions showed higher charge reversal for PAA layers (Figure 3.12B). LbL in buffered solutions also have much less processing time because the SP is more efficient and less titration is required. However, if the case does arise where the buffers are found to negatively interact with the template material, non-buffer solutions can be used instead.

3.2.3.4. PAH/PSS-*co*-MA LbL on 5 nm $AuNP_{MUA}$

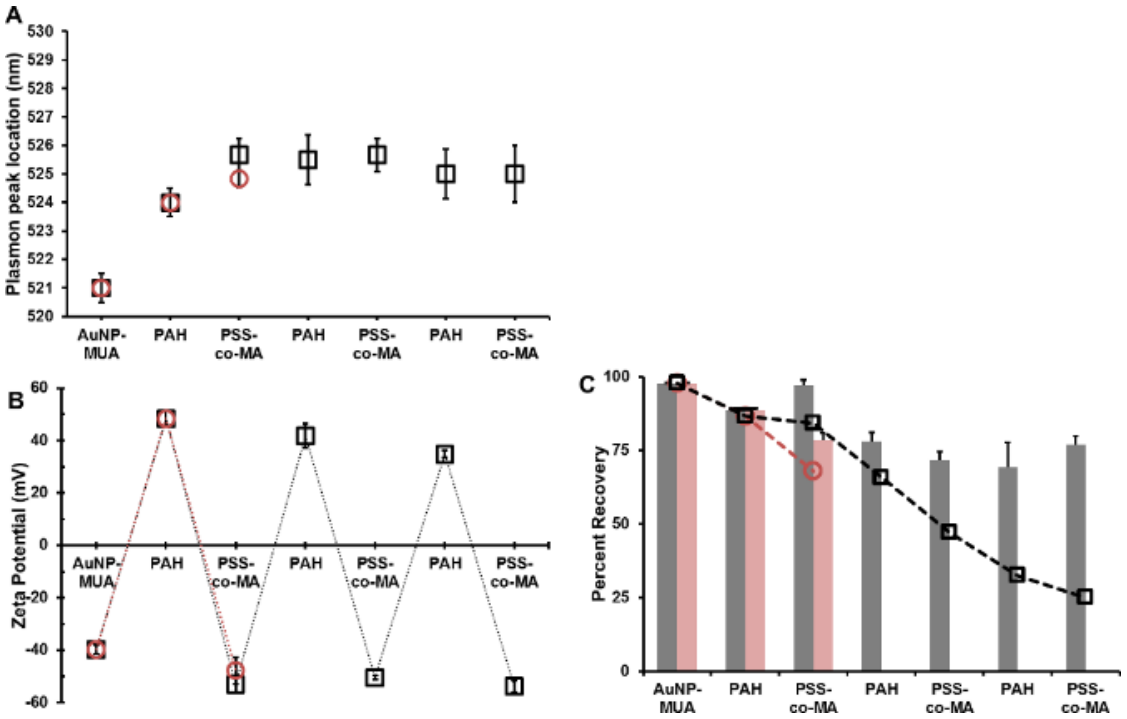

Figure 3.13: (A) Plasmon peak absorbance location and (B) microelectrophoresis measurements after each layer deposition cycle for $AuNP_{MUA}$-($PAH^{9}_{7.2}$/PSS-*co*-MA^{2}_{9} 1:1) (black □) and $AuNP_{MUA}$-($PAH^{9}_{7.2}$/PSS-*co*-MA^{2}_{9} 3:1) (red ○) multilayers. (C) Percent recovery of AuNPs per layer (black) and cumulative (black --□--) for $AuNP_{MUA}$-($PAH^{9}_{7.2}$/PSS-*co*-MA^{2}_{9} 1:1) and per layer (red) and cumulative (red --○--) for $AuNP_{MUA}$-($PAH^{9}_{7.2}$/PSS-*co*-MA^{2}_{9} 3:1). For $AuNP_{MUA}$ the percent recovery is after three rounds of ultracentrifugation only and no SP. Error bars represent standard deviations of three different samples (n = 3).

PSS-*co*-MA is commercially available as two copolymer ratios of 1:1 and 3:1 (SS:MA), each having two pKa values of 2.9/8.8 and 2.7/8.3 respectively.[212] Multilayers of $AuNP_{MUA}$-($PAH^{9}_{7.2}$/PSS-*co*-MA^{2}_{9} 1:1) and $AuNP_{MUA}$-($PAH^{9}_{7.2}$/PSS-*co*-MA^{2}_{9} 3:1) were constructed in TRIS for PAH and in titrated DI-H_2O for both PSS-*co*-MA copolymer ratios. Assembly of both copolymers at pH 2 represents two different cases of PE rigidity where the 1:1 copolymer is expected to be less charged and more

coiled than the 3:1, leading to thicker and thinner coatings respectively. The plasmon peak absorbance location extracted from UV-Vis absorbance measurements shows that after the addition of one layer of PSS-*co*-MA 1:1 the plasmon peak redshifts 2 nm, but no further is shift is observed with additional coating (Figure 3.13A). The first layer of the PSS-*co*-MA 3:1 formed an apparently stable coating and resulting in a 1 nm redshift in the plasmon peak absorbance location, but the addition of another PAH layer causes complete particle flocculation that cannot be recovered after ultracentrifugation for further analyses (Figure 3.13A). We postulate that the higher ratio of SS:MA of PSS-*co*-MA 3:1 makes the PE too rigid to completely wrap the AuNP as effectively as the 1:1 copolymer. The subsequent addition of the third PAH layer removes some PSS-*co*-MA 3:1 chains resulting in charge neutralization and complete particle flocculation. Microelectrophoresis shows high charge reversal after coating with both 3:1 and 1:1 PSS-*co*-MA for all layers, but for PAH terminated layers the zeta potential decreases from about +49 mV to +35 mV from the first to third PAH layer respectively (Figure 3.13B). The percent recovery after the first PSS-*co*-MA 1:1 layer was very high (97%) but subsequent layers show a decreased recovery (70-80%) with a cumulative recovery of only 25% after 6 layers (Figure 3.13C).

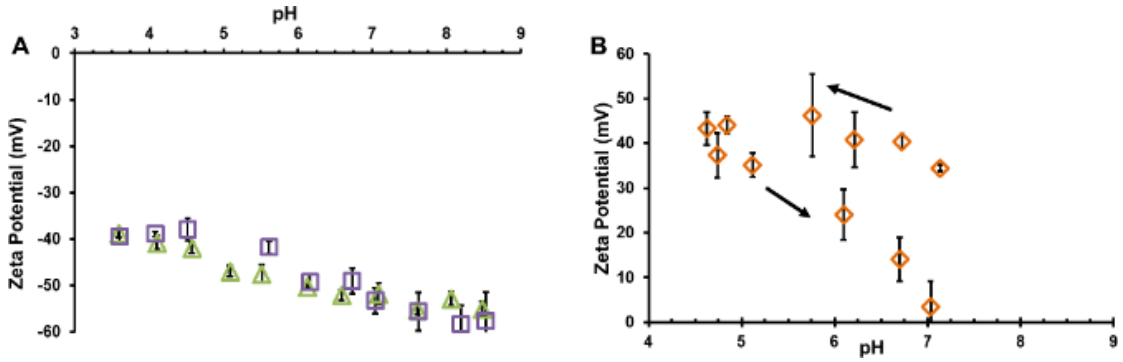

Figure 3.14: Zeta potential measured as a function of pH for (A) $AuNP_{MUA}$-$(PAH^{9}_{7.2}/PSS\text{-}co\text{-}MA^{2}_{9}\ 1{:}1)_1$ (green Δ), $AuNP_{MUA}$-$(PAH^{9}_{7.2}/PSS\text{-}co\text{-}MA^{2}_{9}\ 3{:}1)_1$ (purple □) and (B) $AuNP_{MUA}$-$(PAH^{9}_{7.2}/PSS\text{-}co\text{-}MA^{2}_{9}\ 1{:}1)_{1.5}$ (orange ◊). Arrows indicate direction of titration. Error bars represent standard deviations (n = 4).

The charge density profiles of both 1:1 and 3:1 copolymer ratios of $AuNP_{MUA}$-$(PAH^{9}_{7.2}/PSS\text{-}co\text{-}MA^{2}_{9}\ 1{:}1)_1$ show a strong negative charge of -55 mV at pH 9 and maintain a strong net negative charge of -40 mV even when pH is lowered to pH 3.5 (Figure 3.14A). This shows the ability of PSS-*co*-MA to enhance the electrostatic stability of AuNPs, especially below pH 5. Interestingly, the PSS-*co*-MA 1:1 terminated AuNPs could even be recovered at the end of the titration cycle by centrifugation; however the PSS-*co*-MA 3:1 aggregated upon centrifugation after the end of titration (at pH 3.5). Analysis of $AuNP_{MUA}$-$(PAH^{9}_{7.2}/PSS\text{-}co\text{-}MA^{2}_{9}\ 1{:}1)_{1.5}$ shows the full hysteresis that occurs when the AuNPs are titrated from pH 7.2 to pH 4 and back to pH 7.2 again (Figure 3.14B); the profile is nearly identical to $AuNP_{MUA}$-$(PAH^{9}_{7.2})$. The PSS-*co*-MA/PAH multilayer system is expected to be more stable when exposed to low pH compared to PAA/PAH due to SS groups. However, the similar instability when PAH is deposited on either PAA or PSS-*co*-MA suggests that the source of the dynamic instability may be the increasing charge of the terminal PAH, leading to surface

rearrangement and possibly unwrapping of the AuNP, rather than the loss in charge of the underlying anionic layer. Unfortunately, that cannot be proven from the current data, but it serves as our current working hypothesis to be tested in future studies.

3.2.3.5. PAH/PSS-*co*-MA on MPA AuNPs

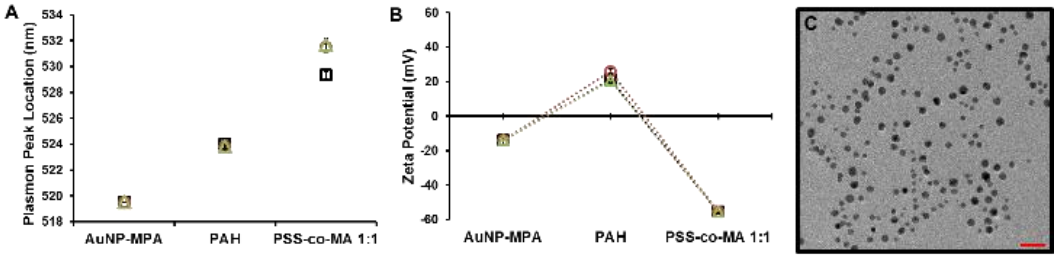

Figure 3.15: (A) Plasmon peak absorbance location and (B) Microelectrophoresis measurements for $AuNP_{MPA}$, $AuNP_{MPA}$-$(PAH^{9}_{7.2})$, and $AuNP_{MPA}$-$(PAH^{9}_{7.2}$/PSS-*co*-MA^{2}_{9} 1:1)$_1$ at PE:AuNP ratios of 60,000:1 (black), 30,000:1 (red ○) and 15,000:1 (green Δ). Error bars present standard deviations of three different samples (n = 3). (C) Representative TEM micrograph of $AuNP_{MPA}$-$(PAH^{9}_{7.2}$/PSS-*co*-MA^{2}_{9} 1:1)$_1$ produced at the 30,000:1 ratio. Scale bar is 20nm.

The smaller capping ligand mercaptoproprionic acid (MPA) was used to stabilize AuNPs ($AuNP_{MPA}$) using the same procedure as $AuNP_{MUA}$. The resulting $AuNP_{MPA}$ MPA stabilized NPs are expected to have a much smaller hydrodynamic size, about 5 nm less than MUA stabilized NPs.[218] This allows us to test the effect of ligand type and hydrodynamic size on this LbL process. Additionally, several different PE:AuNP ratios of 60,000:1, 30,000:1 and 15,000:1 were tested by increasing AuNP concentration, while keeping PE concentration constant. Under weakly ionized conditions the coiled PE's decreased linear size should reduce the probability of interparticle bridging, which could potentially allow increasing the scale of production without compromising the AuNP aggregation state. The PAH/PSS-*co*-MA 1:1 PE combination was used because

previous data indicated this to be a stable combination with the highest percent recovery for the first bilayer. The plasmon peak absorbance location for $AuNP_{MPA}$-($PAH^{9}_{7.2}$) is about 524 nm for all PE:AuNP ratios tested (Figure 3.15A). The added layer of PSS-*co*-MA 1:1 has a much larger shift to 529.3 nm for the 60,000:1 case and to 531.5 nm and 531.7 nm for the 30,000:1 and 15,000:1 respectively (Figure 3.15A). There are no observed secondary peaks in the spectra associated with high levels of interparticle bridging or aggregation for all ratios tested (Figure 3.16).

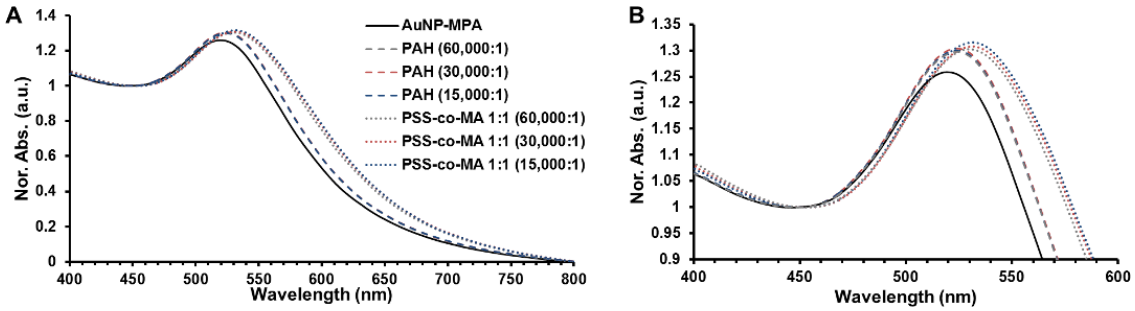

Figure 3.16: (A) UV-Vis spectra for weakly ionized LbL for $AuNP_{MPA}$ (sold line), $AuNP_{MPA}$-$PAH^{9}_{7.2}$ (dashed lines), $AuNP_{MPA}$-($PAH^{9}_{7.2}$/PSS-*co*-MA^{2}_{9} 1:1)$_1$ (dotted lines). (B) Zoomed in graph of same data.

The zeta potential of the initial ligand capped $AuNP_{MPA}$ (-14 mV) is much lower than $AuNP_{MUA}$ (-39.7 mV) and after PAH coating only a modest charge reversal (+20 mV) is achieved for all PE:AuNP ratios (Figure 3.15B). However, the addition of PSS-*co*-MA 1:1 resulted in very high charge reversal (-55 mV) for every case, showing that with only a single bilayer, electrostatic colloidal stability can be greatly enhanced.

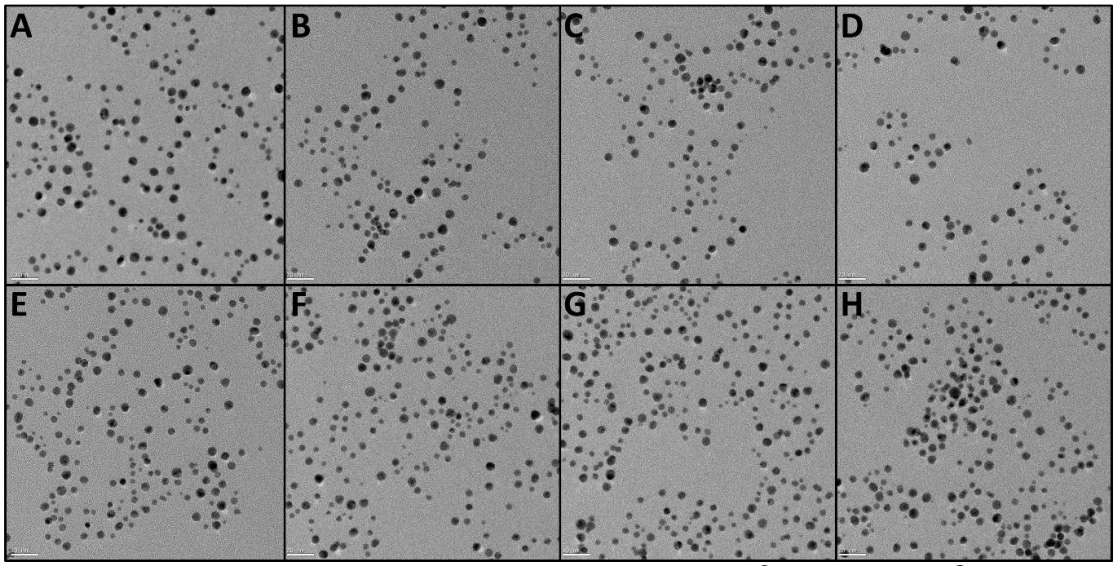

Figure 3.17: (A-H) TEM images of AuNP$_{MPA}$-(PAH$^{9}_{7.2}$/PSS-*co*-MA$^{2}_{9}$ 1:1)$_1$

To further assess the aggregation state after LbL modification, TEM images were acquired for the AuNP$_{MPA}$-(PAH$^{9}_{7.2}$/PSS-*co*-MA$^{2}_{9}$ 1:1)$_1$ produced at the 30000:1 ratio (Figure 3.15C). The image clearly shows that particle monodispersity has been maintained after coating with one bilayer. The PE films cannot be resolved in these images; consequently, for statistical analysis all contacting AuNPs were considered aggregates. Analysis of ~1400 NPs revealed that 95.4% of the AuNP$_{MPA}$-(PAH$^{9}_{7.2}$/PSS-*co*-MA$^{2}_{9}$ 1:1)$_1$ clearly exist as single particles and less than 1% exists as aggregates of 4 or more (Figure 3.17, Table 3.1).

Table 3.1: Statistical analyses of $AuNP_{MPA}$-$(PAH^{9}_{7.2}/PSS\text{-}co\text{-}MA^{2}_{9}$ 1:1)$_1$ aggregation state from TEM images.

AuNPs per Aggregate	Frequency	Percent
1	1338	95.4
2	39	2.8
3	17	1.3
4	4	0.3
≥5	4	0.3
Total	**1402**	

The electrosteric stability of the AuNPs was assessed by exposure to varying concentrations of NaCl in 0.1 phosphate buffer at pH 7.2. The $AuNP_{MPA}$ are stable in DI-H_2O but immediately aggregate when exposed to phosphate buffer with and without NaCl, as noted by the substantial redshift and presence of secondary peaks in the absorbance spectra (Figure 3.18A). In contrast, the $AuNP_{MPA}$-$(PAH^{9}_{7.2}/PSS\text{-}co\text{-}MA^{2}_{9}$ 1:1)$_1$ remain stable immediately after mixing with 0.1 M phosphate buffer with up to 1 M NaCl (Figure 3.18B) and only a small shift in the plasmon peak is observed even at 5 M NaCl (Figure 3.18B). After a 48 h incubation at room temperature $AuNP_{MPA}$-$(PAH^{9}_{7.2}/PSS\text{-}co\text{-}MA^{2}_{9}$ 1:1)$_1$ settling is observed in 500 mM and 1 M NaCl samples, but no decrease in absorbance is observed for 0 - 100 mM NaCl (Figure 3.18C). The 5 M NaCl sample completely precipitated after 48 h and had to be redispersed for measurement and contained substantial aggregation, as noted by the peak shift and peak broadening. After 7 days of storage undisturbed at room temperature, a more notable decrease in absorbance intensity occurs due to AuNPs settling out of solution. However, there is no substantial shift in plasmon peak absorbance location from 0 - 500 mM NaCl.

This clearly shows how just one bilayer of LbL coating can exert such a powerful influence to enhance the AuNP electrosteric stability and to preserve the AuNP optical properties.

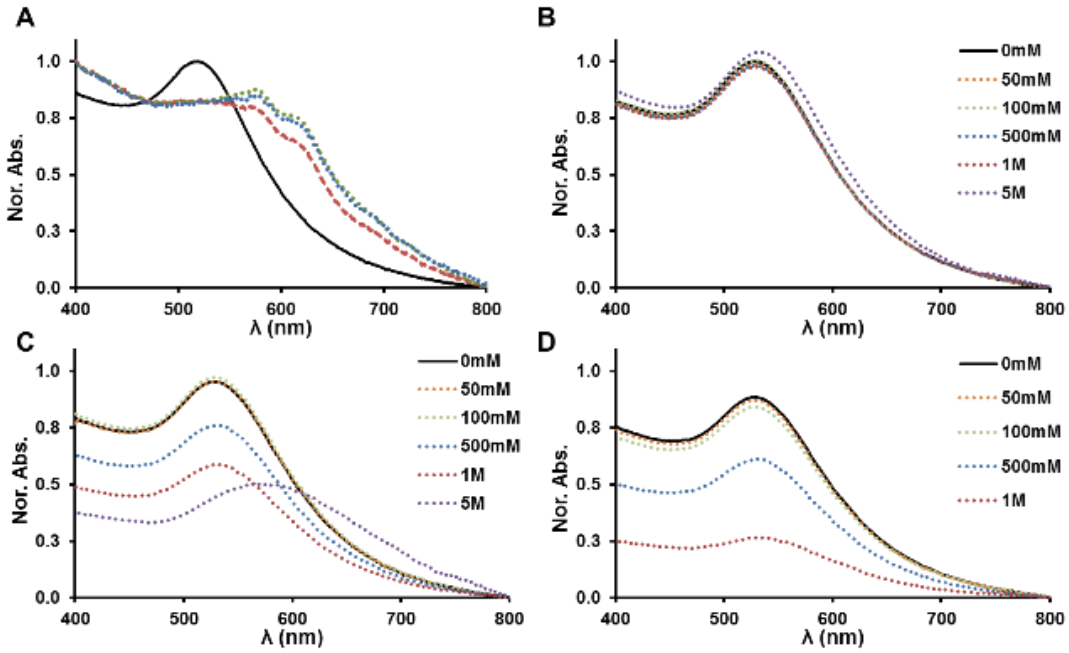

Figure 3.18: (A) $AuNP_{MPA}$ in DI-H_2O (black −) and 0.1 M phosphate buffer pH 7.2 with 0mM (red −−), 50mM (green •) and 100 mM (blue •) NaCl. (B) $AuNP_{MPA}$-$(PAH/PSS\text{-}co\text{-}MA\ 1{:}1)_1$ in 0.1 M phosphate buffer with 0 mM (black −), 50 mM (orange •), 100 mM (green •), 500 mM (blue •), 1 M (red •), or 5 M (purple •) NaCl immediately after mixing, and (C) after 48 h and (D) 7 days at room temperature.

3.2.4. Conclusions

The work has shown the capability for LbL modification of high surface curvature AuNPs with weak and weak-strong PEs using a SP assisted multistep layer deposition process. The choice of solution pH during PE adsorption plays an important role to enhance AuNP surface coverage to increase surface charge and improve recovery throughout the LbL process. In most cases a percent recovery greater than 60% per

layer could be achieved; however, this compounding loss resulted in only 20-30% of AuNPs remaining after 6 layer deposition cycles regardless of the deposition conditions used. It is important to recognize that this compounding loss places limitations on the application of this process for LbL on very small NPs as a multilayer tool; however, this technique was found to be useful as a stabilization method if just a few layers are deposited. The PAH/PSS-*co*-MA 1:1 coated AuNPs could be produced with a very high recovery of 84% and displayed enhanced stability over a broad pH range and in high NaCl concentration. This presents a simple and high yield approach to apply a single bilayer to greatly enhance the electrosteric stability of the AuNP core to preserve the optical properties under adverse conditions. Future work will focus on using this technique on other nanomaterials with an emphasis on the PAH/PSS-*co*-MA formulation, towards functionalization through covalent attachment as multifunctional components for biomedical applications.

3.3. LbL on QD Templates

3.3.1. Background

Nanocrystalline QDs with narrow size distributions and desired optical properties are typically synthesized in non-polar organic solvents and stabilized with hydrophobic ligands.[219] To ready QDs for use in biomedical applications, some modification and engineering of the QD surface is typically necessary. There are many routes to water solubilize QDs, with different methods having various tradeoffs between complexity, conditional stability, hydrodynamic size, and optical properties.[15-17, 169] Mercaptocarboxylic ligands are commonly used because of the simple exchange process

and resulting exposed carboxylic acid groups that provide for further functionalization. Short chain mercaptocarboxylic acid ligands offer the additional benefit of a resulting small hydrodynamic radius, which greatly improves efficiency for distance dependent energy transfer. Commonly used short chain species include monothiolated molecules such as mercaptoproprionic acid (MPA), mercaptoacetic acid (MAA), or mercaptoundecanoic acid (MUA) but more recently the bidentate dihydrolipoic acid (DHLA)[220, 221] has emerged as a more stable alternative because of the higher affinity of the dithiol compared to a monothiol. The high affinity of thiol ligands for metallic surfaces allows the hydrophilic molecule to spontaneously exchange with the more weakly bound hydrophobic trioctylphosphine oxide (TOPO) ligands often used during synthesis.[222] However, the transfer to water is accompanied by a severe and variable decrease in QY[220, 223] with a colloidal stability that is susceptible to photo-oxidation mediated aggregation.[224]

LbL electrostatic self-assembly was explored as a versatile method for surface modification of colloidal DHLA-stabilized QDs (DHLA-QDs). It appears that the work on individual PE coated QDs is limited to two publications. Jaffar *et al.* used one bilayer of poly (allylamine hydrochloride) (PAH) and poly (vinylsulfonic acid) (PVSA) to invert the charge of MAA modified QDs for surface patterning.[189] This work showed the practicality of LbL on QDs but preceded the understanding provided by Schneider to provide the largest quantity of monodisperse LbL-coated QDs. Additionally, characterization of the effects of the PE on the optical properties was not an emphasis. Jin *et al.* used a lipid-PEG-COOH-stabilized QD followed by two bilayers of PAH and

PSS as spacers for dual imaging modality plasmonic QDs. However, the method used for LbL was limited by the low recovery after each wash step even when ultracentrifugation was used.[188] It is also noteworthy that long-chain PEs have been used to produce controlled aggregates as nanocapsules to mitigate QD toxicity[225] and to reverse the surface charge and adsorb negatively charged species for sensing applications.[226-228] However, the intent of these studies was not to produce monodisperse coated QDs, since the conditions used are known to induce flocculation. The resulting QDs were not characterized as monodisperse and were likely unusable as stable suspensions. Based on this limited knowledge, the focus of this work was developing methods to coat and retain large quantities of monodisperse QDs by following the techniques outlined for gold NPs. Preventing aggregation was a major consideration, as availability of individual modified QDs is important for many applications; however, preservation of the QD optical properties was the primary goal. The key to this is understanding how the optical properties, specifically the QY and lifetime, are affected by the interaction of different PEs with the mercaptocarboxylic acid modified QD surface.

3.3.2. Materials and Methods

3.3.2.1. QD Synthesis

CdSe/ZnS core/shell QDs were synthesized according to previously reported procedures.[219, 229, 230] The synthesis was carried out in a single mode CEM Discover microwave reactor operating at 300 W, 2.45 GHz. In a typical experiment, Cadmium oxide (CdO, 99.99%, Alfa Aesar, 0.0514 g, 0.4 mM), tetradecylphosphonic acid

(TDPA,98%, Alfa Aesar, 0.2232 g, 0.8 mM) and TOPO (3.7768, 9 mM) were heated with continuous stirring in a 50 mL glass flask. The mixture was heated to ~300 °C under argon (Ar) flow (~ 1 ml/sec) for 35 min. To this mixture, a selenium stock solution (0.0411 g, 0.5 mM, Aldrich, 99%) dissolved in 2.4 mL (2 g) of tri-n-octylphosphine (TOP, 99%, Aldrich) TOP) was injected at 270 °C and the reaction was continued for 4 min to allow the growth of the CdSe QD cores. This was followed by the addition of Zn and S precursors: 1.6 mL (12 mM) of dimethylzinc (DMZ, 1 M in heptane, Aldrich), 0.42 mL (2 mM) of hexamethyldisilathiane (HMDS, Aldrich), and 6.3 mL (14 mM) of TOP, for the ZnS shell formation. The reaction mixture was heated at 200 °C for 30 min.

3.3.2.2. DHLA Synthesis

DHLA was freshly prepared according to previously reported methods[231]. In a typical experiment, 4 g of (±)-α-lipoic acid (98%, Sigma) was reduced with a fresh stock of excess (3 g) sodium borohydride (NaBH4, 98%, Sigma). The reaction mixture is chilled to 4°C and allowed to stir for 2 h under a constant argon blanket. It is then acidified with 15 mL of 12 M hydrochloric acid followed by the addition of ~100 mLs of toluene. Pure DHLA is extracted from this mixture by evaporation using a rotovap leaving behind ~4 mL of DHLA. About 0.5 mL of pure DHLA was added to few hundred milligrams of QDs and heated at ~90 C on a hot plate with continuous stirring for 12 h. The resulting mixture is suspended in 3 mL of methanol followed by the addition of excess (approximately 1 g) of potassium tert-butoxide (K-tBuO). The solution is centrifuged and the resulting DHLA-QDs were then suspended in TRIS

buffer pH 8-8.5. DHLA-QDs were filtered using a 0.2 μm syringe filter (Nalgene, PES 0.2 μm) and then a 30 kDa centrifuge filter in order to remove any excess K-tBuO in solution.

3.3.2.3. QD Characterization Techniques

Absorption spectra were recorded on a Hitachi U-4100 UV-Vis-NIR spectrophotometer. Steady-state photoluminescence spectra were collected on a QuantaMaster 40 system by Photon Technology International (Ontario, Canada) with a 75 watt continuous xenon arc lamp and digital PMT detection system using 1 nm excitation and emission slit widths, 1 second integration time. Fluorescence lifetime was collected using a TimeMaster LED system by Photon Technology International (Ontario, Canada) using a 405 nm LED (1.5 ns pulse width) for excitation and stroboscopic detection with 25 nm emission slit width, a 495 long pass filter, and sequential scanning with a logarithmic collection interval. Lifetime modeling was performed using the algorithm included in PTI's Felix32 software using a 3 exponential terms to fit the decay traces. The quality of fitting was determined by the reduced chi-squared method. QD samples were imaged using Transmission Electron Microscopy (TEM). TEM grids were glow discharged using PELCO easiGlow (Ted Pella, Inc., Redding,CA) in order to make the grid surface hydrophilic. Two μL of solution was dropped on a 200 lines/inch square mesh copper grids (Electron Microscopy Sciences, Hartfield, PA). Grids were analyzed on a FEI Tecnai G2 F20 at an accelerating voltage of 200 kV. Images were recorded using a Gatan CCD camera. Zeta potential was measured using a ZetaSizer Nano Series ZEN 3600 Spectrometer (Malvern Instruments Ltd, Malvern, Worcestershire, United

Kingdom). The measurement was carried out with a concentration of 100 nmol/L of QDs in 5 mM TRIS buffer.

3.3.2.4. Layer-by-Layer

Poly(allylamine hydrochloride) (PAH) (MW = 15 kDa) (Sigma-Aldrich) , linear poly(ethylenimine) (PEI) MW = 1.8 kDa (Sigma-Aldrich), poly(diallyldimethylammonium chloride) (PDADMAC) (MW = 8.5 kDa) (Polysciences) poly(sodium-4-styrenesulfonate) (PSS) (M_w = 8.5 kDa) (Polysciences), poly(acrylic acid) (PAA) (M_w = 15 kDa) (Sigma-Aldrich), poly(vinylsulfonic acid) (PVSA) M_w = 4-6 kDa (Sigma-Aldrich). All PEs were suspended in desired pH buffer and sonicated for 1 h prior to use in an ultrasonic bath. DHLA-QDs are added to a final concentration of 10 nm to the PAH solution under sonication for 5-7 min with intermittent mixing and vortexing, and then left under mild shaking for 1 h in the dark. Both the QDs and PEs are precipitated by the addition of excess isopropyl alcohol and collected by centrifugation at 10,000 RCF for 15 min at RT in a Beckman Coulter Allegra 64 centrifuge and F0685 rotor. The sediment is dissolved in in a small amount of pH 7.2-8 TRIS and ultracentrifuged overnight (12 h) at 210,000 RCF in a Beckman Coulter Optima Max XP ultracentrifuge and either the MLA-50 rotor with Optiseal tubes or the TLA-50 rotor with polyallomer microfuge tubes. The supernatant is carefully removed, using minimal UV illumination to ensure QD retention. The sediment is re-suspended by pipette aspiration in the same pH buffer and the process is repeated for 3 total wash cycles, the second and third centrifuge cycles are 6 h and 4 h respectively.

This process is repeated to add the second layer of PAA except the adsorption pH is 6-7.2 and the centrifugation pH is 8-8.5.

3.3.3. Results and Discussion

3.3.3.1. Layer by Layer on DHLA-QDs

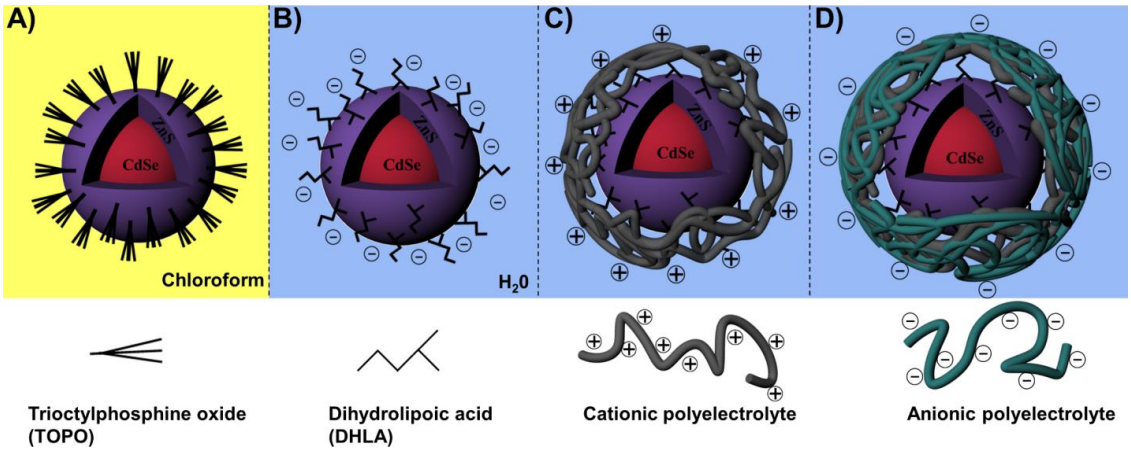

Figure 3.19: (A) TOPO-QDs in chloroform (B) Anionic water soluble DHLA-QDs (A) Cationic PE coated QDs (D) Anionic PE coated QDs.

The basic LbL process is depicted in Figure 3.19 where (A) QDs in chloroform are transferred into water by the addition of (B) DHLA, followed by adsorption of a (C) cationic PE and then an (D) anionic PE with wash cycles between each step. Polyelectrolytes were chosen based on the following criteria: low molecular weight, broad commercial availability, and previous success in coating NPs of similar size and surface coating. It is well understood that PEs should be low molecular weight in order to prevent interparticle bridging. The lower limit is less well defined; theoretical modeling and experimental work has shown that PE chain length should be approximately equivalent to particle circumference,[193, 194] but this choice is greatly

limited by commercial availability. For cationic PEs we chose to study 15 kDa poly (allylamine hydrochloride) (PAH), 1.8 kDa linear poly (ethylenimine) (PEI), and 8.5kDa poly (diallyldimethylammonium chloride) (PDADMAC). For anionic PEs we chose 15kDa poly (acrylic acid) (PAA), 8.5kDa poly (sodium-4-styrenesulfonate) (PSS) and 4-6kDa poly (vinylsulfonic acid) (PVSA).

When using either linear PEI or PVSA initial adsorption produced colloidally stable QDs; however, irreversible aggregation was observed after several wash steps. We believe that the NPs are temporarily stabilized by the very low molecular PE acting similar to a surfactant, but the inability of the PE to effectively wrap the particle results in a weak electrostatic interaction that is disrupted after several wash steps. In contrast, strong PEs such as PSS or PDADMAC result in particle flocculation due to incomplete surface coverage because of their inability to wrap the highly curved QD without increasing ionic strength (DHLA-QDs aggregate in the presence of even very low salt concentrations) or the PE acting as mortar to form bridges between neighboring QDs. Under all conditions studied we were only able to produce colloidally stable and monodisperse QDs with one bilayer using the weak PE pair of PAH and PAA.

The DHLA ligand used to make QDs water soluble imparts colloidal stability resulting from electrostatic repulsion of the acid groups; however, this only holds at a pH above the pI of the surface groups and under low ionic strength conditions, requiring storage and use in a buffer above pH 7.[221] Therefore, to effectively coat these anionic QDs with cationic PAH, the first adsorption step must occur above pH 7 and near or below the pKa of PAH (8.5-9). We found that adsorption of the first layer of PAH at pH

8 or below resulted in substantial loss of QDs (sticking to the container surface) as well as complete aggregation during centrifugation. Increasing the adsorption pH to 8.1 or above increases the QD surface charge density while simultaneously decreasing the PE backbone charge density; producing coated QDs that no longer adhere to the container surface. The interplay of charge density between the QD and PE allows for (1) a higher grafting density or better surface coverage of the QD because of more effective wrapping by the weaker charged PE and/or (2) formation of a thicker coating by an increased the number of PE chains required to overcompensate for the highly charged QD. The resulting QDs are colloidally stable; however, subsequent centrifugation to remove excess PE causes formation of an irreversibly-aggregated pellet. To overcome this problem, a two-step method was developed wherein PAH is first adsorbed to the QD at a pH between 8.1 and 9 to form a stable coating and then the pH is decreased below pH 8 before centrifugation. Increasing the surface charge density of the PAH coated QDs (PAH-DHLA-QDs) before centrifugation prevents pellet formation and aggregation. The strong electrostatic stability imparted by the PE coating as well as the small size and low density of the QD necessitates extended periods of high speed ultracentrifugation to efficiently remove the excess PE, while minimizing the number of wash steps and retaining the maximum amount of sample. Using this procedure, the coated QDs can be ultracentrifuged at 210,000 RCF for more than 12 h without visible pellet formation. Instead, the particles form loose sediment that is easily resuspended by a single pipette aspiration.

The dilute mixing conditions and large PE excess required to inhibit particle crosslinking and aggregation creates a tedious bottleneck for multiple wash steps. This was overcome by introducing a solvent precipitation and concentration step that precipitates both the QD and PE by lowering the solution dielectric constant with the addition of excess isopropyl alcohol. After centrifugation at 10,000 RCF, the sediment mix can then be resuspended in a small amount of buffer, decreasing the volume 25:1 before ultracentrifugation. This first ultracentrifugation step needs to be longer in order to improve QD retention because the concentrated PAH becomes very viscous. The second and third wash cycles were shorter but varied depending on QD and PE concentrations.

3.3.3.2. Percent Recovery

Using this procedure with an adsorption pH of 8.1 or pH 8.25 – 9 and a centrifugation pH of 7.2 in both cases, an average recovery rate of 76% and 86-90% was achieved, respectively, after the three wash steps were completed. This recovery rate is similar to what was found with 13.5nm AuNPs[182] and much higher than the 30% recovery reported for similarly-sized (5 nm) gold NPs.[181] The process is repeated to add a layer of PAA but using a pH of 6-7.2 for adsorption and pH 8-8.5 for centrifugation.

3.3.3.3. Zeta Potential

Zeta potential measurements are reported in Figure 3.20 for DHLA-QDs (-38.6 ± 1.6 mV) in 5 mM pH 8 TRIS buffer and full charge reversal for PAH-DHLA-QDs (+67 ± 7.08 mV) and PAA-PAH-DHLA-QDs (-51.5 ± 2.21 mV) in 5 mM pH 7.2 TRIS buffer. The large magnitude of charge reversal of the PAH layer is higher than observed

with MAA-QDs[189] or iron oxide coated with PAH[186] but similar to that found with gold NPs.[182] One benefit of PAH-DHLA-QDs is the added stability at lower pH conditions. PAH is expected to be fully ionized below pH 7.5, and particles coated with PAH are both highly charged and stable; in contrast, DHLA-QDs aggregate as the solution becomes acidic.

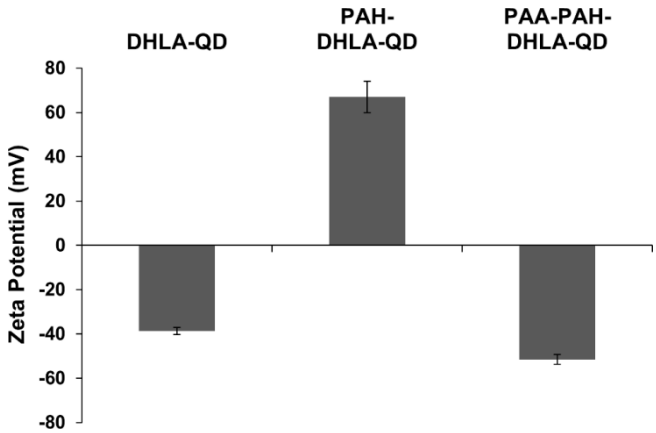

Figure 3.20: Zeta potential of the DHLA-QD in 5 mM TRIS buffer pH 8, PAH-DHLA-QDs and PAA-PAH-DHLA-QDs in 5 mM TRIS pH 7.2 (n = 3).

3.3.3.4. Aggregation Analysis by TEM

TEM was employed to assess aggregation states and morphology of the DHLA-QDs before and after coating with PEs. TEM micrographs in Figure 3.21 show the (A) DHLA-QDs, (B) PAH-DHLA-QDs and (C) PAA-PAH-DHLA-QDs. It is clear from these micrographs that after coating with two PE layers the QDs are still well-defined with little to no visible aggregation.

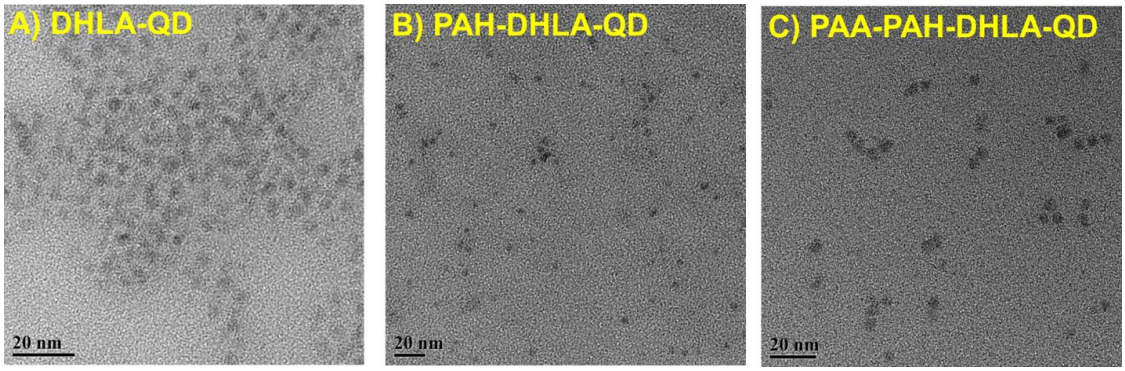

Figure 3.21: TEM images of (A) DHLA-QDs, (B) PAH-DHLA-QDs and (C) PAA-PAH-DHLA-QDs.

3.3.3.5. Optical Properties of LbL Modified QDs

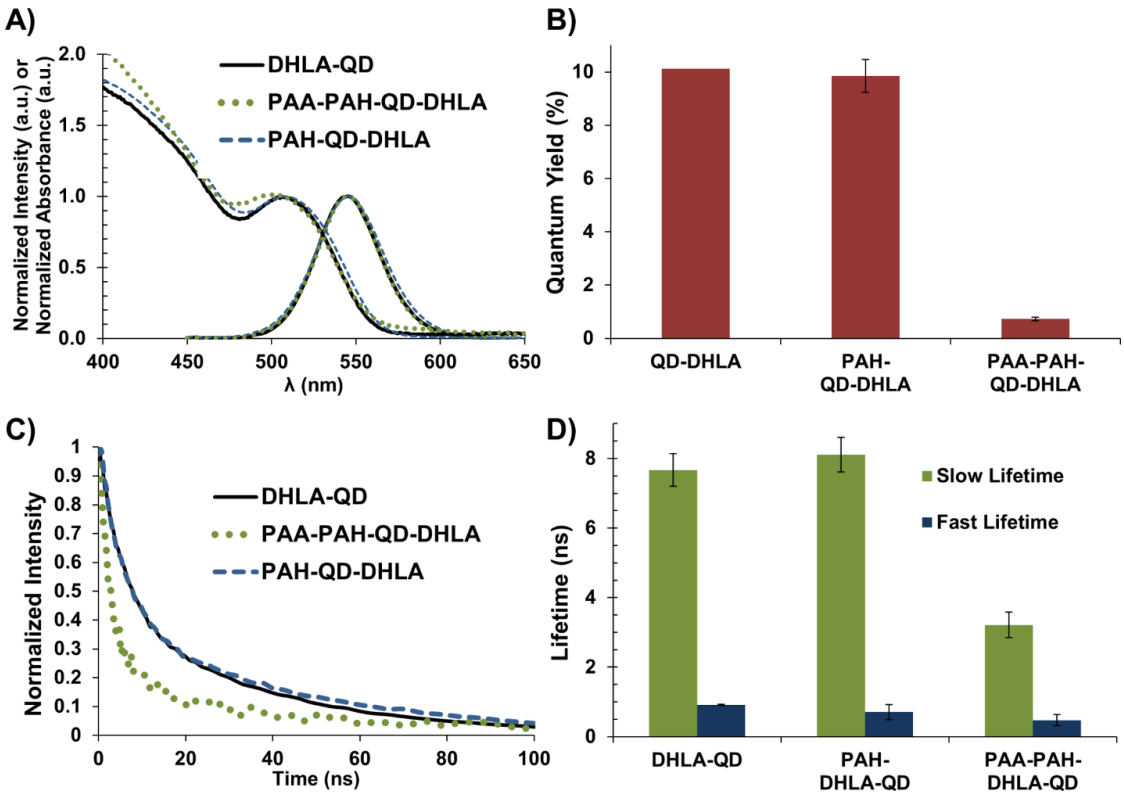

Figure 3.22: (A) Typical emission and absorbance spectra normalized to peak intensity and first exciton peak absorbance respectively (B) QY relative to Rhodamine 6G in water (one batch of DHLA-QD stock suspension, and n = 3 separate, parallel batches of coated QDs prepared from the same DHLA-QD stock) (C) Normalized raw luminescence lifetime (D) Slow and fast lifetime component values (n = 3).

Typical emission and absorption spectra are shown in Figure 3.22A and QY relative to Rhodamine 6G in Figure 3.22B for DHLA-QDs (10.12%), PAH-DHLA-QDs (9.8 ± 0.6%) and PAA-PAH-DHLA-QDs (0.73 ± 0.1%).[232] There appears to be some increased scattering after the addition of PE, but there is no clear shift in the first exciton or emission peak. The adsorption of PAH has an insignificant effect on the QY, while the addition of PAA is accompanied by a substantial decrease in QY. We found the

change in QY after the addition of PAH was variable depending on the initial DHLA coating and the ZnS shell thickness. With a thinner ZnS shell the QY would initially increase, but the addition of an anionic PE layer still resulted in a substantial decrease in QY below that of the original DHLA-QDs (Figure 3.23).

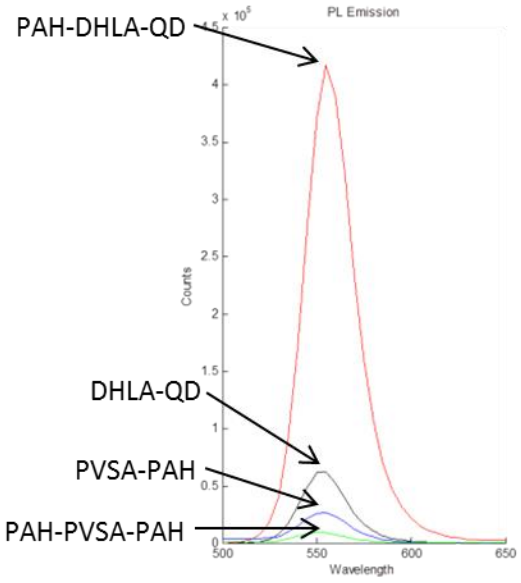

Figure 3.23: Luminescence intensity measurements in counts of DHLA Modified 557 QDs with a thin ZnS shell. After the addition of PAH a large increase is observed, but further modification results in decrease below that of the original DHLA modified QD.

The QY could not be recovered by the addition of more PAH. The strong quenching of QD PL observed in the presence of PAA was also observed for PVSA (Figure 3.23) and PSS (Figure 3.24); both of the latter also triggered aggregation (Figure 3.25).

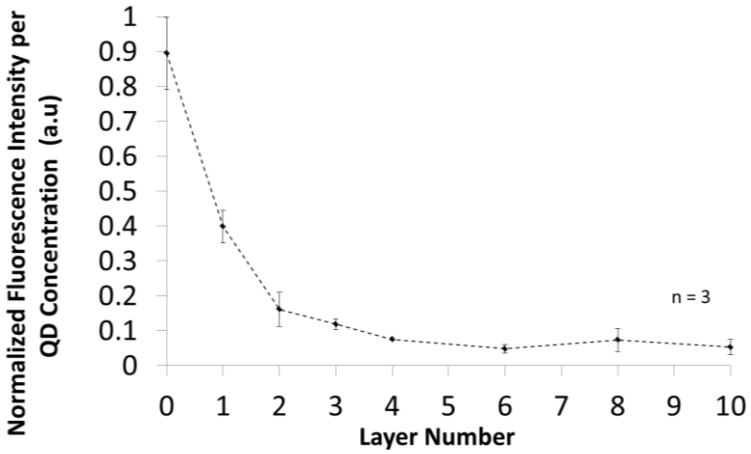

Figure 3.24: Luminescence intensity normalized to QD concentration for DHLA modified 650 QDs (layer 0) after the addition of alternating layers of PAH (Layers 1, 3, 5, 7, 9) and PSS (Layers 2, 4, 6, 8, 10).

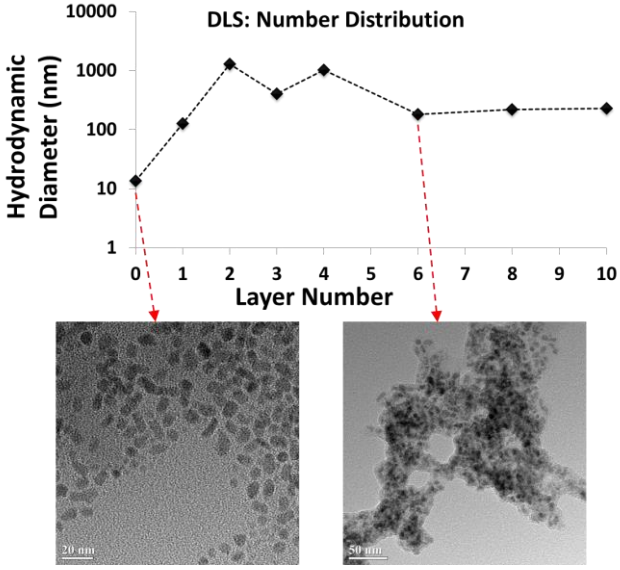

Figure 3.25: DLS measurements and TEM micrographs for DHLA-QD650 (layer 0) after the addition of alternating layers of PAH (Layers 1, 3, 5, 7, 9) and PSS (Layers 2, 4, 6, 8, 10).

The quenching is attributed to a localized acidic environment created by the anionic PEs causing quenching by the same mechanism that renders the DHLA-QDs pH sensitive. To gain further insight into the processes involved, we studied the change in the long and short luminescence lifetime components after the addition of each PE. The mean long lifetime component was 7.66 ± 0.47 ns for DHLA-QDs, 8.11 ± 0.49 ns for PAH-DHLA-QDs and 3.21 ± 0.36 ns for PAA-PAH-DHLA-QDs. (Figure 3.22C & Figure 3.22D). The small lifetime component decreased after the addition of each layer, from 0.92 ± 0.02 ns for DHLA-QDs to 0.71 ± 0.22 ns and 0.47 ± 0.16 ns for PAH-DHLA-QDs and PAA-PAH-DHLA-QDs respectively. The slow lifetime component showed no significant change after the addition of PAH but decreased extensively after the addition of PAA, indicating that PAA might be affecting the surface properties of the QD.[233] This is partially consistent with the findings of Rama *et al*, when the effect of long-chain PEs absorbed on MPA-QDs was studied a minimal effect on QD lifetime was observed for addition of both PAH and PSS.[228] Our results confirm their observations for PAH, but we observe a large decrease with the addition of the anionic PE. This could be attributed to our use of PAA instead of PSS or our LbL method providing more complete surface coverage of the second layer because we are maintaining monodisperse QDs. Based on the conditions used in their study we speculate that their methods produce agglomerates of QDs buried in the PAH, such that many of the QDs contributing to the optical measurements were unable to interact with the second layer of anionic PE.

3.3.3.6. PL Sensitivity to pH

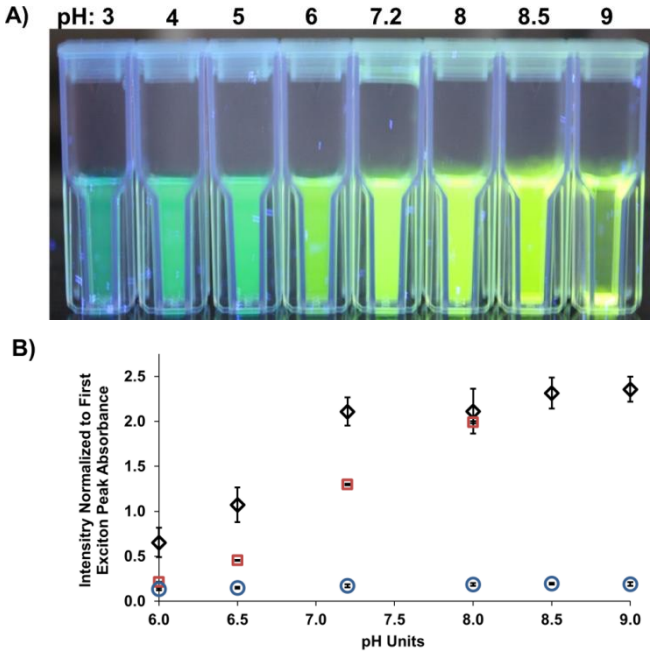

Figure 3.26: (A) Visual colloidal stability and luminescence intensity of PAH-DHLA-QDs in pH 3-9 TRIS buffer under UV illumination (B) Intensity measurements for different pH values normalized to the first exciton peak absorbance for DHLA-QDs (◊), PAH-DHLA-QDs (□), and PAA-PAH-DHLA-QDs (○).

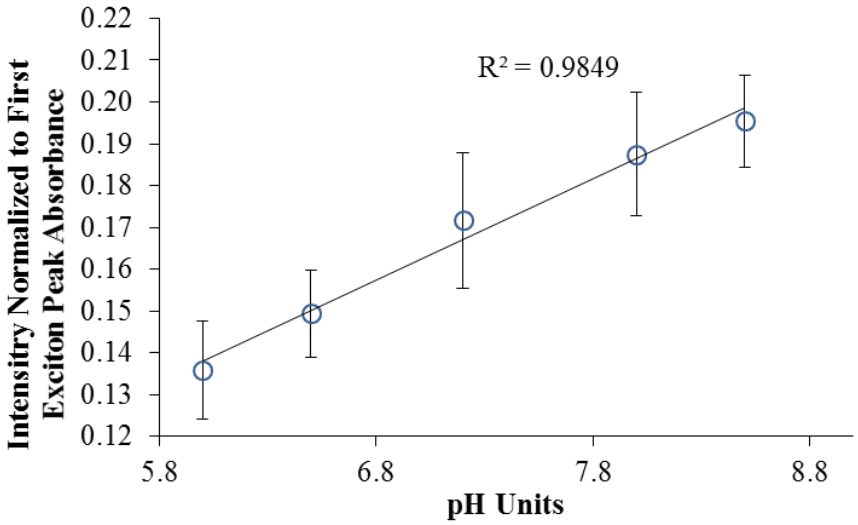

Figure 3.27: Intensity measurements for different pH values normalized to the first exciton peak absorbance for PAA-PAH-DHLA-QDs (○).

Figure 3.26A illustrates the pH-dependent luminescence and stability of the PAH-DHLA-QDs in 50mM TRIS buffer between pH 3-9. As expected, above pH 8 we observe particle settling as the charge density of the PAH-DHLA-QD decreases. Below pH 8, the PAH-DHLA-QDs are colloidally stable. However, below pH 6 there was an irreversible blue shift in the emission (>20 nm), a change also observed with DHLA-QDs that we attribute to the stronger acidic conditions etching the QD surface or reducing the affinity of the ZnS overcoat. The pH dependent intensity measurements of PAA-PAH-DHLA-QDs, PAH-DHLA-QDs and DHLA-QDs are shown in Figure 3.26B. Error bars for the intensity measurements represent triplicate measurements of the same sample taken 5 min apart, showing the stability of PAH-DHLA-QDs for repeated optical interrogation. The intensity of PAH-DHLA-QDs has a linear relationship with pH between pH 6.5 and 8 with a 15.9% change in luminescence for each 0.1 pH units. At pH 8.5 and above the QDs settle out of solution, precluding accurate measurements. QD

surface modification with mercaptocarboxylic acid ligands results in a reduction in overall QY as well as a pH-dependent sensitivity based on protonation of the carboxylic acid group causing changes in trap states and electron-hole recombination.[234, 235] This mechanism has been previously exploited several times to produce both photoluminescence intensity[235-237] and lifetime decay based pH sensors.[234] The PAH-DHLA-QDs retain this sensitivity to the surrounding environment although they exhibit a shift of the linear range towards higher pH. The PAA-PAH-DHLA-QDs are colloidally stable over the pH range of 6 - 9; exhibiting a minimal increase in luminescence intensity with increasing pH that is not significant compared to measurement error (Figure 3.27).

3.3.3.7. Optical and Colloidal Stability of LbL Modified QDs

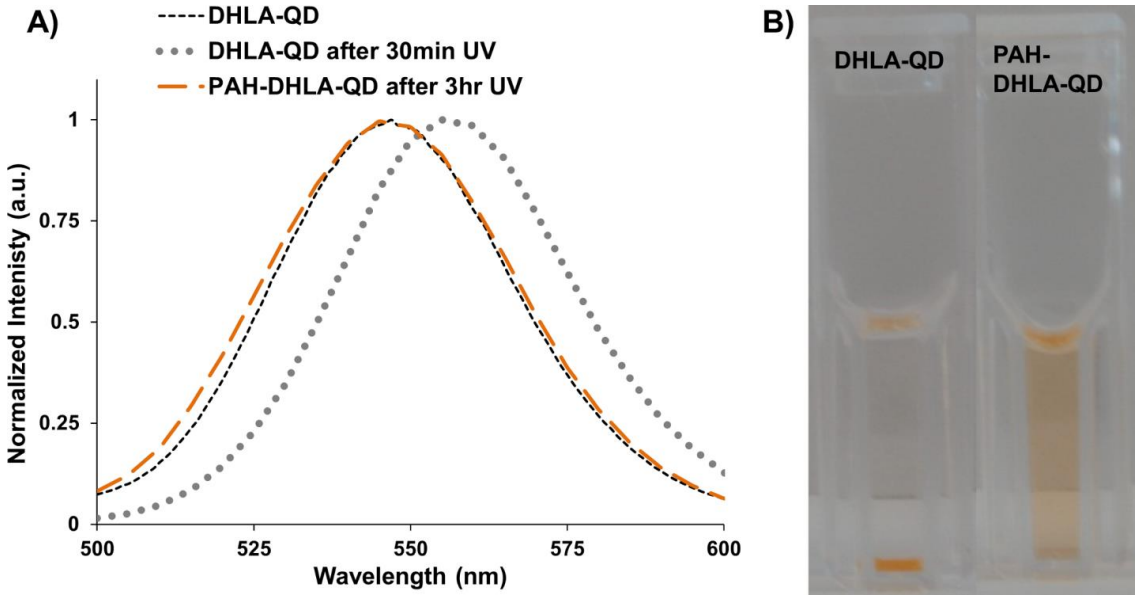

Figure 3.28: (A) Emission peak of DHLA-QDs and PAH-DHLA-QDs after 30 min and 3 h of UV exposure respectively. (B) Visualization of colloidal stability of DHLA-QDs and PAH-DHLA-QDs after 8 months of storage under refrigeration in 50 mM pH 8 TRIS buffer.

Although it has been reported that DHLA-QDs are stable for 6-24 months,[231] we found that irreversible aggregation could be observed as quickly as a few days to weeks after production. It was observed that any exposure to light, including measurements of fluorescence or absorption, may initiate an avalanche of aggregation**.** This makes DHLA-QDs highly unsuitable for sensor applications, as each attempt to interrogate the system with light induces changes in optical properties and stability. When exposed to UV irradiation (100 watt, 365 nm) for 30 min the DHLA-QD emission shifted towards the red and subsequently aggregated, whereas PAH-DHLA-QDs exhibited no shift in emission spectrum or aggregation even after 3 h of UV irradiation (Figure 3.28A). Furthermore, even when refrigerated and protected from light, DHLA-QDs still eventually aggregate; in contrast, PAH-DHLA-QDs remain stable for at least an additional 8 months compared to the very same source batch of uncoated DHLA-QDs (Figure 3.28B). This implies that the PAH coating may ameliorate concerns over batch-to-batch variability and unknown long-term stability of DHLA-QDs by preventing pathways to aggregation.

3.3.4. Conclusions

This work expands on the applicable knowledge for colloidal LbL by taking into account solution pH as a crucial aspect when dealing with electrostatically-stabilized NPs and weak PEs. Separation of the LbL process into two distinct phases provides more effective control of the charge density interplay between the QD and weak PE garnering a high recovery of monodisperse particles. The generality of the LbL process permits the use of these methods to coat a variety of other materials, which is especially

important for low density NPs of similar size which require ultracentrifugation for separation.

An interesting finding is that once the PE is adsorbed in a lower charge density state, a change in the pH to increase charge density does not induce complete desorption. Further study is necessary in order to precisely understand how variable solution pH affects PE grafting density and thickness during and after the adsorption phase. The PAH layer remains on the surface and provides a protective coating that overcomes batch-to-batch variability, affording superior long-term stability for storage. The ability to respond to changes in the local environment while withstanding repeated optical interrogation, makes PAH-DHLA-QDs a suitable alternative to DHLA-QDs for long-term sensing applications.

The low QY of PAA-PAH-DHLA-QDs represents severe limitations for practical applications. Additionally, the PAA coating procedure could not be optimized since the QDs could not be incubated near the pKa of PAA (~4.5) without degradation of the QD. We believe that the anionic PE quenching of QD luminescence would occur for any QD surface coating that imparts pH sensitivity. Future work will focus on alternative methods for water solubilizing QDs that provide surface passivation to prevent pH sensitivity and resistance to acidic degradation. Achieving this protective effect with sufficiently thin layers to preserve nanoscale energy transfer is a key challenge for advancing these materials.

3.4. Investigation of Alternative QD Synthesis and Surface Passivation Methods

3.4.1. Background

The LbL work on both AuNPs and QDs showed that a single bilayer could be used to colloidally stabilize the NP and preserve long-term photo-stability. However, the multilayer growth on DHLA-QDs lead to a substantial decrease in the QY for the second layer. We speculated this could occur for two possible reasons: (1) aggregation is causing self-quenching or (2) the LbL multilayers are introducing defects into the surface states by creating a low pH environment around the QD. The first situation can be ruled out as TEM showed that LbL on AuNPs and QDs was achieved without substantial aggregation. To address the second issue alternative methods for QD water solubilization were explored that could potentially provide better surface passivation during LbL modification.

The techniques for phase transfer of QDs from organic solvent to aqueous solution can be broadly subdivided as either ligand exchange or over-coating methods. Ligand exchange involves replacing the native hydrophobic ligands with hydrophilic ligands. The over-coating method involves coating the QD with amphiphilic polymers through hydrophobic interactions. From the literature two potential candidates were identified; one ligand exchange process and one over-coating method. These methods were chosen because they were reported to produce low hydrodynamic QDs that maintained a high QY when transferred to water; neither method was shown to have pH dependent intensity.[238-242]

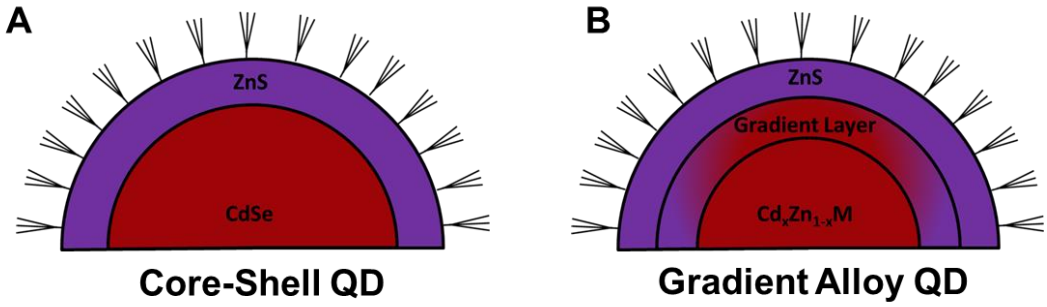

Figure 3.29: Simplified cartoon showing the difference between (A) core shell QD fabrication and (B) gradient alloy.

Another route pursued for reducing QD surface defects was to substitute the previously used core-shell QD fabrication technique with the newer gradient allow (GA) method (Figure 3.29). Core-shell QD fabrication is a two-step hot injection method, where first the CdSe core in synthesized and then the ZnS shell is grown around the core. In contrast, the GA method produces a CdSe core with a radially alloyed ZnS shell that can be grown in a single reaction.[240] GA QDs exhibit less surface defects, which translates to a higher QY and eliminates blinking in both organic solvents and aqueous solution.[243] The overall size of a GA QD is only 5-7 nm regardless of emission wavelength, while core-shell QDs are generally larger with a size dependent on emission wavelength.[244] Additionally, GA QDs are expected to be more resistant to chemical etching according to the manufacturer.

3.4.2. Materials and Methods

CdSe/ZnS GA-QDs with 560 nm and 620 nm emission were purchased from Mesolight. Poly (styrene-*co*-maleic anhydride) (PSMA), ethanolamine (EA), Tetramethylammonium hydroxide pentahydrate (TMAH) and adenosine 5' monophosphate (AMP) were purchased from Sigma.

3.4.2.1. PSMA QD Over-Coating

The PSMA coating of QDs was achieved using the method developed by Lees *et al.* 2009 and modified by Chen *et al.* 2011.[239, 242] A 5 mM solution of PSMA in $CHCl_3$ (5 mg and 10 mL) was prepared in a glass scintillation vial and sonicated for 1 h and mixed for 1 h prior to use to ensure PSMA was completely dissolved. A 0.2 M EA solution was prepared in DI-H_2O. A 1 μM solution of QDs were suspended in 5 mL of $CHCL_3$ were added to 5 mL of PSMA stock under rapid stirring. After 1 h, 10 mL of EA stock was added and the solution was kept stirring for 3 h. The QDs spontaneously transfer to the water phase as the EA ring-opens the anhydride group. Excess PSMA and EA are removed by three rounds of ultracentrifugation at 180,000 RCF, resuspending in DI-H_2O each time.

3.4.2.2. AMP Ligand Exchange

The AMP method used was initially reported by Liu *et al*. with minor modification.[241] The AMP stock solutions was prepared by dissolving 1 g of AMP in 3 mL of ethanol. The pH of the solution was adjusted to pH 10 by the addition of concentrated TMAH, the AMP does not completely dissolve until pH 10 is reached. A 5 mL $CHCl_3$ solution containing 1 μM of QDs was prepared in a glass scintillation vial and stirred vigorously. Then 300 μL of the AMP solution was added dropwise and allowed to stir for 30 min, after which the QDs spontaneously transferred to the upper water phase. Excess AMP was removed by three rounds of ultracentrifugation at 180,000 RCF, resuspending in DI-H_2O each time.

3.4.3. Results and Discussion

The AMP and PSMA protocols were very easy to follow and required very few reagents that were all commercially available. The methods could be completed in one day with a high yield and were very reproducible.

3.4.3.1. DLS and Zeta Potential

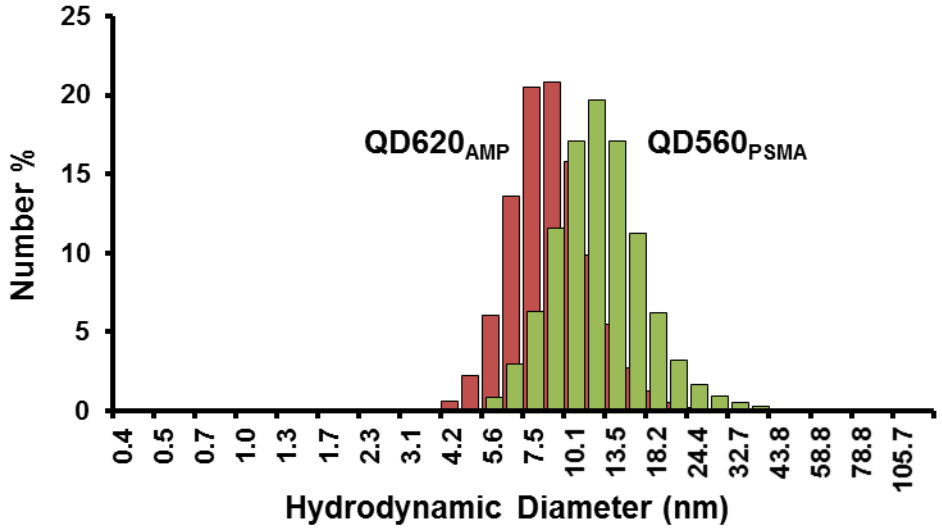

Figure 3.30: DLS size by number histogram for $QD560_{PSMA}$ and $QD620_{AMP}$. Histogram analysis is the average of three separate measurements.

After purification the QDs were initially characterized for quality by DLS and zeta potential measurements. DLS gave a hydrodynamic size of 13.97 ± 2.93 nm for the $QD560_{PSMA}$ compared to the 13.4 nm reported by Lees *et al.* 2009 and a size of 9.1 ± 1.07 nm for $QD620_{AMP}$ compared to 7.1 nm reported by Mu *et al* (Figure 3.30). Both of these methods yielded low hydrodynamic QDs with a size consistent with their reported values. The $QD560_{PSMA}$ had a zeta potential of -25 mV while the $QD620_{AMP}$ had a zeta potential of -31 mV when measured in DI-H_2O.

3.4.3.2. PL Sensitivity to pH

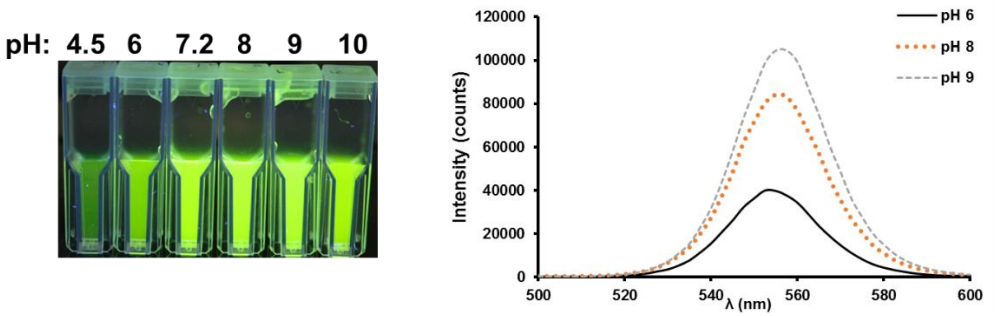

Figure 3.31: (A) Photograph under UV irradiation and (B) PL spectra of QD560$_{PSMA}$ after being stored for 1 day in several different buffers from pH 4.5-10.

The pH sensitivity was investigated for QD560$_{PSMA}$ after storage in different buffer solutions from pH 4.5 - 10. The pH response the QD560$_{PSMA}$ under UV irradiation is clearly seen in Figure 3.31, but no settling is observed. PSMA coated QDs were reported to only be stable between pH 4 - 6, but we found they followed the stability typical of a carboxylic acid coated QD as no settling was observed for pH 6 and above; at pH 4.5 the QDs aggregated and eventually dissolved. Figure 3.31B shows the PL spectra and the large change in PL intensity for pH varying between pH 6 - 9.

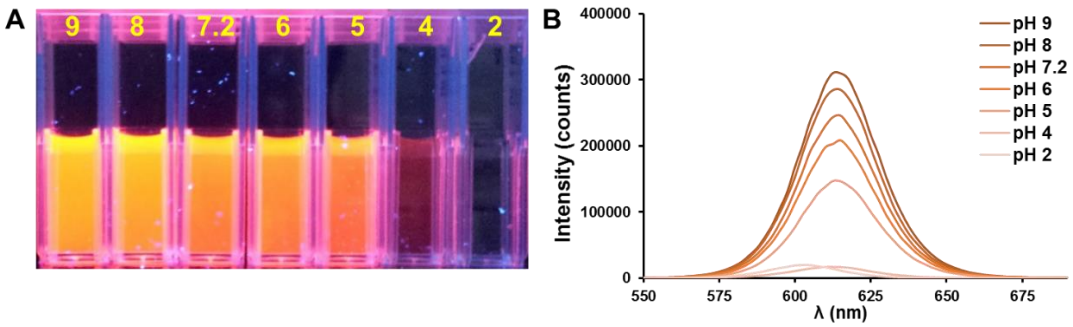

Figure 3.32: (A) Photograph of QD620$_{AMP}$ under UV light stored at pH 2 - 9 after 1 day of incubation. (B) PL spectra of QD620$_{AMP}$ after storage for 1 day.

The pH sensitivity of $QD620_{AMP}$ was investigated by storing the QDs in a various buffers from pH 2 - 9. No aggregation or settling is observed for the $QD620_{AMP}$ from pH 5 - 9 (Figure 3.32A) but they exhibit a strong pH dependent intensity (Figure 3.32B). At pH 4 and below the $QD620_{AMP}$ were degraded as shown by the spectral shift (Figure 3.32B). The pH dependent response of $QD560_{PSMA}$ and $QD620_{AMP}$ had not been previously reported. It also appears that both ligand exchange and over-coating methods are susceptible to acidic degradation even when using GA instead of core-shell QDs.

3.4.3.3. LbL with Amino-Dextran

The $QD560_{PSMA}$ and $QD620_{AMP}$ were coated with amino-dextran to introduce saccharide groups on the QD surface that could later be used to bind ConA. The amino-dextran was coated using the optimized pH dependent LbL process developed for PAH. The QY was monitored throughout this process by measuring the absorbance and PL after each step.

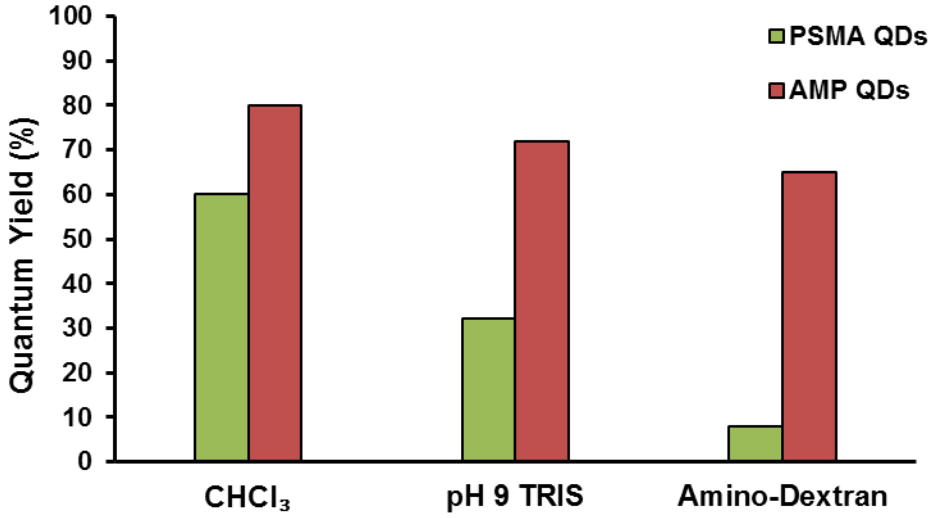

Figure 3.33: QY of QD560$_{PSMA}$ (left, green) and QD620$_{AMP}$ (right, red_ in $CHCl_3$, after suspending in 50mM pH 9 TRIS buffer and after coating with 10 kDa amino-dextran.

The QD QY in $CHCl_3$ was the value reported by the manufacturer. The water soluble QD560$_{PSMA}$ and QD620$_{AMP}$ were suspended in pH 9 TRIS before mixing with amino-dextran. This is also the pH that yields the highest PL intensity. The QD560$_{PSMA}$ QY was 60% in $CHCL_3$ but after phase transfer the QY dropped to 32%, a large decrease but is consistent with previous reports. After dextran modification the QY fell to 8% (Figure 3.33). The QD620$_{AMP}$ had an initial QY of 80% in $CHCl_3$ and only decreased by 8% after transfer to water. After modification with dextran another small decrease occurred to give a QY of 65% (Figure 3.33). The QY of AMP QDs is significantly higher than PSMA QDs and is the highest reported to date for any low hydrodynamic QD and is consistent with previous reports from the original authors.

3.4.3.4. PL Sensitivity to Glucose

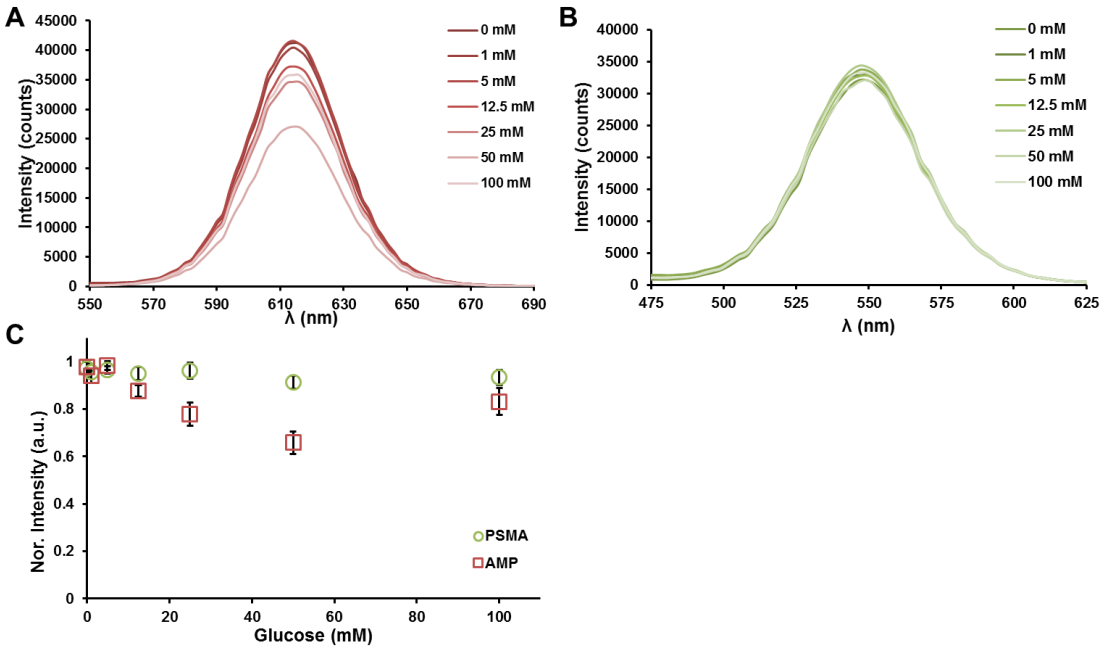

Figure 3.34: PL intensity for (A) QD620$_{AMP}$ and (B) QD560$_{PSMA}$ exposed to varying concentration of glucose. (C) Comparison of intensity change for QD560$_{PSMA}$ (green ○) and QD620$_{AMP}$ (red □) when exposed to glucose.

The glucose sensitivity of QD560$_{PSMA}$ and QD620$_{AMP}$ was checked as a quick negative control as no glucose sensitivity has been reported nor was expected. Unfortunately, the QD620$_{AMP}$ exhibited a large decrease in PL intensity when exposed to glucose (Figure 3.34A), with a 35% decrease at 50 mM. QD560$_{PSMA}$ had a 9% decrease in PL intensity at 50 mM glucose (Figure 3.34B). In both cases, the PL intensity at 100 mM was higher than 50 mM. The QD620$_{AMP}$ also exhibited quenching to mannose and the sensitivity still occurred after coating with dextran (data not shown). While QD620$_{AMP}$ has a better QY when transferred to water and after coating with dextran, it is susceptible to very strong quenching by glucose. In contrast, QD560$_{PSMA}$ had a large

decrease in QY after water solubilization and dextran coating but were less sensitive to glucose. The glucose response of $QD560_{PSMA}$ and $QD620_{AMP}$ has some potential for creating a crude ratiometric glucose sensor by combining the two QDs in a single assay and could potentially be optimized by varying the two different QD concentrations.

3.4.4. Conclusion

The ligand exchange with AMP and over-coating with PSMA were explored as alternative QD solubilization techniques. These methods were easy to perform and were highly reproducible. The AMP ligand exchange procedure proved to be the superior method for maintaining QY after phase transfer and amino-dextran modification compared to PSMA. The core-shell QDs used previously for DHLA-QDs were replaced with the higher quality, commercially synthesized, GA alloy QDs. However, both AMP and PSMA coated QDs exhibited a pH dependent PL intensity with similar response to DHLA-QDs and a degradation at pH 4 or below. Unfortunately, both AMP and PSMA modified QDs showed an unsuspected quenching in the presence of glucose that was not entirely predictable. This prohibits the use of these QDs in energy transfer based glucose assays because the non-specific quenching would act inversely with a quenching assay that should "turn on" in the presence of glucose. Clearly, the current state of research on low hydrodynamic semiconductor QDs for biomedical applications is still lacking. Unfortunately, many of these papers fail to either investigate or report on critical deficiencies, even rudimentary aspects such as pH dependent PL. Moving forward requires identifying alternative photoluminescent materials with clearly reported optical stability against non-specific interference.

4. LOW HYDRODYNAMIC LBL MODIFICATION OF NANOMATERIALS FOR STABLE BIOCONJUGATION

4.1. Introduction

LbL can play a critical role in the development of nanomaterial-enabled energy transfer sensors by providing a generic route for the stabilization and bioconjugation of nanomaterials. The main goals of this section were to investigate LbL modification as a (1) low hydrodynamic size coating for improving colloidal stability and as a (2) transitional coating to provide a stable pathway for bioconjugation.

We wanted to demonstrate the ability of LbL to impart electrosteric stability with a minimally sized hydrodynamic coating. For energy transfer sensors, a thin coating is necessary to minimize the donor/acceptor distance and to maximize energy transfer efficiency. The nanometer precision of LbL has been thoroughly studied on macro- and micro-scale substrates but it has not been fully characterized for NP templates, particularly in the hydrated state. It has been shown that particle stability can be increased by the addition of 5 - 10 PE layers but this also introduces a much thicker coating.[190] However, based on the results the previous section for LbL on AuNPs we believe that a single bilayer is capable of imparting significantly improved stability while still maintaining a thin coating.

The bioconjugation of NPs remains a significant hurdle due to the aggregation that occurs under conditions necessary for chemical reaction and biomolecule stability. One of the problems with current techniques is that they require significant re-optimization as the core material and surface chemistry changes. Additionally, even on

the same material types using the same procedures the modification is not always consistent (*i.e.* QDs). In contrast, LbL can be used to modify any charged substrate regardless of the core material composition or of the initial surface chemistry. Therefore, the process does not become redundant as nanomaterial synthesis continues to evolve and it is less susceptible to variations in the core synthesis or ligand exchange process. Additionally, the LbL coating imparts some steric stability to prevent aggregation under conditions that reduce electrostatic repulsion. This is an important feature when using carbodiimide chemistry because EDC activation reduces surface charge and increase hydrophobicity. The steric stability of the polymer coating should prevent aggregation even under these conditions.

The LbL modification of AgNPs and bioconjugation to proteins with carbodiimide chemistry was investigated by characterizing the NPs throughout the process to monitor their hydrodynamic size, aggregation state, and optical properties. The hydrodynamic sizing of modified NPs is a serious challenge that can potentially be addressed using particle tracking analysis. Thus, much of this section focuses on the broader implications of this NP sizing technique and the development of a robust methodology for obtaining accurate NP size and concentration.

4.2. Background

The effect of nanotechnology in biological systems has gained interest both from medical treatment and environmental contamination perspectives. Colloidal characterization is of vital importance as it is well understood that particle size is a key property that determines biomolecule interaction, cellular uptake, and toxicity.[245]

Particle sizing involves a broad variety of direct and indirect characterization techniques that have varying tradeoffs based on their sample preparation requirements and principles of operation.[246] In these cases, the sample preparation or analysis can be destructive or alter the apparent structural properties. For instance, electron microscopy (TEM and SEM) provides direct visualization of particle size, size distribution, morphology, crystal structure, and elemental composition. However, sample preparation requires sample dehydration, sputter coating, and analysis under high vacuum; all of these conditions alter the sample properties. This is particularly important when dealing with colloids that are hydrated or contain biologically active components (*i.e.* polymers, proteins). Additionally, surface ligands or polymer shells often cannot be resolved due to having poor electron density. AFM provides direct measurement to provide high resolution images and samples can even be measured in hydrated conditions. However, sample analysis is slow, has a limited scanning area, and requires immobilization of the particle to a solid support.

Light scattering techniques such as Dynamic Light Scattering (DLS) and Nanoparticle Tracking Analysis (NTA) have gained popularity for being rapid and accurate methods for particle sizing in environmental and biological media.[247] These techniques both indirectly determine the hydrodynamic size be measuring particle motion in solution. DLS has long been the gold standard for determining particle size and size distribution in liquid media. DLS uses an ensemble measurement of the NP solution that is based on scattering intensity fluctuations. This method is very accurate for low polydispersity samples but becomes inaccurate if the size distribution increases

or if aggregation is present. Since larger particles scatter more light, the size distribution becomes heavily weighted towards larger particles.[248] Additionally, knowledge of the particle refractive index and absorption is required for accurate particle size calculation. This adds variability when sizing particles of unknown optical properties, fluorescent particles, highly absorbing particles, or for core-shell particles that contain multiple layers of different refractive indices. DLS cannot provide concentration information.

NTA has become exceedingly popular as a new technique for particle sizing of nanomaterials and biological materials because it overcomes many of the problems associated with DLS.[249, 250] NTA tracks individual NPs that scatter light within a focused laser beam using a conventional optical microscope.[248, 251] If the viscosity and temperature of the sample are known, then NP velocity can be translated to hydrodynamic diameter using by use of the Stokes-Einstein equation. The method is capable of determining particle hydrodynamic size with nanometer resolution[252] and under the right conditions the results are comparable to TEM and AFM.[251, 253] The individual particle tracking method provides more accurate size distribution data compared to DLS, but does show a higher sensitivity to larger particles. Additionally, the measurement sensitivity and limit of detection depends on particle refractive index,[254] but this can also be leveraged as a route to distinguish between mixed particle populations or for determining the unknown refractive index of particles.[255] It should also be noted that NTA provides hydrodynamic size, which is affected by particle geometry, concentration, and surface charge;[256] all of these factors need to be considered when interpreting the results.

An added advantage of NTA is the capability of rapidly determining NP concentration. Although, the conditions used for measurement and the analysis settings can affect the accuracy of this measurement.[257] For instance, increased scattering due to large particles or very high concentrations can lead to increased noise artifacts that can be misinterpreted as particle counts.[258] The increased scattering can also hide smaller particles or lower refractive index particles which scatter less light.[254, 258] Therefore, obtaining accurate concentration measurement requires carefully selecting measurement and analysis conditions, while keeping in mind that the results are only accurate across a limited sample concentration range.

The concentration of metallic NPs is most commonly determined by absorbance spectroscopy using equations developed through a combination of experimental analysis and Mie scattering models to relate absorbance spectra to particle size and concentration.[217, 259] However, the accuracy of these methods is affected when the SPR is changed due to modification with different stabilizing ligands or macromolecules like polymers, drugs, or proteins. Additionally, any change in absorbance spectra due to aggregation induced plasmonic coupling will also considerably affect the accuracy of these calculations. This coupling is useful for determining the qualitative presence of aggregation but it cannot be used to determine aggregate size or concentration.

In this work, the hydrodynamic size changes and aggregation of PE coated AgNPs is investigated using NTA and UV-Vis. The LbL coating is investigated as a transitional layer to impart improved colloidal stability and chemical functionality for bioconjugation. The stability of the AgNPs before and after modification is investigated

under various buffers, pH, and ionic strength conditions with a focus on conditions necessary for the stability and function of ConA. The bioconjugation of NPs itself is a significant challenge due to the propensity for aggregation during both conjugation and purification. Using both NTA and UV-Vis we can investigate the methodology required for successful NP modification and bioconjugation, while also providing insight into the relationship between UV-Vis and NTA for characterizing NP size and concentration.

4.3. Materials and Methods

4.3.1. Chemicals

Poly (allylamine hydrochloride) (PAH) (MW = 15 kDa), poly (4-styrenesulfonic acid-*co*-maleic acid) sodium salt with a ratio of maleic acid to styrene sulfonate of 1:1 (PSS-*co*-MA 1:1) (MW = 20 kDa), and N-(3-Dimethylaminopropyl)-N'-ethylcarbodiimide hydrochloride (EDC) were obtained from Sigma Aldrich. N-Hydroxysulfosuccinimide (NHS) was purchased from G-Biosciences.

4.3.2. AgNP Synthesis

AgNPs were produced by the reduction of silver nitrate with hydroxylamine following the procedure described by Leopold *et al*.[260]

4.3.3. AgNP LbL

PAH and PSS-*co*-MA 1:1 were dissolved in DI-H_2O at a concentration of 10 mg/mL and sonicated for 1 h. PAH was titrated to pH 9 with 2 M NaOH. A 5 mL aliquot of diluted $AgNP_{OH}$ solution (0.1 - 0.4 nM) was rapidly added to 5 mL of PAH stock under sonication for 10 min. TRIS HCl was added at 60 mg/mL and the solution was precipitated by the addition of isopropanol (2:1 V/V). The solution turns milky

white to indicate precipitation and is then centrifuged at 10000 RCF at room temperature for 10 min. The supernatant was decanted, leaving a gelatinous pellet that was resuspended in 1 mL of 50 mM TRIS pH 7.2. Excess PAH was then removed by three rounds of centrifugation at 12000 RCF for 20 min, resuspending in 50 mM TRIS pH 7.2 each time. A 5 mL 0.1 nM solution of $AgNP_{OH}$-PAH was added to a 5 mL PSS-*co*-MA 1:1 solution under sonication for 10 min and incubated with mild shaking for 1 h. The solution was precipitated by the addition of isopropanol (2:1 V/V) and centrifuged at 10000 RCF at room temperature for 10 min. The supernatant was decanted, leaving a gelatinous pellet that was resuspended in 1 mL of 50 mM CHES pH 9. Excess PSS-*co*-MA 1:1 was then removed by three rounds of centrifugation at 12000 RCF for 20 min, resuspending in 50 mM TRIS pH 7.2 each time.

4.3.4. NTA

AgNP and distributions were obtained with the NanoSight LM10HS with a 65 mW 405 nm source. Video was acquired with a Hamamatsu C11440 digital camera and analysis was completed with included NanoSight 2.3 software with automatic settings.

4.3.5. Microelectrophoresis

The zeta potential of AuNPs were determined with a ZetaSizer Nano Series ZEN 3600 spectrometer (Malvern). A 10 mL, 0.1 nM AgNP solution in DI-H_2O was titrated with either 0.1 M NaOH or 0.1 M HCl at 0.5 pH increments using the MPT-2 autotitrator accessory (Malvern) and pH probe (Malvern). The 10 mL AgNP solution was sampled 4 times for measurement at each pH increment.

4.3.6. UV-Vis

Absorbance spectra were obtained on a Cary 300 UV-Vis spectrophotometer (Agilent) with a 6x6 multi-cell Peltier block (Agilent). Measurements were acquired at 300 nm/min, 0.5 nm resolution, 0.1s integration time. Samples were measured in a semi-micro UV-cuvette and baseline corrected using a cuvette filled with buffer.

4.3.7. Bioconjugation

$AgNP_{OH}$-PAH/PSS-*co*-MA 1:1 was mixed with EDC/NHS in pH 7 HEPES for 20 min at a molar ratio of 25000:10000:1 (NHS:EDC:AgNP). Excess EDC/NHS was removed by three rounds of centrifugation at 7500 RCF for 5 min, resuspending in 50 mM pH 7 HEPES the first two times and 50 mM pH 8 $NaHCO_3$ after the final wash. ConA was prepared in 1 mL of 50 mM pH 8 $NaHCO_3$ with 0.1 M NaCl by nutating for 10 min followed by filtering through a 0.2 μM syringe filter. The ConA solution was transferred to a plastic vial and stirred at 800 RPM. The activated $AgNP_{OH}$-PAH/PSS-*co*-MA 1:1 were added dropwise under stirring, after 5 min stir speed was reduced to 400 RPM and the solution was incubated for 2 h protected from light at room temperature. Excess ConA was removed by dialysis for 48 h against 50 mM pH 7.2 TRIS with 0.15 M NaCl.

4.4. Results and Discussion

4.4.1. LbL Method Development

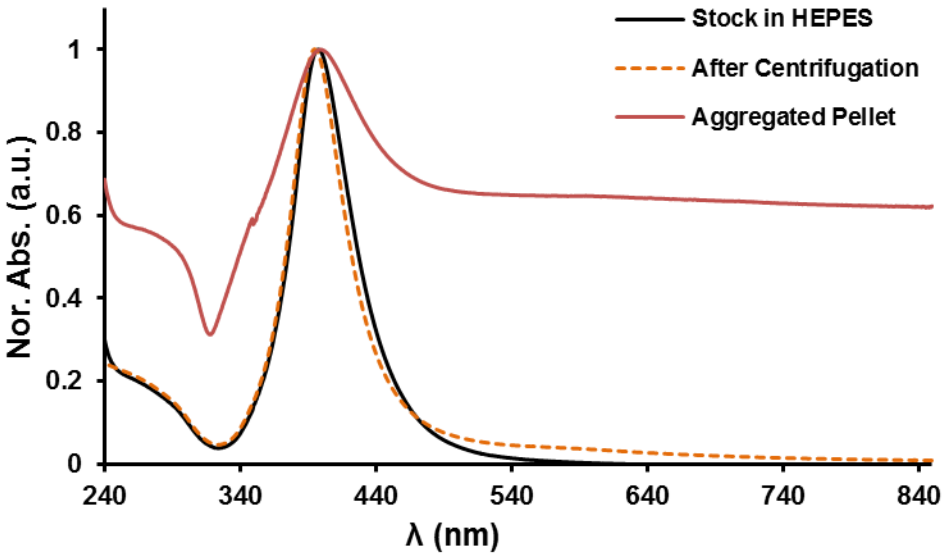

Figure 4.1: UV-Vis absorbance of $AgNP_{OH}$ stock suspended in HEPES pH 7.2 (black −) followed by centrifugation three times and resuspension HEPES pH 7.2 (orange − −). A pellet that can only be redispersed with sonication contains unstable NPs (red −).

The stock of $AgNP_{OH}$ is suspended in HEPES buffer at pH 7.2. To remove aggregated NPs and unreacted components the $AgNP_{OH}$ are subjected to three rounds of centrifugation at 10000 RCF for 30 min then resuspended in 50 mM HEPES pH 7.2 each time. After three rounds of ultracentrifugation the spectra looks nearly identical but the peak shifts from 397 nm for the stock to 394 nm after purification (Figure 4.1). A portion of the stock centrifuges to form a pellet that can only be redispersed by sonication; this portion is discarded as it contains the unstable AgNPs as shown by the large scattering component in the UV-Vis spectra (Figure 4.1). The total recovery after

three rounds of centrifugation is 47% by absorbance intensity. This is initial purification is critical to ensure consistent results for downstream LbL modification.

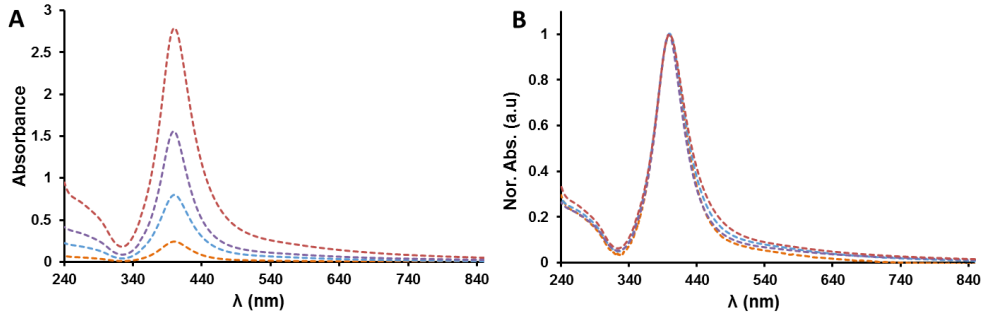

Figure 4.2: UV-Vis absorbance of PAH coating of $AgNP_{OH}$ at 0.1 nM (orange − −), 0.2 nM (blue − −), 0.3 nM (purple − −), and 0.4 nM (red − −).

The concentration of $AgNP_{OH}$ used for PAH coating was varied between 0.1 - 0.4 nM to determine how much the process could be scaled up. From UV-Vis there was little change in spectra and no change in peak location observed when increasing concentration over this range (Figure 4.2A, Figure 4.2B).

4.4.2. LbL on AgNPs

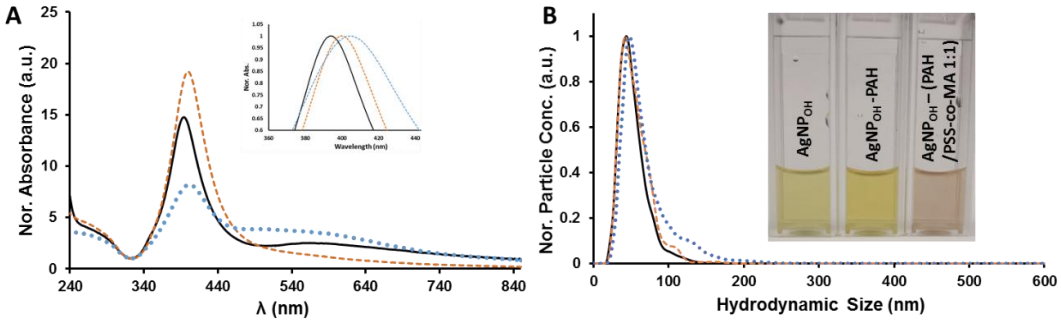

Figure 4.3: (A) UV-Vis absorbance and (B) NTA for $AgNP_{OH}$ (black −) $AgNP_{OH}$-PAH (orange − −) and $AgNP_{OH}$-(PAH/PSS-*co*-MA 1:1) (blue ••). (A) Inset shows the peak location after normalizing to maximum intensity. (B) Inset is photograph of $AgNP_{OH}$ and after coating with PAH and PSS-*co*-MA 1:1 showing the visual color change.

Table 4.1: AgNP size by mode and mean, stdev is the standard deviation of the NP size distribution, from NTA. The standard deviation of the mode, mean and stdev represents 95% confidence interval for n = 3 samples.

	AgNP–OH	AgNP–PAH	AgNP–PAH/PSS-*co*-MA 1:1
Mode (nm)	41.67 ± 0.58	44.67 ± 1.73	47.25 ± 0.96
Mean (nm)	50.39 ± 2.94	51.39 ± 2.55	69.11 ± 2.07
Stdev (nm)	18.03 ± 3.62	14.65 ± 1.92	34.77 ± 4.95

The UV-Vis spectra shows a shift in peak location from 394 nm for the $AgNP_{OH}$ to 400.8 nm after coating with PAH (Figure 4.3A). The peak intensity also increases after PAH coating when normalized to the absorbance at 320 nm, indicating some enhancement of the plasmon resonance. There are no secondary peaks associated with aggregation present (Figure 4.3A). After adding the next layer of PSS-*co*-MA 1:1 the peak location shifts to 406.5 nm and a broad secondary peak appears around 550 nm indicating some plasmon coupling of aggregated AgNPs (Figure 4.3**A**). Additionally, the peak intensity decreases to nearly half of the $AgNP_{OH}$ stock intensity indicating a decrease in plasmon resonance (Figure 4.3A).

NTA analysis was used to determine AgNP size before and after modification and to further assess the degree of aggregation. The initial $AgNP_{OH}$ peak size is 41.67 nm (Table 4.1). After coating with PAH the size increases to 44.67 nm and then after coating with PSS-*co*-MA 1:1 it increases to 47.25 nm; an approximate 3 nm increase for each step (Table 4.1). Since NTA measures hydrodynamic diameter, the size increase measured represents a 1.5 nm thickness increase for each layer. There is very little aggregation after PAH coating, indicated by the single peak in the size distribution with only a small secondary peak at 110 nm (Figure 4.3B). Additionally, the mean size and

the standard deviation of the size distribution do not show a large increase (Table 4.1). After coating with PSS-*co*-MA 1:1 the size distribution still exists primarily as a single peak but slightly more aggregation is observed as a secondary peak (Figure 4.3B). This increase in aggregation can also be observed from the larger increase in the mean size and in the standard deviation of the size distribution (Table 4.1). It is interesting to observe that this small degree of aggregation viewed by NTA translates into a large increase in the secondary peak of the plasmon resonance in the UV-Vis spectra.

4.4.3. Determining Concentration of AgNPs with NTA

The determination of concentration was compared using UV-Vis and NTA. Figure 4.4 shows the NTA data obtained by measuring 3 dilutions of the same sample to show that the concentration measurement was linear in that range.

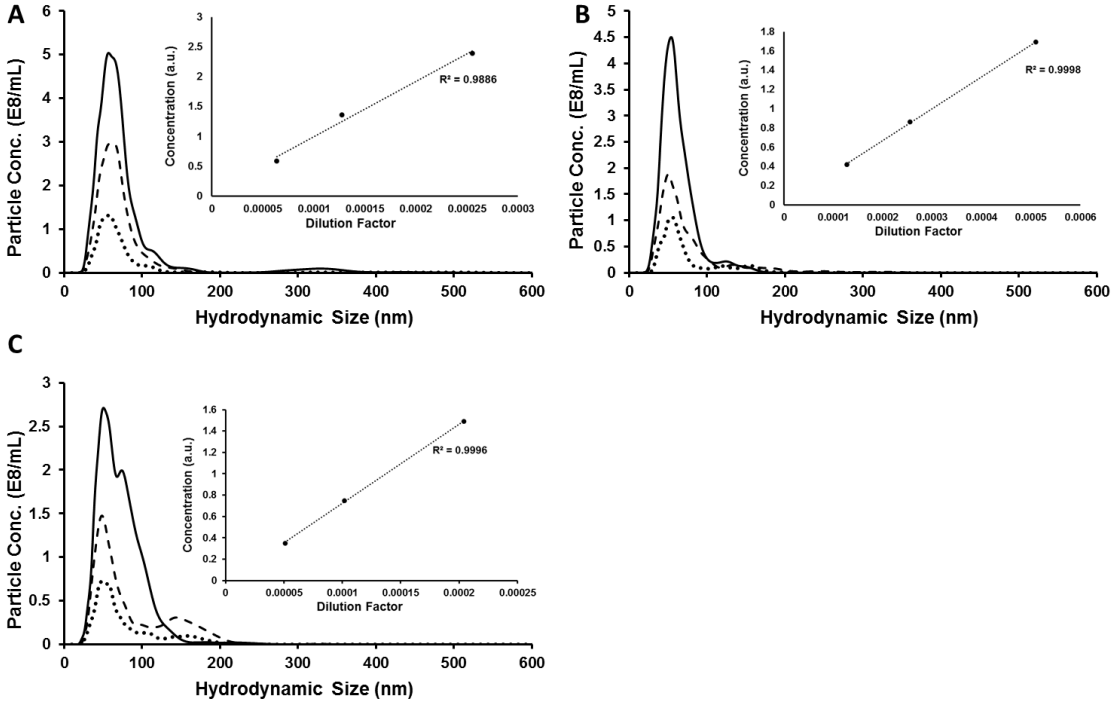

Figure 4.4: Determination of concentration using NTA by measuring the concentration of three dilutions of the same sample (A) $AgNP_{OH}$, (B) $AgNP_{OH}$-PAH, and (C) $AgNP_{OH}$-(PAH/PSS-*co*-MA 1:1). Inset shows linearity of concentration with dilution over this range.

The extinction corresponding to a 40 nm AgNP (the size determine from NTA for L0) 40 nm was used to calculate the concentration from UV-Vis. For $AgNP_{OH}$ the concentration from NTA was 1.6 times higher than concentration determined by UV-Vis. After coating with PAH, the NTA concentration is 1.4 times larger than UV-Vis. However, after coating with PSS-*co*-MA 1:1 the concentration from NTA is 6 times larger than that determined by UV-Vis. The NTA and UV-Vis show agreeable data for $AgNP_{OH}$ and PAH, but the PSS-*co*-MA 1:1 is changing the optical properties enough that the concentration calculation is no longer accurate. The PSS-*co*-MA 1:1 layer has a concentration that is closer to an extinction corresponding to a 20 nm NP.

4.4.4. Colloidal and Optical Stability in Different Buffer Types

The stability of $AgNP_{OH}$ and $AgNP_{OH}$-PAH/PSS-*co*-MA 1:1 was investigated when exposed to HEPES, TRIS and phosphate buffer (PHOS) all at pH 7.2. The $AgNP_{OH}$ were initially stored in HEPES buffer because the HEPES buffer does not contain metal chelating ions. When the $AgNP_{OH}$ are transferred to either TRIS of PHOS buffer aggregation is immediately observed by NTA as a large increase in peak size and broadening of the size distribution (Figure 4.5A and Table 4.2). In contrast, when $AgNP_{OH}$-PAH/PSS-*co*-MA 1:1 are exposed to TRIS and PHOS no change is observed in the size or size distribution (Figure 4.5B). The $AgNP_{OH}$ increase in peak size by 120% while the $AgNP_{OH}$-PAH/PSS-*co*-MA 1:1 size only changed by 2% (Table 4.2). This clearly shows that LbL dramatically enhances stability of the AgNP in different buffers, possible because it is protecting the surface from being exposed to chelating species.

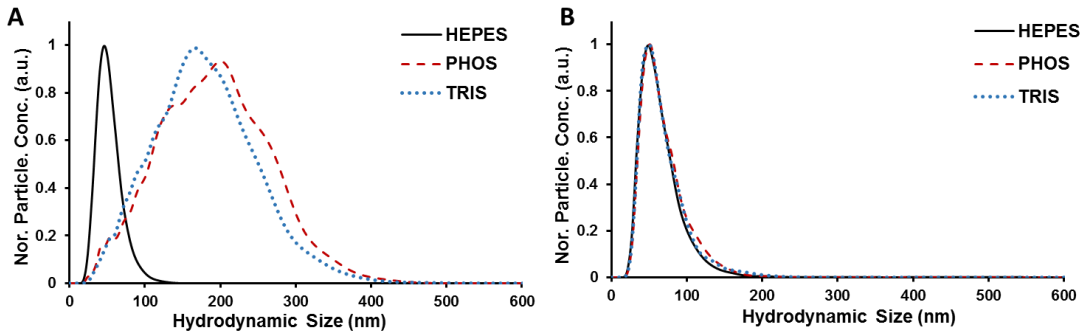

Figure 4.5: (A) NTA for $AgNP_{OH}$ and (B) $AgNP_{OH}$-(PAH/PSS-*co*-MA 1:1) in 50 mM HEPES pH 7.2 (black −) 50 mM phosphate pH 7.2 (red ––) and 50 mM TRIS pH 7.2 (blue ••).

Table 4.2: AgNP size by mode and mean, stdev is the standard deviation of the NP size distribution, from NTA. Percent difference is compared to the AgNPs in HEPES. The standard deviation of the mode, mean and stdev represents a 95% confidence interval for n = 3 samples.

				% Diff.	
AgNP−OH	**HEPES**	**PHOS**	**TRIS**	**PHOS**	**TRIS**
Mode (nm)	45.66 ± 1.52	182.3 ± 35.9	149.6 ± 28.7	120	106
Mean (nm)	53.37 ± 1.42	193.3 ± 20.4	167.3 ± 25.4	113	103
Stdev (nm)	17.08 ± 0.73	69.59 ± 0.51	65.99 ± 5.74	121	36
AgNP−PAH/PSS-*co*-MA	**HEPES**	**PHOS**	**TRIS**	**PHOS**	**TRIS**
Mode (nm)	49.66 ± 2.08	50.66 ± 1.52	49.33 ± 1.15	2.0	0.7
Mean (nm)	65.99 ± 2.23	69.14 ± 4.84	67.92 ± 4.06	4.7	2.9
Stdev (nm)	30.36 ± 6.97	28.94 ± 4.59	30.05 ± 4.14	4.8	1.0

4.4.5. Colloidal and Optical Stability in Binding Buffer

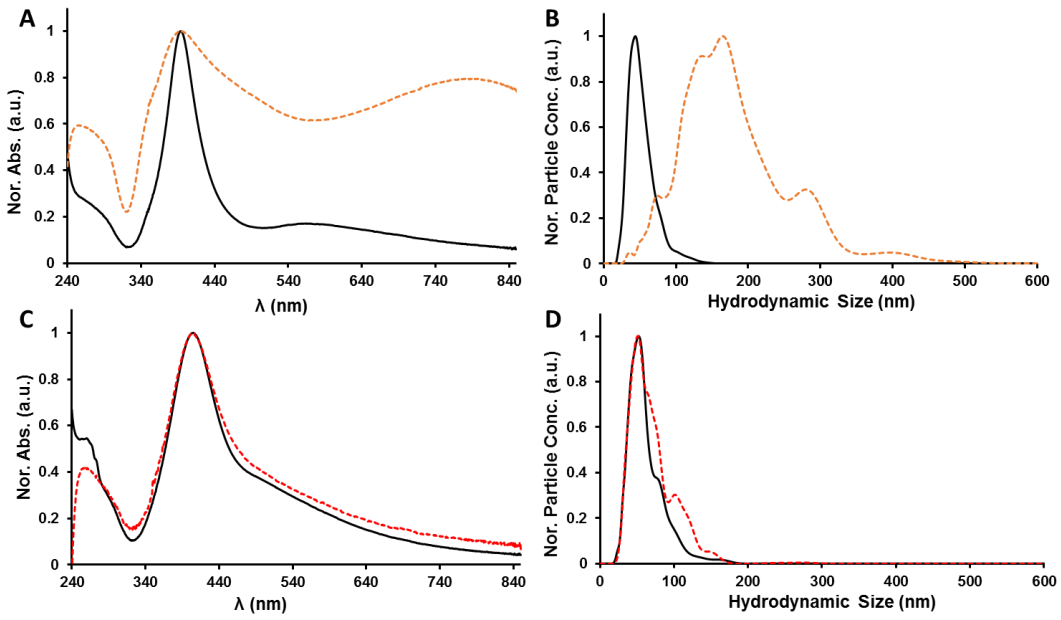

Figure 4.6: (A) UV-Vis absorbance and (B) NTA for $AgNP_{OH}$ in HEPES pH 7.2 (black −) and HEPES binding buffer (orange − −) and $AgNP_{OH}$-(PAH/PSS-*co*-MA 1:1) in HEPES pH 7.2 (black −) and HEPES binding buffer (red − −).

Table 4.3: AgNP size by mode and mean, stdev is the standard deviation of the NP size distribution, from NTA. The standard deviation of the mode, mean and stdev represents 95% confidence interval for n = 3 samples.

AgNP-OH	HEPES	HEPES Binding Buffer	% Diff
Mode (nm)	44.75 ± 0.96	163.0 ± 3.61	114
Mean (nm)	55.75 ± 5.51	184.3 ± 3.83	107
Stdev (nm)	23.47 ± 4.82	69.06 ± 2.69	98.5
AgNP-PAH/PSS-*co*-MA	**HEPES**	**HEPES Binding Buffer**	**% Diff**
Mode (nm)	50.67 ± 4.73	50.33 ± 0.77	0.66
Mean (nm)	69.69 ± 3.69	72.48 ± 0.74	3.93
Stdev (nm)	31.48 ± 3.54	33.53 ± 2.10	6.30

The stability of the AgNPs was further studied under conditions relevant for optical biosensor applications, specifically in the binding buffer required for ConA binding. ConA requires the divalent cations calcium and magnesium as cofactors to bind saccharides and requires at least 20 mM - 150 mM NaCl to ensure protein stability. When $AgNP_{OH}$ are exposed to HEPES binding buffer significant aggregation occurs as shown by the multimodal peak presence and broadening in the UV-Vis spectra (Figure 4.6A). Aggregation is also observed by NTA with a 113.8% increase in mean size and 98.5% increase in the standard deviation of the size distribution (Figure 4.6A Table 4.3). This presents two main problems: (1) aggregation causes a change in the spectral properties which will affect sensor performance and (2) aggregation of NPs coated in sensing components (ConA or saccharide analogue) will affect binding kinetics. In contrast, when $AgNP_{OH}$-PAH/PSS-*co*-MA 1:1 are exposed to binding buffer there is minimal change in the UV-Vis spectra; with no secondary peaks or substantial peak broadening (Figure 4.6C). Additionally, from NTA there is less than a 1% change in peak size and 6.3% change in the standard deviation of the size distribution (Figure 4.6D

and Table 4.3). The LbL coating stabilizes the AgNPs against aggregation in the binding buffer to preserve the core NP optical properties.

4.4.6. Colloidal and Optical Stability at Different pH

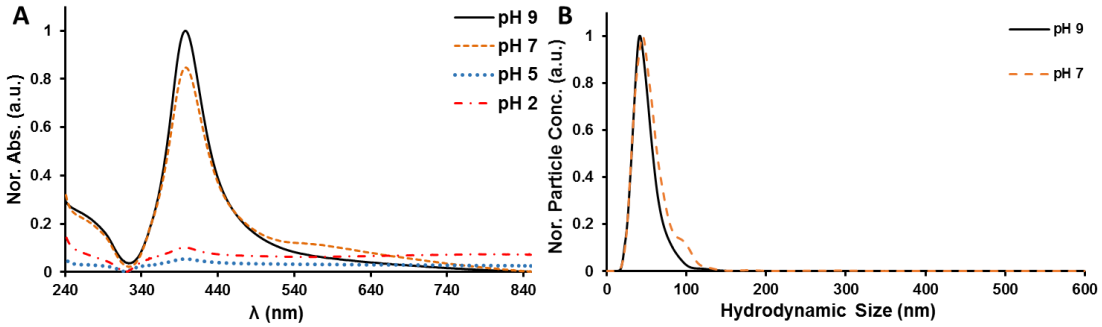

Figure 4.7: (A) UV-Vis and (B) NTA for $AgNP_{OH}$ after incubation in buffer for 1 h in pH 2 sodium acetate (red − • −), pH 5 sodium acetate (blue •), pH 7 HEPES (orange − −) and pH 9 CHES (black −)

The stability of $AgNP_{OH}$, $AgNP_{OH}$-PAH, and $AgNP_{OH}$-PAH/PSS-*co*-MA 1:1 was investigated by UV-Vis and NTA when stored for 1 h at pH 2, pH 5, pH 7, or pH 9. The $AgNP_{OH}$ shows a small increase in aggregation as pH goes from pH 9 to pH 7.2 that can be seen as an introduction of a small secondary peak indicating some plasmonic coupling (Figure 4.7A). At pH 5 and below, a substantial decrease in absorbance is observed, indicating AgNPs were being dissolved. Visually, there were no aggregates present on the bottom of the cuvette to indicate aggregation mediated precipitation. For $AgNP_{OH}$ the NP size at pH 9 is 41.67 nm and increases to 44.3 nm at pH 7.2, for pH 5 and below size could not be measured due to insufficient NP tracking events (Figure 4.7B and Table 4.4).

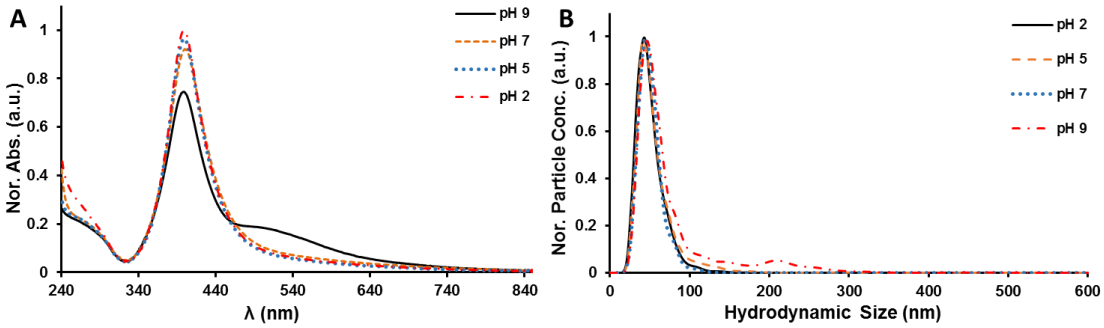

Figure 4.8: (A) UV-Vis and (B) NTA for $AgNP_{OH}$-PAH after incubation in buffer for 1 h in pH 2 sodium acetate (red − • −), pH 5 sodium acetate (blue •), pH 7 HEPES (orange ——) and pH 9 CHES (black −).

For $AgNP_{OH}$-PAH the UV-Vis shows a single peak around 400 nm for pH 2, pH 5, and pH 7.2, with the peak intensity decreasing slightly as pH increases (Figure 4.8A). At pH 9 there is a large increase in peak intensity and the introduction of a secondary peak indicating aggregation. From NTA we see no aggregation for pH 2, pH 5, or pH 7.2 but a small amount of aggregation at pH 9 (Figure 4.8B). This behavior is expected from a PAH terminated NPs because the pKa of PAH is ≈ 8.5, as the surface charge decreases the NPs will aggregate. Interestingly, the peak size of the PAH terminated NPs decreases with increasing pH by about 0.5 nm per pH unit (Table 4.4). This indicates that as the PAH increases in charge density there is a change in the degree of surface PE swelling or conformation change that is causing a change to the apparent AgNP size.

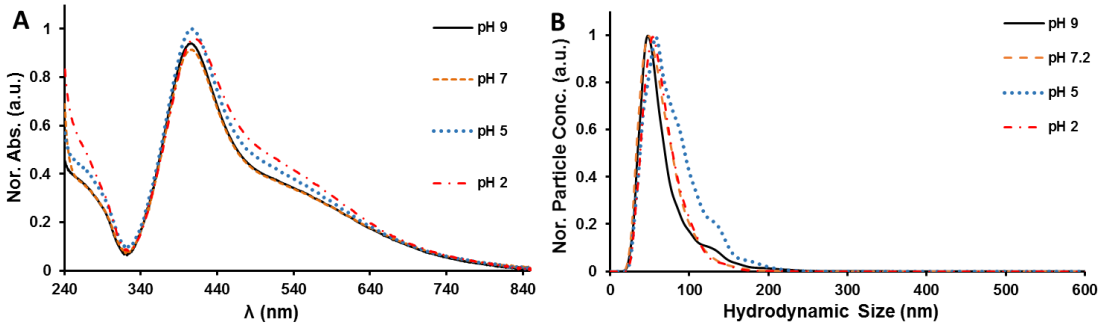

Figure 4.9: (A) UV-Vis and (B) NTA for AgNP$_{OH}$-(PAH/PSS-*co*-MA 1:1) after incubation in buffer for 1 h in pH 2 sodium acetate (red −•−), pH 5 sodium acetate (blue •), pH 7 HEPES (orange ——) and pH 9 CHES (black −).

For the AgNP$_{OH}$-PAH/PSS-*co*-MA 1:1 the UV-Vis shows no difference between pH 9 and pH 7.2 and only a slight broadening is observed at pH 5 or pH 2 (Figure 4.9A). This shows the ability of AgNP$_{OH}$-PAH/PSS-*co*-MA 1:1 to stabilize the optical properties of the NP core over a broad pH range. NTA shows a similar story of minimal change in peak size between pH 2 and pH 9 (Figure 4.9B). Just like PAH terminated AgNPs, the peak size of PSS-*co*-MA 1:1 terminated AgNPs increases by approximately 1 nm per pH unit as the terminal layer becomes more ionized with the exception of pH 5 (Table 4.4).

Table 4.4: AgNP size by mode and mean, stdev is the standard deviation of the NP size distribution from NTA. The standard deviation of the mode, mean and stdev represents 95% confidence interval for n = 3 samples.

AgNP–OH	pH 2	pH 5	pH 7.2	pH 9
Mode (nm)	N/A	N/A	44.33 ± 0.65	41.67 ± 0.65
Mean (nm)	N/A	N/A	53.13 ± 2.41	50.39 ± 3.32
Stdev (nm)	N/A	N/A	21.49 ± 3.83	18.03 ± 4.10
AgNP–PAH	**pH 2**	**pH 5**	**pH 7.2**	**pH 9**
Mode (nm)	42.67 ± 1.31	43.00 ± 2.99	44.67 ± 1.73	46.00 ± 2.99
Mean (nm)	50.83 ± 2.61	56.39 ± 4.25	51.39 ± 2.55	78.49 ± 4.47
Stdev (nm)	17.64 ± 1.95	24.29 ± 12.1	14.65 ± 1.92	58.45 ± 7.57
AgNP–PAH/PSS-*co*-MA	**pH 2**	**pH 5**	**pH 7.2**	**pH 9**
Mode (nm)	53.33 ± 1.73	57.00 ± 1.13	49.67 ± 2.36	47.00 ± 1.13
Mean (nm)	66.87 ± 4.62	80.97 ± 4.02	66.00 ± 2.53	68.41 ± 2.10
Stdev (nm)	23.63 ± 3.10	34.05 ± 3.51	30.36 ± 7.89	35.27 ± 6.71

4.4.7. The pH Dependence of Microelectrophoresis

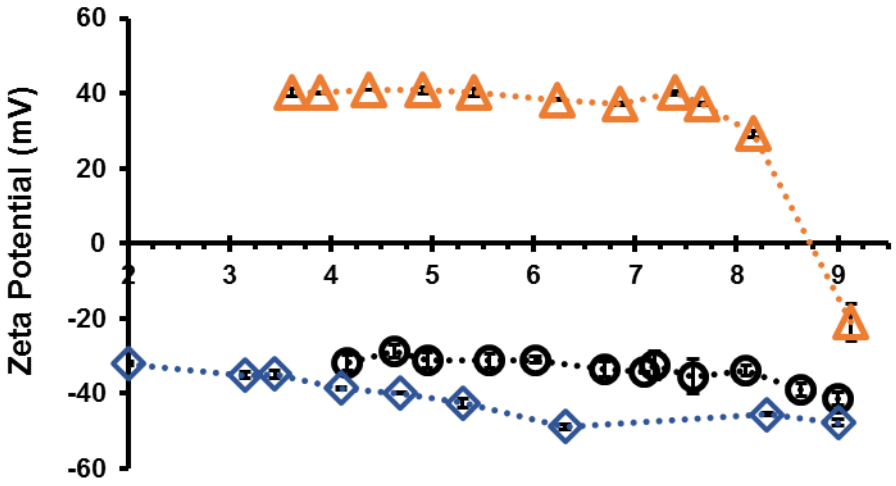

Figure 4.10: Zeta potential as a function of pH for $AgNP_{OH}$ (black ○) $AgNP_{OH}$-PAH (orange Δ) and $AgNP_{OH}$-PAH/PSS-*co*-MA 1:1 (blue ◊). Error bars represent standard deviation (n = 4).

Zeta potential was measured as a function of pH for $AgNP_{OH}$, $AgNP_{OH}$-PAH, and $AgNP_{OH}$-PAH/PSS-*co*-MA 1:1 (Figure 4.10). As $AgNP_{OH}$ were titrated from pH 9 to pH 4 the zeta potential magnitude decreased by 9 mV. Below pH 4 the data could not be collected due to insufficient intensity due to either AgNPs being aggregated or dissolved. After coating with PAH the charge reversed to 40 mV, maintaining this zeta potential when the pH was titrated from pH 3.6 and pH 7.4, then at pH 8.75 the zeta potential reached zero (Figure 4.10). This is the expected behavior of a PAH coated NP. Adding a layer of PSS-*co*-MA 1:1 causes a charge reversal to -48 mV. The zeta potential magnitude decreased by 16 mV when titrated from pH 9 to pH 2 (Figure 4.10). This shows how a single bilayer is protecting the AgNPs from dissolution and/or aggregation.

4.4.8. Bioconjugation of ConA

4.4.8.1. Overview

The electrosteric stability mentioned previously is also beneficial during the bioconjugation process, specifically when using EDC/NHS chemistry. The general method for bioconjugation and the relevant parameters for each step are shown in Figure 4.11.

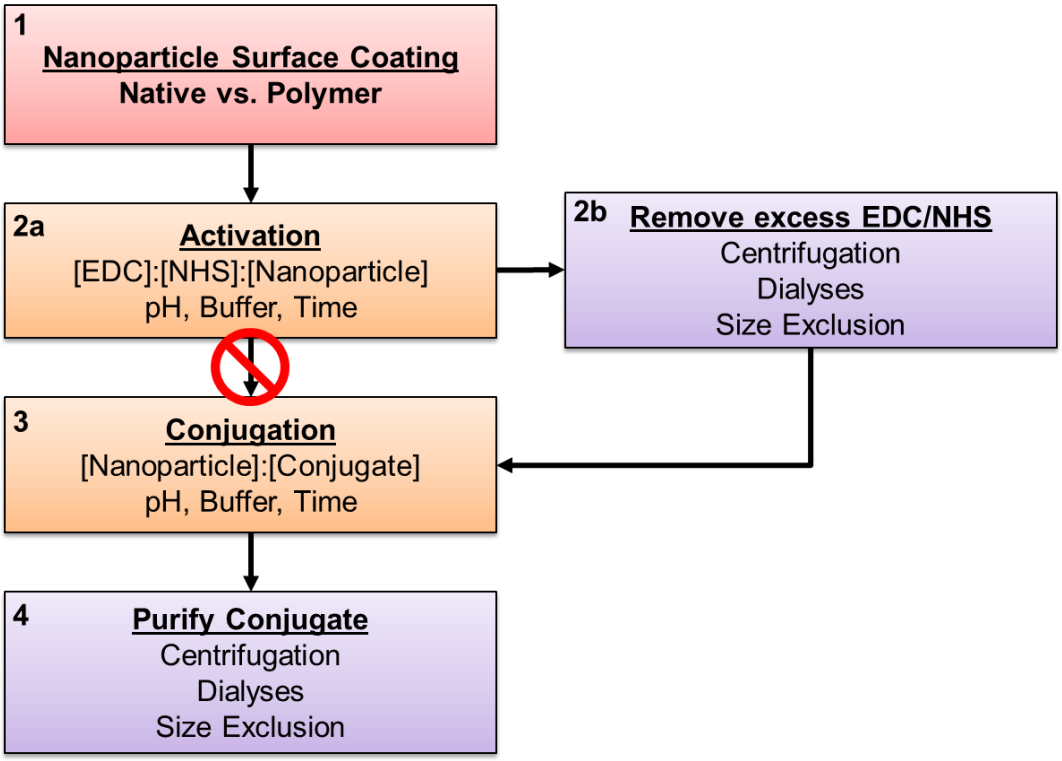

Figure 4.11: Generic flow-chart for the bioconjugation of nanomaterials *via* EDC and NHS chemistry.

The initial NPs are produced with some initial surface chemistry or polymer modification that imparts carboxylic acid functionality. The carboxylic acids are then activated by the addition of EDC and NHS. If the activated NP solution is added directly to the protein solution then interprotein conjugation is likely to occur due to the presence of residual EDC/NHS. Therefore, the excess EDC/NHS must be removed first without introducing aggregation. The purified activated NPs can then be mixed with the protein for conjugation. The protein is added in excess compared to the NP to prevent interparticle conjugation (two NPs conjugating to the same protein). The NP-protein conjugate must then be purified from the excess non-conjugated protein using some process.

4.4.8.2. Purification

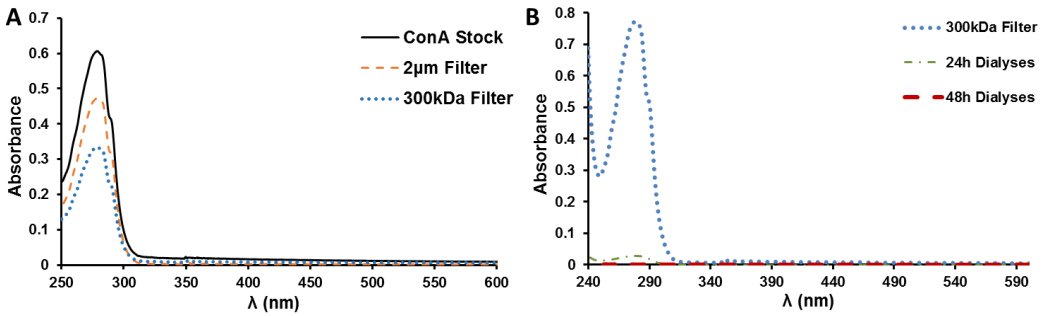

Figure 4.12: (A) UV-Vis absorbance to show change in concentration of ConA stock solution (black −) and after being filtered with a 2 µm Nanosep (orange − −), and 300kDa Nanosep (blue • •). (B) ConA filtered with a 300 kDa Nanosep (blue • •) and then dialyzed with a Floatalyzer G2 after 24 h (green − • −) and 48 h (red − −).

The UV-Vis of ConA dissolved in 0.1 M $NaHCO_3$ pH 8 with 0.1 M NaCl shows the primary peak absorbance at 280 nm but also the presence of scattering that indicates some aggregation is present (Figure 4.12A). After filtering the ConA with a 2 µm syringe filter the absorbance intensity decrease corresponds to a ≈ 22% decrease in ConA concentration. The filtered ConA was then filtered again with a 300kDa Nanosep filter to remove any further aggregation, which corresponded to a ≈ 29% decrease in ConA concentration (Figure 4.12A). This double filtered ConA was used then used for bioconjugation. It is important to note that the 2 µm filtering is required before the 300 kDa filtering to prevent clogging of the Nanosep. The efficacy of removing excess ConA by dialyses was tested by placing the filtered ConA into a 300 kDa Floatalyzer G2 for dialysis for 48 h. It was found that 95% of the ConA passed through the membrane

after 24 h and 98% after 48 h. This makes dialyses an effective method to remove excess ConA after NP conjugation.

4.4.8.3. Bioconjugation

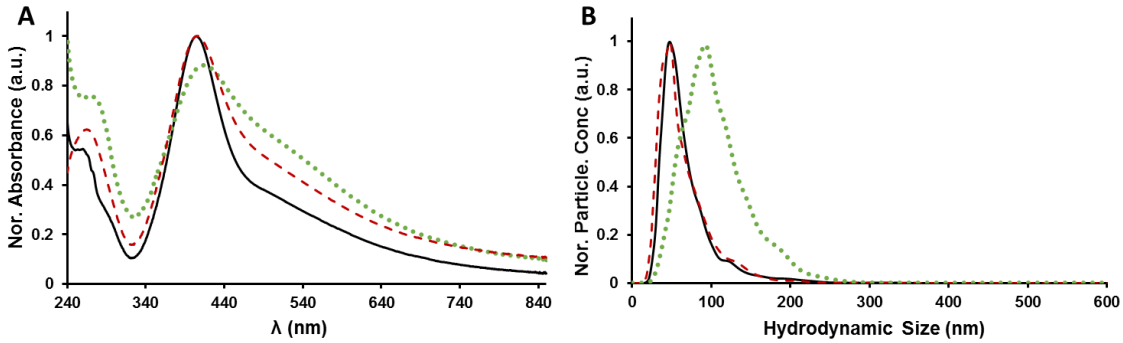

Figure 4.13: (A) UV-Vis absorbance and (B) NTA of $AgNP_{OH}$-PAH/PSS-*co*-MA 1:1 (black −), $AgNP_{OH}$-PAH/PSS-*co*-MA 1:1 after activation with EDC and NHS (red − −), and $AgNP_{OH}$-PAH/PSS-*co*-MA 1:1-ConA (blue • •) after conjugation and dialyses for 48 h.

ConA was conjugated to $AgNP_{OH}$-PAH/PSS-*co*-MA 1:1 activated with EDC/NHS and then excess ConA was removed by dialysis for 48 h. With UV-Vis we can follow the change in optical properties after activation with EDC and NHS and conjugation with ConA (Figure 4.13A). The $AgNP_{OH}$-PAH/PSS-*co*-MA 1:1 are activated with EDC/NHS at pH 7.2 and then excess EDC/NHS is removed by three rounds of centrifugation. The removal of the NHS (and then most likely EDC) can be confirmed from the absence of the NHS absorbance peak at 260 nm (Figure 4.13A**)**. The activation of the $AgNP_{OH}$-PAH/PSS-*co*-MA 1:1 does not cause any change in peak location but it does increase the broadening (Figure 4.13A). The activated $AgNP_{OH}$-PAH/PSS-*co*-MA 1:1 are then added to the ConA and after incubation are transferred to a dialysis membrane for 48 h. The absorbance of the sample after dialysis confirms that

the majority of excess ConA has been removed since there is no strong 280 nm peak present (Figure 4.13A). The conjugation with ConA shifts the peak location to 412.5 nm and increases the broadening (Figure 4.13A). The conjugation of ConA to the $AgNP_{OH}$-PAH/PSS-*co*-MA 1:1 causes a change in the refractive index around the AgNP which causes a shift in the plasmon peak location.

Table 4.5: NTA of AgNPOH-PAH/PSS-*co*-MA 1:1, AgNPOH-PAH/PSS-*co*-MA 1:1 after activation with EDC and NHS, and AgNPOH-PAH/PSS-*co*-MA 1:1-ConA (blue • •) after conjugation and dialyses for 48 h.

	AgNP−PAH/PSS-*co* -MA	EDC/NHS Activated	AgNP−PAH/PSS-*co* -MA-ConA
Mode (nm)	47.25 ± 0.96	47.33 ± 2.08	90.67 ± 4.16
Mean (nm)	69.11 ± 2.07	65.49 ± 6.07	104.8 ± 6.4
Stdev (nm)	34.77 ± 4.95	31.99 ± 5.59	39.36 ± 4.28

NTA was used to evaluate aggregation during the bioconjugation process and confirm ConA conjugation. NTA showed no change in NP size or size distribution to indicate interparticle aggregation after activation of $AgNP_{OH}$-PAH/PSS-*co*-MA 1:1 with EDC/NHS (Figure 4.13B and Table 4.5). This was an important finding because this shows that the PSS-*co*-MA 1:1 coating is providing a stable layer for conjugation even when the carboxylic acid groups are being consumed. There was also concern that the underlying amine containing PAH layer could potentially allow for interparticle bridging; but this did not occur. After conjugation with ConA, the size increases by 43 nm to 90.67 nm, but only an 8 nm increase in size distribution (Figure 4.13B and Table 4.5). This increase in size was larger than expected but does not indicate aggregation because interparticle aggregation would show multiple peaks and a very large increase in broadening.

4.5. Conclusions

This work shows the successful LbL modification of AgNPs without significant aggregation. NTA was used to show the increase in NP size after the addition of each layer. This size change was shown to be pH dependent, following a trend of increasing size with decreasing ionization of the outer layer. To the best of our knowledge, this is the first time the change in hydrodynamic size for multilayer modified NPs has been shown with NTA. Using UV-Vis and NTA the colloidal and optical stability of the LbL modified AgNPs was assessed in different buffer types, in varying ionic strength, and at different pH. In all cases, the LbL modified AgNPs showed superior stability against aggregation compared to the $AgNP_{OH.}$ It also appears that a single bilayer prevents dissolution of the AgNP core at low pH. The thin coating allows for efficient distance dependent energy transfer, while also providing optical and colloidal stability. The bioconjugation of LbL modified AgNPs with ConA *via* EDC/NHS chemistry without aggregation was confirmed by NTA. This shows that PAH/PSS-*co*-MA 1:1 can be used for the EDC/NHS procedure without inducing aggregation due to surface charge instability or interparticle bridging. This shows the potential for using LbL as an intermediary coating to provide a generic route to bioconjugate any core nanomaterial with a desired biomolecule.

5. ENERGY TRANSFER FROM OVALBUMIN GOLD NANOCLUSTERS TO CONCANAVALIN A DECORATED GOLD NANORODS

5.1. Introduction

Developing a nanomaterial-enabled sensor required replacing the initially planned semiconductor QDs with a more stable donor nanomaterial. The problem with QDs was their environmental sensitivity and the difficulty of modification without compromising their optical properties. In contrast, protein encapsulated fluorescent nanoclusters (NCs) have stable PL and high colloidal stability in varying environments due to the properties imparted by the protein shell. Additionally, ovalbumin (OVA) contains a single glycosylation that can be used for binding; negating the need for any further modification. This section explores OVA-AuNCs as photoluminescent probes in a competitive binding energy transfer sensor.

5.2. Background

Noble metal nanoclusters (NCs) are defined as particles less than 2 nm, consisting of a few to hundreds of atoms of Au, Ag, copper, platinum, molybdenum, or bismuth.[261] In this size regime, metallic NPs no longer exhibit plasmonic resonance and instead exhibit molecular like properties that give rise to unique optical[262] and catalytic[263] properties. Due to quantum size effects, the band structure displays discrete energy levels, which give rise to size tunable luminescence from the visible to the NIR region.[264] Luminescent NCs exhibit excellent photo-stability, long lifetimes (μs), a large stokes shift, and excellent biocompatibility.[265-267] These properties make NCs strong candidates as luminescent probes for biosensor and bioimaging applications.

The synthesis of AuNCs involves the reduction of gold ions followed by protection of the NC by a stabilizing ligand. AuNCs have been synthesized using a variety of different stabilizing agents: polymers/dendrimers, peptides/proteins, DNA, or thiol containing molecules.[268, 269] A protein directed synthesis method utilizing bovine serum albumin (BSA) has been demonstrate as a simple and highly reproducible route to produce colloidally stable and highly luminescent AuNCs.[270] This method was extended for the growth of AuNCs with similarly properties using human serum albumin[271] and OVA.[272-274] These protein-protected AuNCs do not exhibit variations in luminescent intensity across broad pH and ionic strength conditions since the AuNCs are imparted the high stability of serum albumin protein shell. Protein stabilized AuNCs have found extensive use in endpoint assays for the detection of heavy metals[275] (mercury, copper, cadmium or lead),[266] hydrogen peroxide,[272] chloramphenicol,[276] ascorbic acid,[277] and folic acid.[278] The detection of analyte in these sensors involves the quenching of the AuNC core either by attachment of the analyte to the Au or by destructions of the protein-AuNC interaction; in both cases the quenching is generally not reversible.

The OVA-AuNCs have a unique property because OVA contains a single glycosylation site with a high affinity for ConA.[279, 280] The use of fluorescently labeled OVA in a ConA based competitive binding assay was demonstrated by Cummins *et al*.[279] Additionally, the OVA-AuNC attachment to ConA was used to develop an aggregation based precipitation assay for the detection of ConA.[274] In this case, OVA is used not only to reduce and stabilize the AuNC, but to also introduce functionality without the need for additional modification.

In this section, OVA-AuNCs are utilized as a luminescent donor for the development of a competitive binding energy transfer sensor (Figure 5.1B). ConA conjugated to a PSS-*co*-MA modified AuNR (Figure 5.1A) was used as the acceptor because AuNRs could be fabricated with an SPR absorption overlapping with the OVA-AuNC emission. The envisioned sensor could then be used to detect glucose based on the quenching and luminescence recovery of OVA-AuNCs in the absence and presence of glucose respectively (Figure 5.1C). Additionally, the interaction of a fluorescent AuNC with another nanomaterial is a very unique situation of energy transfer that has not been thoroughly investigated.[281, 282 283]

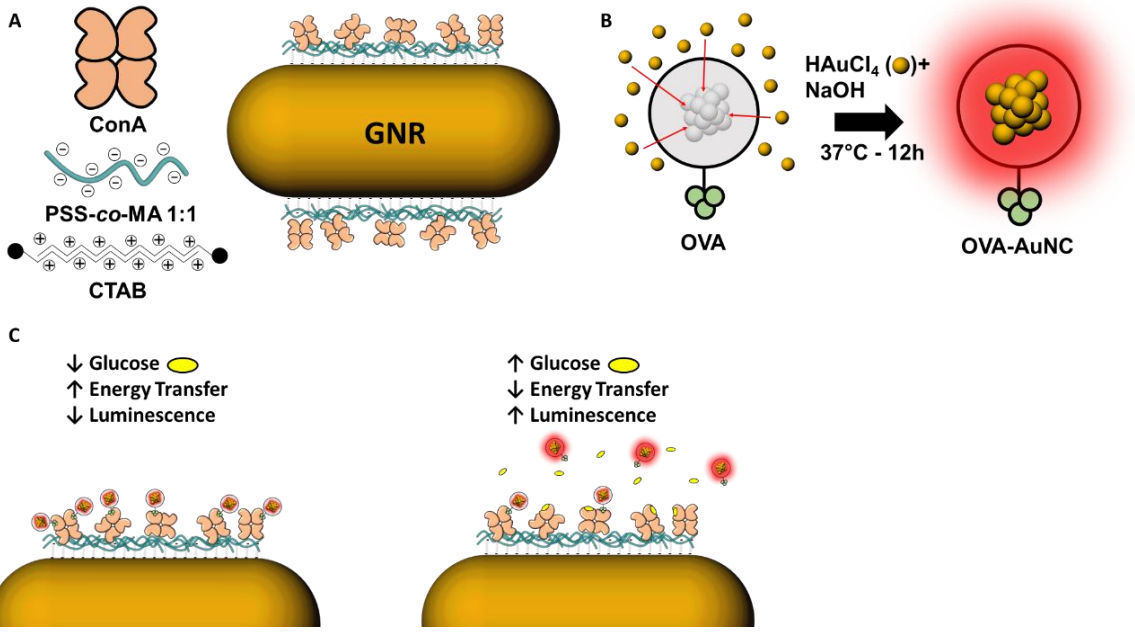

Figure 5.1: (A) The AuNR$_{CTAB}$-PSS-*co*-MA 1:1-ConA construct consisting of PSS-*co*-MA 1:1 modified AuNR$_{CTAB}$ followed by conjugation to ConA. (B) OVA-AuNC synthesized by the sequestration and grown of gold ions into the OVA protein by incubation at 37°C for 12h. (C) The assay concept where OVA-AuNCs are bound by the AuNR$_{CTAB}$-PSS-*co*-MA 1:1-ConA in the absence of glucose resulting in an increase in non-radiative energy transfer and decrease in PL intensity. As glucose enters the system it displaces the OVA-AuNC, decreasing energy transfer and increasing PL intensity as a function of glucose concentration.

5.3. Materials and Methods

5.3.1. Chemicals

Ovalbumin (98%), $MnCL_2$ (ACS, 98%), $CaCL_2$ (ACS, 96%), methyl α-D-mannopyranoside (99%), N-(3-Dimethylaminopropyl)-N'-ethylcarbodiimide hydrochloride (EDC), Gold (III) chloride trihydrate (99.9%), poly (4-styrenesulfonic acid-*co*-maleic acid) sodium salt (PSS-*co*-MA) (Mw = 20000 g · mol^{-1}) with a ratio of maleic acid to styrene sulfonate of 1:1, were all purchased from Sigma-Aldrich. Anhydrous D-glucose (ACS) purchased from Macron. N-Hydroxysulfosuccinimide (NHS) was purchased from G-Biosciences. High Trap ConA 4B 1 mL column was

obtained from GE Life Sciences. AuNR solution A12-25-650 stabilized with 3 mM CTAB in DI-H_2O was purchased from Nanopartz. The $AuNR_{CTAB}$ were 25 nm in diameter and 64nm in length based on TEM reported by the manufacturer with a reported extinction of 7.11E9 $M^{-1}cm^{-1}$ at 650 nm.

5.3.2. Synthesis of OVA-AuNCs

50 mg of OVA was dissolved in 1 mL of ultrapure water on the nutating mixer for 10 min. The OVA solution was combined with 1 mL of 10 mM HAuCl in ultrapure water in a glass vial and stirred for 2 min. 100 µL of 1 M NaOH was added dropwise to increase solution to pH 12. The solution was incubated at 37°C for 12 h under moderate stirring.

5.3.3. Purification of OVA-AuNC

Several buffers were used during the purification process: (1) binding buffer - 50 mM TRIS pH 7.4, 1 mM $CaCl_2$, 1 mM $MnCl_2$, 0.5 M NaCl, (2) storage buffer - 50 mM HEPES pH 7.4, 1 mM $CaCl_2$, 1 mM $MnCl_2$, 0.15 M NaCl, (3) elution buffer - 50 mM TRIS pH 7.4 , 0.2 M methyl-mannose, 0.5 M NaCl (4) assay buffer - 50 mM HEPES pH 7.4, 1 mM $CaCl_2$, 1 mM $MnCl_2$, 20 mM NaCl.

The OVA-AuNC solution was diluted to 10mL in binding buffer and filtered through a 0.2 µm syringe filter to remove any large protein aggregates. A HiTrap ConA 4B 1 mL column was prepared by flowing 10mL of binding buffer at 0.5 mL/min. It is important to prevent air bubbles from entering the column. Approximately 10 mg of OVA-AuNC diluted to a 5 mL volume was flowed through the column at 0.2 mL/min. 10 mL of binding buffer was pumped through at 0.2 mL/min to remove any unbound

OVA-AuNCs. The bound OVA-AuNCs were eluted by flowing 5 mL of elution buffer at 0.2 mL/min while collecting the eluent. An additional 5 mL of binding buffer was flowed through to ensure complete OVA-AuNC removal. The purified OVA-AuNC solution was centrifuged 5 times to remove excess methyl-mannose with a 3 kDa Microsep for 1 h at 3000 RCF at 14°C, resuspending in storage buffer each time. The final product was stored protected from light at 4°C.

5.3.4. AuNR LbL

$AuNR_{CTAB}$ stock solution was diluted 1/3 in in ultrapure water to reduce CTAB concentration to 1 mM and sonicated for 5 min. A 10 mg/mL stock of PSS-*co*-MA 1:1 was dissolved in DI-H_2O and sonicated for 45 min prior to use. A 5 mL aliquot of diluted $AuNR_{CTAB}$ solution (0.05 nM) was rapidly added to 5 mL of PSS-*co*-MA 1:1 under sonication and incubated under sonication for 10 min. Excess PSS-*co*-MA 1:1 was removed by three rounds of centrifugation at 12000 RCF for 20 min, resuspending in 50 mM CHES pH 9 each time. After the final cleaning step the AuNRs-PSS-*co*-MA 1:1 were suspended in 50 mM HEPES pH 7. The solution was filtered using a 0.2 μm Nanosep to remove any large aggregates.

5.3.5. AuNR Bioconjugation

$AuNR_{CTAB}$-PSS-*co*-MA 1:1 was mixed with EDC/NHS at a molar ratio of 25000:10000:1 (NHS:EDC:AuNR). The AuNRs are suspended in 50 mM pH 7 HEPES and placed to stir at 600 RPM in a 1 mL plastic cryovial with a rounded bottom. An NHS stock was made by dissolving at a high concentration (≈1-5 mg/mL) in a small volume (≈100 – 200 μL) in pH 7 HEPES, the required amount was then transferred to

the AuNR solution. An EDC stock solution was made at a high concentration (≈1-5 mg/mL) in small volume (≈100 – 200 µL) in pH 6 MES, the required amount is then transferred to the AuNR solution. The AuNR and EDC/NHS mixture is protected from light and allowed to react for 20 min at room temperature. Excess EDC/NHS was removed by three rounds of centrifugation at 7500 RCF for 5 min, resuspending in 50 mM pH 7 HEPES the first two times and 500 µL of 50 mM pH 8 $NaHCO_3$ after the final wash; sonication should not be required for resuspension. ConA was prepared in 1 mL of 50 mM pH 8 $NaHCO_3$ with 0.15 M NaCl by nutating for 10 min followed by filtering through a 0.2 µM syringe filter or 300 kDa Nanosep (3000 RCF x 5 min). The concentration of the filtered ConA was determined by UV-Vis, the amount required transferred to a plastic cryovial, the volume was increased to 1 mL, and the solution was stirred at 600 RPM. The activated $AuNR_{CTAB}$-PSS-*co*-MA 1:1 were added dropwise under stirring, after 5 min stir speed was reduced to 400 RPM and the solution was incubated for 2 h protected from light at room temperature. A typical reaction involved a 0.1 - 0.2 nM of AuNRs and 1 µM of ConA. The pH was increased to pH 9 by the addition of 300 µL of 0.5 M CHES pH 9 and incubated for 10 min to ensure that unreacted groups were regenerated back to carboxylic acids and that PSS-*co*-MA was fully ionized to provide a maximum charge density before centrifugation. Excess ConA was removed by centrifugation twice in a swinging bucket centrifuge at 1000 RCF for 30 min, resuspending in 50 mM pH 8 $NaHCO_3$ the first time and assay buffer the second time.

5.3.6. NTA

NP size and size distribution was obtained with the NanoSight LM10HS with a 65 mW 405 nm source. Video was acquired with a Hamamatsu C11440 digital camera and analysis was completed with included NanoSight 2.3 software with automatic settings. $AuNR_{CTAB}$ samples were sized in 1mM CTAB in DI-H_2O. $AuNR_{CTAB}$-PSS-*co*-MA 1:1 and $AuNR_{CTAB}$-PSS-*co*-MA 1:1-ConA were sized in 50 mM HEPES pH 7.4.

5.3.7. DLS and Microelectrophoresis

Dynamic light scattering (DLS) and zeta potential were measured using a ZetaSizer Nano Series ZEN 3600 spectrometer (Malvern). For zeta potential measurements AuNRs (0.1 nM) were dispersed in ultrapure water in a DT1070 cuvette and measured 5 times. DLS measurements of OVA and OVA-AuNCs were measured at 1 mg/mL in a 1 cm x 1 cm plastic cuvette (Malvern).

5.3.8. PL Characterization of OVA-AuNCs

Excitation and emission curves were collected on an ISS PC1 spectrophotometer with a xenon arc lamp with 1 mm entrance slits, 1 mm exit slits and a 550 nm long-pass filter. Photo-stability was measured every 60 s on a sample under constant illumination while being stirred in a cuvette with 2 mm entrance slits and 0.5 mm exit slits. For OVA-AuNC the excitation was 400 nm or 550nm, and emission was 650 nm, with a 550 nm long pass filter. For OVA-FITC the excitation was 460 nm and the emission was 518 nm.

5.3.9. Glucose Assay

A stock solution of AuNR-ConA with OVA-AuNC was prepared at a 2x concentration in assay buffer and 100 μL was dispensed into each well of a black flat bottom 96-well microplate. Glucose solutions were prepared at a 2x concentration in assay buffer at least 24 h in advance. The final concentration of 0.1 nM $AuNR_{CTAB}$-PSS-*co*-MA 1:1-ConA (determined by NTA) and 5.575 μM OVA-AuNCs (determined by absorbance) was mixed with 100 μL of glucose solution (200 μL final volume). The reaction was incubated for 20 min in the dark before interrogation.

Fluorescence measurements were made with a Tecan Infinite M200 PRO with i-Control 1.8 software. Samples were placed in a black 96-well flat bottom plate and data was collected with excitation at 340 nm or 400 nm (bandwidth of 9 nm) and emission from 500 – 850 nm (bandwidth of 20 nm) at 5 nm increments, integration time was 100 μs with 0 s lag time, 25 flashes with 0 s settling time.

5.3.10. UV-Vis

Absorbance spectra were obtained on a Cary 300 UV-Vis spectrophotometer (Agilent) with a 6x6 multi-cell Peltier block (Agilent). Measurements were acquired at 300 nm/min, 0.5 nm resolution, and 0.1 s integration time. Samples were measured in a BrandTech semi-micro UV-cuvette baseline corrected with a cuvette filled with the same buffer that the sample was prepared with.

5.3.11. TEM

A 10 μL portion of the AuNR stock solution for analysis was dropped onto a commercially-available carbon film coated-300 square mesh copper grid (CF-300 Cu,

Electron Microscopy Sciences, Hatfield, PA) followed by 24 h of atmosphere drying. The AuNRs and OVA-AuNCs were examined by TEM (HF3300, Hitachi Scientific Instruments, Tokyo, Japan) operated at 300 kV with a cold field emission gun (FEG).

5.4. Results and Discussion

5.4.1. Synthesis and Characterization of $AuNR_{CTAB}$-PSS-*co*-MA 1:1-ConA

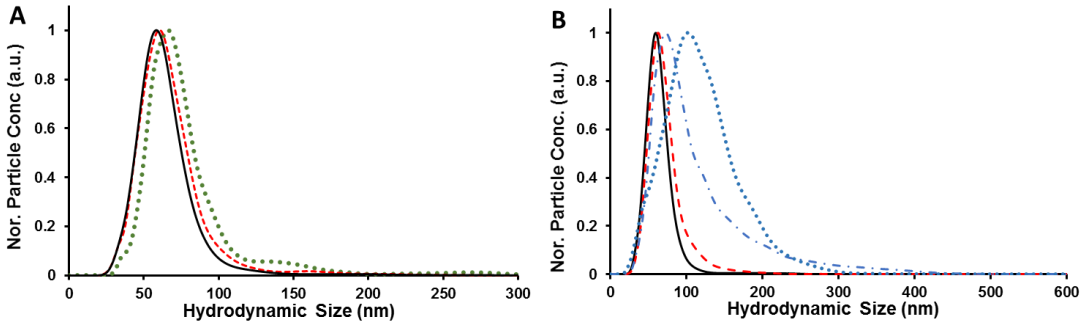

Figure 5.2: (A) NTA of PSS-*co*-MA coated AuNRs when using $AuNR_{CTAB}$ (black −) as a source containing 3 mM excess CTAB (red − −) and 1 mM CTAB (black −). (B) NTA of $AuNR_{CTAB}$ (black −) $AuNR_{CTAB}$-PSS-*co*-MA 1:1 (red ••) and $AuNR_{CTAB}$-PSS-*co*-MA 1:1-ConA (blue − −).

The AuNR was modified with PSS-*co*-MA to introduce carboxyl groups that could be used for bioconjugation. The size increase of the AuNR after modification with PSS-*co*-MA 1:1 and conjugation with ConA was studied using NTA. The CTAB modified AuNRs suspended in 1 mM CTAB had a peak size of 57.55 nm, without any notable aggregation (Figure 5.2A). The positively charged $AuNR_{CTAB}$ in 1 mM were mixed with negatively charged PSS-*co*-MA 1:1 which resulted in a 3.7 nm size increase in the peak size to 61.22 nm, with no aggregation (Figure 5.2A). The $AuNR_{CTAB}$ stock contains 3 mM CTAB that was diluted to 1 mM CTAB before adding the PSS-*co*-MA 1:1. If the PSS-*co*-MA 1:1 was added to the $AuNR_{CTAB}$ containing 3 mM CTAB a size

increase of 8.45 nm occurs and a secondary peak indicating minor aggregation appears (Figure 5.2A). The application of the final product for an energy transfer sensor requires a minimum hydrodynamic size to minimize donor and acceptor distances. It should also be noted that decreasing the CTAB concentration below 1 mM leads to aggregation of the $AuNR_{CTAB}$ before modification can be attempted (data now shown).

The PSS-*co*-MA coated AuNRs now contain surface carboxylic acid groups that can be used for bioconjugation to ConA. The ConA was conjugated to the $AuNR_{CTAB}$-PSS-*co*-MA 1:1 using EDC/NHS in a two-step procedure. The carboxylic acid groups on $AuNR_{CTAB}$-PSS-*co*-MA 1:1 were activated with EDC/NHS for 20 min and followed by removal of excess EDC/NHS by centrifugation. The excess EDC/NHS was removed before adding the ConA to prevent any interprotein cross-linking since ConA contains both carboxylic acid and amine groups. The activated AuNRs were then added to ConA solution that had been filtered with a 0.2 μm syringe filter. After an incubation period under stirring to allow for conjugation, the excess ConA was removed by low speed centrifugation.

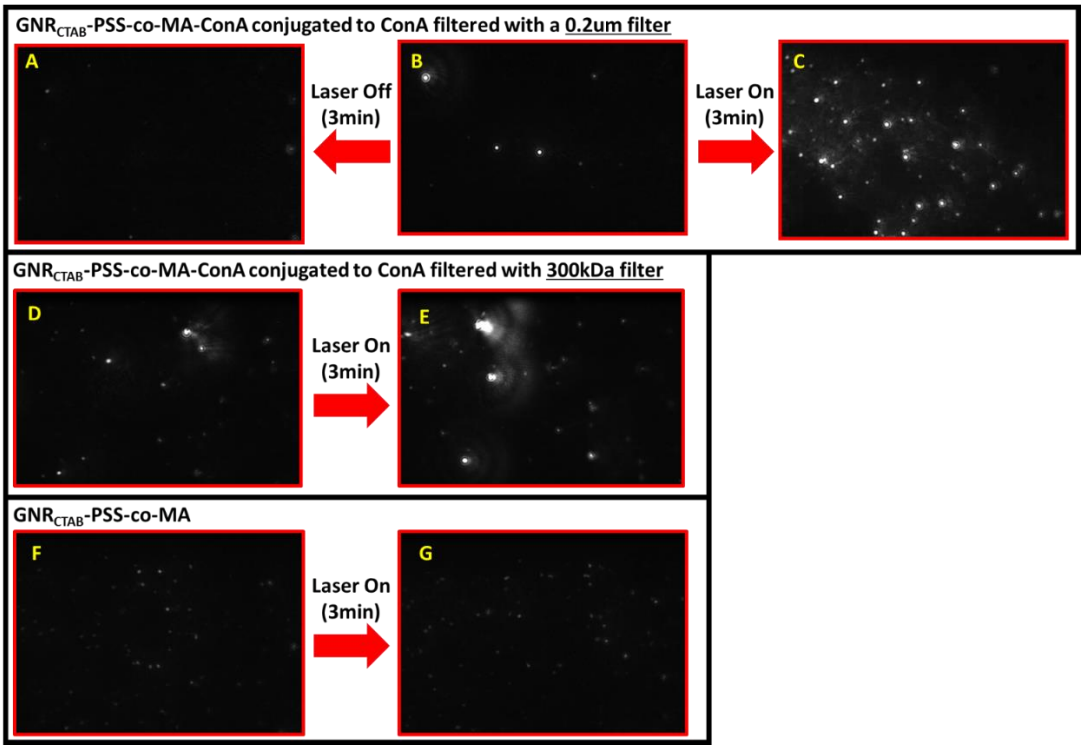

Figure 5.3: NTA images of raw video captured during measurement for AuNR$_{CTAB}$-PSS-*co*-MA 1:1-ConA conjugated with ConA filtered through a 0.2 µm filter (B) at time 0, (A) after 3 min with the laser off, and (C) after 3 min with the laser constantly on. AuNR$_{CTAB}$-PSS-*co*-MA 1:1-ConA conjugated with ConA filtered through a 300 kDa filter (D) at time 0 and (E) after 3 min with the laser constantly on. AuNR$_{CTAB}$-PSS-*co*-MA 1:1 (A) at time 0 and (B) after 3 min of the laser constantly on.

NTA analysis of the AuNR$_{CTAB}$-PSS-*co*-MA 1:1-ConA conjugate showed a substantial size increase to 102.7 nm (Figure 5.2B). The quality of this data was questioned because the video of the analysis showed an increase in NP concentration and an increase in NP size over time. Snapshots of the video were taken immediately after the laser was turned on and then after 3 min of laser exposure. These images showed a very large visual increase in apparent NP concentration (Figure 5.3A-C). If the sample was kept in the NTA testing chamber for 3 min without laser exposure, no increase in NP concentration was observed (Figure 5.3A-C). This indicates that the aggregation that

was occurring over this time frame was a result of laser exposure. Additionally, this phenomenon was not observed for $AuNR_{CTAB}$-PSS-*co*-MA 1:1 (Figure 5.3F, Figure 5.3G). We postulated that this may have been occurring due to the presence of ConA aggregates either conjugated to the AuNR or still in free solution. The low speed centrifugation used to remove excess unconjugated ConA would remove stable non-aggregated ConA, but may still retain the less colloidally stable, aggregated clumps of ConA. Using a 0.2 μm filter removes the very large aggregates but would be less effective in removing smaller aggregates. To remedy this, an additional filtering step using a 300 kDa filter was introduced to remove anything larger than a single ConA (104 kDa). Using 300 kDa filtered ConA for conjugation yielded a $AuNR_{CTAB}$-PSS-*co*-MA 1:1-ConA with a more reasonable 72.33 nm peak size, without the presence of any higher order aggregation (Figure 5.2B). Additionally, the increasing concentration and size with time was no longer observed (Figure 5.3D, Figure 5.3E), allowing for more accurate quantitation of $AuNR_{CTAB}$-PSS-*co*-MA 1:1-ConA concentration.

The effect of the EDC/NHS on NP size was investigated using NTA. The activation of surface carboxylic acid moieties by the addition of EDC reduces the surface charge and increases the hydrophobicity. Adding sulfo-NHS improves the hydrophilicity of the NP and increases the surface charge to enhance the stability. The sulfo-NHS also extends the half-life of the ester at higher pH to improve amine coupling efficiency. However, the activation of the NP even with sulfo-NHS introduces some instability to the NP. This becomes especially apparent when centrifuging the NPs to remove the excess EDC/NHS before adding the biomolecule to be conjugated. The use

of PSS-*co*-MA 1:1 was expected to improve the stability after EDC/NHS activation because even though the carboxylic acid groups were activated, the sulfonate groups remain fully charged to enhance electrostatic stability.

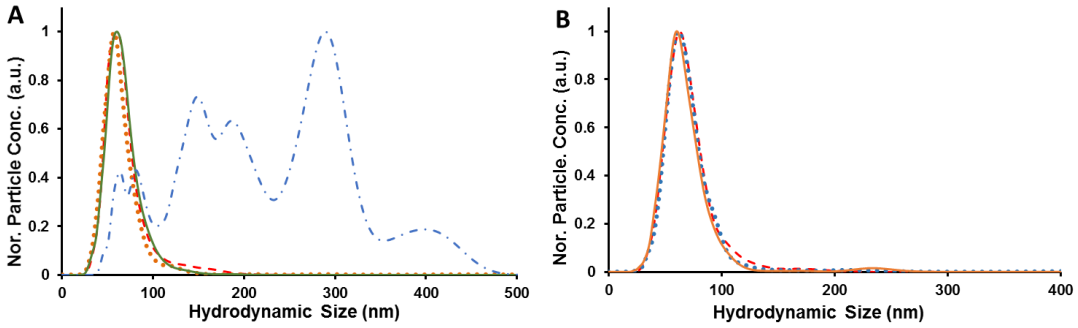

Figure 5.4: (A) NTA and for AuNR$_{CTAB}$-PSS-*co*-MA 1:1(red − −) after activation at pH 6 with EDC/NHS (green −) or after activation at pH 7 with EDC/NHS (orange ••). ConA only mixed with EDC/NHS at pH 7 (blue − • −). (B) The non-specific adsorption determined from NTA for AuNR$_{CTAB}$-PSS-*co*-MA 1:1 (red − −) after mixing with ConA (blue ••) or OVA-AuNC (orange −) without any EDC/NHS activation.

To test this stability, the AuNR$_{CTAB}$-PSS-*co*-MA 1:1 were activated with EDC/NHS, the excess EDC/NHS was removed by centrifugation, but no ConA was added to allow the activated carboxylic acid groups to regenerate. NTA analysis of the AuNR$_{CTAB}$-PSS-*co*-MA 1:1 activated at either pH 6 or pH 7 does not cause any appreciable change in peak size or increase in aggregation (Figure 5.4A). This shows that the PSS-*co*-MA 1:1 coating was providing a stable coating against aggregation using the two-step EDC/NHS activation and conjugation. The importance of being able to use the two-step method was observed when EDC/NHS was directly added to ConA resulting in strong inter-protein aggregation (Figure 5.4A).

The non-specific adsorption of ConA onto $AuNR_{CTAB}$-PSS-*co*-MA 1:1 was investigated with NTA to determine if non-specific adsorption contributes to a NP size increase. From NTA it was apparent that excess ConA does not adsorb to the $AuNR_{CTAB}$-PSS-*co*-MA 1:1 that has not been treated with EDC/NHS since no size change was observed and no aggregation occurred (Figure 5.4B). This shows that the size increase observed when ConA was conjugated to $AuNR_{CTAB}$-PSS-*co*-MA 1:1 was mostly like due to conjugation, and not aggregation or non-specific adsorption. The non-specific adsorption of OVA-AuNC onto $AuNR_{CTAB}$-PSS-*co*-MA 1:1 was also tested and showed no size increase or substantial aggregation (Figure 5.4B). This was important to make sure that any quenching that occurred was due to conjugation between OVA-AuNC and $AuNR_{CTAB}$-PSS-*co*-MA 1:1-ConA and was not the non-specific adsorption of OVA-AuNC directly to the $AuNR_{CTAB}$-PSS-*co*-MA 1:1 surface.

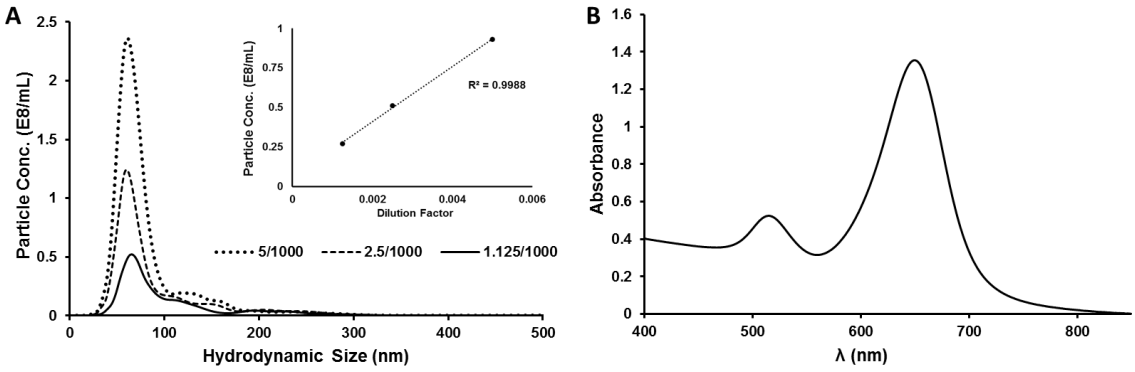

Figure 5.5: Comparison of $AuNR_{CTAB}$ concentration determined from (A) NTA three point calibration curve and (B) from UV-Vis spectra and extinction given by manufacturer.

$AuNR_{CTAB}$-PSS-*co*-MA 1:1 concentration obtained from NTA was compared to concentration obtained from UV-Vis. To verify that NTA results were reliable, a three

point calibration of three dilutions of the same sample was obtained (Figure 5.5A). The sample was diluted by a factor of ½ each time and size was measured at maximum camera gain and shutter speed until < 5 NPs were observed on screen. The three point calibration was then taken at the three dilutions above this. This was done to ensure that there were no hidden NPs not being counted. If concentration of the sample becomes too high, then NPs become hidden in the scattered light leading to inaccurate concentration measurements and non-linear calibration curves. This inaccuracies are magnified due to the large initial dilution factor required for measurement (≈ 1/1000 - 1/5000 for AuNRs). The calibration curve was very accurate for these three points (R^2 = 0.99), giving a stock concentration of 0.34 ± 0.02 nM; the standard deviation was calculated from the variation in the three different dilutions. UV-Vis is the standard method used for determining the concentration of metallic NPs, but the accuracy depends on the estimation of extinction based either on the size (from spectra or TEM) or in this case the value provided by the manufacturer. From the UV-Vis spectra (Figure 5.5B) a concentration of 0.2 nM was calculated from the SPR peak absorbance; this gives a 1.71 factor of difference between UV-Vis and NTA. This difference may be due to the fact that the PSS-*co*-MA 1:1 modification of the AuNRs was affecting the optical properties of the AuNRs enough to skew the concentration calculation that was based off the extinction provided for the bare $AuNR_{CTAB}$.

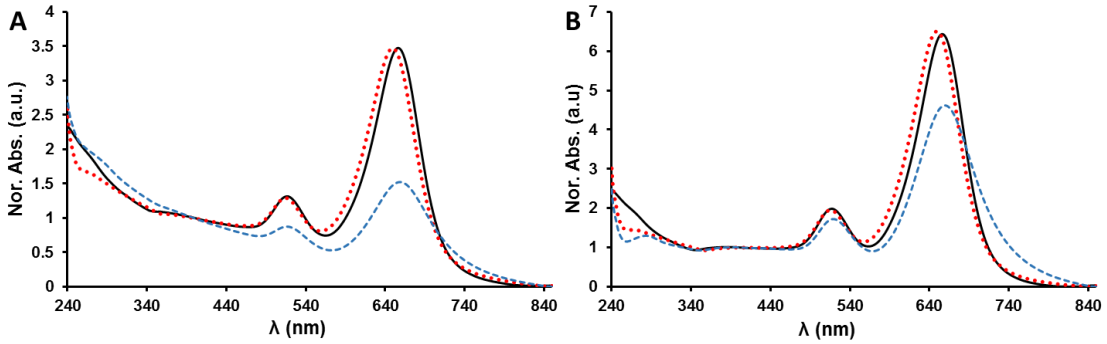

Figure 5.6: (A) Raw data and (B) scatter corrected UV-Vis for $AuNR_{CTAB}$ (black −) $AuNR_{CTAB}$-PSS-*co*-MA 1:1 (red ••) and $AuNR_{CTAB}$-PSS-*co*-MA 1:1-ConA (blue − −).

UV-Vis absorbance of the $AuNR_{CTAB}$, $AuNR_{CTAB}$-PSS-*co*-MA 1:1, and $AuNR_{CTAB}$-PSS-*co*-MA 1:1-ConA shows the spectral change at each step. Figure 5.6A shows the raw absorbance data normalized to the absorbance at 400 nm while Figure 5.6B shows the scatter corrected absorbance normalized at 400 nm. The scatter correction was obtained by a power fit from 340 – 440 nm, the portion of the spectra that should have minimal contribution from the SPR, LSPR, PSS-*co*-MA 1:1 or ConA absorbance. The scatter corrected data was used for further analysis.

For $AuNR_{CTAB}$ the LSPR peak was located at 516nm and the SPR peak was located at 655.7 nm. After modification with PSS-*co*-MA the LSPR peak moves to 515 nm and the SPR peak moves to 649 nm. After conjugation to ConA, the LSPR peak shifts to 518.5 nm and the SPR peak shifts to 659 nm. These peak shifts in both the SPR and LSPR are caused by the small changes in the local refractive index, indicative of modification without aggregation. Additionally, the FWHM of the SPR peak increases by 3 nm after PSS-*co*-MA 1:1 modification and 24 nm after ConA conjugation. This broadening is a typical feature of modified NPs. There are no secondary peaks observed

in the spectra measured to indicate the presence of any aggregation. The absorbance spectra provides an additional confirmation of the AuNR modification without aggregation and also shows how optical properties of the AuNR are affected by this modification.

5.4.2. Buffer Stability of $AuNR_{CTAB}$-PSS-*co*-MA 1:1

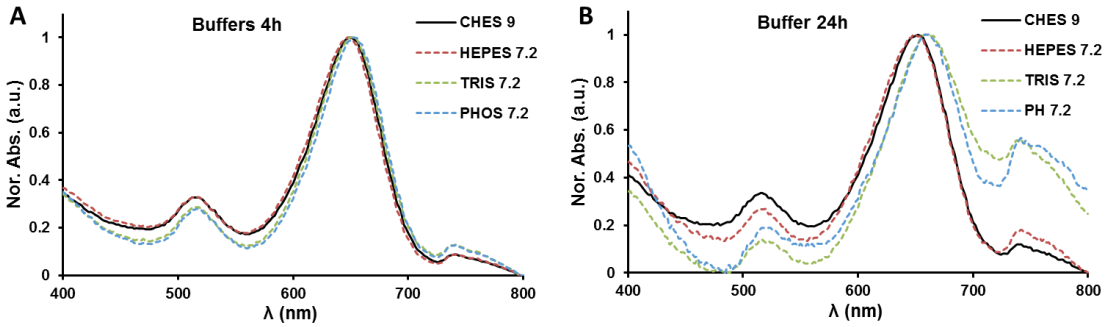

Figure 5.7: UV-Vis for $AuNR_{CTAB}$-PSS-*co*-MA 1:1 when incubated in 50 mM TRIS pH 7.2 (green ——), 50 mM phosphate buffer pH 7.2 (blue – –), 50 mM HEPES pH 7.2 (red – –) and 50 mM CHES pH 9 (black –) after for (A) 4 h and (B) 24 h.

The stability of $AuNR_{CTAB}$-PSS-*co*-MA 1:1 was investigated by suspending in HEPES, TRIS or PHOS buffer at pH 7.2 or CHES buffer at pH 9. After 4 h of incubation, no change in UV-Vis spectra was observed (Figure 5.7A). After 24 h, aggregation was observed for TRIS and PHOS buffer samples indicated by the growth of the secondary peak, while the HEPES and CHES buffer samples remained unchanged (Figure 5.7B). This suggests that the TRIS and PHOS buffers contain ions that are inducing aggregation through some sort of interaction with the gold surface. This was not expected as typically LbL modified nanomaterials exhibit a high degree of stability in different buffers. However, the LbL on AuNRs may only be coating the longitudinal

side of the AuNR, leaving the transverse side unprotected. This may leave the AuNR susceptible to ionic interaction that leads to aggregation.

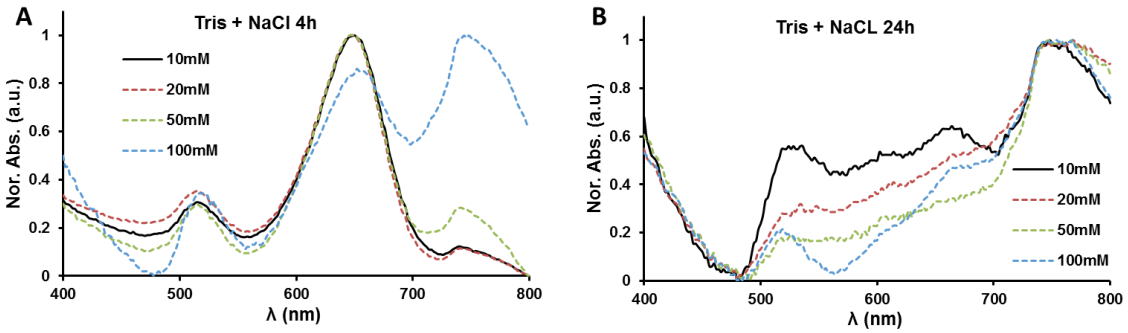

Figure 5.8: UV-Vis for AuNR$_{CTAB}$-PSS-*co*-MA 1:1 when incubated in 50 mM TRIS buffer with 10 mM NaCl (black −), 20 mM NaCl (red − −), 50 mM (green − −), 100 mM NaCl (blue − −) for (A) 4 h and (B) 24 h.

Protein stability is improved by including NaCl in the buffer, typically a TRIS or PHOS based saline solution. Accordingly, the stability of the AuNRCTAB-PSS-*co*-MA 1:1 was investigated under varying ionic strength conditions in TRIS buffer. After 4 h the 10 mM and 20 mM samples remain stable while the 50 mM and 100 mM shows signs of aggregation (Figure 5.8A). After 24 h, all samples had completely aggregated (Figure 5.8B).

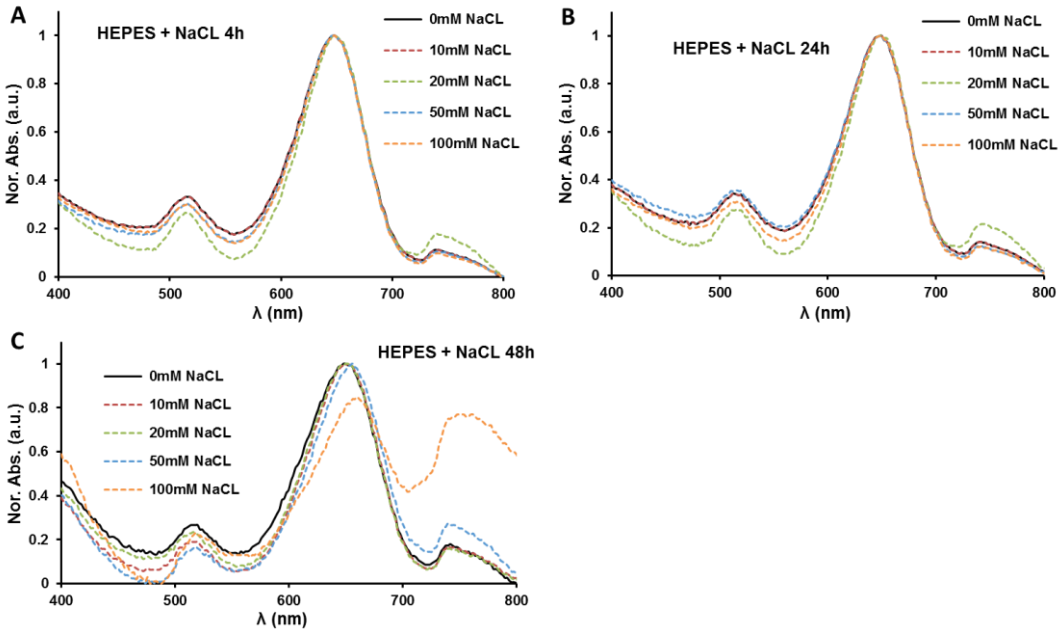

Figure 5.9: UV-Vis for AuNR$_{CTAB}$-PSS-*co*-MA 1:1 when incubated in 50 mM HEPES buffer pH 7.2 with 0 mM NaCl (black −), 10 mM NaCl (red − −), 20 mM (green − −), 50 mM NaCl (blue − −), and 100 mM NaCl (orange − −) for (A) 4 h, (B) 24 h, and (C) 48 h.

The aggregation effect of TRIS on the AuNRs was possibly due to the affinity of the amines for the metal ions of the unprotected AuNR surface. Therefore, HEPES was investigated as an alternative buffer since it does not contain metal chelating ions. After 4 h (Figure 5.9A) and 24 h (Figure 5.9B) there was no aggregation present even up to 100 mM NaCl and after 48 h (Figure 5.9C) aggregation was observed for the 100 mM NaCl only. Using HEPES buffer instead of TRIS allows using up to 50 mM NaCl for 48 h, without inducing aggregation.

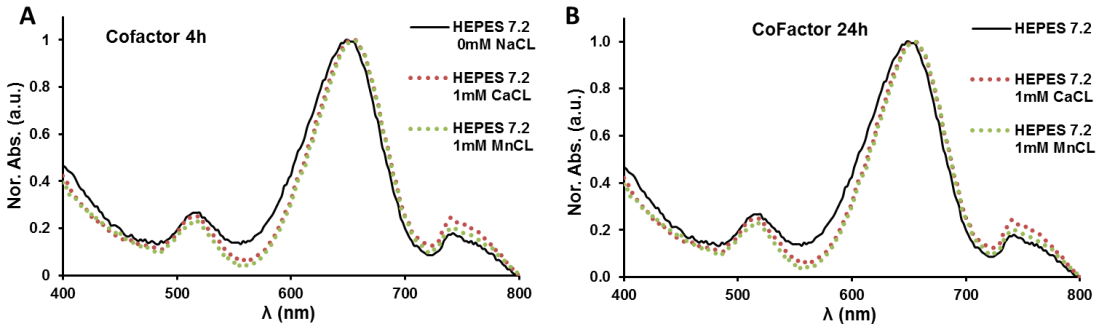

Figure 5.10: UV-Vis for AuNR$_{CTAB}$-PSS-*co*-MA 1:1 when incubated in 50 mM HEPES buffer pH 7.2 only (black −) and with added 1 mM $CaCl_2$ (red − −) or 1 mM $MnCl_2$ (green − −) for (A) 4 h and (B) 24 h.

ConA requires calcium and manganese as cofactors in order to bind carbohydrates. Therefore, the stability of AuNR$_{CTAB}$-PSS-*co*-MA 1:1 was tested in the presence of the typical concentrations used for ConA binding (1 mM $CaCl_2$ and 1 mM $MnCl_2$). After 4 h (Figure 5.10A) and 24 h (Figure 5.10B) no change in the absorbance spectra indicating aggregation was observed. Based on these results, HEPES was used for AuNR buffer solutions.

5.4.3. OVA-AuNC Synthesis and Characterization

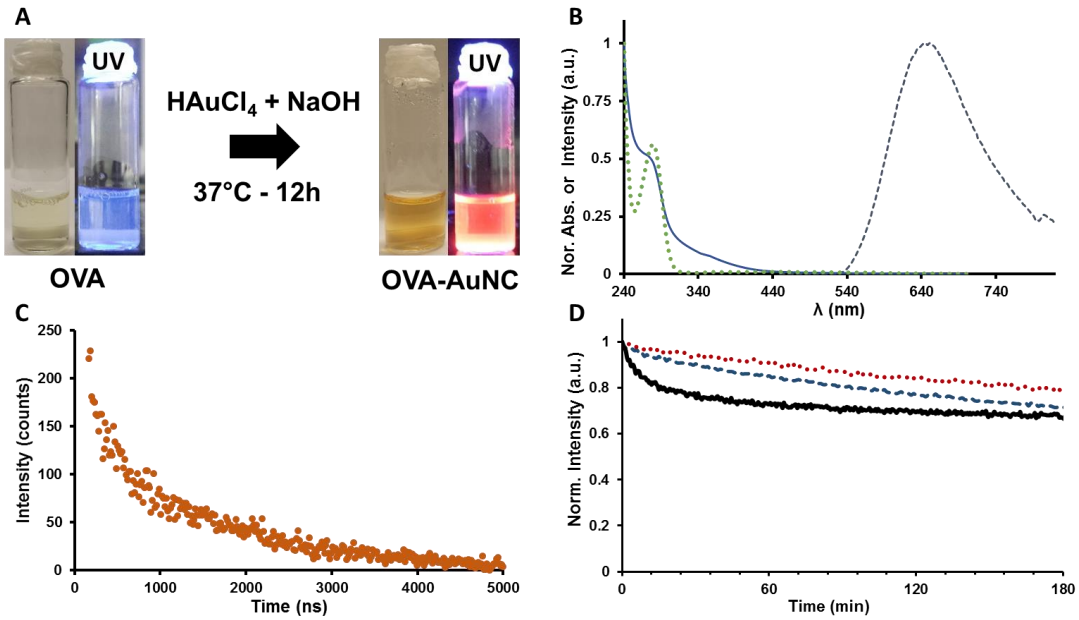

Figure 5.11: (A) Photographs under visible and UV light of OVA with $HAuCL_4$ in water initially and after incubation at 37°C 12 h to grow the AuNCs. (B) Normalized absorption of OVA (green ••) and OVA-AuNC (blue −) and PL emission of OVA-AuNC (green − −) excited at 400 nm. (C) PL lifetime decay of OVA-AuNC (orange ●) excited at 405 nm with an emission gathered at 650 nm. (D) PL intensity decay while stirring under constant xenon arc lamp exposure at Exc/Emi of 400/650 nm for OVA-AuNC (red ●), 500/650 nm for OVA-AuNC (black −), and 460/514 nm for OVB-FITC (blue − −).

The OVA-AuNC growth can be confirmed both visually (Figure 5.11B) and spectroscopically (Figure 5.11A). Initially, the OVA and $HAuCL_4$ mixture is a hazy yellow and no red emission observed under UV (Figure 5.11A). After incubation at 37°C for 12 h, the solution turned an orange-brown color and a under UV a red emission was observed (Figure 5.11A). UV-Vis shows the color change as an increase in scattering but no distinct absorbance peaks are observed. When excited at 400 nm, the OVA-AuNC exhibit a maximum intensity at about 650 nm, within the range of emission

reported by others (640 – 720 nm).[272-274, 277] The PL lifetime decay was measured as 1.4 μs, which was consistent with that reported by Yoshimoto *et al* (Figure 5.11C).[272] However, obtaining sufficient intensity for lifetime regression analysis required using a 10 mg/mL OVA-AuNC solution, ruling out lifetime as a potential measurement technique for studying energy transfer. The photobleaching rate of the OVA-AuNC excited at 400 nm was compared to the commonly used FITC dye (conjugated to OVA) excited at 460 nm (Figure 5.11D). Under constant exposure of a xenon arc lamp with constant stirring the OVA-AuNC PL decayed 21% and 33% after 3 h when excited at 400 nm and 550 nm respectively. For comparison, OVA-FITC decays in intensity by 29% over the same time period when excited at 460 nm. This rapid photobleaching of OVA-AuNCs was a surprising finding considering that AuNCs are considered photostable materials. To our knowledge, the photo-stability of protein encapsulated AuNCs has not been reported for OVA or BSA and therefore it is not clear whether this instability is due to our synthesis technique or if it is applicable to the whole class of NCs.

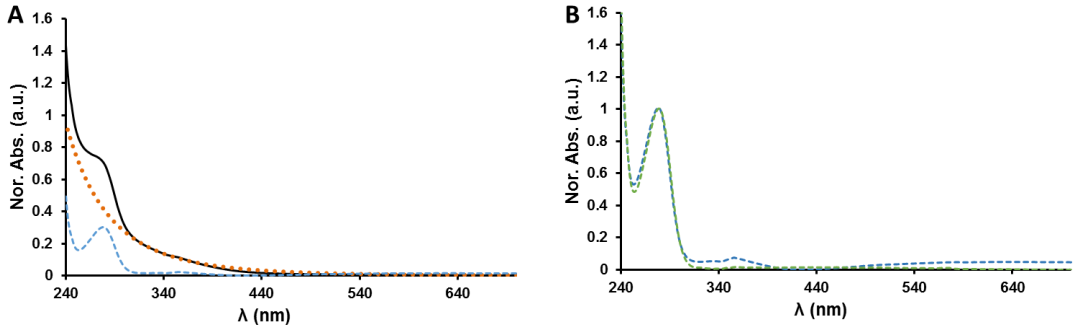

Figure 5.12: (A) OVA-AuNCs absorbance (black −), power fit of scattering (orange •), corrected absorbance of OVA-AuNCs after removing the scattering component (blue − −). (B) Comparison between the absorbance spectra of OVA-AuNC after scattering correction and the absorbance spectra of OVA.

The growth of the AuNC in the OVA introduces scattering into the absorbance spectra that prevents accurate determination of concentration from UV-Vis (Figure 5.12A). The concentration of OVA-AuNCs immediately after synthesis should be close to 25 mg/mL, but from absorbance the concentration was 69.55 mg/mL. To obtain a more accurate measurement of concentration the scattering component of the OVA-AuNC absorbance was removed by subtraction of a power fit (Figure 5.12A). The obtained corrected spectra of the OVA-AuNC looks nearly identical to that of OVA and the concentration obtained from this corrected spectra gives a concentration of 24.63 mg/mL (Figure 5.12B). Accurate quantitation of OVA-AuNC is critical for rational design of a competitive binding assay.

5.4.4. OVA-AuNC Purification

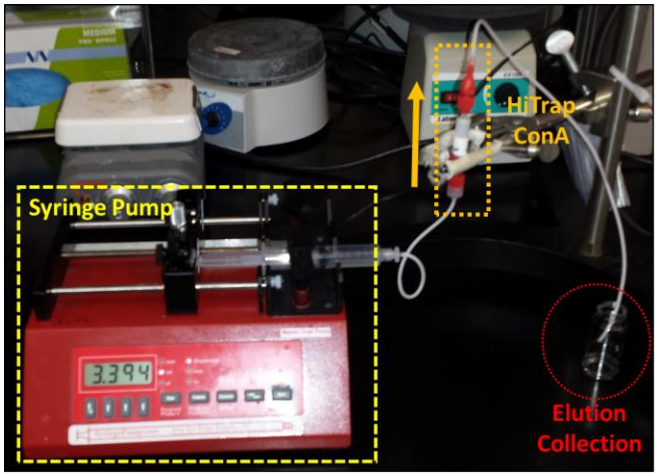

Figure 5.13: Setup of OVA-AuNC purification using a HiTrap ConA column and a syringe pump.

Not all of OVA contains glycosylation sites are capable of binding to ConA and the AuNC may further denature or interfere with ConA binding to these sites. OVA-AuNCs that are not capable of binding to ConA will increase the background luminescence signal present and will introduce batch to batch variation. OVA-AuNCs still capable of binding to ConA were retained by purification with a HiTrap ConA column. Using a syringe pump the OVA-AuNCs were flowed slowly through the HiTrap ConA column (Figure 5.13A). It was important to avoid the introduction of bubbles into the column and the column was kept vertical to prevent bubbles from collecting in the column (Figure 5.13A). The OVA-AuNC fraction that did not bind to the column was discarded. The OVA-AuNCs that were bound to the column were then eluted with excess mannose and collected. The excess mannose was then removed by five rounds of filtration using a 3 kDa filter.

Table 5.1: DLS measurements of size by number for OVA before and after purification and OVA-AuNC before and after purification. Percent recovery of OVA and OVA-AuNC through purification process. Error represents 95% confidence interval (n = 3).

	OVA	OVA Purified	OVA-AuNC	OVA-AuNC Purified
Size by Number (nm)	5.2 ± 0.8	5.0 ± 0.2	7.7 ± 0.5	8.1 ± 0.5
Percent Recovery (%)	49.1 ± 3.5		14.6 ± 2.7	

The size of OVA and OVA-AuNC throughout this process was investigated by DLS to determine how AuNC growth, purification, and filtration affected the protein size (Table 5.1). OVA that was initially dissolved in binding buffer and filtered with a 0.2 μm syringe filter was found to be 5.22 nm by number. After purification and filtration steps, OVA now suspended in storage buffer maintained a similar size of 5 nm by number. The percent recovery of OVA throughout the purification and filtration steps was 49.12%. We suspect that the lost OVA was either unable to bind to the column because they did not contain glycosylation sites or the column binding sites became saturated. The growth of the AuNC increased the size of the OVA-AuNC to 7.68 nm initially and after purification the size increased slightly to 8.08 nm. This showed that the growth of the AuNC and purification of the OVA-AuNC complex can be achieved with only a small size increase and no significant aggregation. However, the percent recovery of the OVA-AuNC was found to be only 14.63% indicating that the growth of the AuNC or the conditions for growth have somehow compromised some of the OVA-AuNCs ability to bind to the column. Without this purification step ≈85% of the OVA-AuNC population would not be capable of binding ConA and would only

increase the background signal of the sensor. Therefore, the purification is a critical step for preparing the OVA-AuNCs as photoluminescent probes based on their binding capability.

5.4.5. TEM

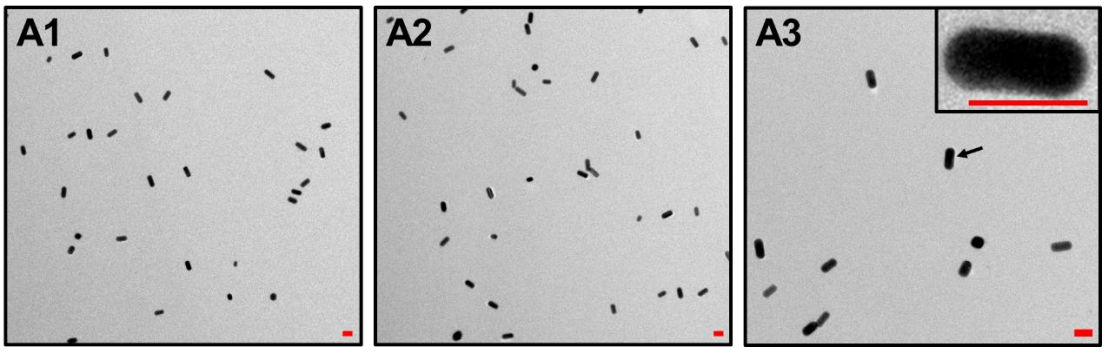

Figure 5.14: (A1-A3) TEM images of AuNR$_{CTAB}$-PSS-*co*-MA 1:1. Inset is digitally zoomed images of the AuNR indicated by black arrow. Scale bars are 50 nm.

TEM micrographs were obtained for AuNR$_{CTAB}$-PSS-*co*-MA 1:1, AuNR$_{CTAB}$-PSS-*co*-MA 1:1-ConA, and AuNR$_{CTAB}$-PSS-*co*-MA 1:1 with added OVA-AuNC. The AuNR$_{CTAB}$-PSS-*co*-MA 1:1 images (Figure 5.14) showed that the majority of the NPs viewed had a rod like shape, with no evidence of significant aggregation.

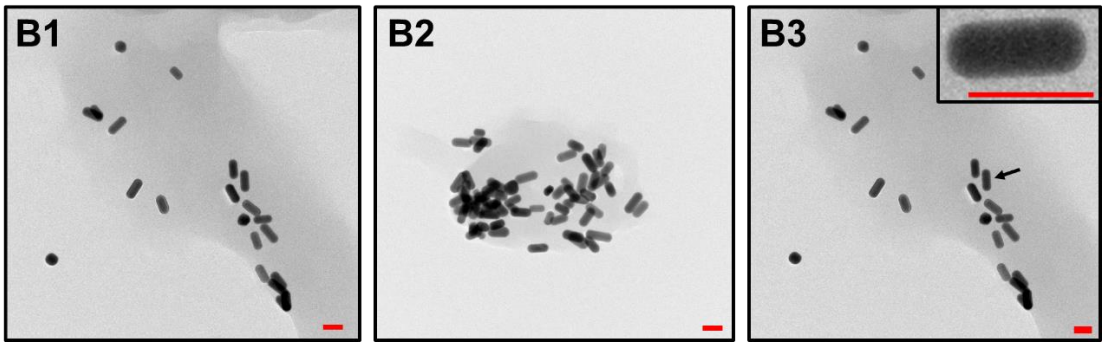

Figure 5.15: (B1-B3) TEM images of AuNR$_{CTAB}$-PSS-*co*-MA 1:1-ConA. Inset is digitally zoomed images of the AuNR indicated by black arrow. Scale bars are 50 nm.

TEM of the AuNR$_{CTAB}$-PSS-*co*-MA 1:1-ConA showed some agglomeration but this commonly occurs during the sample preparation (Figure 5.15). It was not possible to visualize the ConA on the AuNR surface.

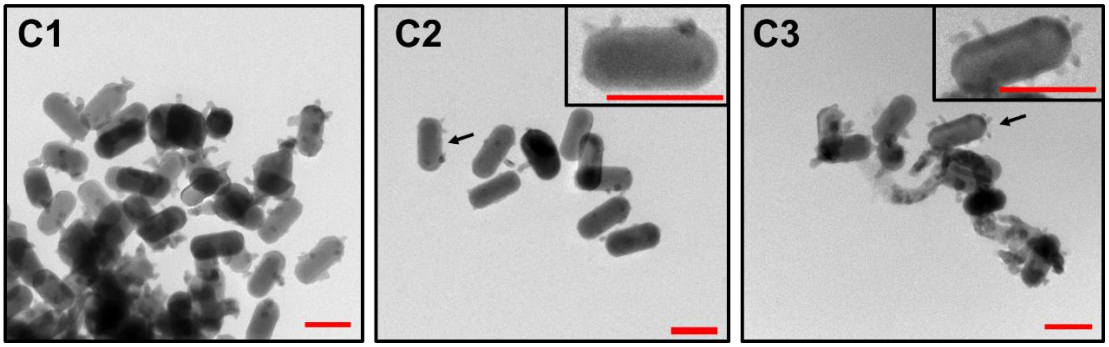

Figure 5.16: (C1-C3) TEM images of AuNR$_{CTAB}$-PSS-*co*-MA 1:1-ConA with OVA-AuNCs. Inset is digitally zoomed images of AuNR indicated by black arrow. Scale bars are 50 nm.

TEM of AuNR$_{CTAB}$-PSS-*co*-MA 1:1 after mixing with OVA-AuNCs is shown in Figure 5.16. The presence of OVA-AuNCs can easily visualized on the surface of the AuNRs. The majority of the OVA-AuNCs are attached to the longitudinal side of the

AuNR but there are a few OVA-AuNCs that appear to be on the transverse side (Figure 5.16C2 inset, Figure 5.16C3 inset).

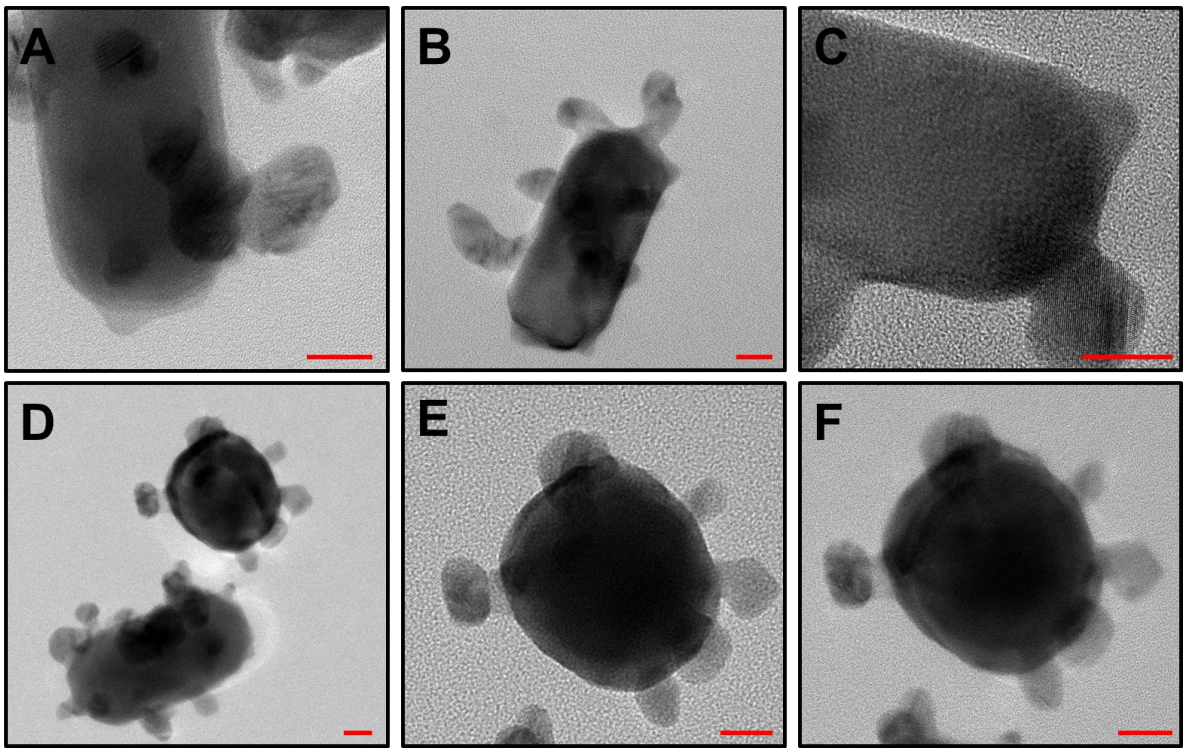

Figure 5.17: High resolution TEM images of AuNR$_{CTAB}$-PSS-*co*-MA 1:1-ConA with OVA-AuNCs. Scale bars are 10 nm.

High resolution TEM images show the OVA-AuNC attached to the AuNR surface more clearly (Figure 5.17) The diameter of the NCs attached to the AuNR range from 5 – 13 nm, which is larger than the 2 – 5 nm size reported for these protein encapsulated NCs.[271, 273] The larger apparent size of the NCs could be attributed to multiple OVA-AuNCs being bound to the same to a single ConA attached to the AuNR surface. The average distance between the edge of the AuNR and the end of the OVA-

AuNC is 8.5 ± 2.5 nm (n = 27). This close distance between the acceptor AuNR and the AuNC donor is essential for the quenching process to occur.

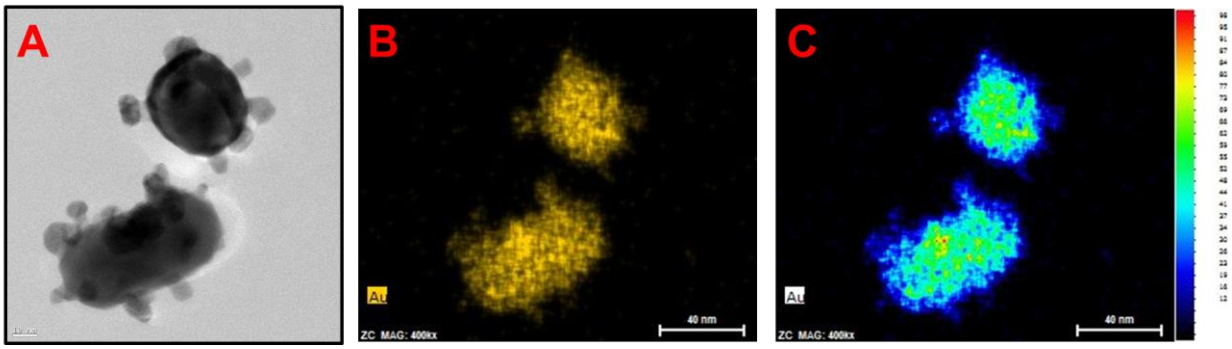

Figure 5.18: High resolution TEM and EDS images of AuNR$_{CTAB}$-PSS-*co*-MA 1:1-ConA with OVA-AuNCs.

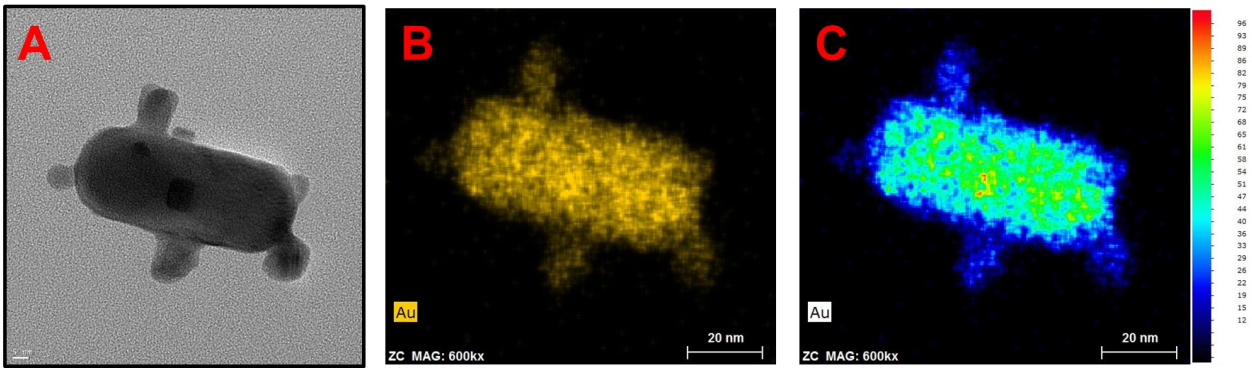

Figure 5.19: High resolution TEM and EDS images of AuNR$_{CTAB}$-PSS-*co*-MA 1:1-ConA with OVA-AuNCs.

EDS was used to show the presence of Au to confirm that the spots attached to the AuNR surface were in fact AuNCs (Figure 5.18, Figure 5.19).

5.4.6. Glucose Response of $AuNR_{CTAB}$-PSS-*co*-MA 1:1-ConA and OVA-AuNC Assay

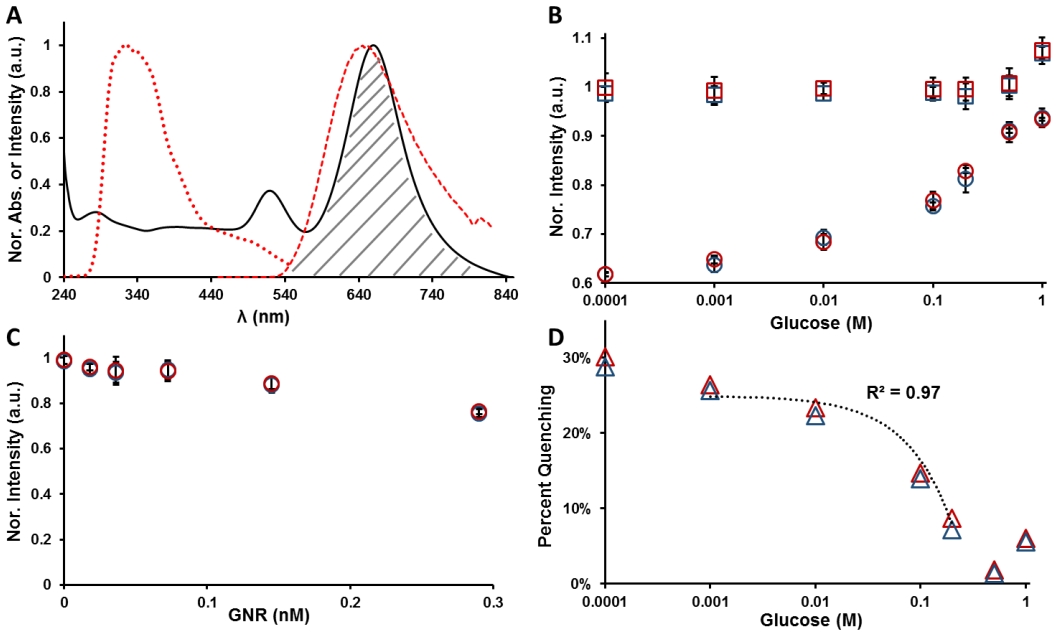

Figure 5.20: Spectral overlap between sensor components. (A) Absorbance of $AuNR_{CTAB}$-PSS-*co*-MA 1:1-ConA (black −), excitation (red ••) and emission (red − −) spectra of OVA-AuNC. The grey diagonal lines indicate the overlap integral. (B) Glucose response of OVA-AuNCs mixed with $AuNR_{CTAB}$-PSS-*co*-MA 1:1-ConA (○) and for OVA-AuNC only (□) when excited at 340 nm (red ○ or □) or 400 nm (blue ○ or □). Data is normalized to the intensity of OVA-AuNCs only at the same concentration. (C) Inner filter effect for increasing concentrations of $AuNR_{CTAB}$-PSS-*co*-MA 1:1 added to OVA-AuNCs when excited at 340 nm (red ○) or 400 nm (blue ○). (D) Percent change in quenching as glucose increases after correcting for static quenching of $AuNR_{CTAB}$-PSS-*co*-MA 1:1 and the effect of glucose directly on OVA-AuNCs. Linear fit (black −) between 1 mM and 200 mM with an R^2 value of 0.97.

The excitation and emission spectra of OVA-AuNC was shown in Figure 5.20A with a view peak excitation at 340nm and peak emission at 650 nm. The excitation maximum in the UV region is attributed to the direct excitation of the OVA tryptophan residue acting as an energy transfer donor for the AuNC emission.[284] The overlap

integral of the OVA-AuNC emission with the $AuNR_{CTAB}$-PSS-*co*-MA 1:1-ConA absorbance is shown by the grey lines (Figure 5.20A). The overlap integral between the AuNR-ConA and OVA-AuNCs was calculated to be $7.62 * 10^{20}$ $M^{-1}cm^{-1}nm^4$ using the reported AuNR extinction of $7.11 * 10^9$ $m^{-1}cm^{-1}$. The overlap integral value was then used to calculate the Forster distance to be 30.8 nm. This large Forster distance means that energy transfer should be very efficient because the expected distance between AuNR-ConA bound OVA-AuNC is approximately 10 - 15 nm.

The glucose assay response was tested using 0.1 nM $AuNR_{CTAB}$-PSS-*co*-MA 1:1-ConA and 5.5 μM OVA-AuNC. The glucose response was collected for excitation at 340 nm and 400 nm but the data was nearly identical; for brevity, only 340 nm data will be discussed. Mixing of the OVA-AuNC with $AuNR_{CTAB}$-PSS-*co*-MA 1:1-ConA in the absence of glucose resulted in an initial OVA-AuNC quenching of 39.5%. As glucose concentration was increased, the luminescence was recovered with a response up to 1 M glucose (Figure 5.20B). Surprisingly, full reversibility (return to 1) was never achieved (Figure 5.20B).

As a negative control, the effect of glucose directly on the OVA-AuNC was investigated. When glucose was added to OVA-AuNCs, less than a 1% change in PL intensity was observed up to 0.5 M glucose; at 1 M glucose a 7.4% enhancement of PL intensity occurs (Figure 5.20B). This may be due to changes in viscosity affecting the OVA structure, similar to the intensity enhancement observed for BSA-AuNCs subjected to high pressure.[285]

The static quenching of the AuNR complex was studied by the addition of varying concentrations of $AuNR_{CTAB}$-PSS-*co*-MA 1:1 to OVA-AuNCs; the x-axis AuNR concentration was based off NTA (Figure 5.20C). As $AuNR_{CTAB}$-PSS-*co*-MA 1:1 concentration was increased, the OVA-AuNC PL intensity decreases, with a 23.4% quenching at 0.29 nM $AuNR_{CTAB}$-PSS-*co*-MA 1:1. This represents the quenching due to absorption of the excitation light by the AuNR. It was shown previously that the $AuNR_{CTAB}$-PSS-*co*-MA 1:1 and OVA-AuNCs do not associate in solution (Figure 5.20B), which suggests that the quenching observed is not due to energy transfer of the OVA-AuNC attaching directly to the AuNR. The static quenching for increase AuNR concentration was interpolated to find a static quenching of 8% at 0.1 nM $AuNR_{CTAB}$-PSS-*co*-MA 1:1, the concentration of AuNRs used for the glucose assay. This static quenching represents a static baseline of quenching for all glucose concentrations; a contributing factor for why full reversibility was never achieved. The large amount of static quenching also illustrates the tradeoff when increasing the $AuNR_{CTAB}$-PSS-*co*-MA 1:1-ConA concentration. The sensor response range can be tuned by increasing ConA concentration, but this will also increase the baseline static quenching.

Table 5.2: Quenching reversibility as a function of glucose. Corrected quenching was calculated by taking the measured assay quenching and subtracting the OVA-AuNC only quenching and the AuNR static quenching.

Excitation at 340nm								
Glucose (M)	**0**	**0.0001**	**0.001**	**0.01**	**0.1**	**0.2**	**0.5**	**1**
Quenching (Assay)	0.60	0.62	0.65	0.68	0.77	0.83	0.91	0.93
Quenching (OVA-AuNC)	1.00	1.00	0.99	1.00	1.00	1.00	1.01	1.07
Quenching (Static)	0.92	0.92	0.92	0.92	0.92	0.92	0.92	0.92
Quenching % (Assay)	39.5%	38.2%	35.2%	31.6%	23.1%	17.1%	9.2%	6.6%
Quenching % (OVA-AuNC)	0.00%	0.11%	0.77%	0.28%	0.42%	0.42%	-0.69%	-7.44%
Quenching % (Static)	8.00%	8.00%	8.00%	8.00%	8.00%	8.00%	8.00%	8.00%
Quenching % (Corrected)	**31.5%**	**30.1%**	**26.4%**	**23.4%**	**14.7%**	**8.7%**	**1.9%**	**6.1%**

Excitation at 400nm								
Glucose (M)	**0**	**0.0001**	**0.001**	**0.01**	**0.1**	**0.2**	**0.5**	**1**
Quenching (Assay)	0.60	0.62	0.65	0.68	0.77	0.83	0.91	0.93
Quenching (OVA-AuNC)	1.00	0.99	0.98	0.99	0.99	0.98	1.00	1.07
Quenching (Static)	0.92	0.92	0.92	0.92	0.92	0.92	0.92	0.92
Quenching % (Assay)	39.5%	38.2%	35.2%	31.6%	23.1%	17.1%	9.2%	6.6%
Quenching % (OVA-AuNC)	0.00%	1.38%	1.59%	1.31%	1.15%	1.93%	-0.24%	-6.94%
Quenching % (Static)	8.00%	8.00%	8.00%	8.00%	8.00%	8.00%	8.00%	8.00%
Quenching % (Corrected)	**31.5%**	**28.8%**	**25.6%**	**22.3%**	**14.0%**	**7.2%**	**1.4%**	**5.6%**

The corrected quenching percent was calculated by removing the contribution of static quenching and the OVA-AuNC quenching only in the presence of glucose (Figure 5.20D and Table 5.2). After removing these other contributions we can see that the actual initial quenching was 31.5% and full reversibility was nearly achieved at 0.5 M. At 1 M glucose the trend is no longer seen. The response in linear between 1 mM and 200 mM with an R^2 value of 0.97, however, the sensitivity is higher in the 10 mM to 500 mM range (Figure 5.20).

5.4.7. Optimization of Assay Conditions and Data Analysis

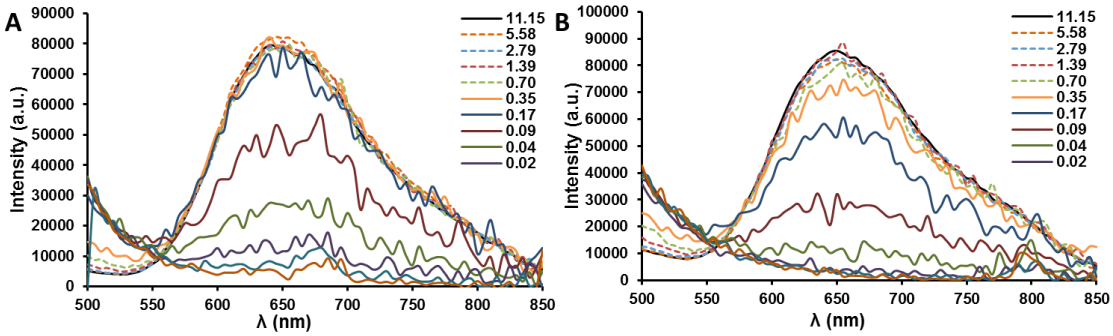

Figure 5.21: Optimizing plate reader gain for different concentration of OVA-AuNCs when the excitation was (A) 340 nm or (B) 400 nm.

Table 5.3: Gain values for excitation at 340nm or 400nm for different OVA-AuNC concentrations.

OVB Conc (uM)	11.15	5.58	2.79	1.39	0.70	0.35	0.17	0.09	0.04	0.02	0.01	0.01
Gain for 400nm Exc.	167	180	195	211	225	240	250	255	255	255	255	255
Gain for 340nm Exc.	162	176	189	204	219	234	248	255	255	255	255	255

Serial dilutions of OVA-AuNCs were measured to determine the lower limit of detection for the plate reader at an excitation of 340 nm or 400 nm. The gain was set to auto adjust for optimal dynamic range at each concentration yielding a value between 0 and 255. For an excitation of 340 nm and OVA-AuNC concentration below 0.35 μM, decreasing PL intensity and large SNR was observed (Figure 5.21A). Even at 0.35 μM the amount of noise was becoming apparent. When the excitation was 400 nm the spectra deteriorates in quality and intensity when OVA-AuNC concentration was below

1.39 μM (Figure 5.21B). A gain larger than 235 generally did not provide good quality data (Table 5.3). This shows there is some room lowering OVA-AuNC concentration to optimize the assay, but further optimization will require increasing the OVA-AuNC QY.

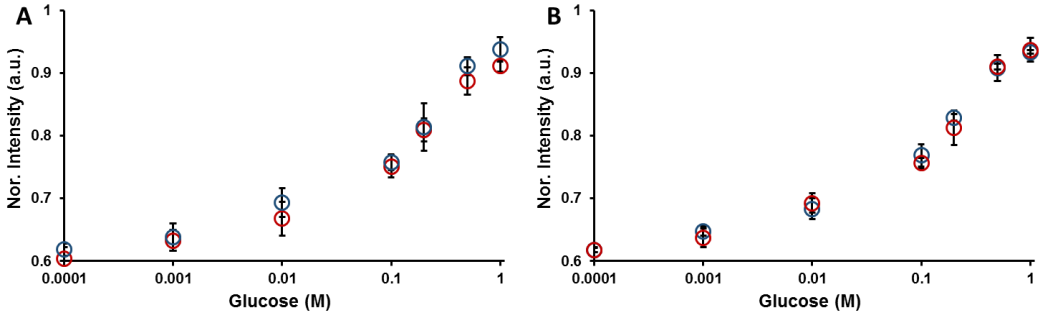

Figure 5.22: Optimization of glucose response data analysis by normalizing PL intensity to the (A) max value of the entire assay or (B) max value in that row for excitation at 340 nm (red ○) or 400 nm (blue ○). Error bars represent 95% confidence intervals (n = 3).

The glucose response of the OVA-AuNC and $AuNR_{CTAB}$-PSS-*co*-MA 1:1-ConA assay when the luminescence intensity was normalized to the max intensity of all samples (Figure 5.22A) and when the luminescence intensity was normalized to the max intensity in that row (Figure 5.22B). There was about a 3.4% difference in one of the replicate wells for the sample of OVA-AuNC only and this error can be seen in this entire row compared to the other two rows. However, normalizing the PL intensity of each row to the OVA-AuNC only sample removes most of this error, reducing the standard deviation between replicates was reduced by an average of 66%, in many cases the error was reduced by more than 80% (Table 5.4).

Table 5.4: Plate setup for glucose response when luminescence intensity was normalized to the max value in the entire assay or to the max value in that row for excitation at 340 nm (left) and 400 nm (right). The percent difference represent the difference between the standard deviation of the two methods of normalization.

Raw Data (340nm Excitation)									
Glucose	0	1E-04	0.001	0.01	0.1	0.2	0.5	1	OVA-AuNC only
Replicate 1	33401	33486	35093	38061	42428	45085	49942	51975	54865
Replicate 2	34252	35356	36433	39396	43782	46445	51783	52409	56957
Replicate 3	33312	34338	36628	36667	42125	46834	49890	51447	55110
Normalized to Max									
Glucose	0	1E-04	0.001	0.01	0.1	0.2	0.5	1	OVA-AuNC only
Replicate 1	0.586	0.588	0.616	0.668	0.745	0.792	0.877	0.913	0.963
Replicate 2	0.601	0.621	0.640	0.692	0.769	0.815	0.909	0.920	1.00
Replicate 3	0.585	0.603	0.643	0.644	0.74	0.822	0.876	0.903	0.968
Avg	0.591	0.604	0.633	0.668	0.751	0.81	0.887	0.912	0.977
Std	0.010	0.019	0.017	0.027	0.018	0.018	0.021	0.010	0.023
Normalized to Max per Row									
Glucose	0	1E-04	0.001	0.01	0.1	0.2	0.5	1	OVA-AuNC only
Replicate 1	0.609	0.610	0.640	0.694	0.773	0.822	0.910	0.947	1.00
Replicate 2	0.601	0.621	0.640	0.692	0.769	0.815	0.909	0.920	1.00
Replicate 3	0.604	0.623	0.665	0.665	0.764	0.850	0.905	0.934	1.00
Avg	0.605	0.618	0.648	0.684	0.769	0.829	0.908	0.934	1.00
Std	0.004	0.008	0.016	0.018	0.005	0.021	0.003	0.015	0.00
									Avg %Diff
% Diff.	84	83	2	41	110	13	151	47	66

Raw Data (400nm Excitation)									
Glucose	0	1E-04	0.001	0.01	0.1	0.2	0.5	1	OVA-AuNC only
Replicate 1	35735	37292	38484	41765	45108	48220	53130	55980	59546
Replicate 2	36573	37650	38862	41552	47080	49314	55101	56168	60332
Replicate 3	35704	35502	36637	40538	43090	47812	54523	55393	58925
Normalized to Max									
Glucose	0	1E-04	0.001	0.01	0.1	0.2	0.5	1	OVA-AuNC only
Replicate 1	0.592	0.618	0.638	0.692	0.748	0.799	0.881	0.928	0.987
Replicate 2	0.606	0.624	0.644	0.689	0.78	0.817	0.913	0.931	1.00
Replicate 3	0.592	0.588	0.607	0.672	0.714	0.792	0.904	0.918	0.977
Avg	0.597	0.610	0.63	0.684	0.747	0.803	0.899	0.926	0.988
Std	0.009	0.022	0.022	0.012	0.037	0.015	0.019	0.008	0.013
Normalized to Max per Row									
Glucose	0	1E-04	0.001	0.01	0.1	0.2	0.5	1	OVA-AuNC only
Replicate 1	0.6	0.626	0.646	0.701	0.758	0.81	0.892	0.94	1.00
Replicate 2	0.606	0.624	0.644	0.689	0.78	0.817	0.913	0.931	1.00
Replicate 3	0.606	0.602	0.622	0.688	0.731	0.811	0.925	0.94	1.00
Avg	0.604	0.618	0.637	0.693	0.756	0.813	0.91	0.937	1.00
Std	0.004	0.015	0.015	0.009	0.028	0.005	0.019	0.006	0.00
									Avg %Diff
% Diff.	82	37	37	36	30	105	0	24	44

Using the plate reader was necessary in order to reduce the reaction volume and assay reagents. However, getting consistent data, especially when protein was being used, requires ensuring a consistent meniscus and no bubbles in each well. To get a consistent meniscus the plate was orbitally shaken for 10-30 s before the measurement cycle. Bubbles are removed by popping them with a metallic syringe needle.

5.5. Conclusion

This work demonstrated the nanomaterial energy transfer between donor fluorescent OVA-AuNCs and ConA decorated AuNRs. A major challenge was the conjugation and separation of the AuNR-ConA conjugate without inducing aggregation and while maintaining ConA binding capability. NTA played a crucial role in this method development process to determine size distribution and concentration. The photo-luminescent OVA-AuNCs were synthesized using established methods but a

purification step was introduced in order to remove the denatured and non-binding portion. This process could be achieved without a significant size increase or aggregation, but with only a 14% recovery. The binding of the OVA-AuNCs with the AuNR-ConA was confirmed visually by TEM and spectroscopically by monitoring the photoluminescence quenching. The OVA-AuNCs were initially quenched by 31.5% when mixed with AuNRs but the luminescence could be almost fully recovered by the addition of glucose. As a sensor, the response was linear from 1 – 200 mM but the sensitivity was higher in the 10 mM – 500 mM range. For glucose sensing applications this range and sensitivity will need to be optimized by tuning the relative and absolute concentrations of the OVA and ConA. However, this presents some challenges that may require additional redesign and optimization. Increasing the AuNR-ConA concentration using the present formulation will result in a large increase in static quenching by the AuNR, which will decrease the SNR. Decreasing the OVA-AuNCs concentration without first increasing the QY will also decrease the SNR. Future work will need to redesign this sensor carefully by taking all of these variables into consideration. However, because the techniques for modification and conjugation developed in this work are generic, they can be adapted for inclusion of different nanomaterial formulations with minimal optimization.

6. CALCIUM CARBONATE AS A TEMPLATE FOR THE FABRICATION OF MICRO- AND NANO- CAPSULE SENSORS[*]

6.1. Introduction

For *in vivo* deployment, the sensing chemistry must be packaged in hollow capsule with a semi-permeable polymer shell. The membrane acts as a barrier between the sensor interior and the host environment. The membrane mesh size must be small enough to keep the sensor chemistry localized and keep the components from leaching out of capsule and interacting with the host environment. This keeps the potentially hazardous components (*i.e.* ConA, nanomaterials) compartmentalized to mitigate their potential toxicity. This also keeps the larger biomolecule components of the host environment from interfering or damaging the sensor components. The mesh size should be large enough to allow the diffusion of analytes like glucose into the capsule interior to be analyzed by the sensor. The capsule shell can be further modified to impart additional functionality by the incorporation of dyes, NPs, or responsive polymers and can be engineered to enhance biocompatibility. A major challenge for the encapsulation of proteins is the ability to encapsulate a large amount of material while

[*] Parts of this section are reprinted with permission from "Poly (vinylsulfonic acid) Assisted Synthesis of Aqueous Solution Stable Vaterite Calcium Carbonate Nanoparticles" by Nagaraja, A. T., Pradhan, S., McShane, M.J. *J Colloid Interface Sci* 2014, *418*, 366-72. Copyright 2014 by Elsevier Inc.

[*] Parts of this section are reprinted with permission from "Fabrication of Nanocapsule Carriers from Multilayer-Coated Vaterite Calcium Carbonate Nanoparticles" by Biswas, A.; Nagaraja, A. T.; McShane, M. J. *ACS Appl Mater Interfaces* 2014, *6* (23), 21193-201. Copyright 2014 by American Chemical Society Inc.

retaining binding capability. This requires gentle processing and mild conditions for entrapment, shell deposition, and dissolution.

Calcium carbonate ($CaCO_3$) is an important material for fundamental and applied study, with implications in industrial,[286] household,[287] and biological processes.[288] $CaCO_3$ exists as three different anhydrous polymorphs: calcite, aragonite and vaterite in order of decreasing thermodynamic stability. Nanoporous $CaCO_3$ particles have attracted much attention because of their biocompatibility, high effective surface area, ability to protect encapsulated components, larger pore size than mesoporous silica, inexpensive production under ambient conditions, and ease of dissolution with mild treatment of EDTA at neutral pH.[289] There is significant interest in producing the vaterite polymorph of $CaCO_3$ because it has better water solubility, higher porosity, and is more easily dissolved than calcite or aragonite.

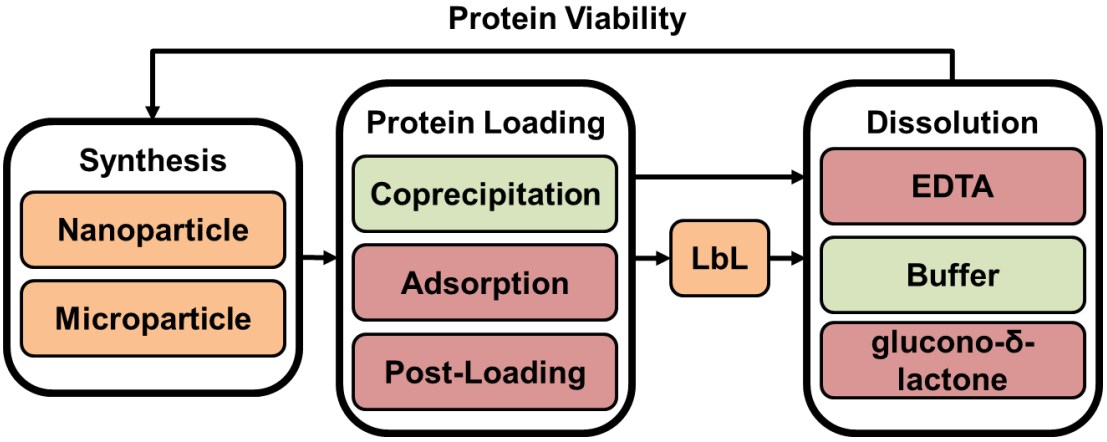

Figure 6.1: Flow chart of the process development for encapsulation using $CaCO_3$ as a template.

This section investigates the encapsulation of ConA based sensing chemistry into $CaCO_3$ nano- and microparticle templates. The overall process development and major considerations are shown in Figure 6.1. This section is divided into three subsections to address the major areas of the process development: (1) synthesis and characterization of the novel regime of nanoparticle $CaCO_3$ templates (CCNPs), (2) investigation and redesign of the LbL on $CaCO_3$ process using CCNPs as the model template, and (3) retention of ConA activity during the encapsulation and carbonate dissolution using buffered dissolution instead of chelation. Each subsection contains more detailed topic specific background.

6.2. Synthesis of PVSA Stabilized CCNPs

6.2.1. Background

The thermodynamic instability of vaterite makes its natural occurrence rare, requiring kinetic stabilization even for laboratory production. Investigation into different crystal growth modifiers for vaterite formation is encompassed by the vast literature studying additive-directed crystallization,[290, 291] for its importance in understanding mesocrystal formation for biomineralization.[292, 293] It is difficult to predict the outcome of different additives from theory; hence, most understanding is gained through empirical observations. Additional factors such as concentration and ratio of Ca^{2+} to CO_3^{2-}, temperature, pH, reaction duration, and mixing speed influence the outcome and further complicate understanding the process. Polymers act to inhibit or stabilize specific crystal structures, reshaping and directing crystal formation depending on chemical composition, charge density, and concentration.[294] A wide

variety of structures and crystal polymorphs can be produced, with even a small amount of additive having a significant influence on the outcome. Copolymers containing both interacting and stabilizing components reshape crystallization based on the affinity of the chemical structure for the mineral salt ions and crystal faces.[295] In recent work, the commercial random copolymer poly (4-styrenesulfonate-*co*-maleic acid) (PSS-*co*-MA) was found to direct crystallization to produce a variety of superstructures depending on its relative concentration to calcium in the reaction.[293, 296] A PEI assisted ultrasonic method was developed for the synthesis of vaterite microparticles that were stable for at least 8 months.[297] Other commonly used PEs include carboxylic or sulfate containing synthetic and biopolymers.[298, 299]

For biosensor or drug delivery applications the production of spherical vaterite is desired because the highly porous structure can serve as a template for biomolecule incorporation. Encapsulation into these particles is achieved either by adsorption to the highly porous structure after particle formation[22] or by addition during nucleation to coprecipitate during particle formation.[300] In many cases, the biomolecule-encapsulating $CaCO_3$ microparticle is used as a template to create hollow capsules by the sequential deposition of oppositely charged PEs using electrostatic layer-by-layer, followed by core dissolution.[301] Applications of $CaCO_3$ NPs (CCNPs) would have vast implications for both drug delivery and sensor applications. In order for a drug-carrying NP to passively enter a subcutaneous tumor cell it must be less than the 200-1200 nm pore size cutoff.[302] For competitive binding glucose biosensors, compartmentalization of macromolecules into nanocapsules should improve response times by decreasing diffusion distances.[303]

Production of CCNPs requires decreasing the particle growth rate and stabilizing the NPs before they agglomerate to form microparticles or recrystallize to calcite. Alginate chains have been used to reduce the nucleation growth rate by sequestering calcium, resulting in the formation of CCNPs.[304] However the resulting CCNPs showed an increase in size and loss of negative surface charge after 4 hours in aqueous solution, indicating surface recrystallization. Ethylene glycol was used to reduce the solubility and crystal growth rate of $CaCO_3$ to produce vaterite NPs down to 430 nm in size.[305] These particles remained as vaterite in ethanol, but recrystallized to calcite in a few hours when transferred to aqueous solutions. Thus, while a few examples of efforts to produce CCNPs have been reported, we have not identified any that yield long-term stable vaterite NPs.

The focus of this work was to study the effect of poly (vinyl sulfonic acid) (PVSA) on CCNP formation and production of vaterite NPs. It has been shown that the presence of sulfonic groups on polymers stabilizes the vaterite structure.[287] We hypothesized that incorporation of commercially available PVSA, a low-molecular-weight and high-charge-density PE, would limit interparticle bridging and aggregation of primary nuclei to prevent microparticle formation. This idea was based on a previous report of the copolymer of PVSA and chitosan which found that the sulfonic acid groups strongly interacted with and attached to the $CaCO_3$ surface.[306] Here we describe a method to obtain vaterite CCNPs and report how PVSA concentration, reaction temperature, and order of reagent addition affect particle size, morphology, surface charge, and crystalline structure.

6.2.2. Materials and Methods

6.2.2.1. Chemicals

PVSA (Sigma) was filtered through a 0.2 μm syringe filter prior to use. Na_2CO_3 and $CaCl_2$ (Sigma) was used as received. PVSA molecular weight of 4000 – 6000 kDa according to manufacturer's specifications, 5000 kDa was used for calculations.

6.2.2.2. CCNP Synthesis

10 mL of 20 mM Na_2CO_3 and PVSA were added to a 100 mL beaker and stirred at 800 RPM with a spinning wedge stir bar (VWR). After 1 min, 10 mL of 20 mM $CaCl_2$ was rapidly injected. The beaker was covered and the solution was allowed to react at RT for 1-14 h depending on the PVSA concentration (Table S1). The mixture was transferred to 50 mL conical tube and centrifuged at 10000 RCF for 5 min to recover the formed particles and remove unreacted components. The particles were washed 3 times with 50 mM pH 9 TRIS buffer and finally resuspended as a 1 mL stock solution in 50 mM pH 9 TRIS buffer. This process was also done in reverse where $CaCl_2$ was added first followed by PVSA and then Na_2CO_3 (Table S2).

6.2.2.3. SEM

Images were obtained with a JEOL FE-SEM 7500. 2 μL of a 1/10 diluted stock dilution was placed on a cleaned silica support and dried in a vacuum chamber overnight followed by gold sputtering for 45 s.

6.2.2.4. XRD

The X-ray source was a 2.2 kW Cu X-ray tube, maintained at an operating current of 40 kV and 40 mA. The standard Bragg-Brentano para-focusing mode with the

X-ray diverging from a DS slit (1 mm) at the tube to strike the sample and then converging at a position sensitive X-ray Detector (Lynx-Eye, Bruker-AXS).

6.2.2.5. DLS & Microelectrophoresis

Dynamic Light Scattering (DLS) and ζ-potential was measured using a Zeta Sizer Nano Series ZEN 3600 Spectrometer (Malvern Instruments Ltd, Malvern, Worcestershire, United Kingdom). A 1 mL, 1/20 diluted stock solution in 5 mM pH 9.0 TRIS buffer was used for measurement.

6.2.2.6. NTA

Particle size and distributions were obtained with the NanoSight LM10HS with a 65 mW 405 nm source. A 300 μL sample of a 1/100 dilution of the sample stock solution in 0.1 M $NaHCO_3$ was used for analysis. Video was acquired with a Hamamatsu C11440 digital camera for 3 min in order to obtain at least 1000 particle tracking events. Analysis was completed with included NanoSight 2.3 software with automatic settings.

6.2.2.7. UV-Vis

UV-Vis absorbance was obtained on a Cary 300 UV-Vis spectrophotometer with a 6x6 multi-cell Peltier block and temperature controller. For the time dependent studies a scaled down reaction in a 3 mL total volume (1.5 mL $CaCl_2$, 1.5 mL Na_2CO_3, and PVSA) was monitored at 500 nm at 20-30 s intervals under constant stirring.

6.2.2.8. Brunauer-Emmett-Teller Method

The surface area and pore size of the CCNPs was determined using the Brunauer-Emmett-Teller (BET) method with nitrogen adsorption and desorption at 77 K using a Micromeritics ASAP 2000.

6.2.3. Results and Discussion

6.2.3.1. Experimental Setup

The simple experimental setup is depicted in Figure 6.2 where equal volumes of equimolar of $CaCl_2$ and Na_2CO_3 are combined under agitation in the presence of PVSA. In the first set of experiments, 10 mL of 0.02 M Na_2CO_3 was combined with PVSA in a beaker and stirred at 800 RPM (stirred solution) for two minutes. Then 10 mL of 0.02 M $CaCl_2$ was rapidly injected (solution added) and the reaction was incubated under constant stirring at room temperature.

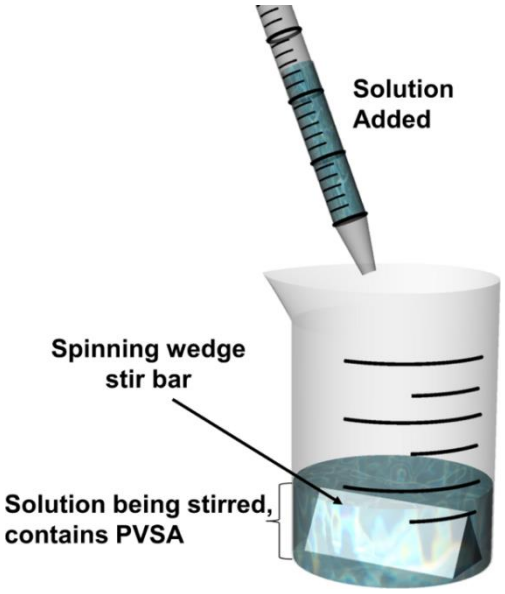

Figure 6.2: Schematic of experimental setup where PVSA, Na_2CO_3 and $CaCl_2$ are combined in a beaker under stirring with a spinning wedge stir bar

The concentration of PVSA in the stirred solution was varied in order to understand how particle size and morphology would be affected. The mixing of $CaCl_2$ and Na_2CO_3 without any additive results in immediate particle formation apparent from the increased turbidity, but the incorporation of PVSA into the reaction significantly delays the onset of the nucleation.

6.2.3.2. Na_2CO_3 as the Stirred Solution

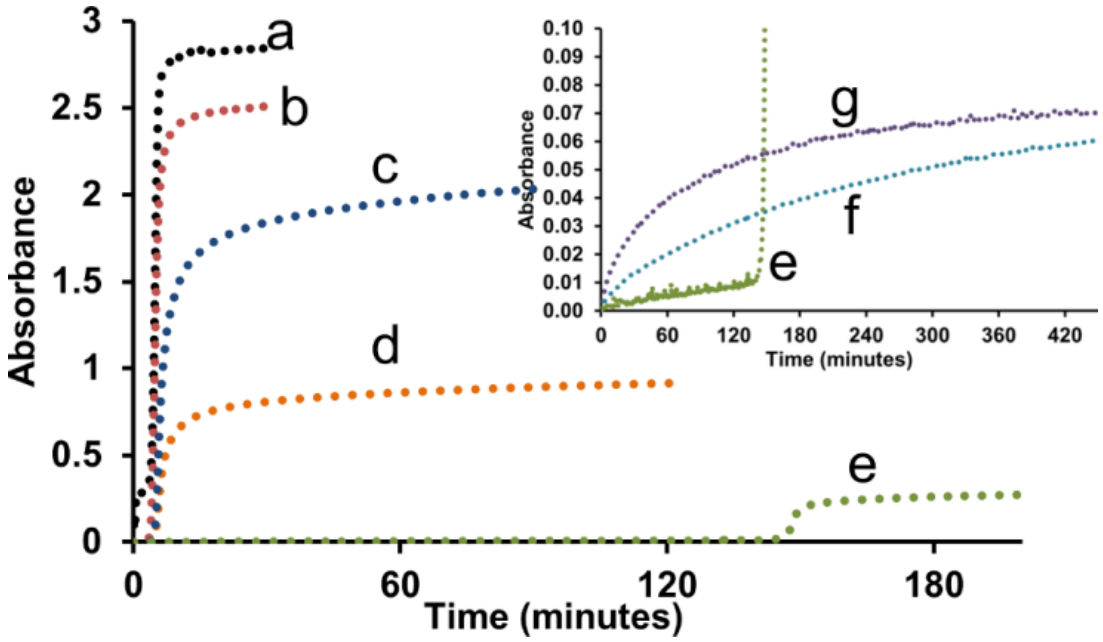

Figure 6.3: Time dependent absorbance at 500 nm for the reaction maintained at 25°C under constant stirring for different PVSA concentrations (a) 0.16 µM (b) 0.31 µM, (c) 0.625 µM, (d) 1.24 µM, (e) 1.84 µM, (f) 2.43 µM, and (g) 3.01 µM.

To understand the process, a scaled-down reaction was performed in a cuvette and monitored with UV-Vis absorbance spectroscopy. The results reported in Figure 6.3 show the time dependent absorption at 500 nm, which is a measure of turbidity and, hence, particle formation or growth. At PVSA concentrations from 0.16 -1.24 µM there

is no apparent particle formation for ≈ 5 - 6 minutes (indicated by the sharp increase in absorbance) and at 1.84 μM it takes ≈ 150 minutes for notable particle formation. With increasing PVSA concentrations from 0.16 - 1.84 μM we also observe a decrease in the peak steady-state absorbance reached, indicating the production of either smaller sized or fewer particles. At 2.43 μM and 3.01 μM PVSA the growth pattern changes: instead of a delay followed by a sharp inflection, a continuous slow growth was observed. A higher reaction slope was observed for the higher PVSA concentration, a trend which continues to at least 4.14 μM. The minimum incubation time required for each PVSA concentration before recovery of the particles by centrifugation was determined by finding the time when the absorbance increase reached steady-state (first derivative equal to 0). After centrifugation at 10000 RCF for 5 minutes, the particles were washed 3 times and suspended in a concentrated 1 mL stock solution for further analysis. The particles were stored in an alkaline buffered solution to prevent acidic dissolution of particles.

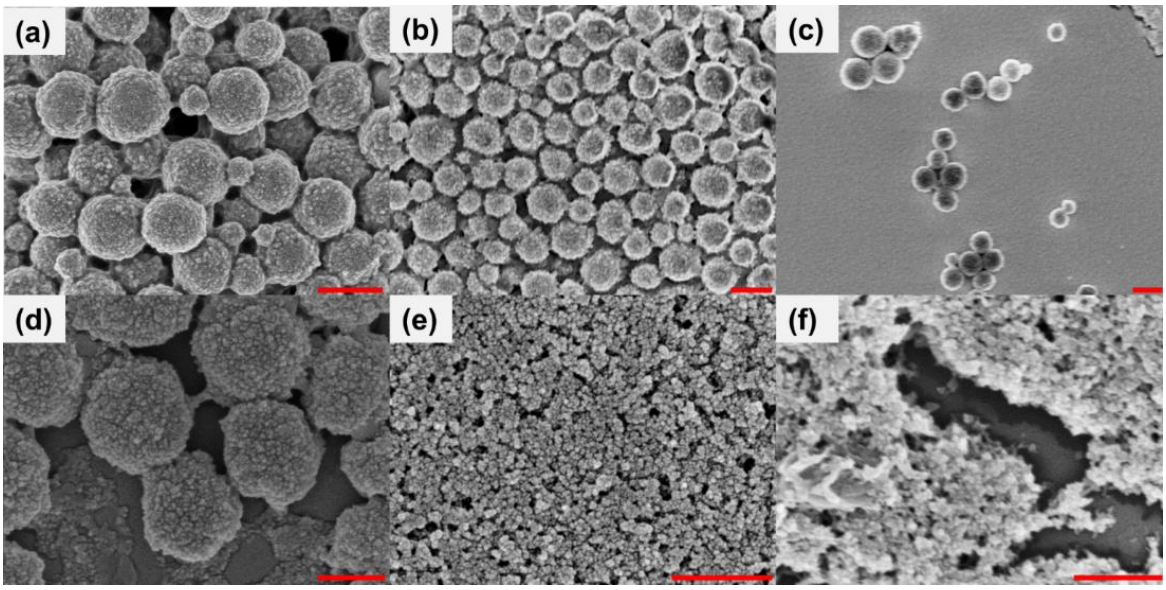

Figure 6.4: SEM images of sputter coated CCNPs produced when Na_2CO_3 was the stirred solution for different PVSA concentrations (a) 0.31 µM, (b) 0.625 µM, (c) 1.24 µM, (d) 1.84µM, (e) 2.43 µM, and (f) 3.01 µM. Scale bars correspond to 500 nm.

Particle morphology was determined by SEM imaging of CCNPs suspended on a silica wafer and gold sputter coated. For the lower PVSA concentrations (Figure 6.4) the particles exhibit spherical morphology associated with vaterite. The surface appears porous and looks very similar to other reports of $CaCO_3$ microparticles. At higher PVSA concentrations (Figure 6.4e, Figure 6.4f) particles cannot be distinctly observed; therefore, size and morphology are not distinguishable because the small particles aggregate during sample drying. For all PVSA concentrations, no calcite rhombohedra were found in the populations observed.

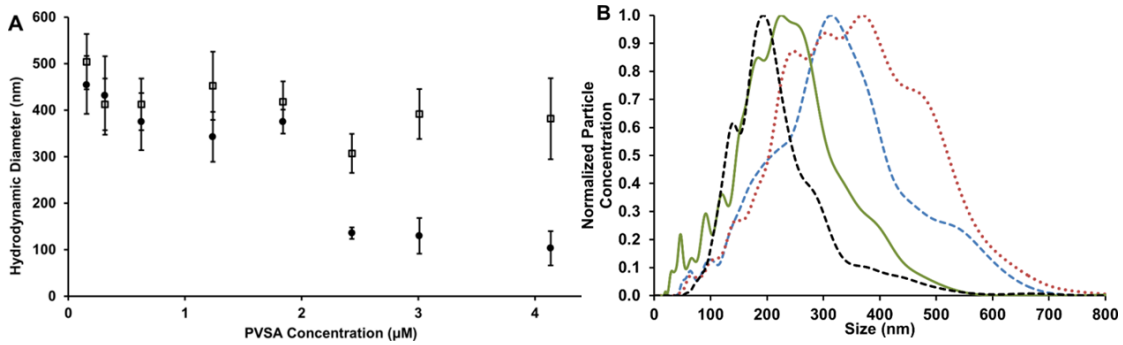

Figure 6.5: (A) DLS results represent average size by intensity (□) and size peak by number (●) for CCNPs at different PVSA concentrations when Na_2CO_3 was the stirred solution. Error bars represent 95% confidence intervals for three separate batches of particles. (B) NTA plots showing changes in size distribution at 0.15 μM (blue - -), 0.62 μM (red ●), 2.43 μM (green −), and 4.13 μM (black - -) PVSA when $CaCl_2$ was the stirred solution.

Dynamic light scattering (DLS) was used as a rapid method to determine the size of the CCNPs for different PVSA concentrations. The results reported in Figure 6.5A show the change in average size by intensity and size peak by number of the resulting particles formed. As concentration of PVSA was increased from 0.16 – 1.84 μM, peak size by number shows a slight downward trend but no significant differences were observed. Particles were all above 300 nm average diameter. At a concentration between 1.84 μM and 2.43 μM, an apparent threshold is crossed and peak size by number decreases to less than 150 nm. No significant change in size was found with further increase in PVSA concentration. Characterization of CCNPs with NP tracking analysis (NTA) was obtained (Figure 6.5B) to gain further understanding of hydrodynamic particle size. A limitation of DLS is the intensity based measurement which is weighted towards the higher scattering cross section of larger particles.[254] By tracking individual particle movement NTA provides additional understanding of particle size and size distribution. From these data we observe that increasing PVSA

concentration decreases peak particle size but there are some larger particles present even at higher PVSA concentrations. The size by DLS and NTA is summarized in Table 6.1.

Table 6.1: Summary of CCNP hydrodynamic size and zeta potential produced for given PVSA concentration and incubation time when Na_2CO_3 was the stirred solution (n = 3).

Na_2CO_3 Stirred Solution					
PVSA (µM)	Incubation Time (h)	Intensity Average Size (nm)	Size Peak by Number (nm)	NTA Peak (nm)	Zeta Potential (mV)
0.16	1	504.2 ± 59.6	454.2 ± 62.1	333±118	-21.9±1.94
0.31		412.7 ± 55.6	431.7 ± 84.3		-26.4±5.54
0.63	1.5	412.7 ± 55.6	375.4 ± 61.1	361±123.8	-17.9±1.96
1.24	2	421.1 ± 107.4	291 ± 34.1		-25.5±0.61
1.84	4	472.7 ± 19.6	404 ± 68.2		-28.5±1.71
2.43	14	307.1 ± 41.7	135.9 ± 12.3	249±106	-28.8±1.98
3.01		391.6 ± 53.5	129.7 ± 38.5		-36.1±0.58
4.13		381.8 ± 87	103.2 ± 36.7	235.7±131.6	-39.9±2.43

6.2.3.3. $CaCl_2$ as the Stirred Solution

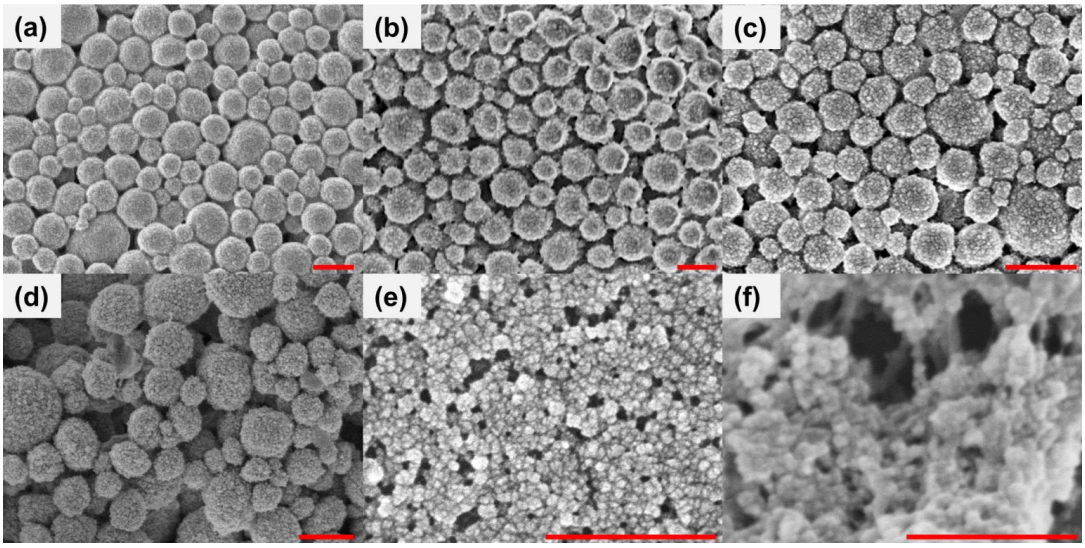

Figure 6.6: SEM images of sputter coated CCNPs produced when $CaCl_2$ was the stirred solution for different PVSA concentrations (a) 0.31 µM, (b) 0.625 µM, (c) 1.24 µM, (d) 1.84 µM, (e) 2.43 µM, and (f) 3.01 µM. Scale bars correspond to 500 nm.

To understand how order of addition affects the reaction dynamics the experiments were repeated for each PVSA concentration using the same setup in Scheme 1 but instead with $CaCl_2$ and PVSA as the stirred solution and Na_2CO_3 as the solution added. The SEM images (Figure 6.6) of the resulting CCNPs reveal the spherical morphology, but again at higher PVSA concentrations (Figure 4e, 4f) a clear distinction between particles was not observed.

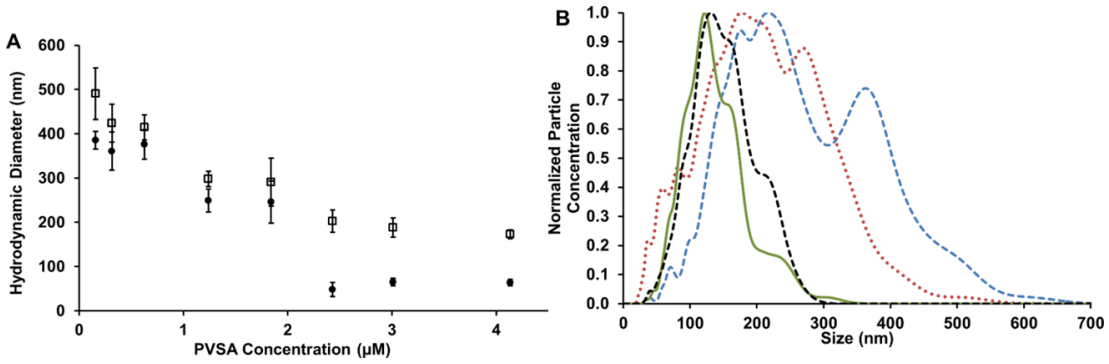

Figure 6.7: (A) DLS results represent average size by intensity (□) and size peak by number (●) for CCNPs at different PVSA concentrations when $CaCl_2$ was the stirred solution. Error bars represent 95% confidence intervals for three separate batches of particles. (B) NTA plots showing changes in size distribution at 0.15 μM (blue - -), 0.62 μM (red ●), 2.43 μM (green −), and 4.13 μM (black - -) PVSA when $CaCl_2$ was the stirred solution.

The DLS results for particles produced when $CaCl_2$ was the stirred solution (Figure 6.7A) show a similar trend and threshold transition to what was observed previously when Na_2CO_3 was the stirred solution. However, as PVSA concentration increases we observe smaller particle size by number and intensity and less error between triplicates compared to when Na_2CO_3 was the stirred solution. There is also less divergence between intensity and number distribution measurements, indicating less aggregation and greater monodispersity. From NTA (Figure 6.7B) we observe that at lower PVSA concentrations (0.15 μM and 0.62 μM) a broad multimodal distribution is present, but at higher PVSA concentrations (2.43 μM and 4.13 μM) average particle size decreases and becomes more monodisperse. The size by DLS and NTA are summarized in Table 6.2.

Table 6.2: Summary of CCNP hydrodynamic size and zeta potential produced for given PVSA concentration and incubation time when $CaCl_2$ was the stirred solution (n = 3).

$CaCl_2$ Stirred Solution					
PVSA (μM)	Incubation Time (h)	Intensity Average Size (nm)	Size Peak by Number (nm)	NTA Peak (nm)	Zeta Potential (mV)
0.16	1	490.5 ± 58.2	385.6 ± 19.8	277±109.2	-20.4 ± 0.88
0.31		424.0 ± 42.4	360.8 ± 43.1		-20.3 ± 0.84
0.63	1.5	414.6 ± 28.3	376.3 ± 33.2	239±101.9	-18.6 ± 0.75
1.24	2	298.2 ± 17.5	249.1 ± 25.6		-19.8 ± 1.19
1.84	4	291.0 ± 54.0	246.2 ± 47.5		-18.7 ± 1.68
2.43	14	202.5 ± 25.27	47.96 ± 15.9	140.5±48.2	-21.2 ± 1.01
3.01		188.4 ± 21.4	64.8 ± 8.2		-20.6 ± 1.98
4.13		173 ± 9.8	63.6 ± 7.1	152.7±46.6	-38.7 ± 0.59

6.2.3.4. XRD

XRD data were obtained for particles produced with 0.62 μM PVSA when Na_2CO_3 or $CaCl_2$ (Figure 6.8) was the stirred solution. All peaks on the diffraction spectra were associated with vaterite, indicating that the NPs produced are of the desired vaterite polymorph. It is also noteworthy that the data shown were obtained from samples after storage for 5 months in pH 9 TRIS buffer at room temperature. This indicates that the PVSA has stabilized the particles to prevent calcification for an extended period of time.

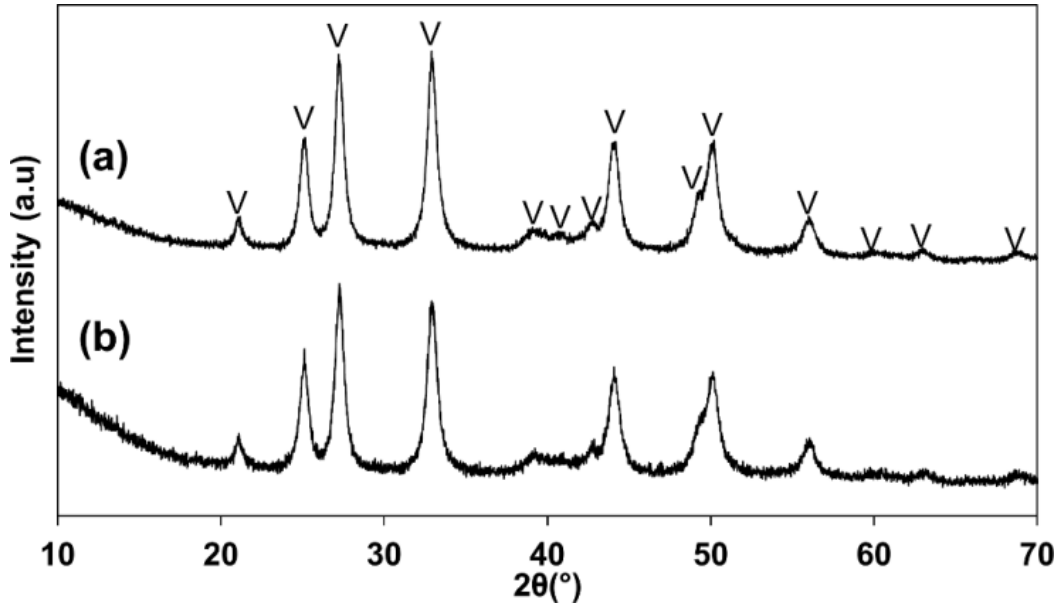

Figure 6.8: XRD of CCNPs formed when (a) Na_2CO_3 or (b) $CaCl_2$ was the stirred solution for 3.01 μM PVSA. Peaks associated with the vaterite polymorph are marked with a (V).

6.2.3.5. BET

BET analysis of CCNPs produced with 0.62 μM PVSA and $CaCl_2$ as the stirred solution revealed a surface area of 33.88 m^2/g, a single point pore volume of 0.065 cm^3/g, and an average pore size of 10 nm (Figure 6.9). PVSA stabilized CCNPs have a surface area higher than reported values for $CaCO_3$ microparticles[307, 308] and other vaterite CCNPs,[309] but have a smaller average pore size than both. The high surface area and porous nature of these CCNPs make then a suitable reservoir for material encapsulation.

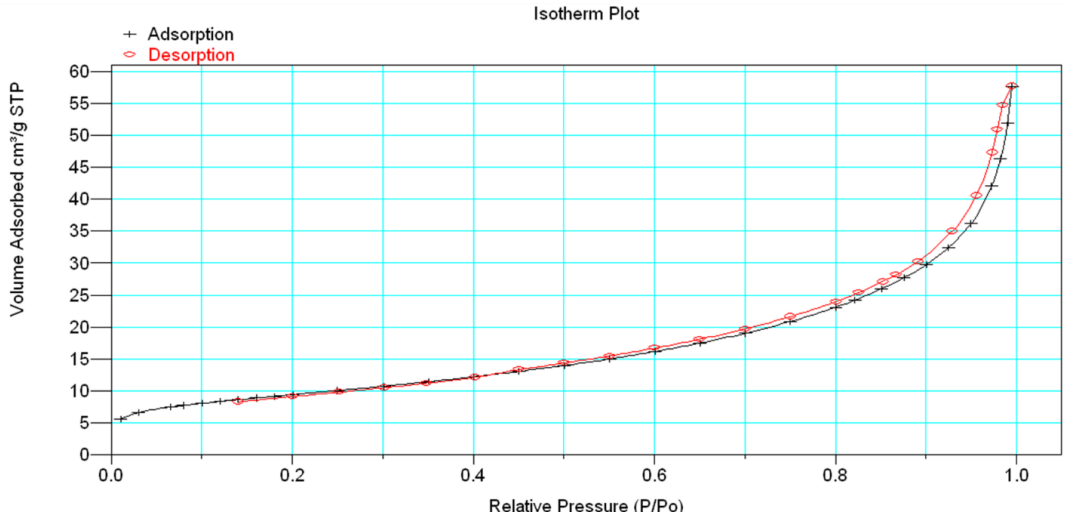

Figure 6.9: BET nitrogen adsorption/desorption isotherm plot for CCNPs with $CaCl_2$ as the stirred solution and 0.62 µM PVSA.

6.2.3.6. Zeta Potential

Zeta potential measurements for particles made in both $CaCl_2$ and Na_2CO_3 as the stirred solutions are reported in Figure 6.10. When Na_2CO_3 was the stirred solution we observe an increasing magnitude of a negative zeta potential with increasing PVSA concentration, indicating more surface coverage by PVSA. In contrast, when $CaCl_2$ is the stirred solution the zeta potential remains at ≈ 20 mV until the highest PVSA concentration. The sequestration of calcium by PVSA is either preventing complete adsorption of polymer on the CCNP surface or is neutralizing some of the surface charge. The particles had a negative surface charge for all PVSA concentrations and maintained this charge even after 5 months of storage in TRIS buffer (time of this measurement), indicating the PVSA has stabilized the surface to prevent calcification.

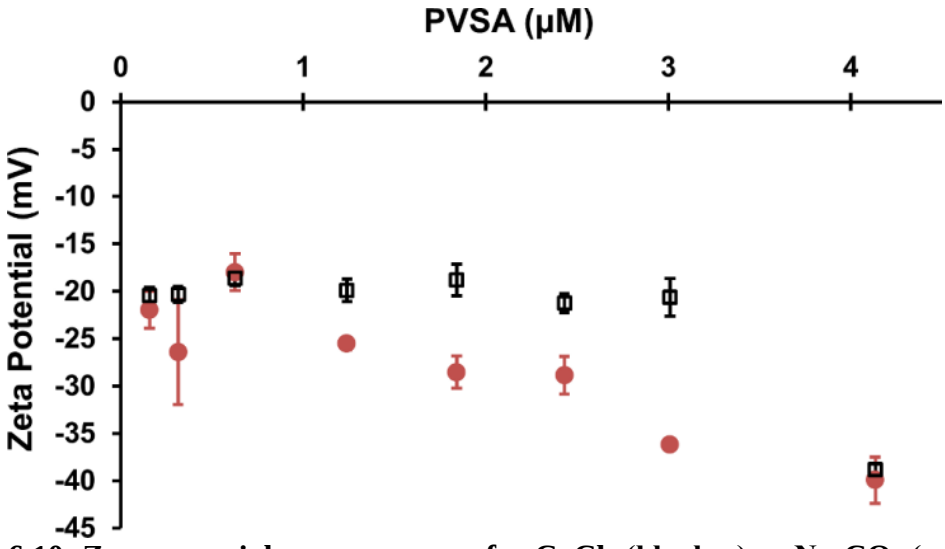

Figure 6.10: Zeta potential measurements for $CaCl_2$ (black □) or Na_2CO_3 (red ●) as the stirred solution. Error bars represent 95% confidence intervals for three separate batches of particles.

6.2.3.7. Temperature Dependent Nucleation

The influence of temperature on the reaction rate kinetics and resulting particle size and size distribution were studied using both UV-Vis spectroscopy and NTA. The time dependent nucleation when Na_2CO_3 was the stirred solution (Figure 6.11A**)** at three different temperatures shows that by decreasing temperature from 25°C to 5°C the onset of nucleation is delayed and the peak steady-state absorbance reached is less. The first derivative of the time dependent reaction (inset of Figure 6.11A) shows that the peak reaction rate reached is also decreasing with decreasing temperature. Sizing with NTA (Figure 6.11B) revealed that decreasing temperature decreased the CCNPs peak size to less than 200 nm at 5°C. Decreasing temperature also greatly improves the monodispersity decreasing the coefficient of variance from 107.7% at 25°C to 24.5% at 5°C. When $CaCl_2$ was the stirred solution (Figure 6.11C) there was a longer delay in the onset of peak nucleation compared to Na_2CO_3, but a similar trend with decreasing

temperature. NTA again reveals the smaller peak size and decrease in the coefficient of variance with decreasing temperature from 42.5% at 25°C to 27% at 4°C **(**Figure 6.11D**)**. The size by NTA and coefficient of variance for different temperatures are reported in Table 6.3.

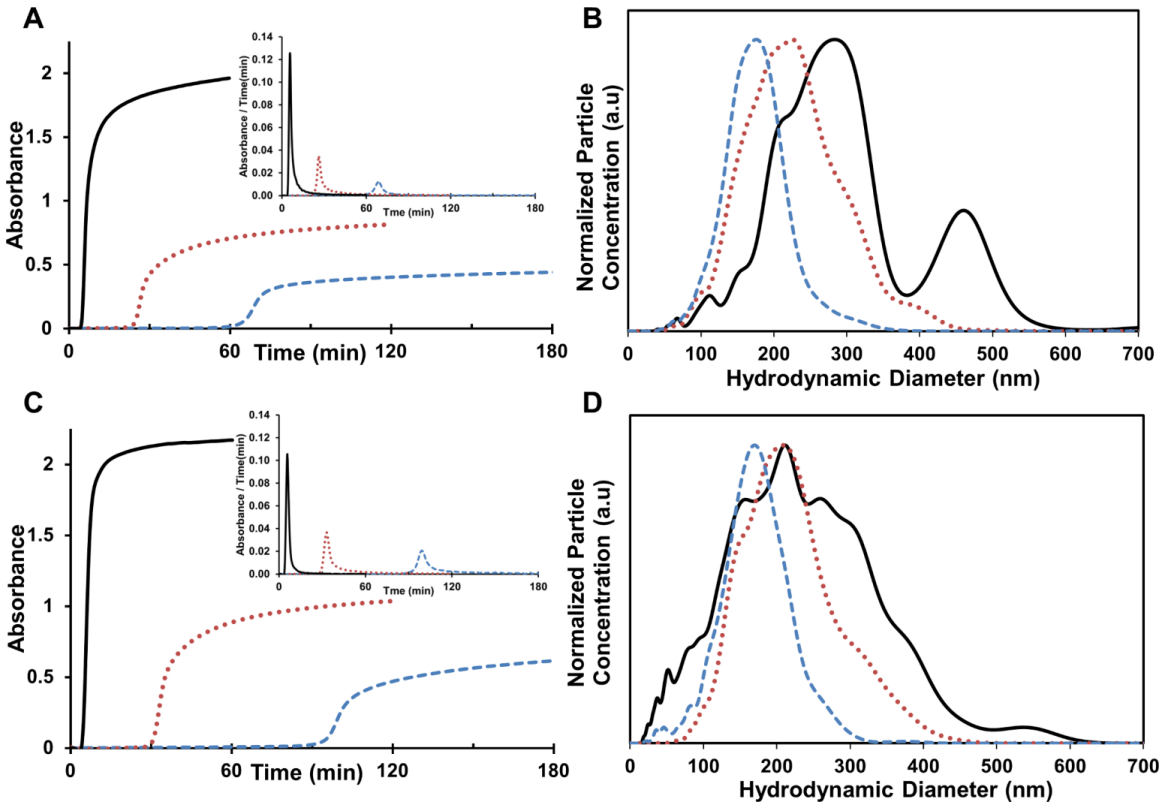

Figure 6.11: Time dependent UV-Vis absorbance at 500nM monitoring the nucleation and (inset) first derivative when (A) Na_2CO_3 or (C) $CaCl_2$was the stirred solution and NTA plots of CCNPs produced for 0.625 µM PVSA when (B) Na_2CO_3 or (D) $CaCl_2$ was the stirred solution at 5°C (blue - -), 10°C (red ●), and 25°C (black −).

Table 6.3: Temperature dependent (25°C, 10°C, 5°C) peak size achieved as determined by NTA and coefficient of variance (%CV) when either Na_2CO_3 or $CaCl_2$ was the stirred solution.

Stirred Solution		25°C	10°C	5°C
Na_2CO_3	Peak Size	210	208	170
	%CV	42.5%	29.40%	27%
$CaCl_2$	Peak Size	283	223	176
	%CV	107.7%	28.7%	24.5%

6.2.4. Conclusions

We have demonstrated an easy and rapid method to synthesize CCNPs requiring no specialized chemicals, equipment, or setup. We have shown that size of particles produced can by selected by controlling PVSA concentration. The PVSA is stabilizing the particles in solution as the vaterite polymorph with a strong negative surface charge and maintains this crystal structure and surface charge even when stored in a buffered solution for up to 5 months. This is an important distinction primarily because other methods that produced vaterite CCNPs were not stable in water.[304, 305] The time dependent analysis revealed the kinetics of particle formation and growth, including the influence of different concentrations of PVSA as well as different temperatures. Increasing the PVSA concentration or decreasing the temperature both delayed the onset of the peak nucleation rate as well as decreased the reaction rate. Decreasing reaction temperature provides an easy method to further decrease size and greatly improve monodispersity. The difference in result when either $CaCl_2$ or Na_2CO_3 was the stirred solution is interesting because when no additive is present it should not matter. However, when an additive is involved it is important to consider its interaction with the

two components. The interaction of PVSA with calcium causes dependence on order of addition that affects the outcome of particle size, monodispersity, and surface charge. While better control on size is achieved when $CaCl_2$ is the stirred solution, a more negative surface charge was attained when Na_2CO_3 was the stirred solution. Interestingly, at 5°C the difference in particle size and distribution when Na_2CO_3 or $CaCl_2$ was the stirred solution was much less than at 25°C. Hence, the difference in order of addition can be mitigated by decreasing reaction temperature.

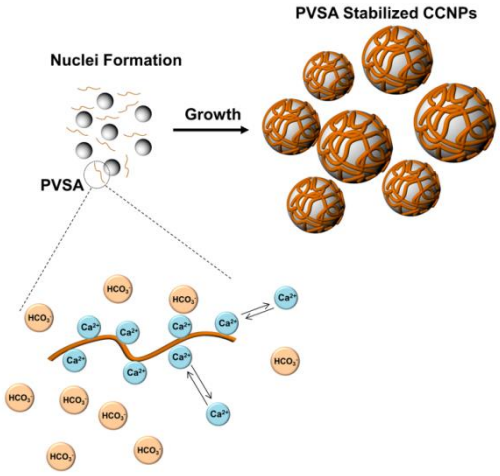

Figure 6.12: Proposed mechanism of PVSA assisted growth wherein PVSA plays a dual role to: (1) sequester calcium through ionic interactions to slow down nucleation rate and (2) stabilize the resulting NPs to prevent agglomeration into microparticles or recalcification into calcite.

From the results reported in this paper we suspect that PVSA is playing a dual role in (1) slowing the nucleation growth rate by sequestering excess calcium and (2) stabilizing the resulting CCNPs to prevent surface calcification or aggregation to form microparticles (Figure 6.12). As free calcium complexes with carbonate to form particles the concentration gradient causes more sequestered calcium to be released.

This results in a feeding process, which acts to control growth. Eventually the PVSA is no longer charge shielded by the free calcium and it then binds to the particle surface. The polymer imparts a high surface charge density and electrostatic repulsion between NPs to prevent aggregation into microparticles.

6.3. LbL on CCNPs for Fabrication of Capsules

6.3.1. Background

The vaterite form of $CaCO_3$ has received significant attention for sensor and drug release application because of its high porosity, easy synthesis, and mild dissolution conditions. However, the thermodynamic instability of the vaterite polymorph poses a problem of premature dissolution or recrystallization to calcite during the LbL process for capsule formation.

This problem became especially apparent when using CCNPs as the template for LbL and under commonly used conditions the CCNPs completely dissolved. A redesign of the typical microparticle LbL process was required in order to achieve similar results for NP templates. The additional problems associated with coating NPs was initially discovered when trying to analyze particle size with NTA, which requires a very high dilution of particles. $NaHCO_3$ buffer was required when diluting these particle to obtain accurate particle size and size distributions. When the particles were diluted in TRIS, CHES, or water they particles dissolved or aggregated. Therefore, LbL had to use $NaHCO_3$ buffer in order to prevent dissolution. Our work with LbL on NPs (AuNPs, AgNPs, and QDs) also showed that much higher PE concentrations were required to prevent interparticle bridging and obtain high charge reversal. When using CCNPs the

concentration was increased to at least 10 mg/mL to compensate for the increase in surface area of the smaller NPs compared to microparticles and the higher surface area of highly porous vaterite.

This work aimed to redesign the typical LbL procedure by investigating the process in more detail. Optimal conditions for CCNP stability such as suspension media, pH, PE type, and PE concentration were either studied or rationally chosen to improve particle stability. CCNPs require these optimized conditions because the instability results in complete dissolution. However, we suspect that a similar dissolution is occurring with microparticle templates but rather than complete dissolution, a recrystallization of the surface to calcite is occurring. These mixed morphology microparticles could still form spherical capsules, but they would be more difficult to dissolve and may contain holes in the capsule shell due to the calcite rhombohedra or aragonite spike formation. Therefore, we believe that the process development for CCNPs could also be extended for improving the LbL process for microparticle templates.

6.3.2. Materials and Methods

6.3.2.1. Chemicals

Poly (vinylsulfonic acid) (PVSA), sodium carbonate (Na_2CO_3), calcium chloride ($CaCl_2$), poly (sodium 4-styrenesulfonate) (PSS, average Mw 70 kDa), poly (diallyldimethylammonium chloride) (PDADMAC, average Mw 100-200 kDa), ethylenediaminetetraacetic acid (EDTA) and buffer salts ($NaHCO_3$, CHES and TRIS) were obtained from Sigma and used as received.

6.3.2.2. LbL Deposition of PEMs on CCNPs

PEMs were deposited on the CCNPs using LbL. CCNPs suspended in 1 mL of 0.1 M $NaHCO_3$ buffer pH 9 were added dropwise to PE solutions subjected to constant sonication for 10 min. The PEs employed were PDADMAC and PSS, each prepared at 20 mg/mL in 0.1 M $NaHCO_3$. The CCNPs were rinsed with 0.1 M $NaHCO_3$ pH 9 buffer between each deposition step to remove excess PE. PDADMAC was deposited initially followed by PSS/PDADAMAC until 10 bilayers were achieved. Hollow capsules were produced from the final PEM-coated CCNPs by exposing them to excess EDTA at pH 7.2.

6.3.2.3. SEM

CCNP and NC images were captured using a JEOL 7500 SEM with a field emission source. Stock solutions of CCNPs/NCs were diluted to 1/20 and 2µl of the diluted solution was placed on a clean silica support and dried in a vacuum chamber overnight. All samples were sputter coated with 4 nm of palladium/platinum prior to taking the images. All EDS spectrum were obtained using an Oxford Energy Dispersive X-ray Spectrometry system attached to the SEM system.

6.3.3. Results and Discussion

6.3.3.1. Buffer Stability

The LbL process entails repeated cycles of washing and resuspension of the CCNPs. Determining the optimal buffer (both type and pH) to use when coating $CaCO_3$ without dissolving the core and releasing the encapsulated material is critical. Therefore, the first step in developing this process was to understand the influence of

buffer on particle stability. It has been reported that vaterite CCNPs are more stable in alkaline conditions,[310] but we observed that the type of buffer used has an effect on CCNP stability as well. The CCNPs were not stable in all buffer systems at alkaline pH; for example, the CCNPs formed aggregates when suspended in alkaline phosphate buffer. The stability of the particles was analyzed for three different buffer systems (CHES, TRIS and $NaHCO_3$) keeping the pH constant at 9. For these studies, the fabrication process of the CCNPS was scaled down by adding 1.5 mL of 20 mM Na_2CO_3 to a stirred solution of 1.5 mL of 20 mM $CaCl_2$ containing 0.16 µM PVSA. The formed CCNPs were suspended in 5mL of buffer and washed under sonication. This process was repeated six times. The CCNPs were washed repeatedly in buffer solutions to imitate the repeated cycles of washing and resuspension characteristic of the LbL process. The size distribution and concentration of the CCNPs were measured before and after washing (under sonication) in the three buffer systems (Figure 6.13). It was evident that CCNPs (mean dia. 170 nm) suspended in 0.1 M $NaHCO_3$ buffer pH 9.0 had greater concentration both before and after repeated washing compared to CCNPs suspended in 0.1 M CHES buffer (pH 9.0) and 0.1 M TRIS buffer (pH 9.0). Cumulative concentration of CCNPs suspended in $NaHCO_3$ before repeated washing was 637% and 249% greater than the cumulative concentration of CCNPs suspended in CHES and TRIS respectively. No significant decrease in particle concentration after washing the particles repeatedly in $NaHCO_3$ was observed (Figure 6.13 inset). This established that the CCNPs are most stable in 0.1 M $NaHCO_3$ pH 9.0 buffer. Therefore, the PEs

PDADMAC and PSS were suspended in 0.1 M $NaHCO_3$ pH 9.0 buffer and 0.1 M $NaHCO_3$ pH 9.0 buffer was used in all the rinsing steps of the LbL process.

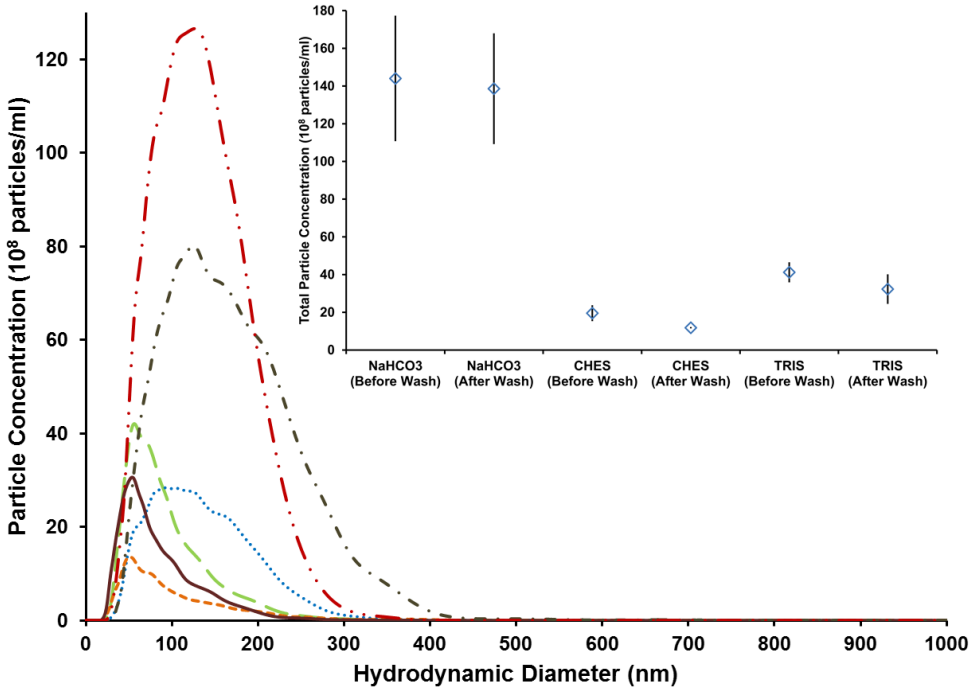

Figure 6.13: NTA plots showing the change in concentration of CCNPs before washing in $NaHCO_3$ (red — • • —), CHES (maroon —), TRIS (blue • •) and after washing in $NaHCO_3$ (black — • —), CHES (orange - - -), TRIS (green — —). Inset: Data representing cumulative concentration of CCNPs before and after washing in $NaHCO_3$, CHES and TRIS buffer. Error bars represent 95% confidence intervals for three separate batches.

6.3.3.2. LbL Deposition

Using LbL assembly, PE multilayers (PEMs) were deposited on the CCNPs. Briefly, CCNPs suspended in 1mL of 0.1 M $NaHCO_3$ buffer (pH 9) were added dropwise to PE solutions subjected to constant sonication for 10 min. The PEs employed were PDADMAC and PSS, each prepared at 20 mg/mL in 0.1 M $NaHCO_3$. The PEs PDADMAC and PSS were chosen because they remain sufficiently charged at

alkaline pH. The CCNPs were rinsed with 0.1 M $NaHCO_3$pH 9 buffer between each deposition step to remove excess PE. PDADMAC was deposited initially followed by PSS/PDADAMAC until 10 bilayers were achieved. Hollow capsules were produced from the final PEM-coated CCNPs by exposing them to excess EDTA at pH 7.2.

The zeta potential for the CCNPs was measured after each PE deposition step to confirm surface charge reversal. The results reported in Figure 6.14 shows the zeta potential reversal after each deposition step of the cationic/anionic PE. The magnitude of the surface charge for the cationic and anionic PE-coated CCNPs is large (36.15 ± 4.70 mV; -43.31 ± 5.01 mV), suggesting colloidal stability of the suspended PE coated CCNPs. The zeta potential progressively increases in magnitude, revealing the more complete PE coating with the increase in the number of PE layers that is commonly seen in PEM systems applied to small particulates. After the deposition of 10 bilayers, the PEM-coated CCNPs were well dispersed when suspended in 0.1 M $NaHCO_3$ pH 9.0 buffer.

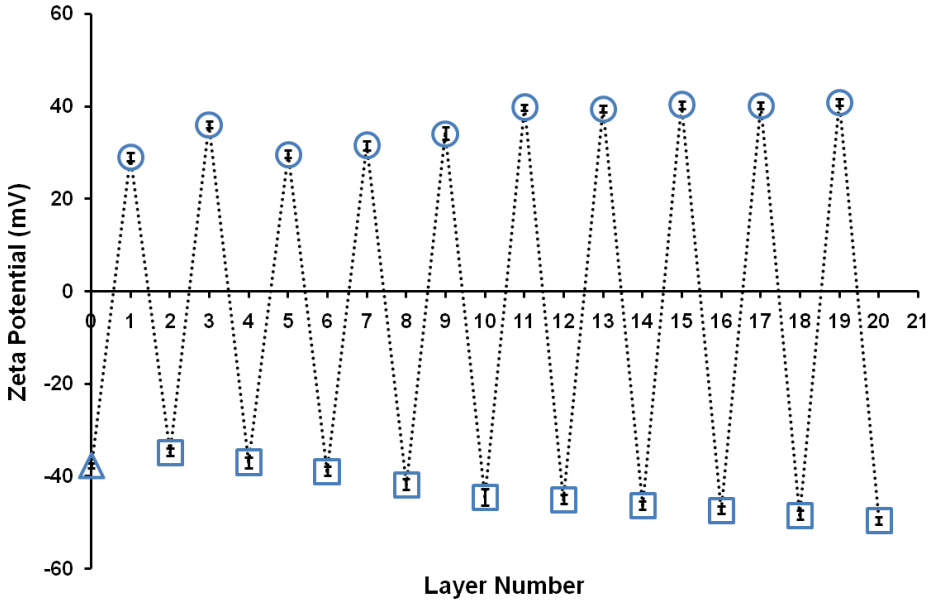

Figure 6.14: Zeta potential change with increase in the number of polymer layers coated on CCNPs.Δ = CCNP, ○ = PDADMAC and □ = PSS. Error bars represent 95% confidence intervals for three separate batches.

6.3.3.3. Capsule Formation

Hollow nanocapsules were made using the process described earlier. The morphology of the CCNPs and the nanocapsules was visualized by SEM imaging (Figure 6.15). The images of the CCNPs show a spherical morphology, which is typical for vaterite $CaCO_3$ particles. The SEM images of the nanocapsules are similar to SEM images of microspheres consisting of a mixed population of spherical nanocapsules and collapsed nanocapsules.[308] This is expected, as dried capsules collapse revealing folds and crevices because of their hollow interior. The average increase in diameter of colloidal particles coated with PDADMAC/PSS has been reported to be 5 nm per bilayer.[311] Comparing the diameters of the nanocapsules and the CCNPs we found an average increase of 33.6 nm with each bilayer of PDADMAC/PSS added. The unusual

increase in the nanocapsule wall thickness may be attributed to the highly porous structure of the CCNPs which favors the formation of thicker capsule walls, which has been observed in case of micro capsules fabricated from $CaCO_3$ micro particles templates as well.[312]

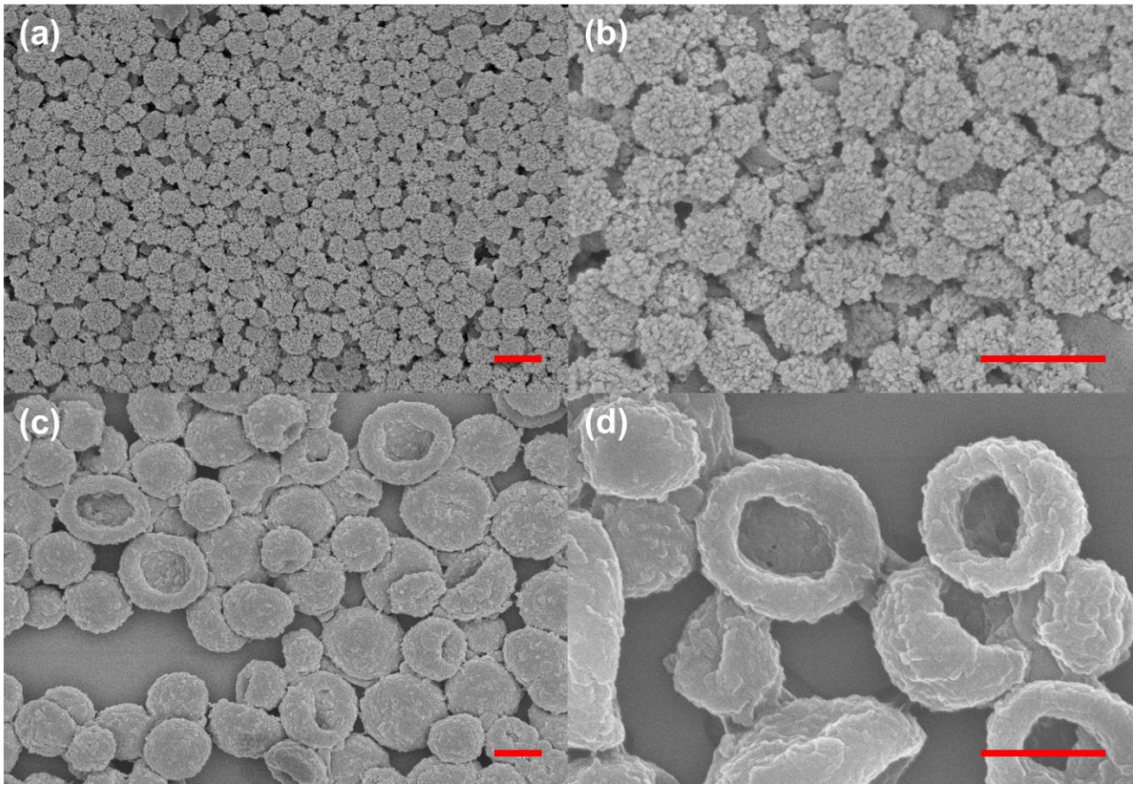

Figure 6.15: SEM images of sputter-coated CCNPs (a) 20,000 X magnification (b) 50,000 X magnification and NCs (c) 20,000 X magnification (d) 50,000 X magnification. Scale bars correspond to 500 nm.

Elemental analysis under higher magnification was carried out using an EDS system attached to the SEM to confirm that $CaCO_3$ was no longer present in the nanocapsules. The EDS spectrum (Figure 6.16A) of the CCNPs shows a distinct calcium peak that is absent in the EDS spectrum of the nanocapsules (Figure

6.16B).Both of the EDS spectra indicate the presence of platinum, palladium and silicon resulting from the silicon substrate and the sputter-coated film.

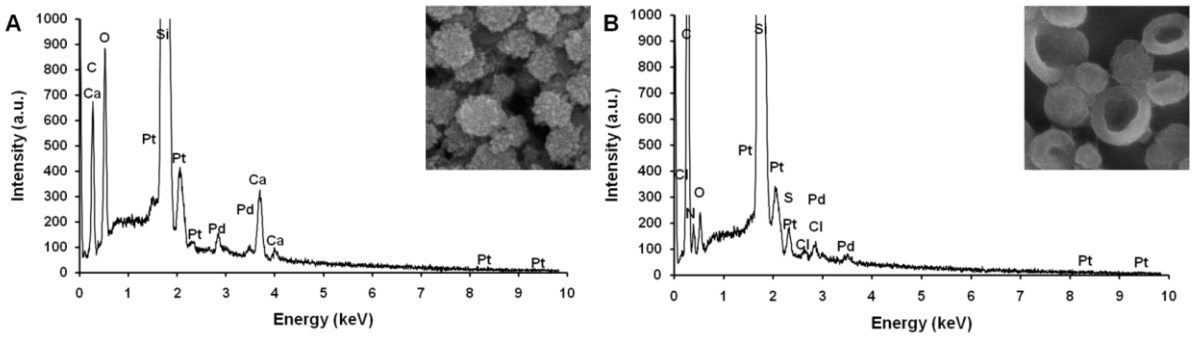

Figure 6.16: Energy Dispersive X-ray Spectroscopy spectra for sputter coated (A) CCNPs and (B) nanocapsules.

6.3.4. Conclusion

This section showed the redevelopment of the LbL process for coating CCNPs followed by complete dissolution of the CCNP core to form a capsule. This LbL technique shown in this sections represents a significant redesign of the commonly used procedures for LbL on $CaCO_3$ templates. Typically, PEs were used at a concentration of 2 mg/mL and were suspended in DI-H_2O without any control on pH and wash steps also used DI-H_2O.[20, 22, 313] The LbL method is quite robust, so even under non-ideal conditions capsule formation can still be achieved. However, this will lead to overall poorer quality capsules, more aggregation, more batch to batch variation, and more operator to operator variation. This is particularly important when the LbL is used as a diffusion limiting membrane for drug release or sensor applications. Even small changes in the PEM properties will prevent proper operation. We believe that more consistent

results can be achieved for all $CaCO_3$ based LbL by using the optimized conditions reported in this section.

6.4. Encapsulation of ConA into $CaCO_3$

6.4.1. Background

The encapsulation of ConA *via* $CaCO_3$ coprecipitation requires 2 major considerations: (1) the stability of ConA during the coprecipitation process and (2) the binding capability of ConA after dissolution of the $CaCO_3$ core. Successful implementation of an encapsulated ConA assay requires addressing both of these issues. To the best of our knowledge, the encapsulation of ConA into carbonate templates has not been studied.

ConA is notably unstable in free solution.[46] The coprecipitation process has a high loading capability but requires rapid stirring for 1 – 10 min, which leads to bubble formation and interfacial forces that can denature protein. To mitigate this stability issue, PEGylated ConA was used because it was shown to have better stability in free solution.[99] Alternative methods to coprecipitation include pre-loading by adsorption onto preformed $CaCO_3$ and post-loading by diffusing into preformed capsules. Post-loading and adsorption approaches have been shown to maintain the stability of enzymes better than coprecipitation, but only a significantly lower amount of material could be encapsulated.[314] Additionally, the post-loading or adsorption of sterically stabilized, high charge density, and larger materials such as NPs and PEGylated ConA would be even less efficient.[315]

After the coprecipitation and LbL shell formation, a hollow capsule is produced by dissolving the carbonate core. EDTA, citric acid, and GDL are widely accepted as gentle approaches to achieve carbonate dissolution by the chelation of calcium ions.[23, 314, 316-318] This is acceptable for most application (*i.e.* enzymes, antibodies), however both calcium and a transition metal are required as cofactors for ConA to bind sugars and chelation of these cofactors deactivates ConA.[319] The reintroduction of these divalent metals to reactivate ConA is possible but the results are concentration dependent and inconsistent.[320] This is further complicated when the ConA is inside a capsule, where the introduction of Ca^{2+} and Mn^{2+} across the membrane is not trivial.[321] To avoid these problems a method for complete carbonate dissolution without the use of chelation was developed.

6.4.2. Materials and Methods

6.4.2.1. Chemicals

$MnCL_2$ (ACS, 98%), $CaCL_2$ (ACS, 96%), Poly (vinylsulfonic acid) (PVSA), sodium carbonate (Na_2CO_3), calcium chloride ($CaCl_2$), poly (sodium 4-styrenesulfonate) (PSS, average Mw 70 kDa), poly (diallyldimethylammonium chloride) (PDADMAC, average Mw 100-200 kDa), and MES sodium salt were all obtained from Sigma Aldrich.

6.4.2.2. Buffers

Buffer 1 - 5 mM $NaHCO_3$ pH 9, Buffer 2 - 5 mM TRIS pH 7.2, Dissolution buffer - MES buffer 0.5 M pH 6.1 stock, 0.2 M pH 6.1 used for dissolution, PDADMAC solution - 20 mg/mL PDADMAC in buffer 1, PSS solution 1 - 20 mg/mL PSS in buffer

1, PAH solution - 10 mg/mL PAH in buffer 2, PSS solution 2 - 10 mg/mL PSS in buffer 2, TRIS binding buffer - 50 mM TRIS pH 7.4, 1 mM $CaCl_2$, 1 mM $MnCl_2$, 0.5 M NaCl.

6.4.2.3. Synthesis of PEGylated ConA

ConA was PEGylated with 5 kDa PEG using the procedure reported by Locke *et al*. with minor modification.[99] ConA was prepared at a concentration of 10 mg/mL in 0.1 M $NaHCO_3$ pH 8.5 with 0.15 M NaCl with 1.9 mg of methyl-mannose. Under mild stirring 8 mg of PEG-SVA was added. The solution of incubated under stirring for 6 h at RT and then left for 12 h at 4°C. Excess PEG and mannose was removed by filtering with a 30 kDa microsep 5 times at 4000 RCF for 15 min.

6.4.2.4. Encapsulation of PEGylated ConA

PEG-ConA was buffer exchanged twice with 0.2 M Na_2CO_3 with 30 kDa Nanosep at 5000 RCF for 15 min immediately before encapsulation. PEG-ConA was mixed with fluorescently labeled competing ligand in a 500 μL total volume of 0.2 M Na_2CO_3 incubating for 5 min while stirring at 400 RPM. Stirring was increased to 800 RPM and 500 μL of 0.2 M $CaCl_2$ was rapidly added and kept stirring for 5 min. A 40 μL amount of PVSA was added, the speed was reduced to 600 RPM, and the solution was stirred for another 5 min. Particles were collected by centrifugation at 1000 RCF for 1 min and the supernatant was discarded. The particles were washed once more and then used for LbL modification.

6.4.2.5. Binding Capability of ConA after Encapsulation and Dissolution with MES

PEGylated ConA was encapsulated in to $CaCO_3$ spheres *via* coprecipitation. The particles were washed twice with 5 mM $NaHCO_3$ pH 8 buffer to remove non-

encapsulated ConA. The $CaCO_3$ particles containing ConA were then dissolved by exposing to 5 mL of 0.1 M MES for 5 mins. The solution was then filtered with a 10 kDa microsep to retain ConA while removing dissolved $CaCO_3$. This process was repeated 2 more times, and the ConA was finally resuspended in TRIS binding buffer. Fluorescence anisotropy was used to determine the binding affinity of ConA using a procedure described elsewhere.[96]

6.4.2.6. LbL on $CaCO_3$ Microparticles with PDADMAC and PSS

The particles were resuspended in 1000 μL of buffer 1 and mixed thoroughly by pipette to redisperse the particles. 1000 μL of PDADMAC solution was added and mixed by pipette for 1 min. The particles were collected at 1000 RCF for 1 min, discarding the supernatant containing excess PE and washed once with 1000 μL of buffer 1. The sample was resuspended in 500 μL of buffer 1 and mix thoroughly by pipette. 1000 μL of PSS solution 1 was added and the solution was mixed by pipette for 1 min. The particles were collected at 1000 RCF for 1 min, discarding the supernatant containing excess PE and washed once with 1000 μL of buffer 1. This completes 1 bilayer, the process was repeated to add the desired number of bilayers.

6.4.2.7. LbL on $CaCO_3$ Microparticles with PAH and PSS

The particles were resuspended in 1000 μL of buffer 2 and mixed thoroughly by pipette to redisperse the particles. 1000 μL of PAH solution was added and mixed by pipette for 1 min. The particles were collected at 1000 RCF for 1 min, discarding the supernatant containing excess PE and washed once with 1000 μL of buffer 2. The sample was resuspended in 500 μL of buffer 2 and mix thoroughly by pipette. 1000 μL

of PSS solution 2 was added and the solution was mixed by pipette for 1 min. The particles were collected at 1000 RCF for 1 min, discarding the supernatant containing excess PE and washed once with 1000 μL of buffer 2. This completed 1 bilayer, the process was repeated to add the desired number of bilayers.

6.4.2.8. Carbonate Dissolution for Capsule Formation

The $CaCO_3$ core was dissolved by washing 4 times with 5 mL of dissolution buffer, incubating for 5 min and then centrifuging at 1000 RCF for 5 min. The capsules were then washed twice with TRIS binding buffer by centrifuging at 1000 RCF for 5 min.

6.4.2.9. SEM

Microcapsule images were captured using a JEOL 7500 SEM with a field emission source. Microcapsule containing sample was placed on a clean silica support and dried in a vacuum chamber overnight. Samples were sputter coated with 4 nm of palladium/platinum prior to taking the images. All EDS spectrum were obtained using an Oxford Energy Dispersive X-ray Spectrometry system attached to the SEM system.

6.4.3. Results and Discussion

6.4.3.1. Dissolution of $CaCO_3$ Without Chelation

$CaCO_3$ can be dissolved using calcium chelating chemicals or by lowering the pH to increase the solubility. For the dissolution of ConA containing carbonate particles the acidic dissolution process is preferred in order to preserve the divalent cation cofactors. Acidic dissolution can be achieved by titration with acid or by incubation in a buffer. Titration with acid is not suitable for dissolving protein containing capsules

because if the pH gets too low then the protein will be denatured. Additionally, ConA forms a dimer below pH 5.7 which should be avoided with PEGylated ConA since the outcome is unknown. Therefore, the best way to achieve dissolution is by controlling the pH to be low enough to induce carbonate solubility (pH < 7) but high enough to prevent denaturation and dimerization (pH > 5.7). By exposing the carbonate particles to a buffer in this pH region, dissolution could be achieved without affecting the protein. The buffer used must be chosen carefully because most will complex with metal ions to some degree. Buffer that contains amines, carboxylic acids, phosphates, hydroxymethyl, or hydroxyl ethyl groups are all known to complex with cationic metals.[322] A buffer that does not interact with metals was discovered when using commonly used assays for protein quantification (*i.e.* bicinchoninic, Lowry) that rely on a Cu^{2+} catalyst to determine protein concentration. The presence of metal complexing ions in these assays prevents accurate protein quantification. Out of all of Good's buffers, only MES, MOPS, and PIPES were found to not interfere with the assay.[323] Of these buffers, MES is the most suitable for carbonate dissolution because its pKa of 6.1 allows dissolution at a pH that does not denature or induce dimerization of ConA.

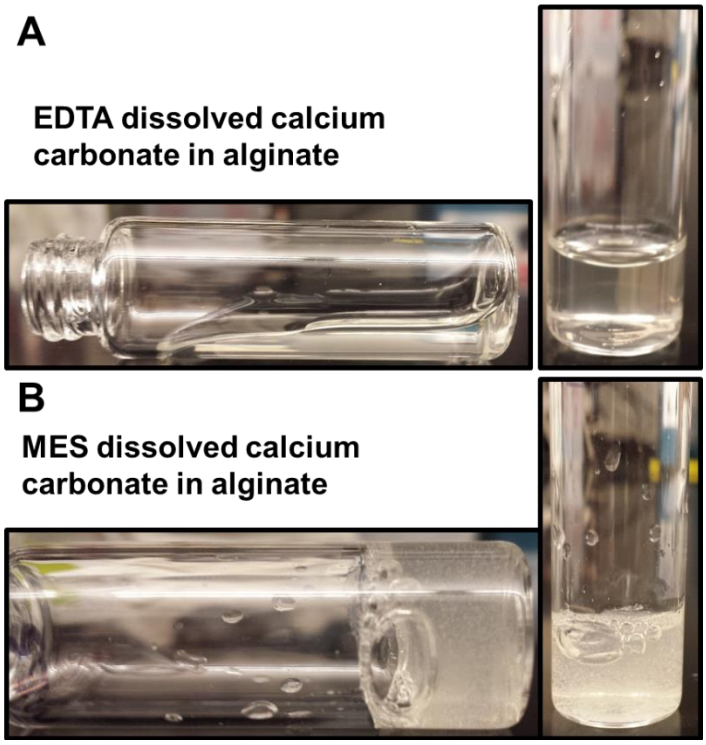

Figure 6.17: Photographs of sodium alginate with $CaCO_3$ after dissolution of the $CaCO_3$ with (A) EDTA or (B) MES.

The dissolution capability of MES without chelating calcium was demonstrated visually by dissolving $CaCO_3$ mixed with sodium alginate. When EDTA was used the solutions turns clear to indicate that the $CaCO_3$ is dissolved, but the alginate does not form a gel (Figure 6.17). The EDTA chelates the calcium which prevents it from cross-linking the alginate strands. In contrast, when MES is used to dissolve $CaCO_3$, the liberated calcium is capable of cross-linking the alginate to form a solid gel (Figure 6.17). This shows that MES is capable of dissolving $CaCO_3$ without chelation of the calcium. However, gel formed by MES still appeared cloudy, this is possibly due to incomplete dissolution of $CaCO_3$ (Figure 6.17). For this reason, further investigation of the dissolving capability of MES was needed.

6.4.3.2. MES Dissolution of $CaCO_3$ Templates for Capsule Formation

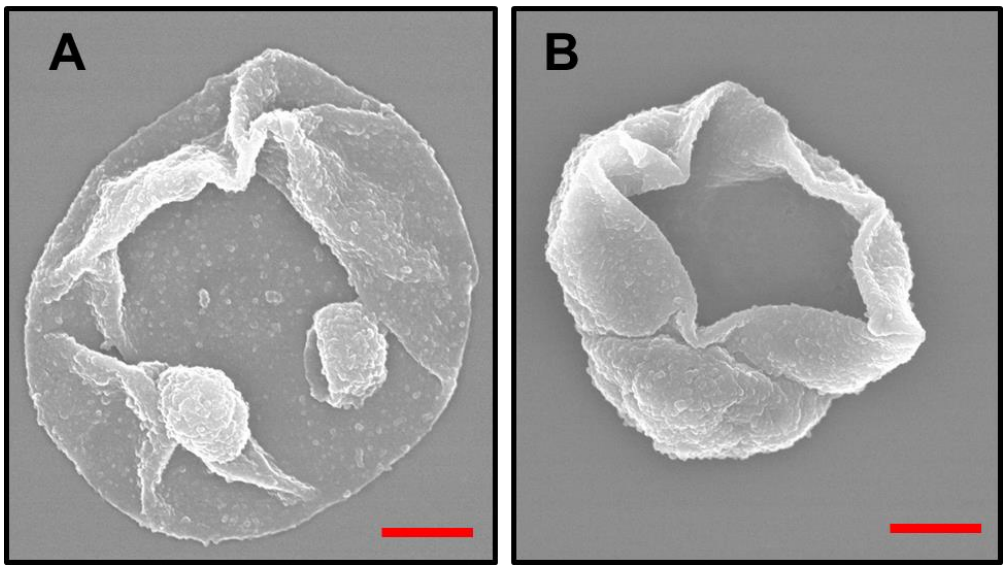

Figure 6.18: SEM images of capsules produced by dissolving the carbonate core with MES buffer. Scale bars correspond to 1 µm.

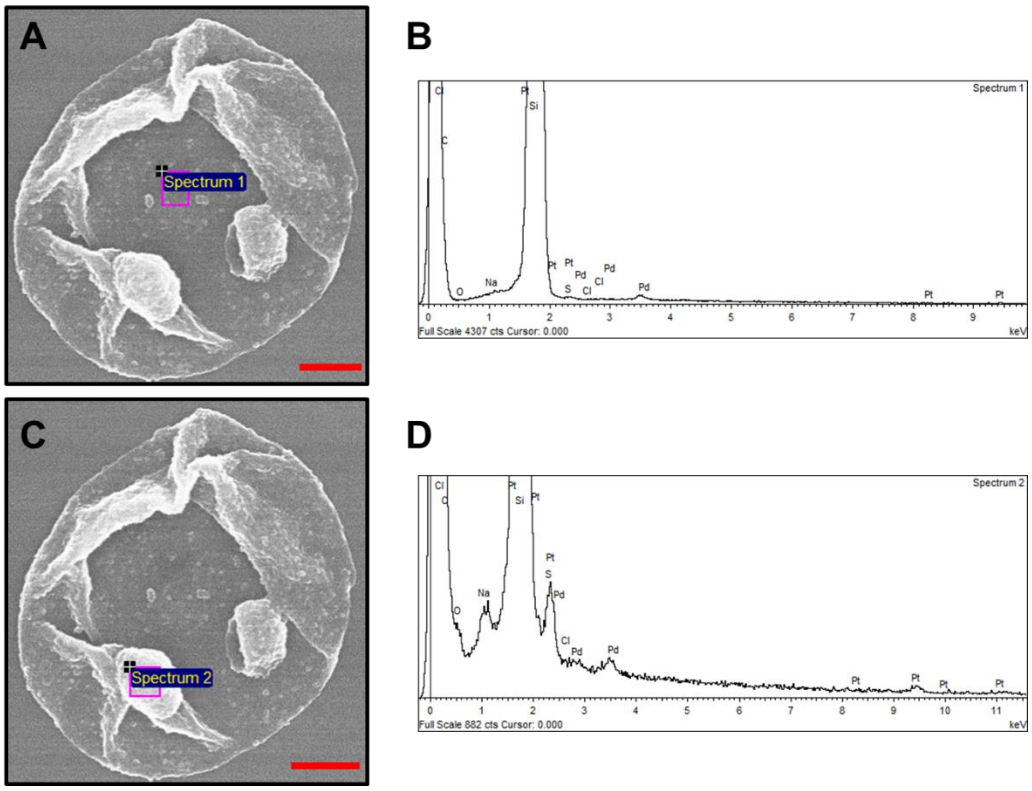

Figure 6.19: SEM images and EDX spectra of microcapsules produced by dissolution of the carbonate core with MES buffer. Scale bars correspond to 1 µm.

The ability of MES to dissolve $CaCO_3$ was tested using PEM coated microparticles. The complete dissolution of the $CaCO_3$ core to produce a microcapsule using MES buffer was confirmed by SEM. Figure 6.18A and Figure 6.18B show two capsules produced using MES buffer to dissolve the core. Figure 6.19B and Figure 6.19D show the EDX spectra of two portions of one of the capsules confirming the absence of any measurable calcium.

Table 6.4: Dissolution of CCNPs and CCMPs Synthesized with PVSA using MES

Conditions						Results	
Trial	$CaCl_2$ (M)	Na_2CO_3 (M)	Total Vol. (mL)	PVSA (uL)	Time of PVSA Addition (s)	MES Washes (#)	Add. Notes
1	0.02	0.02	4	20	0	1	
2				10		2	
3				5		3	
4				2		4	
5				0		7	Did not completely dissolve
6				40	1	1	
7					30	2	
8					60	2	
9					180	2	
10					600	2	
11	0.2	0.2	1	50	600	2	

A series of qualitative screening experiments were used to determine the effectiveness of MES dissolution of $CaCO_3$ particles synthesized with PVSA (Table 6.4). Effectiveness of dissolution was determined by visual inspection. The PVSA is used to produce CCNPs but also servers to maintain the vaterite polymorph. Decreasing PVSA concentration increases the amount of MES wash steps required to completely dissolve the $CaCO_3$. When no PVSA was present the particles could not be completely dissolved even with 7 washes. This may be due to the formation of calcite without PVSA present. It was found that PVSA could even be added up to 600 seconds after the nucleation began and still provided the particle stability needed for dissolution in two washes. The PVSA stabilization was even effective under conditions that produced microparticle templates.

6.4.3.3. Encapsulation of PEGylated ConA

Table 6.5: Encapsulation of PEGylated ConA into carbonate particles under various conditions.

Conditions						Results		
Trial	$CaCl_2$ (M)	Na_2CO_3 (M)	Total Vol. (mL)	PVSA (uL)	Time of PVSA Addition (s)	ConA Added (mg)	ConA Encapsulated (mg)	EE%
1	0.02	0.02	4	20	0	4.8	0.11	**2.29**
2				10				
3				5				
4				2				
5				0				
6				40	1	2	0.036	**1.80**
7					30			
8					60			
9					180			
10					600	1	0.073	**7.30**
11	0.2	0.2	1	50	600	1	0.142	**14.20**
12						5	0.578	**11.56**

The encapsulation efficiency (EE) of PEGylated ConA under various conditions was tested, focusing on conditions that produced the easily dissolvable particles (Table 6.5). When PVSA was added during the particle formation process an EE of 2.29% was achieved. If the PVSA was added immediately after nucleation EE was 1.8% but if PVSA was added 10 minutes after nucleation then EE was 7.3%. This large increase in EE is likely due to the fact that a large portion of material encapsulation is expected to be due to adsorption so the particle surface. When PVSA is added during synthesis quickly afterwards, it assembles on the surface and prevents protein adsorption through electrostatic repulsion. When using conditions for microparticle formation the EE is 14.2%, but under the same conditions with higher PEGylated ConA the EE goes down to 12%. There is a maximum amount of ConA that can be encapsulated, so increasing the

initial amount to be encapsulated will produce depreciating returns. This shows that PEGylated ConA can be successfully encapsulated, with much higher EE in microparticles.

6.4.3.4. Binding Affinity of ConA After MES Dissolution

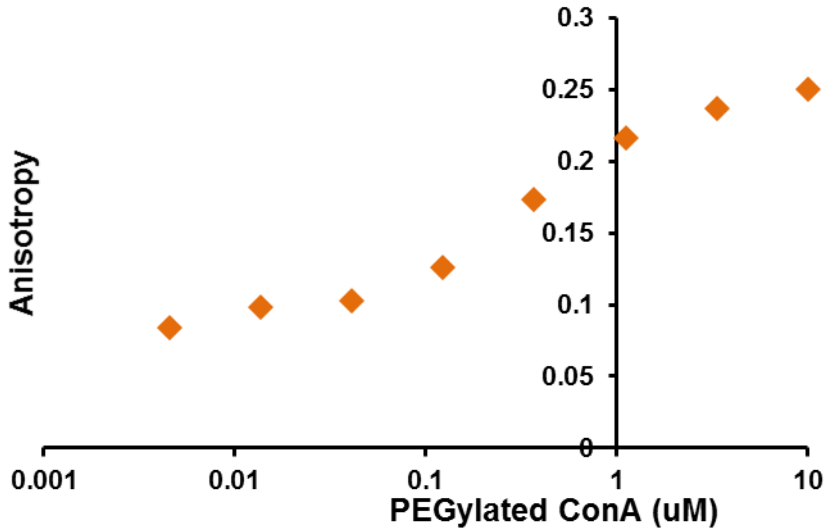

Figure 6.20: Fluorescence anisotropy of fluorescently labeled competing ligand with PEGylated ConA that had been encapsulated in $CaCO_3$ and released by MES dissolution.

The binding capability of PEGylated ConA was tested after encapsulation and dissolution with MES using fluorescence anisotropy (Figure 6.20). These results showed that PEGylated ConA was still capable to of binding sugars after encapsulation and dissolution, with a $K_A = 2.8 \times 10^6\ M^{-1}$. This is only a slight decrease compared to the initial binding affinity PEGylated ConA in free solution, which has a K_A of $5 \times 10^6\ M^{-1}$.

6.4.3.5. Encapsulation of a ConA Assay into $CaCO_3$ Microcapsules

PEGylated ConA-TRITC and fluorescently labeled competing ligand were encapsulated using the process described earlier in this section. The encapsulation of the assay was confirmed by fluorescence microscopy after particle synthesis (Figure 6.21) and capsule formation after dissolution with MES (Figure 6.22). The presence of PEGylated ConA-TRITC and fluorescently labeled competing ligand was confirmed by the highly fluorescent signal localized inside the particles. Glucose exposure of the encapsulated sensor showed some function; unfortunately, these results were initially poor and could not be consistently replicated (data not shown).

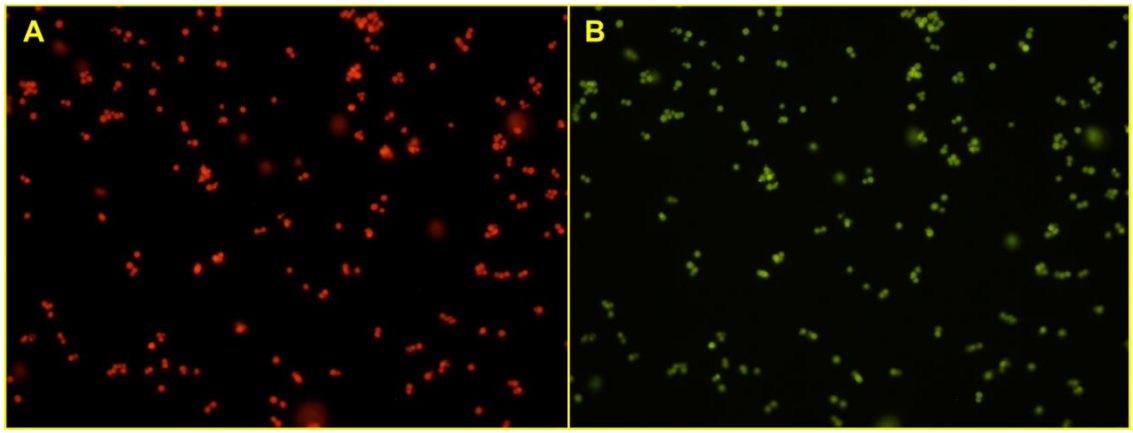

Figure 6.21: Encapsulation of PEGylated ConA-TRITC and a fluorescently labeled competing ligand into $CaCO_3$ particles. (A) excitation/emission for TRITC and (B) excitation/emission for FITC.

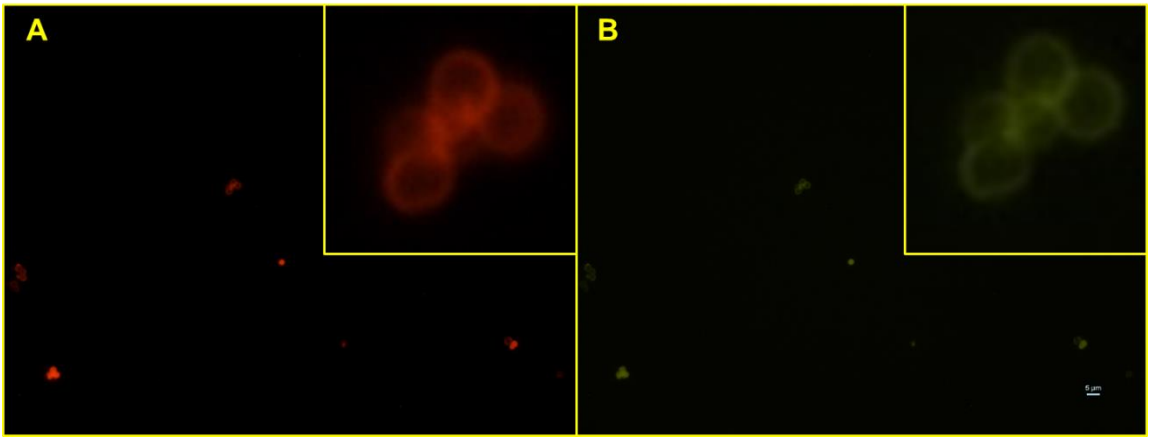

Figure 6.22: PEGylated ConA-TRITC and fluorescently labeled competing ligand in microcapsules made by dissolution with MES. (A) excitation/emission for TRITC and (B) excitation/emission for FITC.

6.4.4. Conclusions

In this section, the dissolution of PVSA stabilized $CaCO_3$ with MES was shown as an effective method for complete particle dissolution for capsule formation without chelating calcium. This process was shown as an alternative method for the commonly used EDTA method when encapsulating materials sensitive to chelation. The encapsulation of PEGylated ConA and release with MES was performed and the PEGylated ConA was found to retain most of its binding affinity. However, the capsule containing the PEGylated ConA-TRITC and fluorescently labeled competing ligand assay was found not to consistently respond to glucose; it was not completely clear why this did not work. One major limitation faced was the low EE and encapsulation amount of PEGylated ConA-TRITC. The assay production and encapsulation is both expensive and time consuming. The poor encapsulation results in a large amount of wasted sample and time, making the entire process extremely inefficient. Additionally, we were unable to accurately determine the concentration of the encapsulated components due to

interference from spectral overlap and scattering. This makes it difficult to tune the absolute concentration and relative ratios of the encapsulated components, which is required for optimizing a competitive binding assay. The encapsulation of a nanomaterial assay was not attempted because the problems would only be further magnified. We believe that overcoming the encapsulation problems will require utilizing an entirely different encapsulation methodology.

7. CONCLUSIONS AND FUTURE DIRECTION

7.1. LbL on Nanomaterials

A novel method was developed for the pH-dependent LbL modification of nanomaterials using solvent precipitation, providing a new capability to modify a variety of nanoscale particles with different core material, surface ligand, surface charge, size, and morphology with both weak and weak-strong PEs (Table 7.1). The efficient modification without aggregation was confirmed by UV-Vis, TEM, and NTA. The pH dependent process was particularly critical for the coating of high surface curvature NPs with high recovery. A generalized process was developed by considering the surface charge density of the NP template in relation to the charge density of the PE. This provides a framework for rationalizing the choice of deposition conditions when coating any core materials with any PE. Because of the time consuming nature of LbL on NPs, minimizing the processing steps and increasing the yield was seen as critical advance to make the method practical.

A solvent precipitation step was introduced for buffer exchange and concentration the NPs before ultracentrifugation. This allows for PE adsorption under the dilute conditions necessary for minimizing aggregation, while still allowing for processing a large amount of sample in a reasonable amount of time. Without this step it would take 10 – 25 times longer to process the same amount of sample. Again, these are practical advances with solid scientific foundation that enable more efficient processing for practical application of LbL to modify a broad spectrum of nanomaterials.

Table 7.1: Summary of materials and PEs studied for LbL modification.

Material	Size	Surface Ligand	Polyelectrolytes
AuNP	5nm	MUA	PAH/PAA
			PAH/PSS-co-MA 1:1
			PAH/PSS-co-MA 3:1
		MPA	PAH/PSS-co-MA 1:1
AgNP	40nm	Hydroxylamine	PAH/PSS-co-MA 1:1
CdSe/ZnS QD	7nm	DHLA	PAH/PAA
AuNR	25 nm x 64 nm	CTAB	PSS-co-MA 1:1

The LbL coating imparted enhanced electrosteric stability by increasing the magnitude of the surface charge and providing a steric barrier. This can be observed as enhanced colloidal stability and consistent optical properties across varying pH and ionic strength conditions (Table 7.2). The colloidal stability of the NP can generally be predicted by the terminal PE coating, with some variation depending on particle size and material type. Interestingly, this enhanced stability was found even with only a single bilayer of PE coating of PAH and PSS-*co*-MA 1:1. This formulation was found to have the highest stability in varying pH and ionic strength (Table 7.2). The hydrodynamic size of the coated nanomaterials was investigated by NTA and revealed a 1 - 3 nm increase per layer of added polyelectrolyte. This makes LbL modification a useful tool for the stabilization of nanomaterials with a minimal hydrodynamic size; an important feature for the development of energy transfer sensors.

The major drawback of LbL was the inconsistent effect on the optical properties of the different nanomaterials. This was found for both metal NPs and semiconductor QDs, but the change varied depending on the PE used and the material type. For

instance, the quantum yield of QDs was unaffected by the addition of PAH, but decreased dramatically after being coated with PAA. However, AuNPs showed enhancement of the plasmon resonance for PAH, PAA, and PSS-*co*-MA. AgNPs were unaffected by PAH, but showed a decreased plasmon resonance for PSS-*co*-MA. The inconsistent nature of these changes makes determining the root cause difficult, but we suspect two factors may be contributing: (1) the change in refractive index after each layer and/or (2) the chemical interaction the PE with the NP surface is changing the electronic properties. Future work to explore these potential causes would require experimental design guided by modeling of the PE wrapping and associated changes in optical properties.

Table 7.2: Summary of colloidal properties for different materials, surface ligands, and polymer coatings. Zeta potential is reported at a pH where the particles is expected to be fully ionized.[1] pH stability is the range over which the zeta potential magnitude remains above 30 mV.[2] Ionic strength stability was determined by change in UV-Vis plasmon peak location or NTA peak size changes.[3]

Core Material	Terminal Coating / Surface Ligand	Zeta Potential[1] (mV)	Colloidal Stability	
			pH Stability[2]	Ionic Strength[3] NaCl (mM)
AuNP	MUA	-38.0 ± 1.8	4.5 - 9	
	MUA-(PAH)	46.5 ± 0.9	4.5 - 7	
	MUA-(PAH/PAA)	-48.2 ± 1.3	4.5 - 9	
	MUA-(PAH/PSS-co-MA 1:1)	-53.1 ± 2.8	3.5 - 9	
	MUA-(PAH/PSS-co-MA 3:1)	-47.8 ± 5.1	3.5 - 9	
	MPA	-14.1 ± 2.7		0
	MPA-(PAH)	21.3 ± 2.6		
	MPA-(PAH/PSS-co-MA 1:1)	-55.4 ± 1.2		0 - 1000
AgNP	HA	-41.0 ± 1.7	4 - 9	0 - 50
	HA-(PAH)	41.0 ± 0.1	3.5 - 8.1	
	HA-(PAH/PSS-co-MA 1:1)	-48.0 ± 0.7	2 - 9	0 - 500
AuNR	CTAB	30.8 ± 0.4		
	CTAB-(PSS-co-MA 1:1)	-41.3 ± 0.7		0 - 50
CdSe/ZnS QD	DHLA	-38.6 ± 1.6		
	DHLA-PAH	67.0 ± 7.1		
	DHLA-(PAH/PAA)	-51.5 ± 2.2		

The utilization of the weak-strong copolymer for bioconjugation was an important feature for maintaining stability during bioconjugation with carbodiimide chemistry. The dual character of the copolymer allows for bioconjugation with the weak groups (maleic acid), while the strong groups (styrene sulfonate) remain charged to improve colloidal stability during the bioconjugation. This stability is critical for successfully implementing the two-step method required to prevent interprotein crosslinking when using carbodiimide chemistry. This effectiveness of this process was demonstrated with AgNPs but was also easily extended to AuNR bioconjugation. Both materials were conjugated to ConA using nearly identical procedures even though they

are different core materials that initially had different surface charge and chemistry. This demonstrated LbL as a general coating procedure and transitional coating for bioconjugation.

7.2. Nanomaterial-Enabled Affinity Sensors

The reversible energy transfer between donor OVA-AuNCs and acceptor AuNR-ConA was demonstrated for the application of glucose sensing. The sensor demonstrated a linear response to glucose between 1 – 200 mM glucose but the sensitivity was highest from 10 – 500 mM. Blood glucose levels of a diabetic patient typically fluctuates between 2 – 40 mM,[324] therefore further optimization of the sensor is necessary to optimize the sensitivity within this range. This can be achieved by increasing the ratio of receptor to ligand by decreasing the concentration of OVA-AuNCs or increasing the concentration of GNR-ConA. Decreasing the OVA-AuNC concentration would require first increasing the quantum yield. This could be achieved by alternative synthesis techniques such as microwave assisted synthesis or alloying with other noble metals.[272] The effect of these different synthesis methods on the binding capability will need to be studied. Increasing AuNR-ConA concentration also increases the static quenching, which would decrease SNR. Plasmonic nanomaterials have a broad extinction spectra that would cause static quenching of excitation light. Therefore, overcoming this problem would require using alternative acceptor nanomaterials such as non-fluorescent and non-plasmonic NCs or alternative donor nanomaterials such as upconverting NPs (UCNPs). These two potential sensor schemes using either UCNPs or NCs are shown in Figure 7.1.

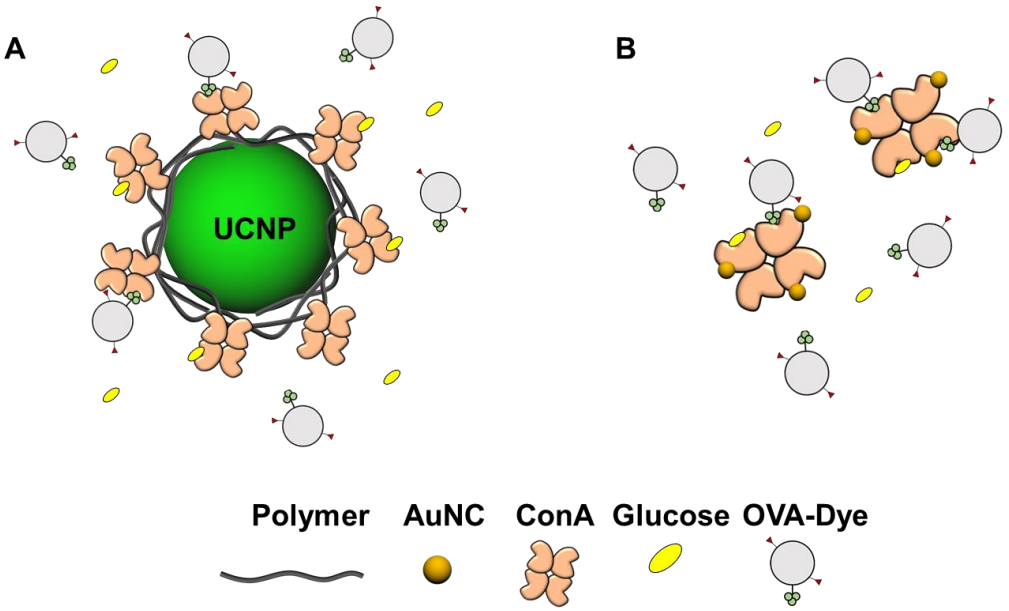

Figure 7.1: Alternative energy transfer schemes utilizing ConA and OVA with (A) UCNPs as a donor material or (B) AuNCs as an acceptor.

NCs are potentially ideal acceptor nanomaterials because they quench at higher efficiencies by following the NSET formalism and their quenching is not based on spectral overlap. Therefore, a single NC – protein complex would have higher quenching efficiency and would be capable of quenching a broad spectrum of donor materials. Additionally, the small size of the NCs would allow the attachment of multiple clusters per protein, further increasing quenching efficiency. The challenge of fabricating such a sensor is the construction of the NC-protein complex. NCs are challenging to manipulate without aggregating and are very close to the size of proteins, making separation by size exclusion methods extremely ineffective. Also, since NCs do not have a plasmon resonance it is difficult to determine their concentration; their size is well below the threshold for NTA.

UCNPs could be used as alternative donor nanomaterials because they are excited at lower energy where plasmonic NPs do not have absorption. For instance, UCNPs are commercially available with a 980 nm excitation and a 650 nm emission. The same process of coating AuNRs could be used to make UCNPs coated with ConA. This could be coupled with an OVA-dye acceptor to create a sensor (Figure 7.1). UCNPs have several advantages for *in vivo* applications: (1) longer (μs) lifetimes, (2) excitation in NIR (better tissue penetration), (3) photobleaching resistance, and (4) no toxicity.[325] Unfortunately, reliable methods for synthesis and coating of UCNPs is still lacking.[325] If these techniques could be improved, potentially using LbL, this material would present the most promise as a donor nanomaterial for moving forward in developing an *in vivo* nanomaterial-enabled glucose sensor.

7.3. Encapsulation of Competitive Binding Assays

This work investigated the encapsulation of ConA based competitive binding sensing chemistry using $CaCO_3$ templates. Because this has never been demonstrated before, the entire process was investigated systematically. The major concern was the stability of the ConA during the encapsulation and dissolution process. However, the use of PEGylated ConA and non-chelating dissolution with MES proved to be a successful method to maintain ConA affinity. Unfortunately, a consistent sensor could not be fabricated but it was not clear what the source of the error was. The main difficulties that prevented this from moving forward were (1) low EE of ConA and (2) the inability to accurately quantify or control the amount of encapsulated material. For a competitive binding sensor the optimization of the receptor and ligand concentrations is

critical. However, the $CaCO_3$ coprecipitation did not allow for good control over the amount of material that could be encapsulated. Additionally, the overall low EE meant a large amount of the sensing chemistry that was not encapsulated had to be discarded. This made the optimization process slow as new material needed to be constantly produced. This is a critical issues when dealing with nanomaterial modified sensing chemistry which is significantly more difficult to synthesize and scale up. We believe that moving forward with encapsulation will require using an alternative encapsulation scheme that allows for better EE efficiency and control of the concentration of encapsulated components.

An alternative approach could utilize the immobilization of ConA into a matrix rather than encapsulation. Such a matrix would need to be highly porous and provide chemical groups capable of conjugation to proteins. A strong candidate for this is the commercially available cross-linked agarose microparticles produced by GE Healthcare under the trade name Sepharose. The Sepharose beads can also be purchased with ConA already conjugated; this is the same material used for producing the High Trap ConA column used for the purification of OVA-AuNCs in section 5. The immobilization of ConA onto Sepharose provides steric stability and prevents self-agglutination to make the ConA extremely stable over time without PEGylation. Additionally, the microparticle form factor makes labeling the ConA with dye or NCs much easier because separation can be achieved at low speed centrifugation or under low flow rates in a chromatography setup. The main question is whether the Sepharose bead can be used as a template for capsule formation. This so far has not been investigated and may

present many challenges that may require further chemical modification of the Sepharose frame. If successful, this could provide a new format for the capsule formation of competitive binding sensors and could easily be extended for other affinity and even enzymatic systems.

REFERENCES

1. Ward, B. W.; Schiller, J. S.; Goodman, R. A., Multiple Chronic Conditions among US Adults: A 2012 Update. *Prev Chronic Dis* **2014,** *11*, E62.

2. Gerteis J, Izrael D, Deitz D, LeRoy L, Ricciardi R, Miller T, Basu J. Multiple Chronic Conditions Chartbook. AHRQ Publications No,Q14-0038. Rockville, MD: Agency for Healthcare Research and Quality. April 2014.

3. American Diabetes Assoication. The Cost of Diabetes. http://www.diabetes.org/advocate/resources/cost-of-diabetes.html (accessed Sept 1, 2015).

4. Gifford, R., Continuous Glucose Monitoring: 40 Years, What We've Learned and What's Next. *Chemphyschem* **2013,** *14* (10), 2032-44.

5. Klonoff, D. C., A Review of Continuous Glucose Monitoring Technology. *Diabetes Technol Ther* **2005,** *7* (5), 770-5.

6. Klonoff, D. C., Continuous Glucose Monitoring: Roadmap for 21st Century Diabetes Therapy. *Diabetes Care* **2005,** *28* (5), 1231-1239.

7. Algar, W. R.; Krull, U. J., New Opportunities in Multiplexed Optical Bioanalyses Using Quantum Dots and Donor-Acceptor Interactions. *Anal Bioanal Chem* **2010,** *398* (6), 2439-49.

8. Algar, W. R.; Krull, U. J., Quantum Dots as Donors in Fluorescence Resonance Energy Transfer for the Bioanalysis of Nucleic Acids, Proteins, and Other Biological Molecules. *Anal Bioanal Chem* **2008,** *391* (5), 1609-18.

9. Sapsford, K. E.; Pons, T.; Medintz, I. L.; Mattoussi, H., Biosensing with Luminescent Semiconductor Quantum Dots. *Sensors* **2006,** *6* (8), 925-953.

10. Hoppener, C.; Novotny, L., Exploiting the Light-Metal Interaction for Biomolecular Sensing and Imaging. *Q Rev Biophys* **2012,** *45* (2), 209-55.

11. Ling, J.; Huang, C. Z., Energy Transfer with Gold Nanoparticles for Analytical Applications in the Fields of Biochemical and Pharmaceutical Sciences. *Analytical Methods* **2010,** *2* (10), 1439.

12. Yun, C. S.; Javier, A.; Jennings, T.; Fisher, M.; Hira, S.; Peterson, S.; Hopkins, B.; Reich, N. O.; Strouse, G. F., Nanometal Surface Energy Transfer in Optical Rulers, Breaking the Fret Barrier. *J Am Chem Soc* **2005,** *127* (9), 3115-9.

13. Sapsford, K. E.; Algar, W. R.; Berti, L.; Gemmill, K. B.; Casey, B. J.; Oh, E.; Stewart, M. H.; Medintz, I. L., Functionalizing Nanoparticles with Biological Molecules: Developing Chemistries That Facilitate Nanotechnology. *Chem Rev* **2013,** *113* (3), 1904-2074.

14. Geszke-Moritz, M.; Moritz, M., Quantum Dots as Versatile Probes in Medical Sciences: Synthesis, Modification and Properties. *Materials Science and Engineering: C* **2013,** *33* (3), 1008-1021.

15. Sperling, R. A.; Parak, W. J., Surface Modification, Functionalization and Bioconjugation of Colloidal Inorganic Nanoparticles. *Philos. Trans. R. Soc., A* **2010,** *368* (1915), 1333-1383.

16. Brichkin, S. B.; Chernykh, E. V., Hydrophilic Semiconductor Quantum Dots. *High Energy Chem.* **2011,** *45* (1), 1-12.

17. Zhang, Y. J.; Clapp, A., Overview of Stabilizing Ligands for Biocompatible Quantum Dot Nanocrystals. *Sensors* **2011,** *11* (12), 11036-11055.

18. De Koker, S.; De Cock, L. J.; Rivera-Gil, P.; Parak, W. J.; Auzely Velty, R.; Vervaet, C.; Remon, J. P.; Grooten, J.; De Geest, B. G., Polymeric Multilayer Capsules Delivering Biotherapeutics. *Adv Drug Deliv Rev* **2011,** *63* (9), 748-61.

19. Morse, J. W.; Arvidson, R. S.; Luttge, A., Calcium Carbonate Formation and Dissolution. *Chem Rev* **2007,** *107* (2), 342-81.

20. Petrov, A. I.; Volodkin, D. V.; Sukhorukov, G. B., Protein-Calcium Carbonate Coprecipitation: A Tool for Protein Encapsulation. *Biotechnol Prog* **2005,** *21* (3), 918-25.

21. Sukhorukov, G. B.; Volodkin, D. V.; Gunther, A. M.; Petrov, A. I.; Shenoy, D. B.; Mohwald, H., Porous Calcium Carbonate Microparticles as Templates for Encapsulation of Bioactive Compounds. *Journal of Materials Chemistry* **2004,** *14* (14), 2073.

22. Volodkin, D. V.; Larionova, N. I.; Sukhorukov, G. B., Protein Encapsulation Via Porous Caco3 Microparticles Templating. *Biomacromolecules* **2004,** *5* (5), 1962-1972.

23. Wang, Y.; Price, A. D.; Caruso, F., Nanoporous Colloids: Building Blocks for a New Generation of Structured Materials. *Journal of Materials Chemistry* **2009,** *19* (36), 6451.

24. Nagaraja, A. T.; Sooresh, A.; Meissner, K. E.; McShane, M. J., Processing and Characterization of Stable, Ph-Sensitive Layer-by-Layer Modified Colloidal Quantum Dots. *ACS Nano* **2013,** *7* (7), 6194-202.

25. Nagaraja, A. T.; Pradhan, S.; McShane, M. J., Poly (Vinylsulfonic Acid) Assisted Synthesis of Aqueous Solution Stable Vaterite Calcium Carbonate Nanoparticles. *J Colloid Interface Sci* **2014,** *418*, 366-72.

26. Biswas, A.; Nagaraja, A. T.; McShane, M. J., Fabrication of Nanocapsule Carriers from Multilayer-Coated Vaterite Calcium Carbonate Nanoparticles. *ACS Appl Mater Interfaces* **2014,** *6* (23), 21193-201.

27. National Diabetes Statistics Report: Estimates of Diabetes and Its Burden in the United States. (accessed Septermber 1, 2015).

28. Clark, C. M., Jr.; Lee, D. A., Prevention and Treatment of the Complications of Diabetes Mellitus. *N Engl J Med* **1995,** *332* (18), 1210-7.

29. Sheetz, M. J., Molecular Understanding of Hyperglycemia's Adverse Effects for Diabetic Complications. *Jama* **2002,** *288* (20), 2579.

30. Pickup, J. C.; Hussain, F.; Evans, N. D.; Sachedina, N., In Vivo Glucose Monitoring: The Clinical Reality and the Promise. *Biosens Bioelectron* **2005,** *20* (10), 1897-902.

31. Keenan, D. B.; Mastrototaro, J. J.; Voskanyan, G.; Steil, G. M., Delays in Minimally Invasive Continuous Glucose Monitoring Devices: A Review of Current Technology. *Journal of Diabetes Science and Technology* **2009,** *3* (5), 1207-1214.

32. Tanenberg, R.; Bode, B.; Lane, W.; Levetan, C.; Mestman, J.; Harmel, A. P.; Tobian, J.; Gross, T.; Mastrototaro, J., Use of the Continuous Glucose Monitoring System to Guide Therapy in Patients with Insulin-Treated Diabetes: A Randomized Controlled Trial. *Mayo Clin Proc* **2004,** *79* (12), 1521-6.

33. Deiss, D.; Bolinder, J.; Riveline, J. P.; Battelino, T.; Bosi, E.; Tubiana-Rufi, N.; Kerr, D.; Phillip, M., Improved Glycemic Control in Poorly Controlled Patients with Type 1 Diabetes Using Real-Time Continuous Glucose Monitoring. *Diabetes Care* **2006,** *29* (12), 2730-2.

34. Garg, S.; Jovanovic, L., Relationship of Fasting and Hourly Blood Glucose Levels to Hba1c Values: Safety, Accuracy, and Improvements in Glucose Profiles Obtained Using a 7-Day Continuous Glucose Sensor. *Diabetes Care* **2006,** *29* (12), 2644-9.

35. Nakamura, K.; Balo, A., The Accuracy and Efficacy of the Dexcom G4 Platinum Continuous Glucose Monitoring System. *J Diabetes Sci Technol* **2015**.

36. Gehlaut, R. R.; Dogbey, G. Y.; Schwartz, F. L.; Marling, C. R.; Shubrook, J. H., Hypoglycemia in Type 2 Diabetes - More Common Than You Think: A Continuous Glucose Monitoring Study. *J Diabetes Sci Technol* **2015**.

37. Chetty, V. T.; Almulla, A.; Odueyungbo, A.; Thabane, L., The Effect of Continuous Subcutaneous Glucose Monitoring (Cgms) Versus Intermittent Whole Blood Finger-Stick Glucose Monitoring (Sbgm) on Hemoglobin A1c (Hba1c) Levels in Type I Diabetic Patients: A Systematic Review. *Diabetes Res Clin Pract* **2008,** *81* (1), 79-87.

38. Brodbeck, W. G.; Anderson, J. M., Giant Cell Formation and Function. *Curr Opin Hematol* **2009,** *16* (1), 53-7.

39. Novak, M. T.; Yuan, F.; Reichert, W. M., Modeling the Relative Impact of Capsular Tissue Effects on Implanted Glucose Sensor Time Lag and Signal Attenuation. *Anal Bioanal Chem* **2010,** *398* (4), 1695-705.

40. Koschwanez, H. E.; Reichert, W. M., In Vitro, in Vivo and Post Explantation Testing of Glucose-Detecting Biosensors: Current Methods and Recommendations. *Biomaterials* **2007,** *28* (25), 3687-703.

41. Gifford, R.; Batchelor, M. M.; Lee, Y.; Gokulrangan, G.; Meyerhoff, M. E.; Wilson, G. S., Mediation of in Vivo Glucose Sensor Inflammatory Response Via Nitric Oxide Release. *J Biomed Mater Res A* **2005,** *75* (4), 755-66.

42. Bryers, J. D.; Giachelli, C. M.; Ratner, B. D., Engineering Biomaterials to Integrate and Heal: The Biocompatibility Paradigm Shifts. *Biotechnol Bioeng* **2012,** *109* (8), 1898-911.

43. Dehennis, A.; Mortellaro, M. A.; Ioacara, S., Multisite Study of an Implanted Continuous Glucose Sensor over 90 Days in Patients with Diabetes Mellitus. *J Diabetes Sci Technol* **2015**.

44. Nielsen, J. K.; Christiansen, J. S.; Kristensen, J. S.; Toft, H. O.; Hansen, L. L.; Aasmul, S.; Gregorius, K., Clinical Evaluation of a Transcutaneous Interrogated Fluorescence Lifetime-Based Microsensor for Continuous Glucose Reading. *Journal of Diabetes Science and Technology* **2009,** *3* (1), 98-109.

45. Joseph, J. I.; Hipszer, B.; Mraovic, B.; Chervoneva, I.; Joseph, M.; Grunwald, Z., Clinical Need for Continuous Glucose Monitoring in the Hospital. *Journal of Diabetes Science and Technology* **2009,** *3* (6), 1309-1318.

46. Steiner, M. S.; Duerkop, A.; Wolfbeis, O. S., Optical Methods for Sensing Glucose. *Chem Soc Rev* **2011,** *40* (9), 4805-39.

47. Oliver, N. S.; Toumazou, C.; Cass, A. E.; Johnston, D. G., Glucose Sensors: A Review of Current and Emerging Technology. *Diabet Med* **2009,** *26* (3), 197-210.

48. Zanon, M.; Sparacino, G.; Facchinetti, A.; Riz, M.; Talary, M. S.; Suri, R. E.; Caduff, A.; Cobelli, C., Non-Invasive Continuous Glucose Monitoring: Improved Accuracy of Point and Trend Estimates of the Multisensor System. *Med Biol Eng Comput* **2012,** *50* (10), 1047-57.

49. Chinnayelka, S.; McShane, M. J., Competitive Binding Assays in Microcapsules as "Smart Tattoo" Biosensors. **2005**, 1304-1307.

50. Heo, Y. J.; Takeuchi, S., Towards Smart Tattoos: Implantable Biosensors for Continuous Glucose Monitoring. *Adv Healthc Mater* **2013,** *2* (1), 43-56.

51. Russell, R. J.; Pishko, M. V.; Gefrides, C. C.; McShane, M. J.; Coté, G. L., A Fluorescence-Based Glucose Biosensor Using Concanavalin a and Dextran Encapsulated in a Poly(Ethylene Glycol) Hydrogel. *Analytical Chemistry* **1999,** *71* (15), 3126-3132.

52. Martinkova, P.; Pohanka, M., Biosensors for Blood Glucose and Diabetes Diagnosis: Evolution, Construction, and Current Status. *Analytical Letters* **2015**, 150615065703003.

53. Hussain, F.; Birch, D. J.; Pickup, J. C., Glucose Sensing Based on the Intrinsic Fluorescence of Sol-Gel Immobilized Yeast Hexokinase. *Anal Biochem* **2005,** *339* (1), 137-43.

54. D'Auria, S.; DiCesare, N.; Staiano, M.; Gryczynski, Z.; Rossi, M.; Lakowicz, J. R., A Novel Fluorescence Competitive Assay for Glucose Determinations by Using a Thermostable Glucokinase from the Thermophilic Microorganism Bacillus Stearothermophilus. *Anal Biochem* **2002,** *303* (2), 138-44.

55. Singh, S.; McShane, M., Enhancing the Longevity of Microparticle-Based Glucose Sensors Towards 1 Month Continuous Operation. *Biosens Bioelectron* **2010,** *25* (5), 1075-81.

56. Collier, B. B.; McShane, M. J., Time-Resolved Measurements of Luminescence. *Journal of Luminescence* **2013,** *144*, 180-190.

57. Collier, B. B.; McShane, M. J., Dynamic Windowing Algorithm for the Fast and Accurate Determination of Luminescence Lifetimes. *Anal Chem* **2012,** *84* (11), 4725-31.

58. Stein, E. W.; Grant, P. S.; Zhu, H.; McShane, M. J., Microscale Enzymatic Optical Biosensors Using Mass Transport Limiting Nanofilms. 1. Fabrication and Characterization Using Glucose as a Model Analyte. *Anal Chem* **2007,** *79* (4), 1339-48.

59. Stein, E. W.; Singh, S.; McShane, M. J., Microscale Enzymatic Optical Biosensors Using Mass Transport Limiting Nanofilms. 2. Response Modulation by Varying Analyte Transport Properties. *Anal Chem* **2008,** *80* (5), 1408-17.

60. Collier, B. B.; McShane, M. J., Temperature Compensation of Oxygen Sensing Films Utilizing a Dynamic Dual Lifetime Calculation Technique. *IEEE Sensors Journal* **2014,** *14* (8), 2755-2764.

61. Collier, B. B.; McShane, M. J., Enzymatic Glucose Sensor Compensation for Variations in Ambient Oxygen Concentration. *Proc SPIE Int Soc Opt Eng* **2015,** *8591*.

62. Arugula, M. A.; Simonian, A., Novel Trends in Affinity Biosensors: Current Challenges and Perspectives. *Measurement Science and Technology* **2014,** *25* (3), 032001.

63. Leech, D. n., Affinity Biosensors. *Chemical Society Reviews* **1994,** *23* (3), 205.

64. Feng, C.; Dai, S.; Wang, L., Optical Aptasensors for Quantitative Detection of Small Biomolecules: A Review. *Biosens Bioelectron* **2014,** *59*, 64-74.

65. Chen, J.-K.; Chang, C.-J., Fabrications and Applications of Stimulus-Responsive Polymer Films and Patterns on Surfaces: A Review. *Materials* **2014,** *7* (2), 805-875.

66. Pisoschi, A. M., Biosensors as Bio-Based Materials in Chemical Analysis: A Review. *Journal of Biobased Materials and Bioenergy* **2013,** *7* (1), 19-38.

67. Schultz, J. S., Sensitivity and Dynamics of Bioreceptor-Based Biosensors. *Annals of the New York Academy of Sciences* **1987,** *506* (1 Biochemical E), 406-414.

68. Schultz, J. S.; Mansouri, S.; Goldstein, I. J., Affinity Sensor: A New Technique for Developing Implantable Sensors for Glucose and Other Metabolites. *Diabetes Care* **1982,** *5* (3), 245-253.

69. Chinnayelka, S.; Zhu, H.; McShane, M., Near-Infrared Resonance Energy Transfer Glucose Biosensors in Hybrid Microcapsule Carriers. *Journal of Sensors* **2008,** *2008*, 1-11.

70. Huet, C.; Lonchampt, M.; Huet, M.; Bernadac, A., Temperature Effects on the Concanavalin a Molecule and on Concanavalin a Binding. *Biochimica et Biophysica Acta (BBA) - Protein Structure* **1974,** *365* (1), 28-39.

71. Paek, S. H.; Cho, I. H.; Kim, D. H.; Jeon, J. W.; Lim, G. S.; Paek, S. H., Label-Free, Needle-Type Biosensor for Continuous Glucose Monitoring Based on Competitive Binding. *Biosens Bioelectron* **2013,** *40* (1), 38-44.

72. Ogoshi, T.; Harada, A., Chemical Sensors Based on Cyclodextrin Derivatives. *Sensors* **2008,** *8* (8), 4961-4982.

73. Ballerstadt, R.; Evans, C.; Gowda, A.; McNichols, R., Fiber-Coupled Fluorescence Affinity Sensor for 3-Day in Vivo Glucose Sensing. *Journal of Diabetes Science and Technology* **2007,** *1* (3), 384-393.

74. Dutt-Ballerstadt, R.; Evans, C.; Gowda, A.; McNichols, R., Preclinical in Vivo Study of a Fluorescence Affinity Sensor for Short-Term Continuous Glucose Monitoring in a Small and Large Animal Model. *Diabetes Technol Ther* **2008,** *10* (6), 453-60.

75. Ballerstadt, R.; Evans, C.; Gowda, A.; McNichols, R., In Vivo Performance Evaluation of a Transdermal near- Infrared Fluorescence Resonance Energy Transfer Affinity Sensor for Continuous Glucose Monitoring. *Diabetes Technol Ther* **2006,** *8* (3), 296-311.

76. Ballerstadt, R.; Gowda, A.; McNichols, R., Fluorescence Resonance Energy Transfer-Based near-Infrared Fluorescence Sensor for Glucose Monitoring. *Diabetes Technol Ther* **2004,** *6* (2), 191-200.

77. Cummin, B. M.; Lim, J.; Simanek, E. E.; Pishko, M. V.; Cote, G. L., Encapsulation of a Concanavalin a/Dendrimer Glucose Sensing Assay within Microporated Poly (Ethylene Glycol) Microspheres. *Biomed Opt Express* **2011,** *2* (5), 1243-57.

78. Ibey, B. L.; Beier, H. T.; Rounds, R. M.; Cote, G. L.; Yadavalli, V. K.; Pishko, M. V., Competitive Binding Assay for Glucose Based on Glycodendrimer-Fluorophore Conjugates. *Anal Chem* **2005,** *77* (21), 7039-46.

79. Chinnayelka, S.; McShane, M. J., Glucose-Sensitive Nanoassemblies Comprising Affinity-Binding Complexes Trapped in Fuzzy Microshells. *Journal of Fluorescence* **2004,** *14* (5), 585-595.

80. Rolinski, O. J.; Birch, D. J. S.; McCartney, L.; Pickup, J. C., Molecular Distribution Sensing in a Fluorescence Resonance Energy Transfer Based Affinity Assay for Glucose. *Spectrochimica Acta Part A: Molecular and Biomolecular Spectroscopy* **2001,** *57* (11), 2245-2254.

81. Lim, K. R.; Ahn, K.-S.; Lee, W.-Y., Detection of Concanavalin a Based on Attenuated Fluorescence Resonance Energy Transfer between Quantum Dots and Mannose-Stabilized Gold Nanoparticles. *Anal. Methods* **2013,** *5* (1), 64-67.

82. Hu, B.; Zhang, L. P.; Chen, M. L.; Chen, M. L.; Wang, J. H., The Inhibition of Fluorescence Resonance Energy Transfer between Quantum Dots for Glucose Assay. *Biosens Bioelectron* **2012,** *32* (1), 82-8.

83. Zhang, C.; Yuan, Y.; Zhang, S.; Wang, Y.; Liu, Z., Biosensing Platform Based on Fluorescence Resonance Energy Transfer from Upconverting Nanocrystals to Graphene Oxide. *Angew Chem Int Ed Engl* **2011,** *50* (30), 6851-4.

84. Peng, J.; Wang, Y.; Wang, J.; Zhou, X.; Liu, Z., A New Biosensor for Glucose Determination in Serum Based on up-Converting Fluorescence Resonance Energy Transfer. *Biosens Bioelectron* **2011,** *28* (1), 414-20.

85. Wang, J.-H.; Li, Y.-Q.; Zhang, H.-L.; Wang, H.-Q.; Lin, S.; Chen, J.; Zhao, Y.-D.; Luo, Q.-M., Bioconjugation of Concanavalin and Cdte Quantum Dots and the Detection of Glucose. *Colloids and Surfaces A: Physicochemical and Engineering Aspects* **2010,** *364* (1-3), 82-86.

86. Tang, B.; Cao, L.; Xu, K.; Zhuo, L.; Ge, J.; Li, Q.; Yu, L., A New Nanobiosensor for Glucose with High Sensitivity and Selectivity in Serum Based on Fluorescence Resonance Energy Transfer (Fret) between Cdte Quantum Dots and Au Nanoparticles. *Chemistry* **2008,** *14* (12), 3637-44.

87. Wang, Y.; Qu, K.; Tang, L.; Li, Z.; Moore, E.; Zeng, X.; Liu, Y.; Li, J., Nanomaterials in Carbohydrate Biosensors. *TrAC Trends in Analytical Chemistry* **2014,** *58*, 54-70.

88. Chen, Q.; Wei, W.; Lin, J. M., Homogeneous Detection of Concanavalin a Using Pyrene-Conjugated Maltose Assembled Graphene Based on Fluorescence Resonance Energy Transfer. *Biosens Bioelectron* **2011,** *26* (11), 4497-502.

89. Liao, K. C.; Chang, S. C.; Chiu, C. Y.; Chou, Y. H., Acute Response in Vivo of a Fiber-Optic Sensor for Continuous Glucose Monitoring from Canine Studies on Point Accuracy. *Sensors (Basel)* **2010,** *10* (8), 7789-802.

90. Aloraefy, M.; Pfefer, T. J.; Ramella-Roman, J. C.; Sapsford, K. E., In Vitro Evaluation of Fluorescence Glucose Biosensor Response. *Sensors (Basel)* **2014,** *14* (7), 12127-48.

91. McCartney, L. J.; Pickup, J. C.; Rolinski, O. J.; Birch, D. J., Near-Infrared Fluorescence Lifetime Assay for Serum Glucose Based on Allophycocyanin-Labeled Concanavalin A. *Anal Biochem* **2001,** *292* (2), 216-21.

92. Rolinski, O. J.; Birch, D. J. S.; McCartney, L. J.; Pickup, J. C., A Time-Resolved near-Infrared Fluorescence Assay for Glucose: Opportunities for Trans-Dermal Sensing. *Journal of Photochemistry and Photobiology B: Biology* **2000,** *54* (1), 26-34.

93. Lim, K. R.; Park, J.-M.; Choi, H. N.; Lee, W.-Y., Gold Glyconanoparticle-Based Colorimetric Bioassay for the Determination of Glucose in Human Serum. *Microchemical Journal* **2013,** *106*, 154-159.

94. Tsai, C.-S.; Chen, C.-T., Rapid-Throughput Competitive Colorimetric Assay Based on Monosaccharide-Capped Gold Nanoparticles for Detecting Lectin-Protein Interactions. *ChemPlusChem* **2012,** *77* (4), 314-322.

95. Aslan, K.; Lakowicz, J. R.; Geddes, C. D., Nanogold-Plasmon-Resonance-Based Glucose Sensing. *Anal Biochem* **2004,** *330* (1), 145-55.

96. Cummins, B. M.; Garza, J. T.; Cote, G. L., Optimization of a Concanavalin a-Based Glucose Sensor Using Fluorescence Anisotropy. *Anal Chem* **2013,** *85* (11), 5397-404.

97. Cummins, B. M.; Li, M.; Locke, A. K.; Birch, D. J.; Vigh, G.; Cote, G. L., Overcoming the Aggregation Problem: A New Type of Fluorescent Ligand for Cona-Based Glucose Sensing. *Biosens Bioelectron* **2015,** *63*, 53-60.

98. Meadows, D., Fiber-Optic Biosensors Based on Fluorescence Energy Transfer. *Talanta* **1988,** *35* (2), 145-150.

99. Locke, A. K.; Cummins, B. M.; Abraham, A. A.; Cote, G. L., Pegylation of Concanavalin a to Improve Its Stability for an in Vivo Glucose Sensing Assay. *Anal Chem* **2014,** *86* (18), 9091-7.

100. D'Auria, S.; Herman, P.; Rossi, M.; Lakowicz, J. R., The Fluorescence Emission of the Apo-Glucose Oxidase from Aspergillus Niger as Probe to Estimate Glucose Concentrations. *Biochem Biophys Res Commun* **1999,** *263* (2), 550-3.

101. D'Auria, S.; Di Cesare, N.; Gryczynski, Z.; Gryczynski, I.; Rossi, M.; Lakowicz, J. R., A Thermophilic Apoglucose Dehydrogenase as Nonconsuming Glucose Sensor. *Biochem Biophys Res Commun* **2000,** *274* (3), 727-31.

102. Chinnayelka, S.; McShane, M. J., Resonance Energy Transfer Nanobiosensors Based on Affinity Binding between Apo-Enzyme and Its Substrate. *Biomacromolecules* **2004,** *5* (5), 1657-61.

103. Wong, C. M.; Wong, K. H.; Chen, X. D., Glucose Oxidase: Natural Occurrence, Function, Properties and Industrial Applications. *Appl Microbiol Biotechnol* **2008,** *78* (6), 927-38.

104. Chinnayelka, S.; McShane, M. J., Glucose Sensors Based on Microcapsules Containing an Orange/Red Competitive Binding Resonance Energy Transfer Assay. *Diabetes Technol Ther* **2006,** *8* (3), 269-78.

105. Chaudhary, A.; Raina, M.; Harma, H.; Hanninen, P.; McShane, M. J.; Srivastava, R., Evaluation of Glucose Sensitive Affinity Binding Assay Entrapped in Fluorescent Dissolved-Core Alginate Microspheres. *Biotechnol Bioeng* **2009,** *104* (6), 1075-85.

106. Chaudhary, A.; Srivastava, R., Glucose Sensing Using Competitive Binding Assay Co-Encapsulated in Uniform Sized Alginate Microspheres. *Sensor Letters* **2008,** *6* (2), 253-260.

107. Marvin, J. S.; Hellinga, H. W., Engineering Biosensors by Introducing Fluorescent Allosteric Signal Transducers: Construction of a Novel Glucose Sensor. *Journal of the American Chemical Society* **1998,** *120* (1), 7-11.

108. Khan, F.; Gnudi, L.; Pickup, J. C., Fluorescence-Based Sensing of Glucose Using Engineered Glucose/Galactose-Binding Protein: A Comparison of Fluorescence Resonance Energy Transfer and Environmentally Sensitive Dye Labelling Strategies. *Biochem Biophys Res Commun* **2008,** *365* (1), 102-6.

109. Khan, F.; Saxl, T. E.; Pickup, J. C., Fluorescence Intensity- and Lifetime-Based Glucose Sensing Using an Engineered High-Kd Mutant of Glucose/Galactose-Binding Protein. *Anal Biochem* **2010,** *399* (1), 39-43.

110. Saxl, T.; Khan, F.; Ferla, M.; Birch, D.; Pickup, J., A Fluorescence Lifetime-Based Fibre-Optic Glucose Sensor Using Glucose/Galactose-Binding Protein. *Analyst* **2011,** *136* (5), 968-72.

111. Saxl, T.; Khan, F.; Matthews, D. R.; Zhi, Z. L.; Rolinski, O.; Ameer-Beg, S.; Pickup, J., Fluorescence Lifetime Spectroscopy and Imaging of Nano-Engineered

Glucose Sensor Microcapsules Based on Glucose/Galactose-Binding Protein. *Biosens Bioelectron* **2009,** *24* (11), 3229-34.

112. Thomas, J.; Sherman, D. B.; Amiss, T. J.; Andaluz, S. A.; Pitner, J. B., Synthesis and Biosensor Performance of a near-Ir Thiol-Reactive Fluorophore Based on Benzothiazolium Squaraine. *Bioconjug Chem* **2007,** *18* (6), 1841-6.

113. Thomas, K. J.; Sherman, D. B.; Amiss, T. J.; Andaluz, S. A.; Pitner, J. B., A Long-Wavelength Fluorescent Glucose Biosensor Based on Bioconjugates of Galactose/Glucose Binding Protein and Nile Red Derivatives. *Diabetes Technol Ther* **2006,** *8* (3), 261-8.

114. Tian, Y.; Cuneo, M. J.; Changela, A.; Hocker, B.; Beese, L. S.; Hellinga, H. W., Structure-Based Design of Robust Glucose Biosensors Using a Thermotoga Maritima Periplasmic Glucose-Binding Protein. *Protein Sci* **2007,** *16* (10), 2240-50.

115. Tolosa, L.; Gryczynski, I.; Eichhorn, L. R.; Dattelbaum, J. D.; Castellano, F. N.; Rao, G.; Lakowicz, J. R., Glucose Sensor for Low-Cost Lifetime-Based Sensing Using a Genetically Engineered Protein. *Anal Biochem* **1999,** *267* (1), 114-20.

116. Ge, X.; Tolosa, L.; Rao, G., Dual-Labeled Glucose Binding Protein for Ratiometric Measurements of Glucose. *Anal Chem* **2004,** *76* (5), 1403-10.

117. Veetil, J. V.; Jin, S.; Ye, K., A Glucose Sensor Protein for Continuous Glucose Monitoring. *Biosens Bioelectron* **2010,** *26* (4), 1650-5.

118. Fehr, M.; Lalonde, S.; Lager, I.; Wolff, M. W.; Frommer, W. B., In Vivo Imaging of the Dynamics of Glucose Uptake in the Cytosol of Cos-7 Cells by Fluorescent Nanosensors. *J Biol Chem* **2003,** *278* (21), 19127-33.

119. Ye, K.; Schultz, J. S., Genetic Engineering of an Allosterically Based Glucose Indicator Protein for Continuous Glucose Monitoring by Fluorescence Resonance Energy Transfer. *Analytical Chemistry* **2003,** *75* (14), 3451-3459.

120. Taneoka, A.; Sakaguchi-Mikami, A.; Yamazaki, T.; Tsugawa, W.; Sode, K., The Construction of a Glucose-Sensing Luciferase. *Biosens Bioelectron* **2009,** *25* (1), 76-81.

121. Hsieh, H. V.; Pfeiffer, Z. A.; Amiss, T. J.; Sherman, D. B.; Pitner, J. B., Direct Detection of Glucose by Surface Plasmon Resonance with Bacterial Glucose/Galactose-Binding Protein. *Biosensors and Bioelectronics* **2004,** *19* (7), 653-660.

122. Siegrist, J.; Kazarian, T.; Ensor, C.; Joel, S.; Madou, M.; Wang, P.; Daunert, S., Continuous Glucose Sensor Using Novel Genetically Engineered Binding Polypeptides Towards in Vivo Applications. *Sensors and Actuators B: Chemical* **2010,** *149* (1), 51-58.

123. Joel, S.; Turner, K. B.; Daunert, S., Glucose Recognition Proteins for Glucose Sensing at Physiological Concentrations and Temperatures. *ACS Chem Biol* **2014,** *9* (7), 1595-602.

124. Mader, H. S.; Wolfbeis, O. S., Boronic Acid Based Probes for Microdetermination of Saccharides and Glycosylated Biomolecules. *Microchimica Acta* **2008,** *162* (1-2), 1-34.

125. Lacina, K.; Skladal, P.; James, T. D., Boronic Acids for Sensing and Other Applications - a Mini-Review of Papers Published in 2013. *Chem Cent J* **2014,** *8* (1), 60.

126. Larkin, J. D.; Frimat, K. A.; Fyles, T. M.; Flower, S. E.; James, T. D., Boronic Acid Based Photoinduced Electron Transfer (Pet) Fluorescence Sensors for Saccharides. *New Journal of Chemistry* **2010,** *34* (12), 2922.

127. Mesch, M.; Zhang, C.; Braun, P. V.; Giessen, H., Functionalized Hydrogel on Plasmonic Nanoantennas for Noninvasive Glucose Sensing. *ACS Photonics* **2015,** *2* (4), 475-480.

128. Li, A.; Guo, Z.; Peng, Q.; Du, C.; Han, X.; Liu, L.; Guo, J.; He, Y.; Ji, Y., A Saccharides Sensor Developed by Symmetrical Optical Waveguide-Based Surface Plasmon Resonance. *Journal of Innovative Optical Health Sciences* **2015,** *08* (02), 1550003.

129. Sugnaux, C.; Klok, H. A., Glucose-Sensitive Qcm-Sensors Via Direct Surface Raft Polymerization. *Macromol Rapid Commun* **2014,** *35* (16), 1402-7.

130. Vezouviou, E.; Lowe, C. R., A near Infrared Holographic Glucose Sensor. *Biosens Bioelectron* **2015,** *68*, 371-81.

131. Egawa, Y.; Seki, T.; Takahashi, S.; Anzai, J.-i., Electrochemical and Optical Sugar Sensors Based on Phenylboronic Acid and Its Derivatives. *Materials Science and Engineering: C* **2011,** *31* (7), 1257-1264.

132. James, T. D., Saccharide-Selective Boronic Acid Based Photoinduced Electron Transfer (Pet) Fluorescent Sensors. **2007,** *277*, 107-152.

133. Hosseinzadeh, R.; Mohadjerani, M.; Pooryousef, M.; Eslami, A.; Emami, S., A New Boronic Acid Fluorescent Sensor Based on Fluorene for Monosaccharides at Physiological Ph. *Spectrochim Acta A Mol Biomol Spectrosc* **2015,** *144*, 53-60.

134. DiCesare, N.; Lakowicz, J. R., Spectral Properties of Fluorophores Combining the Boronic Acid Group with Electron Donor or Withdrawing Groups. Implication in the Development of Fluorescence Probes for Saccharides. *The Journal of Physical Chemistry A* **2001,** *105* (28), 6834-6840.

135. Karnati, V. V.; Gao, X.; Gao, S.; Yang, W.; Ni, W.; Sankar, S.; Wang, B., A Glucose-Selective Fluorescence Sensor Based on Boronicacid-Diol Recognition. *Bioorganic & Medicinal Chemistry Letters* **2002,** *12* (23), 3373-3377.

136. James, T. D.; Sandanayake, K. R. A. S.; Iguchi, R.; Shinkai, S., Novel Saccharide-Photoinduced Electron Transfer Sensors Based on the Interaction of Boronic Acid and Amine. *Journal of the American Chemical Society* **1995,** *117* (35), 8982-8987.

137. Mortellaro, M.; DeHennis, A., Performance Characterization of an Abiotic and Fluorescent-Based Continuous Glucose Monitoring System in Patients with Type 1 Diabetes. *Biosens Bioelectron* **2014,** *61*, 227-31.

138. Colvin, A. E.; Jiang, H., Increased in Vivo Stability and Functional Lifetime of an Implantable Glucose Sensor through Platinum Catalysis. *J Biomed Mater Res A* **2013,** *101* (5), 1274-82.

139. Yuan, L.; Lin, W.; Zheng, K.; Zhu, S., Fret-Based Small-Molecule Fluorescent Probes: Rational Design and Bioimaging Applications. *Acc Chem Res* **2013,** *46* (7), 1462-73.

140. Zadran, S.; Standley, S.; Wong, K.; Otiniano, E.; Amighi, A.; Baudry, M., Fluorescence Resonance Energy Transfer (Fret)-Based Biosensors: Visualizing Cellular Dynamics and Bioenergetics. *Appl Microbiol Biotechnol* **2012,** *96* (4), 895-902.

141. Lei, J.; Ju, H., Signal Amplification Using Functional Nanomaterials for Biosensing. *Chem Soc Rev* **2012,** *41* (6), 2122-34.

142. Bhowmick, S.; Saini, S.; Shenoy, V. B.; Bagchi, B., Resonance Energy Transfer from a Fluorescent Dye to a Metal Nanoparticle. *J Chem Phys* **2006,** *125* (18), 181102.

143. Chen, H.; Shao, L.; Li, Q.; Wang, J., Gold Nanorods and Their Plasmonic Properties. *Chem Soc Rev* **2013,** *42* (7), 2679-724.

144. Li, M.; Cushing, S. K.; Wu, N., Plasmon-Enhanced Optical Sensors: A Review. *Analyst* **2015,** *140* (2), 386-406.

145. Jennings, T. L.; Singh, M. P.; Strouse, G. F., Fluorescent Lifetime Quenching near D = 1.5 Nm Gold Nanoparticles: Probing Nset Validity. *J Am Chem Soc* **2006,** *128* (16), 5462-7.

146. Chowdhury, S.; Wu, Z.; Jaquins-Gerstl, A.; Liu, S.; Dembska, A.; Armitage, B. A.; Jin, R.; Peteanu, L. A., Wavelength Dependence of the Fluorescence Quenching Efficiency of Nearby Dyes by Gold Nanoclusters and Nanoparticles: The Roles of Spectral Overlap and Particle Size. *J Phys Chem C Nanomater Interfaces* **2011,** *115* (41), 20105-20112.

147. Anger, P.; Bharadwaj, P.; Novotny, L., Enhancement and Quenching of Single-Molecule Fluorescence. *Physical Review Letters* **2006,** *96* (11).

148. Dulkeith, E.; Morteani, A. C.; Niedereichholz, T.; Klar, T. A.; Feldmann, J.; Levi, S. A.; van Veggel, F. C. J. M.; Reinhoudt, D. N.; Möller, M.; Gittins, D. I., Fluorescence Quenching of Dye Molecules near Gold Nanoparticles: Radiative and Nonradiative Effects. *Physical Review Letters* **2002,** *89* (20).

149. Chhabra, R.; Sharma, J.; Wang, H.; Zou, S.; Lin, S.; Yan, H.; Lindsay, S.; Liu, Y., Distance-Dependent Interactions between Gold Nanoparticles and Fluorescent Molecules with DNA as Tunable Spacers. *Nanotechnology* **2009,** *20* (48), 485201.

150. Dulkeith, E.; Ringler, M.; Klar, T. A.; Feldmann, J.; Munoz Javier, A.; Parak, W. J., Gold Nanoparticles Quench Fluorescence by Phase Induced Radiative Rate Suppression. *Nano Lett* **2005,** *5* (4), 585-9.

151. Geng, J.; Liang, J.; Wang, Y.; Gurzadyan, G. G.; Liu, B., Metal-Enhanced Fluorescence of Conjugated Polyelectrolytes with Self-Assembled Silver Nanoparticle Platforms. *J Phys Chem B* **2011,** *115* (13), 3281-8.

152. Reineck, P.; Gomez, D.; Ng, S. H.; Karg, M.; Bell, T.; Mulvaney, P.; Bach, U., Distance and Wavelength Dependent Quenching of Molecular Fluorescence by Au@Sio2 Core-Shell Nanoparticles. *ACS Nano* **2013,** *7* (8), 6636-48.

153. Ray, K.; Badugu, R.; Lakowicz, J. R., Polyelectrolyte Layer-by-Layer Assembly to Control the Distance between Fluorophores and Plasmonic Nanostructures. *Chem Mater* **2007,** *19* (24), 5902-5909.

154. Pustovit, V. N.; Shahbazyan, T. V., Resonance Energy Transfer near Metal Nanostructures Mediated by Surface Plasmons. *Physical Review B* **2011,** *83* (8).

155. Chan, Y. H.; Chen, J.; Wark, S. E.; Skiles, S. L.; Son, D. H.; Batteas, J. D., Using Patterned Arrays of Metal Nanoparticles to Probe Plasmon Enhanced Luminescence of Cdse Quantum Dots. *ACS Nano* **2009,** *3* (7), 1735-44.

156. Li, Y. Q.; Guan, L. Y.; Zhang, H. L.; Chen, J.; Lin, S.; Ma, Z. Y.; Zhao, Y. D., Distance-Dependent Metal-Enhanced Quantum Dots Fluorescence Analysis in Solution by Capillary Electrophoresis and Its Application to DNA Detection. *Anal Chem* **2011,** *83* (11), 4103-9.

157. Ray, K.; Badugu, R.; Lakowicz, J. R., Metal-Enhanced Fluorescence from Cdte Nanocrystals: A Single-Molecule Fluorescence Study. *J Am Chem Soc* **2006,** *128* (28), 8998-9.

158. Kulakovich, O.; Strekal, N.; Yaroshevich, A.; Maskevich, S.; Gaponenko, S.; Nabiev, I.; Woggon, U.; Artemyev, M., Enhanced Luminescence of Cdse Quantum Dots on Gold Colloids. *Nano Letters* **2002,** *2* (12), 1449-1452.

159. Pons, T.; Medintz, I. L.; Sapsford, K. E.; Higashiya, S.; Grimes, A. F.; English, D. S.; Mattoussi, H., On the Quenching of Semiconductor Quantum Dot Photoluminescence by Proximal Gold Nanoparticles. *Nano Lett* **2007,** *7* (10), 3157-64.

160. Li, M.; Cushing, S. K.; Wang, Q.; Shi, X.; Hornak, L. A.; Hong, Z.; Wu, N., Size-Dependent Energy Transfer between Cdse/Zns Quantum Dots and Gold Nanoparticles. *The Journal of Physical Chemistry Letters* **2011,** *2* (17), 2125-2129.

161. Samanta, A.; Zhou, Y.; Zou, S.; Yan, H.; Liu, Y., Fluorescence Quenching of Quantum Dots by Gold Nanoparticles: A Potential Long Range Spectroscopic Ruler. *Nano Lett* **2014,** *14* (9), 5052-7.

162. Focsan, M.; Gabudean, A. M.; Vulpoi, A.; Astilean, S., Controlling the Luminescence of Carboxyl-Functionalized Cdse/Zns Core–Shell Quantum Dots in Solution by Binding with Gold Nanorods. *The Journal of Physical Chemistry C* **2014,** *118* (43), 25190-25199.

163. Ray, P. C.; Fan, Z.; Crouch, R. A.; Sinha, S. S.; Pramanik, A., Nanoscopic Optical Rulers Beyond the Fret Distance Limit: Fundamentals and Applications. *Chem Soc Rev* **2014,** *43* (17), 6370-404.

164. West, J. L.; Halas, N. J., Engineered Nanomaterials for Biophotonics Applications: Improving Sensing, Imaging, and Therapeutics. *Annu Rev Biomed Eng* **2003,** *5*, 285-92.

165. Laroui, H.; Rakhya, P.; Xiao, B.; Viennois, E.; Merlin, D., Nanotechnology in Diagnostics and Therapeutics for Gastrointestinal Disorders. *Dig Liver Dis* **2013,** *45* (12), 995-1002.

166. Bao, G.; Mitragotri, S.; Tong, S., Multifunctional Nanoparticles for Drug Delivery and Molecular Imaging. *Annu Rev Biomed Eng* **2013,** *15*, 253-82.

167. Sanna, V.; Pala, N.; Sechi, M., Targeted Therapy Using Nanotechnology: Focus on Cancer. *Int J Nanomedicine* **2014,** *9*, 467-83.

168. Wong, I. Y.; Bhatia, S. N.; Toner, M., Nanotechnology: Emerging Tools for Biology and Medicine. *Genes Dev* **2013,** *27* (22), 2397-408.

169. Zhang, F.; Lees, E.; Amin, F.; Gil, P. R.; Yang, F.; Mulvaney, P.; Parak, W. J., Polymer-Coated Nanoparticles: A Universal Tool for Biolabelling Experiments. *Small* **2011,** *7* (22), 3113-3127.

170. Pelaz, B.; Charron, G.; Pfeiffer, C.; Zhao, Y.; de la Fuente, J. M.; Liang, X. J.; Parak, W. J.; Del Pino, P., Interfacing Engineered Nanoparticles with Biological Systems: Anticipating Adverse Nano-Bio Interactions. *Small* **2013,** *9* (9-10), 1573-84.

171. Chapel, J. P.; Berret, J. F., Versatile Electrostatic Assembly of Nanoparticles and Polyelectrolytes: Coating, Clustering and Layer-by-Layer Processes. *Curr. Opin. Colloid Interface Sci.* **2012,** *17* (2), 97-105.

172. Caruso, F., Nanoengineering of Particle Surfaces. *Advanced Materials* **2001,** *13* (1), 11-22.

173. Ariga, K.; Hill, J. P.; Ji, Q., Layer-by-Layer Assembly as a Versatile Bottom-up Nanofabrication Technique for Exploratory Research and Realistic Application. *Phys Chem Chem Phys* **2007,** *9* (19), 2319-40.

174. Hammond, P. T., Polyelectrolyte Multilayered Nanoparticles: Using Nanolayers for Controlled and Targeted Systemic Release. *Nanomedicine (Lond)* **2012,** *7* (5), 619-22.

175. Yan, Y.; Björnmalm, M.; Caruso, F., Assembly of Layer-by-Layer Particles and Their Interactions with Biological Systems. *Chemistry of Materials* **2014,** *26* (1), 452-460.

176. Decher, G., Fuzzy Nanoassemblies: Toward Layered Polymeric Multicomposites. *Science* **1997,** *277* (5330), 1232-1237.

177. Decher, G.; Hong, J. D.; Schmitt, J., Buildup of Ultrathin Multilayer Films by a Self-Assembly Process: Iii. Consecutively Alternating Adsorption of Anionic and Cationic Polyelectrolytes on Charged Surfaces *Thin Solid Films* **1992,** *210* (1-2), 831-835.

178. Ariga, K.; Yamauchi, Y.; Rydzek, G.; Ji, Q.; Yonamine, Y.; Wu, K. C. W.; Hill, J. P., Layer-by-Layer Nanoarchitectonics: Invention, Innovation, and Evolution. *Chemistry Letters* **2014,** *43* (1), 36-68.

179. Sukhorukov, G. B.; Donath, E.; Davis, S.; Lichtenfeld, H.; Caruso, F.; Popov, V. I.; Mohwald, H., Stepwise Polyelectrolyte Assembly on Particle Surfaces: A Novel Approach to Colloid Design. *Polymers for Advanced Technologies* **1998,** *9* (10-11), 759-767.

180. Gittins, D. I.; Caruso, F., Tailoring the Polyelectrolyte Coating of Metal Nanoparticles. *J. Phys. Chem. B* **2001,** *105* (29), 6846-6852.

181. Dorris, A.; Rucareanu, S.; Reven, L.; Barrett, C. J.; Lennox, R. B., Preparation and Characterization of Polyelectrolyte-Coated Gold Nanoparticles. *Langmuir* **2008,** *24* (6), 2532-2538.

182. Schneider, G.; Decher, G., Functional Core/Shell Nanoparticles *Via* Layer-by-Layer Assembly. Investigation of the Experimental Parameters for Controlling Particle Aggregation and for Enhancing Dispersion Stability. *Langmuir* **2008,** *24* (5), 1778-1789.

183. Schneider, G.; Decher, G., From Functional Core/Shell Nanoparticles Prepared *Via* Layer-by-Layer Deposition to Empty Nanospheres. *Nano Lett.* **2004,** *4* (10), 1833-1839.

184. Gittins, D. I.; Caruso, F., Multilayered Polymer Nanocapsules Derived from Gold Nanoparticle Templates. *Adv. Mater.* **2000,** *12* (24), 1947-1949.

185. Mayya, K. S.; Schoeler, B.; Caruso, F., Preparation and Organization of Nanoscale Polyelectrolyte-Coated Gold Nanoparticles. *Adv. Funct. Mater.* **2003,** *13* (3), 183-188.

186. Hong, X.; Li, J.; Wang, M. J.; Xu, J. J.; Guo, W.; Li, J. H.; Bai, Y. B.; Li, T. J., Fabrication of Magnetic Luminescent Nanocomposites by a Layer-by-Layer Self-Assembly Approach. *Chem. Mater.* **2004,** *16* (21), 4022-4027.

187. Caruso, F.; Schuler, C.; Kurth, D. G., Core-Shell Particles and Hollow Shells Containing Metallo-Supramolecular Components. *Chem. Mater.* **1999,** *11* (11), 3394-3399.

188. Jin, Y. D.; Gao, X. H., Plasmonic Fluorescent Quantum Dots. *Nat. Nanotechnol.* **2009,** *4* (9), 571-576.

189. Jaffar, S.; Nam, K. T.; Khademhosseini, A.; Xing, J.; Langer, R. S.; Belcher, A. M., Layer-by-Layer Surface Modification and Patterned Electrostatic Deposition of Quantum Dots. *Nano Lett.* **2004,** *4* (8), 1421-1425.

190. Mandal, S.; Bonifacio, A.; Zanuttin, F.; Sergo, V.; Krol, S., Synthesis and Multidisciplinary Characterization of Polyelectrolyte Multilayer-Coated Nanogold with Improved Stability toward Aggregation. *Colloid and Polymer Science* **2010,** *289* (3), 269-280.

191. Taladriz-Blanco, P.; Perez-Juste, J.; Kandoth, N.; Herves, P.; Sortino, S., Layer-by-Layer Assembled Gold Nanoparticles with a Tunable Payload of a Nitric Oxide Photocage. *J Colloid Interface Sci* **2013,** *407*, 524-8.

192. Pereira, S. O.; Barros-Timmons, A.; Trindade, T., Biofunctionalisation of Colloidal Gold Nanoparticles Via Polyelectrolytes Assemblies. *Colloid and Polymer Science* **2013,** *292* (1), 33-50.

193. Kunze, K. K.; Netz, R. R., Salt-Induced DNA-Histone Complexation. *Phys. Rev. Lett.* **2000,** *85* (20), 4389-4392.

194. Netz, R. R.; Joanny, J. F., Complexation between a Semiflexible Polyelectrolyte and an Oppositely Charged Sphere. *Macromolecules* **1999,** *32* (26), 9026-9040.

195. Sun, B.; Flessner, R. M.; Saurer, E. M.; Jewell, C. M.; Fredin, N. J.; Lynn, D. M., Characterization of Ph-Induced Changes in the Morphology of Polyelectrolyte Multilayers Assembled from Poly(Allylamine) and Low Molecular Weight Poly(Acrylic Acid). *J Colloid Interface Sci* **2011,** *355* (2), 431-41.

196. Bieker, P.; Schönhoff, M., Linear and Exponential Growth Regimes of Multilayers of Weak Polyelectrolytes in Dependence on Ph. *Macromolecules* **2010,** *43* (11), 5052-5059.

197. Choi, J.; Rubner, M. F., Influence of the Degree of Ionization on Weak Polyelectrolyte Multilayer Assembly. *Macromolecules* **2005,** *38* (1), 116-124.

198. Itano, K.; Choi, J.; Rubner, M. F., Mechanism of the Ph-Induced Discontinuous Swelling/Deswelling Transitions of Poly(Allylamine Hydrochloride)-Containing Polyelectrolyte Multilayer Films. *Macromolecules* **2005,** *38* (8), 3450-3460.

199. Mendelsohn, J. D.; Barrett, C. J.; Chan, V. V.; Pal, A. J.; Mayes, A. M.; Rubner, M. F., Fabrication of Microporous Thin Films from Polyelectrolyte Multilayers. *Langmuir* **2000,** *16* (11), 5017-5023.

200. Shiratori, S. S.; Rubner, M. F., Ph-Dependent Thickness Behavior of Sequentially Adsorbed Layers of Weak Polyelectrolytes. *Macromolecules* **2000,** *33* (11), 4213-4219.

201. Yoo, D.; Shiratori, S. S.; Rubner, M. F., Controlling Bilayer Composition and Surface Wettability of Sequentially Adsorbed Multilayers of Weak Polyelectrolytes. *Macromolecules* **1998,** *31* (13), 4309-4318.

202. Mauser, T.; Dejugnat, C.; Mohwald, H.; Sukhorukov, G. B., Microcapsules Made of Weak Polyelectrolytes: Templating and Stimuli-Responsive Properties. *Langmuir* **2006,** *22* (13), 5888-93.

203. Kato, N.; Schuetz, P.; Fery, A.; Caruso, F., Thin Multilayer Films of Weak Polyelectrolytes on Colloid Particles. *Macromolecules* **2002,** *35* (26), 9780-9787.

204. Schuetz, P.; Caruso, F., Copper-Assisted Weak Polyelectrolyte Multilayer Formation on Microspheres and Subsequent Film Crosslinking. *Advanced Functional Materials* **2003,** *13* (12), 929-937.

205. Schuetz, P.; Caruso, F., Semiconductor and Metal Nanoparticle Formation on Polymer Spheres Coated with Weak Polyelectrolyte Multilayers. *Chemistry of Materials* **2004,** *16* (16), 3066-3073.

206. Petrov, A. I.; Antipov, A. A.; Sukhorukov, G. B., Base−Acid Equilibria in Polyelectrolyte Systems: From Weak Polyelectrolytes to Interpolyelectrolyte Complexes and Multilayered Polyelectrolyte Shells. *Macromolecules* **2003,** *36* (26), 10079-10086.

207. Burke, S. E.; Barrett, C. J., Acid−Base Equilibria of Weak Polyelectrolytes in Multilayer Thin Films. *Langmuir* **2003,** *19* (8), 3297-3303.

208. Sadeghpour, A.; Seyrek, E.; Szilagyi, I.; Hierrezuelo, J.; Borkovec, M., Influence of the Degree of Ionization and Molecular Mass of Weak Polyelectrolytes on Charging and Stability Behavior of Oppositely Charged Colloidal Particles. *Langmuir* **2011,** *27* (15), 9270-6.

209. Burke, S. E.; Barrett, C. J., Ph-Responsive Properties of Multilayered Poly(L-Lysine)/Hyaluronic Acid Surfaces. *Biomacromolecules* **2003,** *4* (6), 1773-83.

210. Tjipto, E.; Quinn, J. F.; Caruso, F., Layer-by-Layer Assembly of Weak-Strong Copolymer Polyelectrolytes: A Route to Morphological Control of Thin Films. *Journal of Polymer Science Part A: Polymer Chemistry* **2007,** *45* (18), 4341-4351.

211. Gong, X.; Gao, C., Influence of Salt on Assembly and Compression of Pdadmac/Pssma Polyelectrolyte Multilayers. *Phys Chem Chem Phys* **2009,** *11* (48), 11577-86.

212. Tjipto, E.; Quinn, J. F.; Caruso, F., Assembly of Multilayer Films from Polyelectrolytes Containing Weak and Strong Acid Moieties. *Langmuir* **2005,** *21* (19), 8785-92.

213. Yap, H. P.; Hao, X.; Tjipto, E.; Gudipati, C.; Quinn, J. F.; Davis, T. P.; Barner-Kowollik, C.; Stenzel, M. H.; Caruso, F., Synthesis, Multilayer Film Assembly, and Capsule Formation of Macromolecularly Engineered Acrylic Acid and Styrene Sulfonate Block Copolymers. *Langmuir* **2008,** *24* (16), 8981-90.

214. Gong, X., Controlling Surface Properties of Polyelectrolyte Multilayers by Assembly Ph. *Phys Chem Chem Phys* **2013,** *15* (25), 10459-65.

215. Brust, M.; Walker, M.; Bethell, D.; Schiffrin, D. J.; Whyman, R., Synthesis of Thiol-Derivatised Gold Nanoparticles in a Two-Phase Liquid?Liquid System. *Journal of the Chemical Society, Chemical Communications* **1994,** (7), 801.

216. Gittins, D. I.; Caruso, F., Biological and Physical Applications of Water-Based Metal Nanoparticles Synthesised in Organic Solution. *ChemPhysChem* **2002,** *3* (1), 110-113.

217. Haiss, W.; Thanh, N. T.; Aveyard, J.; Fernig, D. G., Determination of Size and Concentration of Gold Nanoparticles from Uv-Vis Spectra. *Anal Chem* **2007,** *79* (11), 4215-21.

218. Jin, T.; Fujii, F.; Sakata, H.; Tamura, M.; Kinjo, M., Calixarene-Coated Water-Soluble Cdse-Zns Semiconductor Quantum Dots That Are Highly Fluorescent and Stable in Aqueous Solution. *Chem Commun (Camb)* **2005,** (22), 2829-31.

219. Peng, Z. A.; Peng, X. G., Formation of High-Quality Cdte, Cdse, and Cds Nanocrystals Using Cdo as Precursor. *J. Am. Chem. Soc.* **2001,** *123* (1), 183-184.

220. Zhang, Y. J.; Schnoes, A. M.; Clapp, A. R., Dithiocarbamates as Capping Ligands for Water-Soluble Quantum Dots. *ACS Appl. Mater. Interfaces* **2010,** *2* (11), 3384-3395.

221. Clapp, A. R.; Goldman, E. R.; Mattoussi, H., Capping of Cdse-Zns Quantum Dots with Dhla and Subsequent Conjugation with Proteins. *Nat. Protoc.* **2006,** *1* (3), 1258-1266.

222. Gaponik, N.; Rogach, A. L., Thiol-Capped Cdte Nanocrystals: Progress and Perspectives of the Related Research Fields. *Phys. Chem. Chem. Phys.* **2010,** *12* (31), 8685-8693.

223. Mattoussi, H.; Mauro, J. M.; Goldman, E. R.; Anderson, G. P.; Sundar, V. C.; Mikulec, F. V.; Bawendi, M. G., Self-Assembly of Cdse-Zns Quantum Dot Bioconjugates Using an Engineered Recombinant Protein. *J. Am. Chem. Soc.* **2000,** *122* (49), 12142-12150.

224. Aldana, J.; Wang, Y. A.; Peng, X. G., Photochemical Instability of Cdse Nanocrystals Coated by Hydrophilic Thiols. *J. Am. Chem. Soc.* **2001,** *123* (36), 8844-8850.

225. Adamczak, M.; Hoel, H. J.; Gaudernack, G.; Barbasz, J.; Szczepanowicz, K.; Warszynski, P., Polyelectrolyte Multilayer Capsules with Quantum Dots for Biomedical Applications. *Colloids Surf., B* **2012,** *90*, 211-216.

226. Ruedas-Rama, M. J.; Hall, E. A. H., Multiplexed Energy Transfer Mechanisms in a Dual-Function Quantum Dot for Zinc and Manganese. *Analyst* **2009,** *134* (1), 159-169.

227. Ruedas-Rama, M. J.; Hall, E. A. H., A Quantum Dot-Lucigenin Probe for Cl(-). *Analyst* **2008,** *133* (11), 1556-1566.

228. Ruedas-Rama, M. J.; Orte, A.; Hall, E. A. H.; Alvarez-Pez, J. M.; Talavera, E. M., Effect of Surface Modification on Semiconductor Nanocrystal Fluorescence Lifetime. *Chemphyschem* **2011,** *12* (5), 919-929.

229. Majithia, R.; Patterson, J.; Bondos, S. E.; Meissner, K. E., On the Design of Composite Protein-Quantum Dot Biomaterials *Via* Self-Assembly. *Biomacromolecules* **2011,** *12* (10), 3629-3637.

230. Zylstra, J.; Amey, J.; Miska, N. J.; Pang, L. S.; Hine, C. R.; Langer, J.; Doyle, R. P.; Maye, M. M., A Modular Phase Transfer and Ligand Exchange Protocol for Quantum Dots. *Langmuir* **2011,** *27* (8), 4371-4379.

231. Clapp, A. R.; Medintz, I. L.; Mattoussi, H., Forster Resonance Energy Transfer Investigations Using Quantum-Dot Fluorophores. *Chemphyschem* **2006,** *7* (1), 47-57.

232. Velapoldi, R. A.; Tonnesen, H. H., Corrected Emission Spectra and Quantum Yields for a Series of Fluorescent Compounds in the Visible Spectral Region. *J. Fluoresc.* **2004,** *14* (4), 465-472.

233. Byrne, S. J.; Corr, S. A.; Rakovich, T. Y.; Gun'ko, Y. K.; Rakovich, Y. P.; Donegan, J. F.; Mitchell, S.; Volkov, Y., Optimisation of the Synthesis and Modification of Cdte Quantum Dots for Enhanced Live Cell Imaging. *J. Mater. Chem.* **2006,** *16* (28), 2896-2902.

234. Ruedas-Rama, M. J.; Orte, A.; Hall, E. A. H.; Alvarez-Pez, J. M.; Talavera, E. M., Quantum Dot Photoluminescence Lifetime-Based Ph Nanosensor. *Chem. Commun.* **2011,** *47* (10), 2898-2900.

235. Zhang, H.; Zhou, Z.; Yang, B.; Gao, M. Y., The Influence of Carboxyl Groups on the Photoluminescence of Mercaptocarboxylic Acid-Stabilized Cdte Nanoparticles. *J. Phys. Chem. B* **2003,** *107* (1), 8-13.

236. Hardzei, M.; Artemyev, M., Influence of Ph on Luminescence from Water-Soluble Colloidal Mn-Doped Znse Quantum Dots Capped with Different Mercaptoacids. *J. Lumin.* **2012,** *132* (2), 425-428.

237. Liu, Y. S.; Sun, Y. H.; Vernier, P. T.; Liang, C. H.; Chong, S. Y. C.; Gundersen, M. A., Ph-Sensitive Photoluminescence of Cdse/Znse/Zns Quantum Dots in Human Ovarian Cancer Cells. *J. Phys. Chem. C* **2007,** *111* (7), 2872-2878.

238. Mu, Q.; Xu, H.; Li, Y.; Ma, S.; Zhong, X., Adenosine Capped Qds Based Fluorescent Sensor for Detection of Dopamine with High Selectivity and Sensitivity. *Analyst* **2014,** *139* (1), 93-8.

239. Lees, E. E.; Nguyen, T. L.; Clayton, A. H.; Muir, B. W.; Mulvaney, P., The Preparation of Colloidally Stable, Water-Soluble, Biocompatible, Semiconductor Nanocrystals with a Small Hydrodynamic Diameter. *ACS Nano* **2009,** *3* (5), 1121-8.

240. Zhang, W.; Zhang, H.; Feng, Y.; Zhong, X., Scalable Single-Step Noninjection Synthesis of High-Quality Core/Shell Quantum Dots with Emission Tunable from Violet to near Infrared. *ACS Nano* **2012,** *6* (12), 11066-73.

241. Liu, L.; Zhong, X., A General and Reversible Phase Transfer Strategy Enabling Nucleotides Modified High-Quality Water-Soluble Nanocrystals. *Chem Commun (Camb)* **2012,** *48* (46), 5718-20.

242. Chen, H. S.; Ando, M.; Murase, N., Synthesis and Photoluminescence of Bright Water-Soluble Cdse/Zns Quantum Dots Overcoated by Hybrid Organic Shell. *Materials Letters* **2011,** *65* (19-20), 3146-3149.

243. Wang, X.; Ren, X.; Kahen, K.; Hahn, M. A.; Rajeswaran, M.; Maccagnano-Zacher, S.; Silcox, J.; Cragg, G. E.; Efros, A. L.; Krauss, T. D., Non-Blinking Semiconductor Nanocrystals. *Nature* **2009,** *459* (7247), 686-9.

244. Smith, A. M.; Nie, S., Next-Generation Quantum Dots. *Nat Biotechnol* **2009,** *27* (8), 732-3.

245. Shang, L.; Nienhaus, K.; Nienhaus, G. U., Engineered Nanoparticles Interacting with Cells: Size Matters. *J Nanobiotechnology* **2014,** *12*, 5.

246. Domingos, R. F.; Baalousha, M. A.; Ju-Nam, Y.; Reid, M. M.; Tufenkji, N.; Lead, J. R.; Leppard, G. G.; Wilkinson, K. J., Characterizing Manufactured Nanoparticles in the Environment: Multimethod Determination of Particle Sizes. *Environmental Science & Technology* **2009,** *43* (19), 7277-7284.

247. James, A. E.; Driskell, J. D., Monitoring Gold Nanoparticle Conjugation and Analysis of Biomolecular Binding with Nanoparticle Tracking Analysis (Nta) and Dynamic Light Scattering (Dls). *Analyst* **2013,** *138* (4), 1212-8.

248. Dragovic, R. A.; Gardiner, C.; Brooks, A. S.; Tannetta, D. S.; Ferguson, D. J.; Hole, P.; Carr, B.; Redman, C. W.; Harris, A. L.; Dobson, P. J., *et al.*, Sizing and Phenotyping of Cellular Vesicles Using Nanoparticle Tracking Analysis. *Nanomedicine* **2011,** *7* (6), 780-8.

249. Nikitin, N.; Trifonova, E.; Karpova, O.; Atabekov, J., Examination of Biologically Active Nanocomplexes by Nanoparticle Tracking Analysis. *Microsc Microanal* **2013,** *19* (4), 808-13.

250. Filipe, V.; Hawe, A.; Jiskoot, W., Critical Evaluation of Nanoparticle Tracking Analysis (Nta) by Nanosight for the Measurement of Nanoparticles and Protein Aggregates. *Pharm Res* **2010,** *27* (5), 796-810.

251. Boyd, R. D.; Pichaimuthu, S. K.; Cuenat, A., New Approach to Inter-Technique Comparisons for Nanoparticle Size Measurements; Using Atomic Force Microscopy, Nanoparticle Tracking Analysis and Dynamic Light Scattering. *Colloids and Surfaces A: Physicochemical and Engineering Aspects* **2011,** *387* (1-3), 35-42.

252. Mehtala, J. G.; Wei, A., Nanometric Resolution in the Hydrodynamic Size Analysis of Ligand-Stabilized Gold Nanorods. *Langmuir* **2014,** *30* (46), 13737-43.

253. De Temmerman, P.-J.; Verleysen, E.; Lammertyn, J.; Mast, J., Size Measurement Uncertainties of near-Monodisperse, near-Spherical Nanoparticles Using Transmission Electron Microscopy and Particle-Tracking Analysis. *Journal of Nanoparticle Research* **2014,** *16* (10).

254. Gallego-Urrea, J. A.; Tuoriniemi, J.; Hassellöv, M., Applications of Particle-Tracking Analysis to the Determination of Size Distributions and Concentrations

of Nanoparticles in Environmental, Biological and Food Samples. *TrAC Trends in Analytical Chemistry* **2011,** *30* (3), 473-483.

255. van der Pol, E.; Coumans, F. A.; Sturk, A.; Nieuwland, R.; van Leeuwen, T. G., Refractive Index Determination of Nanoparticles in Suspension Using Nanoparticle Tracking Analysis. *Nano Lett* **2014,** *14* (11), 6195-201.

256. Varga, Z.; Yuana, Y.; Grootemaat, A. E.; van der Pol, E.; Gollwitzer, C.; Krumrey, M.; Nieuwland, R., Towards Traceable Size Determination of Extracellular Vesicles. *J Extracell Vesicles* **2014,** *3*.

257. Du, S.; Kendall, K.; Morris, S.; Sweet, C., Measuring Number-Concentrations of Nanoparticles and Viruses in Liquids on-Line. *Journal of Chemical Technology & Biotechnology* **2010,** *85* (9), 1223-1228.

258. Shang, J.; Gao, X., Nanoparticle Counting: Towards Accurate Determination of the Molar Concentration. *Chem Soc Rev* **2014,** *43* (21), 7267-78.

259. Paramelle, D.; Sadovoy, A.; Gorelik, S.; Free, P.; Hobley, J.; Fernig, D. G., A Rapid Method to Estimate the Concentration of Citrate Capped Silver Nanoparticles from Uv-Visible Light Spectra. *Analyst* **2014,** *139* (19), 4855-61.

260. Leopold, N.; Haberkorn, M.; Laurell, T.; Nilsson, J.; Baena, J. R.; Frank, J.; Lendl, B., On-Line Monitoring of Airborne Chemistry in Levitated Nanodroplets: In Situ Synthesis and Application of Sers-Active Ag-Sols for Trace Analysis by Ft-Raman Spectroscopy. *Anal Chem* **2003,** *75* (9), 2166-71.

261. Sun, H.-T.; Sakka, Y., Luminescent Metal Nanoclusters: Controlled Synthesis and Functional Applications. *Science and Technology of Advanced Materials* **2014,** *15* (1), 014205.

262. Yu, P.; Wen, X.; Toh, Y.-R.; Ma, X.; Tang, J., Fluorescent Metallic Nanoclusters: Electron Dynamics, Structure, and Applications. *Particle & Particle Systems Characterization* **2015,** *32* (2), 142-163.

263. Korotcenkov, G.; Brinzari, V.; Cho, B. K., What Restricts Gold Clusters Reactivity in Catalysis and Gas Sensing Effects: A Focused Review. *Materials Letters* **2015,** *147*, 101-104.

264. Cui, M.; Zhao, Y.; Song, Q., Synthesis, Optical Properties and Applications of Ultra-Small Luminescent Gold Nanoclusters. *TrAC Trends in Analytical Chemistry* **2014,** *57*, 73-82.

265. Retnakumari, A.; Setua, S.; Menon, D.; Ravindran, P.; Muhammed, H.; Pradeep, T.; Nair, S.; Koyakutty, M., Molecular-Receptor-Specific, Non-Toxic, near-

Infrared-Emitting Au Cluster-Protein Nanoconjugates for Targeted Cancer Imaging. *Nanotechnology* **2010,** *21* (5), 055103.

266. Chen, L. Y.; Wang, C. W.; Yuan, Z.; Chang, H. T., Fluorescent Gold Nanoclusters: Recent Advances in Sensing and Imaging. *Anal Chem* **2015,** *87* (1), 216-29.

267. Zhang, L.; Wang, E., Metal Nanoclusters: New Fluorescent Probes for Sensors and Bioimaging. *Nano Today* **2014,** *9* (1), 132-157.

268. Li, J.; Zhu, J.-J.; Xu, K., Fluorescent Metal Nanoclusters: From Synthesis to Applications. *TrAC Trends in Analytical Chemistry* **2014,** *58*, 90-98.

269. Liu, J., DNA-Stabilized, Fluorescent, Metal Nanoclusters for Biosensor Development. *TrAC Trends in Analytical Chemistry* **2014,** *58*, 99-111.

270. Xie, J.; Zheng, Y.; Ying, J. Y., Protein-Directed Synthesis of Highly Fluorescent Gold Nanoclusters. *J Am Chem Soc* **2009,** *131* (3), 888-9.

271. Yan, L.; Cai, Y.; Zheng, B.; Yuan, H.; Guo, Y.; Xiao, D.; Choi, M. M. F., Microwave-Assisted Synthesis of Bsa-Stabilized and Hsa-Protected Gold Nanoclusters with Red Emission. *J. Mater. Chem.* **2012,** *22* (3), 1000-1005.

272. Yoshimoto, J.; Tanaka, N.; Inada, M.; Arakawa, R.; Kawasaki, H., Microwave-Assisted Synthesis of near-Infrared-Luminescent Ovalbumin-Protected Gold Nanoparticles as a Luminescent Glucose Sensor. *Chemistry Letters* **2014,** *43* (6), 793-795.

273. Joseph, D.; Geckeler, K. E., Synthesis of Highly Fluorescent Gold Nanoclusters Using Egg White Proteins. *Colloids Surf B Biointerfaces* **2014,** *115*, 46-50.

274. Selvaprakash, K.; Chen, Y. C., Using Protein-Encapsulated Gold Nanoclusters as Photoluminescent Sensing Probes for Biomolecules. *Biosens Bioelectron* **2014,** *61*, 88-94.

275. Chansuvarn, W.; Tuntulani, T.; Imyim, A., Colorimetric Detection of Mercury(Ii) Based on Gold Nanoparticles, Fluorescent Gold Nanoclusters and Other Gold-Based Nanomaterials. *TrAC Trends in Analytical Chemistry* **2015,** *65*, 83-96.

276. Tan, Z.; Xu, H.; Li, G.; Yang, X.; Choi, M. M., Fluorescence Quenching for Chloramphenicol Detection in Milk Based on Protein-Stabilized Au Nanoclusters. *Spectrochim Acta A Mol Biomol Spectrosc* **2015,** *149*, 615-620.

277. Li, Y.; Chen, Y.; Huang, L.; Ma, L.; Lin, Q.; Chen, G., A Fluorescent Sensor Based on Ovalbumin-Modified Au Nanoclusters for Sensitive Detection of Ascorbic Acid. *Anal. Methods* **2015,** *7* (10), 4123-4129.

278. Hemmateenejad, B.; Shakerizadeh-shirazi, F.; Samari, F., Bsa-Modified Gold Nanoclusters for Sensing of Folic Acid. *Sensors and Actuators B: Chemical* **2014,** *199*, 42-46.

279. Coté, G. L.; Cummins, B.; Simpson, J.; Gryczynski, Z.; Sørensen, T. J.; Laursen, B. W.; Graham, D.; Birch, D.; Coté, G., Cona-Based Glucose Sensing Using the Long-Lifetime Azadioxatriangulenium Fluorophore. **2014,** *8951*, 89510A.

280. Nisbet, A. D.; Saundry, R. H.; Moir, A. J. G.; Fothergill, L. A.; Fothergill, J. E., The Complete Amino-Acid Sequence of Hen Ovalbumin. *European Journal of Biochemistry* **1981,** *115* (2), 335-345.

281. Qin, L.; He, X.; Chen, L.; Zhang, Y., Turn-on Fluorescent Sensing of Glutathione S-Transferase at near-Infrared Region Based on Fret between Gold Nanoclusters and Gold Nanorods. *ACS Appl Mater Interfaces* **2015,** *7* (10), 5965-71.

282. Wang, H.; Zheng, C.; Dong, T.; Liu, K.; Han, H.; Liang, J., Wavelength Dependence of Fluorescence Quenching of Cdte Quantum Dots by Gold Nanoclusters. *The Journal of Physical Chemistry C* **2013,** *117* (6), 3011-3018.

283. Aldeek, F.; Ji, X.; Mattoussi, H., Quenching of Quantum Dot Emission by Fluorescent Gold Clusters: What It Does and Does Not Share with the Förster Formalism. *The Journal of Physical Chemistry C* **2013,** *117* (29), 15429-15437.

284. Raut, S.; Chib, R.; Butler, S.; Borejdo, J.; Gryczynski, Z.; Gryczynski, I., Evidence of Energy Transfer from Tryptophan to Bsa/Hsa Protected Gold Nanoclusters. *Methods and Applications in Fluorescence* **2014,** *2* (3), 035004.

285. Zhang, M.; Dang, Y.-Q.; Liu, T.-Y.; Li, H.-W.; Wu, Y.; Li, Q.; Wang, K.; Zou, B., Pressure-Induced Fluorescence Enhancement of the Bsa-Protected Gold Nanoclusters and the Corresponding Conformational Changes of Protein. *The Journal of Physical Chemistry C* **2013,** *117* (1), 639-647.

286. Martinod, A.; Euvrard, M.; Foissy, A.; Neville, A., Progressing the Understanding of Chemical Inhibition of Mineral Scale by Green Inhibitors. *Desalination* **2008,** *220* (1-3), 345-352.

287. Verdoes, D.; Van Landschoot, R. C.; Van Rosmalen, G. M., Crystallization in Detergent Performance. *Journal of Crystal Growth* **1990,** *99* (1-4), 1124-1129.

288. Morse, J. W.; Arvidson, R. S.; Luttge, A., Calcium Carbonate Formation and Dissolution. *Chem. Rev.* **2007,** *107* (2), 342-381.

289. Wang, Y.; Price, A. D.; Caruso, F., Nanoporous Colloids: Building Blocks for a New Generation of Structured Materials. *J. Mater. Chem.* **2009,** *19* (36), 6451-6464.

290. Naka, K.; Chujo, Y., Control of Crystal Nucleation and Growth of Calcium Carbonate by Synthetic Substrates. *Chem. Mater.* **2001,** *13* (10), 3245-3259.

291. Song, R.-Q.; Cölfen, H., Additive Controlled Crystallization. *CrystEngComm* **2011,** *13* (5), 1249-1276.

292. Niederberger, M.; Colfen, H., Oriented Attachment and Mesocrystals: Non-Classical Crystallization Mechanisms Based on Nanoparticle Assembly. *Phys. Chem. Chem. Phys.* **2006,** *8* (28), 3271-3287.

293. Song, R. Q.; Colfen, H., Mesocrystals--Ordered Nanoparticle Superstructures. *Adv. Mater.* **2010,** *22* (12), 1301-1330.

294. Song, R. Q.; Colfen, H.; Xu, A. W.; Hartmann, J.; Antonietti, M., Polyelectrolyte-Directed Nanoparticle Aggregation: Systematic Morphogenesis of Calcium Carbonate by Nonclassical Crystallization. *ACS Nano* **2009,** *3* (7), 1966-1978.

295. Dalas, E.; Klepetsanis, P.; Koutsoukos, P. G., The Overgrowth of Calcium Carbonate on Poly(Vinyl Chloride-Co-Vinyl Acetate-Co-Maleic Acid). *Langmuir* **1999,** *15* (23), 8322-8327.

296. Song, R. Q.; Xu, A. W.; Antonietti, M.; Colfen, H., Calcite Crystals with Platonic Shapes and Minimal Surfaces. *Angew Chem Int Ed Engl* **2009,** *48* (2), 395-399.

297. López-Marzo, A.; Pons, J.; Merkoçi, A., Controlled Formation of Nanostructured Caco3–Pei Microparticles with High Biofunctionalizing Capacity. *J. Mater. Chem.* **2012,** *22* (30), 15326-15335.

298. Arias, J. L.; Neira-Carrillo, A.; Arias, J. I.; Escobar, C.; Bodero, M.; David, M.; Fernandez, M. S., Sulfated Polymers in Biological Mineralization: A Plausible Source for Bio-Inspired Engineering. *J. Mater. Chem.* **2004,** *14* (14), 2154-2160.

299. Butler, M. F.; Glaser, N.; Weaver, A. C.; Kirkland, M.; Heppenstall-Butler, M., Calcium Carbonate Crystallization in the Presence of Biopolymers. *Cryst. Growth Des.* **2006,** *6* (3), 781-794.

300. Petrov, A. I.; Volodkin, D. V.; Sukhorukov, G. B., Protein-Calcium Carbonate Coprecipitation: A Tool for Protein Encapsulation. *Biotechnol. Prog.* **2005,** *21* (3), 918-925.

301. Sukhorukov, G. B.; Volodkin, D. V.; Gunther, A. M.; Petrov, A. I.; Shenoy, D. B.; Mohwald, H., Porous Calcium Carbonate Microparticles as Templates for Encapsulation of Bioactive Compounds. *J. Mater. Chem.* **2004,** *14* (14), 2073-2081.

302. Hobbs, S. K.; Monsky, W. L.; Yuan, F.; Roberts, W. G.; Griffith, L.; Torchilin, V. P.; Jain, R. K., Regulation of Transport Pathways in Tumor Vessels: Role of Tumor Type and Microenvironment. *Proc. Natl. Acad. Sci.* **1998,** *95* (8), 4607-4612.

303. Russell, R. J.; Pishko, M. V.; Gefrides, C. C.; McShane, M. J.; Coté, G. L., A Fluorescence-Based Glucose Biosensor Using Concanavalin a and Dextran Encapsulated in a Poly(Ethylene Glycol) Hydrogel. *Anal. Chem.* **1999,** *71* (15), 3126-3132.

304. Zhao, D.; Zhuo, R. X.; Cheng, S. X., Alginate Modified Nanostructured Calcium Carbonate with Enhanced Delivery Efficiency for Gene and Drug Delivery. *Mol Biosyst* **2012,** *8* (3), 753-759.

305. Parakhonskiy, B. V.; Haase, A.; Antolini, R., Sub-Micrometer Vaterite Containers: Synthesis, Substance Loading, and Release. *Angew. Chem., Int. Ed.* **2012,** *51* (5), 1195-1197.

306. Neira-Carrillo, A.; Mercade-Jaque, P.; Diaz-Dosque, M.; Tapia-Villanueva, C.; Yazdani-Pedram, M., Influence of Chitosan Grafted Poly(Vinyl Sulfonic Acid) as Template on the Calcium Carbonate Crystallization. *J. Iran. Chem. Soc.* **2011,** *8* (3), 811-824.

307. Kim, S.; Ko, J. W.; Park, C. B., Bio-Inspired Mineralization of Co2 Gas to Hollow Caco3 Microspheres and Bone Hydroxyapatite/Polymer Composites. *Journal of Materials Chemistry* **2011,** *21* (30), 11070.

308. Volodkin, D. V.; Petrov, A. I.; Prevot, M.; Sukhorukov, G. B., Matrix Polyelectrolyte Microcapsules: New System for Macromolecule Encapsulation. *Langmuir* **2004,** *20* (8), 3398-3406.

309. Parakhonskiy, B. V.; Foss, C.; Carletti, E.; Fedel, M.; Haase, A.; Motta, A.; Migliaresi, C.; Antolini, R., Tailored Intracellular Delivery Via a Crystal Phase Transition in 400 Nm Vaterite Particles. *Biomaterials Science* **2013**.

310. Chen, S.-F.; Colfen, H.; Antonietti, M.; Yu, S.-H., Ethanol Assisted Synthesis of Pure and Stable Amorphous Calcium Carbonate Nanoparticles. *Chemical Communications* **2013,** *49* (83), 9564-9566.

311. Sukhorukov, G. B.; Donath, E.; Lichtenfeld, H.; Knippel, E.; Knippel, M.; Budde, A.; Möhwald, H., Layer-by-Layer Self Assembly of Polyelectrolytes on Colloidal Particles. *Colloids and Surfaces A: Physicochemical and Engineering Aspects* **1998,** *137* (1–3), 253-266.

312. Volodkin, D. V.; Petrov, A. I.; Prevot, M.; Sukhorukov, G. B., Matrix Polyelectrolyte Microcapsules: New System for Macromolecule Encapsulation. *Langmuir* **2004,** *20* (8), 3398-3406.

313. Roberts, J. R.; Ritter, D. W.; McShane, M. J., A Design Full of Holes: Functional Nanofilm-Coated Microdomains in Alginate Hydrogels. *J Mater Chem B Mater Biol Med* **2013,** *107* (25), 3195-3201.

314. Balabushevich, N. G.; Lopez de Guerenu, A. V.; Feoktistova, N. A.; Skirtach, A. G.; Volodkin, D., Protein-Containing Multilayer Capsules by Templating on Mesoporous Caco Particles: Post- and Pre-Loading Approaches. *Macromol Biosci* **2015**.

315. Balabushevich, N. G.; Lopez de Guerenu, A. V.; Feoktistova, N. A.; Volodkin, D., Protein Loading into Porous Caco3 Microspheres: Adsorption Equilibrium and Bioactivity Retention. *Phys Chem Chem Phys* **2015,** *17* (4), 2523-30.

316. Szarpak, A.; Pignot-Paintrand, I.; Nicolas, C.; Picart, C.; Auzely-Velty, R., Multilayer Assembly of Hyaluronic Acid/Poly(Allylamine): Control of the Buildup for the Production of Hollow Capsules. *Langmuir* **2008,** *24* (17), 9767-74.

317. De Temmerman, M. L.; Demeester, J.; De Vos, F.; De Smedt, S. C., Encapsulation Performance of Layer-by-Layer Microcapsules for Proteins. *Biomacromolecules* **2011,** *12* (4), 1283-9.

318. Fischer, K.; Bipp, H. P., Removal of Heavy Metals from Soil Components and Soil by Natural Chelating Agents. *Water, Air, and Soil Pollution* **2002,** *138* (1/4), 271-288.

319. Kalb, A. J.; Levitzki, A., Metal-Binding Sites of Concanavalin a and Their Role in the Binding of A-Methyl D-Glucopyranoside. *Biochemical Journal* **1968,** *109* (4), 669-672.

320. Agrawal, B. B. L.; Goldstein, I. J., Protein–Carbohydrate Interaction. Xv. The Role of Bivalent Cations in Concanavalin a – Polysaccharide Interaction. *Canadian Journal of Biochemistry* **1968,** *46* (9), 1147-1150.

321. Cho, K. L.; Hill, A. J.; Caruso, F.; Kentish, S. E., Chlorine Resistant Glutaraldehyde Crosslinked Polyelectrolyte Multilayer Membranes for Desalination. *Adv Mater* **2015,** *27* (17), 2791-6.

322. Yu, Q.; Kandegedara, A.; Xu, Y.; Rorabacher, D. B., Avoiding Interferences from Good's Buffers: A Contiguous Series of Noncomplexing Tertiary Amine Buffers Covering the Entire Range of Ph 3-11. *Anal Biochem* **1997,** *253* (1), 50-6.

323. Kaushal, V.; Barnes, L. D., Effect of Zwitterionic Buffers on Measurement of Small Masses of Protein with Bicinchoninic Acid. *Analytical Biochemistry* **1986,** *157* (2), 291-294.

324. Aslan, K.; Lakowicz, J. R.; Geddes, C. D., Plasmonic Glucose Sensing. **2006,** *11*, 259-282.

325. Achatz, D. E.; Ali, R.; Wolfbeis, O. S., Luminescent Chemical Sensing, Biosensing, and Screening Using Upconverting Nanoparticles. *Top Curr Chem* **2011,** *300*, 29-50.